Syntheses and Analyses of Semi-active Control Algorithms for a Magneto-Rheological Damper for Vehicle Suspensions

En Rong Wang

A Thesis

in

The Department

of

Mechanical and Industrial Engineering

Presented in Partial Fulfillment of the Requirements
for the Degree of Doctor of Philosophy (Mechanical Engineering) at
Concordia University
Montreal, Quebec, Canada

December 2005

© En Rong Wang, 2005

Library and
Archives Canada

Published Heritage
Branch

395 Wellington Street
Ottawa ON K1A 0N4
Canada

Bibliothèque et
Archives Canada

Direction du
Patrimoine de l'édition

395, rue Wellington
Ottawa ON K1A 0N4
Canada

Your file Votre référence
ISBN: 978-0-494-16299-6
Our file Notre référence
ISBN: 978-0-494-16299-6

NOTICE:
The author has granted a non-exclusive license allowing Library and Archives Canada to reproduce, publish, archive, preserve, conserve, communicate to the public by telecommunication or on the Internet, loan, distribute and sell theses worldwide, for commercial or non-commercial purposes, in microform, paper, electronic and/or any other formats.

The author retains copyright ownership and moral rights in this thesis. Neither the thesis nor substantial extracts from it may be printed or otherwise reproduced without the author's permission.

AVIS:
L'auteur a accordé une licence non exclusive permettant à la Bibliothèque et Archives Canada de reproduire, publier, archiver, sauvegarder, conserver, transmettre au public par télécommunication ou par l'Internet, prêter, distribuer et vendre des thèses partout dans le monde, à des fins commerciales ou autres, sur support microforme, papier, électronique et/ou autres formats.

L'auteur conserve la propriété du droit d'auteur et des droits moraux qui protège cette thèse. Ni la thèse ni des extraits substantiels de celle-ci ne doivent être imprimés ou autrement reproduits sans son autorisation.

In compliance with the Canadian Privacy Act some supporting forms may have been removed from this thesis.

While these forms may be included in the document page count, their removal does not represent any loss of content from the thesis.

Conformément à la loi canadienne sur la protection de la vie privée, quelques formulaires secondaires ont été enlevés de cette thèse.

Bien que ces formulaires aient inclus dans la pagination, il n'y aura aucun contenu manquant.

Canada

ABSTRACT

Syntheses and Analyses of Semi-active Control Algorithms for a Magneto-Rheological Damper for Vehicle Suspensions

En Rong Wang

Vehicle suspensions impose conflicting design requirements to satisfy the performance goals related to ride, handling and road holding. Semi-active damping suspensions, with their low cost and low power requirement, have been extensively investigated to achieve better compromises among different performance measures. The magneto-rheological (MR) fluid dampers offer superior potential to achieve rapid variations in the damping force and thus the wide bandwidth. The MR dampers, however, exhibit strong nonlinearities associated with force saturation and hysteresis, which affect the force-tracking performance of the controller in an adverse manner. This dissertation research focuses on characterization and modeling of the hysteretic force -velocity (*F-v*) characteristics of a MR-fluid damper, and analyses of different semi-active controller syntheses to achieve improved multi-objective vehicle suspension performance. The force-limiting and hysteresis properties of a prototype MR-damper are characterized in the laboratory as functions of applied magnetic field, and response and excitation variables. An asymmetric force generation algorithm is formulated and integrated into the command current circuit to achieve asymmetric force in compression and rebound from the symmetric damper hardware. The measured data are used to identify the low-speed pre-yield, post-yield, force-limiting and hysteretic force-velocity characteristics in both symmetric as well as asymmetric damping modes.

A generalized analytical model of the MR-damper is developed using symmetric and asymmetric sigmoid functions. The validity of the proposed model is demonstrated under wide ranges of control current and excitations. A number of control syntheses are formulated to achieve semi-active modulation in drive current of the MR-damper, including four different on-off and "skyhook"-based hi-lo, and "inverse-model"-based hi-lo and sliding-mode controllers. Continuous modulation (CM) and asymmetric damping force generation (ADFG) algorithms are proposed and integrated within the control policies to minimize switching transients in the symmetric and asymmetric modes. The "inverse model"-based sliding mode semi-active controller offers effective suppression of damper hysteresis effect and enhanced robustness on vehicle loading uncertainties. The relative performance characteristics of different controllers are evaluated for a "quarter-vehicle" model under deterministic and random road excitations using a set of performance measures. The results suggest that inverse model-based syntheses yield poor force-tracking performance, while the "skyhook"-based hi-lo control algorithm yields superior performance.

A hardware-in-the-loop (HiL) test platform is developed to validate the MR-damper model and the "quarter-vehicle" model with the proposed semi-active controller syntheses. A drive circuit is designed to amplify the command signal and a PID feedback technique is employed to compensate for the delays in the drive current. The performance characteristics of the "quarter-vehicle" model with both the passive and "skyhook"-based hi-lo semi-active damping are evaluated in symmetric as well as asymmetric damping modes under different excitations. The measured data are used to demonstrate the validity of MR-damper model and the hi-lo semi-active controller model in SCM and ACM modes.

ACKNOWLEDGEMENTS

First and foremost, I would like to pay my great appreciation to my supervisors Dr. Subhash Rakheja and Dr. Chun-Yi Su for their initiation of the project, and their constant guidance and dedication throughout the thesis work. Financial supports, provided by Concordia University Graduate Fellowship and Concordia University Graduate International Student Fee Remission Awards, are gratefully acknowledged. Without the supervision from my supervisors and the financial supports from the university, this endeavor would not have been possible.

I also would like to acknowledge the support provided by Mr. Danius Juras in the experimental setups and the assistance provided by Mr. Cedric Boudinet in assistaing for preparing the HiL monitor. I also would like to extend my thanks to my colleague, Ms. Xiao Qing Ma, for her collaborations.

Finally, I would like to dedicate this thesis to my wife Yuan-Xia Lu and my son Peng-Yu Wang, for their great help during the thesis completion, as well as to Chinese Scholarship Council and Nanjing Normal University in China, for their partial financial supports.

TABLE OF CONTENTS

CHAPTER 1 INTRODUCTION AND LITERATURE REVIEW

CHAPTER 2 CHARACTERIZATION AND MODELING OF A MR-DAMPER

CHAPTER 3 SYNTHESES OF SEMI-ACTIVE MR-DAMPER CONTROLLERS

CHAPTER 4 PERFORMANCE ANALYSES OF HI-LO SEMI-ACTIVE DAMPING

CHAPTER 5 PERFORMANCE ANALYSES OF INVERSE MODEL BASED HI-LO SEMI-ACTIVE DAMPING

CHAPTER 8 CONCLUSIONS AND RECOMMENDATIONS FOR FUTURE WORK

LIST OF FIGURES

LIST OF TABLES

NOMENCLATURE

a_0	Constant value of model parameter
a_1	Constant value of model parameter ($(\mathrm{m/s})^{-1}$)
a_2	Constant value of model parameter (A^{-1})
a_3	Constant value of model parameter (A^{-1})
a_4	Constant value of model parameter ($(\mathrm{m/s})^{-1}$)
a_m	Peak magnitude of displacement excitation (m)
a_s	Acceleration of sprung mass ($\mathrm{m/s^2}$)
a_u	Acceleration of unsprung mass ($\mathrm{m/s^2}$)
$a_\mathrm{s}(f)$	RMS acceleration of sprung mass in function of frequency
$a_\mathrm{u}(f)$	RMS acceleration of unsprung mass in function of frequency
$a_\mathrm{r}(f)$	RMS suspension displacement in function of frequency
$a_\mathrm{i}(f)$	RMS acceleration of road excitation in function of frequency
$C_\mathrm{i}(\cdot)$	Command current gain function of MR-damper F-v model
c_s	Viscous damping coefficient of suspension damper (kNs/m)
c_t	Viscous damping coefficient of tire (kNs/m)
c_0	Viscous damping coefficient of base-supported suspension damper (kNs/m)
DLC	Dynamic load coefficient due to tire force
DTR	Deviation in peak tire force ratio
e_i	Current error between the given and inverse currents (A)
e_s	Position error between sprung masses of plant and referenodel (m)
$\dot{e}_\mathrm{s}$	Velocity error between sprung masses of plant and reference model (m/s)
$f_\mathrm{d}^{-1}(\cdot)$	Function of inverse model
f	Frequency (Hz)
$f_\mathrm{n\text{-}s0}$	Nominal natural frequency of sprung mass (Hz)
$f_\mathrm{n\text{-}s}$	Natural frequency of sprung mass (Hz)
$f_\mathrm{n\text{-}u0}$	Nominal natural frequency of unsprung mass (Hz)
$f_\mathrm{n\text{-}u}$	Natural frequency of unsprung mass (Hz)
f_T	transition frequency (Hz)
F_d0	Nominal target force of the sliding mode control (kN)
F_c	Target damping force of sliding mode control (kN)

F_d	Damping force (kN)
F_k	Suspension spring force (kN)
F_T	Dynmic force due to tire kN)
F_m	Maximum damping force corresponding to v_m (kN)
F_h	Passive hysteron damping force (kN)
F_0	Constant value of model parameter (kN)
F_t	Transition mean damping force (kN)
F_T	Dynamic tire force (kN)
F_{T0}	Peak magnitude of nominal shock tire force (kN)
$\bar{F}_t$	Mean tire force (kN)
F_{Trms}	RMS tire force (kN)
F_{mc}	Maximum damping forces corresponding to v_m developed in compression (kN)
F_{me}	Maximum damping forces corresponding to v_m developed in rebound (kN)
F_{tc}	Transition forces in compression corresponding to v_{tc} (kN)
F_{te}	Transition forces in rebound corresponding to v_{te} (kN)
F_b	Force offset from asymmetric coordinate system to symmetric coordinate (kN)
i_d	Drive current (A)
i_c	Control current (A)
i_s	Asymmetric control current (A)
i_z	Command currnt derived from the inverse model (A)
i_L	Lower value of drive current in compression (A)
i_H	Upper limit of drive current in rebound (A)
I_0	Constant value of model parameter (A)
I_1	Constant value of model parameter (A)
k_s	Stiffness of suspension spring (kN/m)
k_t	Stiffness of tire (kN/m)
k_0	Constant value of model parameter
k_1	Constant value of model parameter
k_{1c}	Constant value of model parameter
k_{1e}	Constant value of model parameter
k_2	Constant value of model parameter
k_3	Constant value of model parameter

k_4	Constant value of model parameter
k_5	Constant value of model parameter
k_6	Constant value of model parameter
k_c	Gain of "skyhook"-based controller
K	Gain of sliding mode control
m_{s0}	Nominal value of sprung mass (kg)
m_s	Sprung mass (kg)
m_u	Unsprung mass (kg)
∇m	Variations between sprung mass and its nominal value
$M_p(\cdot)$	Multipler of asymmetric damping force generation (ADFG) algorithm
$M_c(\cdot)$	Multipler of continuous modulation (CM) algorithm
n	Order of controller
p	Asymmetry factor of ADFG algorithm
p_c	Asymmetry factor of CM algorithm
RDR	Peak relative displacement ratio
s	Defined sliding surface
$\mathrm{sgn}(\cdot)$	Sign function
$\mathrm{sat}(\cdot)$	Saturation function
SDR_s	Shock displacement of sprung mass
SDR_u	Shock displacement of unsprung mass
SAR_s	Shock acceleration of sprung mass
SAR_u	Shock acceleration of unsprung mass
T_{as}	Transmissibility of sprung mass acceleration
T_{au}	Transmissibility of unsprung mass acceleration
T_{dr}	Transmissibility of relative displacement of suspension damper
U	Squared error cost function for model parameter identification
V	Lyapunov function
v_r	Suspension velocity (m/s)
v_m	Peak value of the damper velocity (m/s)
v_h	Zero-force velocity intercept corresponding to the zero damping force (m/s)
v_t	Transition velocity corresponding to onset of force-limiting property (m/s)
v_{tc}	Transition velocities in compression to onset of force-limiting property (m/s)

v_{te}	Transition velocities in rebound to onset of force-limiting property (m/s)
v_b	Velocity offset from asymmetric coordinate to symmetric coordinate (kN)
x_{s0}	Displacement of sprung mass for the reference model (m)
x_s	Displacement of sprung mass (m)
x_u	Displacement of unsprung mass (m)
Δx_s	Static deflection of suspension spring (m)
Δx_u	Static deflection of tire (m)
x_i	Displacement of road excitation (m)
$\ddot{x}_i$	Acceleration of road excitation (m/s^2)
x_r	Relative displacement of MR-damper (m)
x_{s0}	Displacement of nominal sprung mass (m)
$\dot{x}_{s0}$	Velocity of sprung mass for the reference model (m/s)
x_s	Displacement of sprung mass (m)
$\dot{x}_s$	Velocity of sprung mass (m/s)
$\ddot{x}_s$	Acceleration of sprung mass (m/s^2)
x_u	Displacement of unsprung mass (m)
$\dot{x}_u$	Velocity of unsprung mass (m/s)
$\ddot{x}_u$	Acceleration of unsprung mass (m/s^2)
$\ddot{x}_r$	Relative acceleration of MR-damper (m/s^2)
z_c	Logic switching condition of semi-active controller
μ	Pulse severity parameter of rounded pulse excitation function
ω_0	Fundamental frequency of rounded pulse excitation function (rad/s)
ξ	Smoothing factor of ADFG algorithm
ξ_c	Smoothing factor of CM algorithm
γ	Asymmetric ratio of damping force in reboud to compression
β	Variation limit of sprung mass with respect to its nominal value
β_L, β_h	Low and high speed damping coefficients of mean F-v curve (kNs/m)
β_{hc}, β_{he}	High speed viscous damping coefficients in compression and rebound (kNs/m)
λ	Slope of sliding surface
φ	Sliding condition gain
ε	Small postive value for sliding mode control syhthesis

CHAPTER 1

INTRODUCTION AND LITERATURE REVIEW

1.1 Introduction

The suspension system of a road vehicle performs two important tasks: (i) isolation of the vehicle body from external road disturbances; and (ii) maintain the desired vehicle body attitude through appropriate road holding and guidance control. The vehicle suspensions are invariably designed with nonlinear characteristics to achieve satisfactory ride, road-holding, handling and directional performances. These performance measures, however, impose conflicting design requirements for the suspension system [1]. A soft suspension coupled with light damping would be most desirable to achieve improved ride performance, while the rattle space, handling and control performance enhancements necessitate relatively stiffer suspension and higher damping [2]. The performance characteristics of road vehicles with passive suspensions are thus limited partly due to uncontrollable property of the hydraulic dampers.

A vast number of variable damping concepts based upon semi-active or active control have evolved during the past 4 decades, to achieve intelligent vehicle suspension designs (IVSD) that could provide better compromise among the different conflicting performance measures. Despite the evolutions in active and semi-active suspension systems, the implementations of such systems to road vehicles have been extremely limited due to many factors. The use of fully-active suspension systems has been justified when the associated high cost, hardware complexities and the power demand, outweigh the performance gain [3]. The use of semi-active suspension dampers, on the other hand, has been limited due to undesired dynamics associated with switching discontinuities, insufficient dynamic range, limited bandwidth, etc. [4]. The magneto-rheological (MR) fluid dampers offer superior potential to achieve variable damping with minimal power requirement and relatively high bandwidth [5-11]. The MR-suspension systems are thus believed to offer high potential to satisfy the afore-mentioned conflicting design requirements.

The MR dampers offer high viscous damping corresponding to low velocities in the pre-yield condition, while the post-yield saturation at high velocities can be characterized by low viscous damping [5-8]. The variations in the low-velocity rise and post-yield saturation can be achieved in a highly rapid manner with only minimal current. Moreover, the MR dampers can provide a fail-safe suspension damping, since they continue to provide light damping in a passive manner, in the event of a control hardware malfunction. The MR dampers, however, provide highly nonlinear and hysteretic force-velocity (*F-v*) properties, which pose considerable complexities for the controller design.

A number of control concepts have been developed to achieve variable MR-damping in a semi-active manner. These include the “skyhook”, “sliding-mode”, and “clipped semi-active” control schemes [12-15]. All of these studies consider mean *F-v* characteristics of the damper, while neglecting the hysteretic behaviour. The hysteretic *F-v* properties of a damper could yield considerable errors in the tracking control [16]. A few studies have also developed regression-based models to characterize the hysteretic *F-v* properties of the MR-damper [6-12], which may be applied to simplify the controller synthesis. These models, however, cannot characterize the hysteretic properties as functions of the applied current and the nature of excitation.

The proposed dissertation research focuses on modeling the hysteretic *F-v* characteristics of a MR-fluid damper and synthesizing different semi-active controllers for realizing the intelligent vehicle suspension design. For this purpose, a generalized hysteretic *F-v* model of MR-fluid damper is developed to characterize both symmetric and asymmetric direct current (DC) controlled hysteretic *F-v* properties of the MR-fluid damper. The hysteretic *F-v* properties are characterized as functions of the intensity of the applied electro-magnetic field, displacement and velocity of the piston, and the nature of road excitation (magnitude and frequency), and integrated into the model synthesis. Based on the proposed model, a hysteretic inverse model of the MR-damper is further developed for compensating the hysteresis effects of the MR-damper in the controller syntheses. Furthermore, a "skyhook"-based reference model of the suspension system is suggested as the ideal suspension control index and used as reference model for the controller synthesis, which could address the needed compromise between different requirements. Since the MR-fluid damper exhibits strong hysteresis and force-limiting properties, and the road vehicles invariably face with the parameter uncertainties, a "sliding mode"-based robust control with hysteresis rejection abilities would be highly desirable. A hybrid semi-active control (HSC) scheme, named as the "inverse model"-based sliding mode semi-active controller, is formulated to realize the multi-objective optimization including the fundamental semi-active suspension performance index control, parameter adaptive control, hysteresis rejection control, and asymmetric damping force generation (ADFG) control using the symmetric MR-fluid damper. The performance potentials of the proposed HSC synthesis and the well-established "skyhook"-based hi-lo and "inverse model"-based hi-lo semi-active syntheses are assessed in the laboratory through development of a hardware-in-the-loop (HiL) test platform.

1.2 Literature Review

The development of a controller synthesis for the hysteretic MR-suspension damping properties involves thorough understanding of the MR-fluid damper behavior, the role of various operating parameters, the control concepts and design, the vehicle ride dynamics and road holding properties, etc.. The reported studies relevant to these topics are thus thoroughly reviewed to build the necessary knowledge and background, and to formulate the scope of the dissertation research. The reported studies, grouped under relevant topics of interest, are discussed in the following subsections.

1.2.1 Developments and considerations in vehicle suspension design

Suspension design plays an important role in the performance characteristics of road vehicles, namely the ride, handling and road-holding performances. The design task for the road vehicle suspension is quite complex, since the road vehicles inevitably encounter a wide range of road conditions involving varying surface roughness and discontinuities (potholes), loads and speeds. Furthermore, the ride and handling measures impose conflicting requirements for the suspension design [1, 2, 17]. A soft and lightly damped suspension is desirable for attenuation of continuous vibration arising from tires interactions with randomly rough road surfaces. Such interactions with abruptness of the road surface, however, require relatively higher suspension damping to suppress the resonant oscillation. Relatively hard and damped suspensions are desirable to achieve improved handling and directional control performance [1, 17]. The vehicle interactions with the road irregularities cause comprehensive magnitudes of shock and vibration that may deteriorate the comfort and handling properties of the vehicle. The vehicle suspension systems are thus designed to satisfy two essential performance requirements: (i) isolation of the vehicle body from disturbances arising from the roads; and (ii) maintaining the vehicle body attitude and a firm contact between the road and the tires to provide reliable guidance along the track. The suspension designs are thus attempted to achieve a satisfactory compromise between the two measures [18-22].

A number of studies have investigated the role of suspension on the ride and handling properties of road vehicles [1, 19, 23, 24] and various concepts in passive damping variations to achieve better compromise between the two measures [25-29]. A thorough review of these studies on the role of suspension system in view of ride, infrastructure damage, suspension working space, energy consumption, rollover stability and yaw stability, braking and traction performances has been presented by Cole [24]. Rakheja *et al.* [1], Tong *et al.* [28], Nishiyama *et al.* [30] have investigated the role of suspension damping in enhancement of vehicle road friendliness, ride quality and attenuation of whole-body vibration transmitted to the seated drivers. Various concepts in nonlinear damping forces asymmetric in compression and rebound have also been investigated using piecewise linear formulations for the *F-v* characteristics [1, 31-33]. A few studies have suggested that higher damping in rebound yields improved road holding and ride, while lower damping coefficient at higher velocities could provide better ride [1, 33].

A passive vehicle suspension system is usually designed with energy restoring and dissipating components. Soft suspension springs are desirable to achieve attenuation of body vertical vibration at frequencies above 4.0 Hz, where the human riders exhibit most sensitivity to vehicle vibration [2, 17, 30, 34, 35]. The suspension systems are thus designed with soft springs to yield the vertical mode resonance of the body in the 1.5-2 Hz range. Although a softer suspension would be desirable to enhance the ride vibration environment and dynamic pavement loading performance, the need for excessive rattle space requirement is prohibitive in lowering the spring rates further. Moreover, soft springs would cause excessive body roll due to reduced effective roll stiffness of the suspension. The anti-roll bars are thus used in conjunction with soft suspension to limit the roll deflection of the body. The design of improved suspension systems would thus be limited to selection of appropriate damping characteristics, apart from the suspension linkages. A higher damping is essential to suppress the resonant motions of the car-body, while a lightly damped suspension may provide effective isolation from the road-induced vibration [2, 17]. Moreover, a higher damping would lead to less variation in the dynamic forces and thus reduce the road damage potential. A higher damping would also improve the handing performance by minimizing the wheel-hop and thus the potential for loss of tire-road contact.

The vehicle suspension system can be mainly classified into two types: (i) conventional passive suspension; and (ii) intelligent suspension. The conventional passive suspension system has been widely utilized in modern vehicles and comprises passive hydraulic suspension damper, while an intelligent suspension is intended to realize optimal performance with fully-active or semi-active controllable dampers. These may include the active suspensions, slow active suspensions and the semi-active suspensions [2, 36, 37]. A slow active suspension differs from an active suspension, as it employs a low bandwidth hydraulic actuator in series with a soft suspension spring to achieve control of vibration at low frequencies [2]. Considerable efforts have also been made to derive optimal passive suspension to achieve particular objectives involving either ride or tire pavement loads. Lu [20] and Naude *et al.* [29] proposed an optimum suspension design to realize "road-friendly" vehicle suspension systems. Goncalves *et al.* [21] proposed optimal vehicle suspension to achieve improved comfort performance using flexible multi-body dynamics. These studies focus only on one objective, either the ride comfort or road-friendliness. The design of a suspension damper, however, necessitates consideration of all of the desired performance measures.

Different concepts in intelligent suspension systems have evolved in the recent years that utilize the MR fluids to achieve rapid variation in damping forces. These studies are reviewed in further subsection. Chalasani [23] proposed criteria for assessing the suspension performances in terms of ride comfort, suspension stroke and the road holding, which are the time-averaged statistics of root-mean-square (RMS) body acceleration, RMS suspension deflection and RMS dynamic tire force, respectively. The RMS tire force influences the road damage caused by the vehicle and also its road holding. RMS body acceleration is a useful criterion for assessing driver ride comfort and payload vibration. RMS suspension deflection is a measure of the working space required by the suspension.

A wide range of methods are applied to assess the performance characteristics of vehicle suspensions. These include methods based upon field and laboratory measurements, and analysis of analytical models. The methodologies, however, differ depending upon the goals of the study. The assessments of ride vibration responses of a suspension system often evaluate the nature of sprung mass vibration (magnitude and frequency contents) and relative suspension travel. The ride quality of a vehicle is mostly assessed in terms of sprung mass acceleration, which has been distinctly related to the human perception of discomfort [38]. A number of studies on ride assessments of road and off-road vehicles based upon field measurements and analyses of analytical models have been reported in the literature [23, 28, 34, 35, 39, 40]. The ride performance of a vehicle is often assessed in terms of overall frequency-weighted RMS acceleration due to vibration encountered at the occupant location. The frequency-weighting filters recommended in ISO-2631-1 (1997) for different axis of translational and rotational vibration are used to account for human response to vibration.

A few studies have also assessed the relative ride quality of different suspensions on the basis of subjective responses of the drivers [13, 17, 30]. Other studies have assessed the suspension performance in terms of dynamic tire loads transmitted to the pavement in terms of variation in tire forces, expressed as dynamic load coefficient (DLC).

1.2.2 Semi-active and active suspension systems

A wide range of variable damping concepts have evolved to maximize the passenger comfort, increase the handing stability and reduce the tire-induced road damage [13, 17, 25]. Controllable damping devices have been proposed to realize the intelligent vehicle suspension designs. The active and semi-active suspension systems have been proposed since the early 1950's, which could generate variable damping forces in accordance with the varying excitation and response variables to satisfy various conflicting suspension requirements [36, 40-42]. The relative structures of passive, semi-active and active suspension dampers are illustrated in Figure1.1, using a single-DOF formulation.

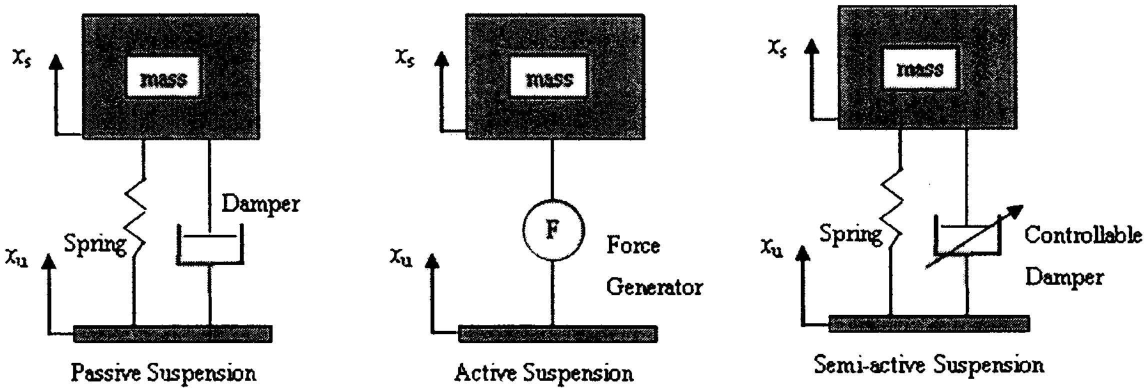

Figure 1.1: Schematics of passive, active and semi-active suspensions.

The passive suspensions offer limited performance due to uncontrollable nature of the dampers, they can only temporarily store and dissipate energy at a constant rate, and the forces generated depend on the local relative motions. The active suspensions refer to those where the suspension spring and damper are replaced by a high performance hydraulic actuator with a high bandwidth valve and hydraulic power supply. It can generate forces in response to response and excitation variables, and can be adapted to changes in responses and operating conditions. A semi-active suspension offers controllable damping forces with minimal power requirement, and can provide variable rate of energy dissipation. A wide range of optimal control strategies have also been developed to realize variable suspension forces to satisfy a selected objective, and to realize active and semi-active vehicle suspensions [41-44]. Owing to the high cost and power requirement of a fully-active suspension, the semi-active suspensions are considered to be meritorious for vehicle application.

Crosby *et al.* [43] proposed the concept of an active damper for shock and vibration control, and Alanoly *et al.* [44] investigated different concepts in semi-active force generators for shock isolation. Both the proposed active and semi-active dampers are based on the conventional hydraulic damper and provide modulation of hydraulic flows through controllable valves in response to vehicle responses and the control logic. These studies focused on the issues involving sprung mass acceleration alone, while the analyses were based on simple vehicle models. The discontinuities associated with switching of the valve deteriorated the performance. Moreover, the limited bandwidth of the valve permitted damping variation at low frequencies only.

Margolis [3] presented a comparison of the vibration isolation properties of different suspension mechanisms (passive, semi-active, active), and examined the effects of using realistic feedback signals when controlling active and semi-active suspension systems.

The study suggested a number of control strategies for realizing semi-active control of suspension damping and concluded that the performance of an effective semi-active damper could closely follow that of a fully active suspension performance. Hwang *et al.* [19] presented a method for assessment of a continuously controlled semi-active suspension using hardware-in-the-loop (HiL) simulation technique. Sammier *et al.* [22] proposed the "skyhook" control scheme to achieve the optimum suspension with semi-active dampers. Graf *et al.* [31] investigated a semi-active suspension to control the energy dissipation, while the proposed concept did not require an external power source. Youn *et al.* [36] proposed a semi-active optimal control law on the basis of a performance index comprising ride comfort, road holding and suspension rattle space, and presented relative performance characteristics of passive, active and semi-active suspension designs. The study concluded that a semi-active suspension could offer performance benefits comparable to that of a fully-active suspension. This finding concurs with the conclusion derived by Margolis [3]. The reported semi-active control schemes, however, invariably do not consider the transient responses associated with switching of the command input, which may cause undesirable effect on the suspension performance.

1.2.3 Characterization of MR-fluid dampers

Owing to the limited bandwidth of semi-active suspensions and the need for high bandwidth valves, a few studies have explored alternative damping fluids that could eliminate the need for the valves. These include the electro-rheological (ER) and magneto-rheological (MR) fluid-based dampers, which can provide variable damping attributed to variable rheological properties of the fluids [45]. A number of recent studies have established that these fluids have significant potential for realizing controlled damping forces with minimal response time, minimal power consumption, high reliability, low cost, and easy implementation in practical applications [45-51]. Carlson *et al.* [45] introduced the ER and MR fluid-based controllable dampers to realize damping variations in a rapid manner. A few studies have concluded that the MR fluid-based dampers offer superior potential in realizing variable damping using only low level current. The MR-fluid dampers are, therefore, becoming attractive choice for developing semi-active controllable dampers.

Rabinow [52] initially proposed the concept of MR fluids in the early 1950's, which appeared almost at the same time as the ER fluids, proposed by Winslow [53]. Both the ER and MR fluids are considered as the smart materials, which respond to an applied magnetic and an electric field with a change in their rheological behavior, respectively. A variety of prototype MR fluid-based dampers have been developed for vehicle applications since the mid-1990 [45, 54-57]. Figure 1.2 shows a schematic configuration of a MR-fluid damper, as an example. The damper consists of a nitrogen-charged accumulator and two MR-fluid chambers separated by a piston. The piston with annular orifice also comprises coils to generate magnetic field for the fluid. The variations in the viscous and shear properties of the fluid, caused by the applied magnetic field, yield variations in the damping force developed by the damper. For the particular damper illustrated in the figure, a DC current, limited to 2 A at 12 V, serves as the command signal for the coils.

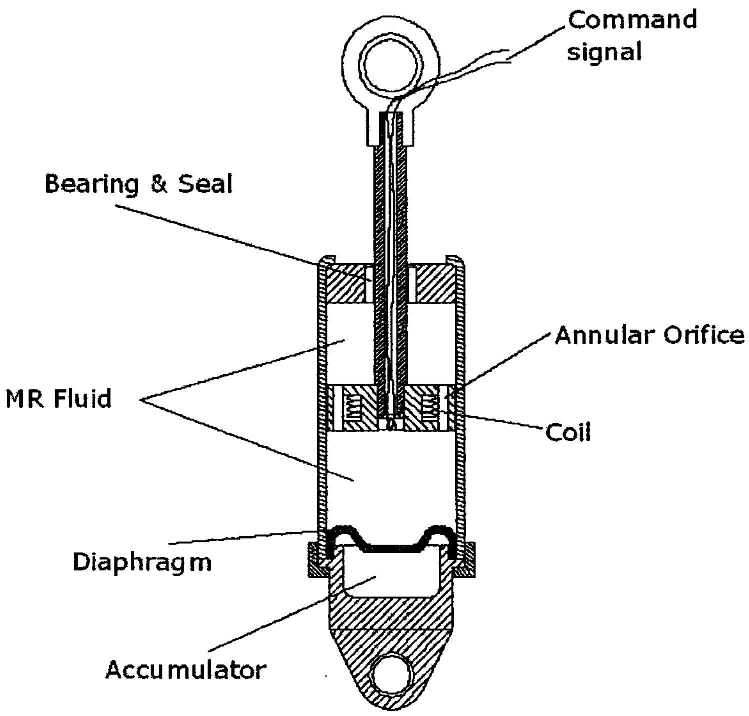

Figure 1.2: Schematic of a MR-fluid damper.

The ER and MR fluids exhibit considerable variations in their rheological properties in response to an applied electric and magnetic fields, respectively. This property has been used to realize semi-active devices for vehicular applications. Although a vast number of semi-active variable damping concepts based upon hydraulic flow modulation and ER fluids have been developed, clear advantages of the MR-fluid dampers have been established [45, 54, 56]. These include significantly higher yield stress and a wider operating temperature range [45, 62]. Moreover, the ER fluids require considerably higher voltage, while the MR fluids offer considerable variations in rheological properties with minimal power in the order of 40 W.

Extensive studies have been conducted to characterize the behaviour of the MR fluids. McManus *et al.* [57] and Simon *et al.* [62] studied the magnetic properties of the MR fluids, which revealed rapid, reversible, reliable, and tunable transition from a free-flowing state to a semi-solid state upon the application of an external magnetic field. The study also demonstrated that the fluid possesses many attractive features, such as high yield strength, low viscosity and stable hysteretic behavior over a broad temperature range. Snyder *et al.* [63] concluded that the MR fluid-based dampers exhibit superior performance than the ER fluid-based dampers, and has the most significant potential for easy implementation in practical engineering applications. The command current sets up a magnetic field created by the coil, which causes the iron particles in the MR-fluid to form a chain in the direction perpendicular to the flow of fluid through the orifice, increasing the fluid's apparent viscosity [57]. This effect is illustrated in Figure 1.3. The MR fluid is capable of changing from a free-flowing liquid to a near-solid state in under 10 ms, enabling real-time control of the damping force.

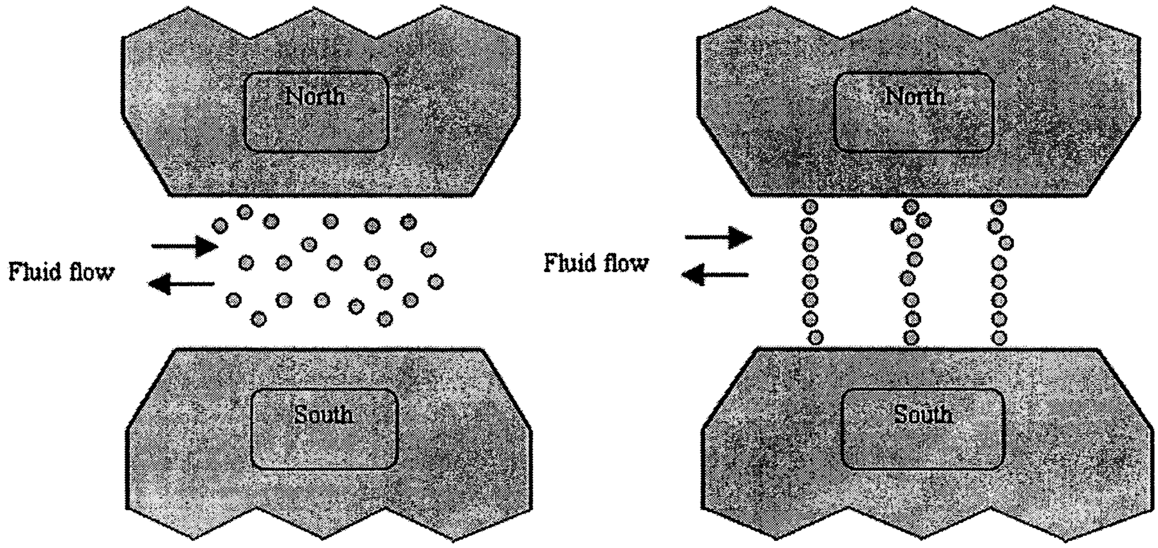

Figure 1.3: Response of MR-fluid to the applied magnetic field.

A wide range of MR fluid-based dampers are currently being explored for their potential implementation in various systems, such as vibration control devices and vehicle suspension. A number of analytical and experimental studies have clearly established superior potential performance benefits of MR dampers in vehicle applications in relation to conventional hydraulic dampers [54-61]. The MR dampers offer high viscous damping corresponding to low velocities in the pre-yield condition, while the post-yield saturation corresponding to high velocities can be characterized by a considerably lower viscous damping coefficient. The requirement of adequate ride, road-holding, handling and directional control stability performance of road vehicles entails variable damping [33], which could be achieved with MR dampers with only minimal power consumption. The MR-damper is considered to be a continuously controlled semi-active damping device, since it offers only variable damping force with minimal power requirement, unlike a fully-active suspension that could add or remove energy depending upon the demand with the help of an elaborate power supply. The semi-actively controlled MR dampers offer rapid variation in damping properties in a reliable fail-safe manner, since they continue to provide adequate damping, in a passive manner, in the event of a control hardware malfunction [45].

The instantaneous damping force developed by the MR-damper is directly related to the command current generated by the controller. Figure 1.4 illustrates the force-velocity (*F-v*) characteristics of a MR-damper under different values of constant current, ranging from 0 to 1.5 A [57]. The figure reveals symmetric *F-v* characteristics in compression and rebound. Under low-to-medium levels of control current, the *F-v* curve can be considered to provide three-stage damping: a high damping coefficient at low velocities and a lower coefficient at higher velocity. The transition from high-to-low damping coefficient occurs at a preset velocity. Under higher levels of control current, the *F*-*v* curve can be considered to provide three sequential stages defining a maximum damping coefficient at velocities less than 0.02 m/s, an intermediate value at velocities from 0.02 to 0.06 m/s and a low coefficient at higher velocities. The results further show that only minimal power is required to achieve considerable variations in damping force.

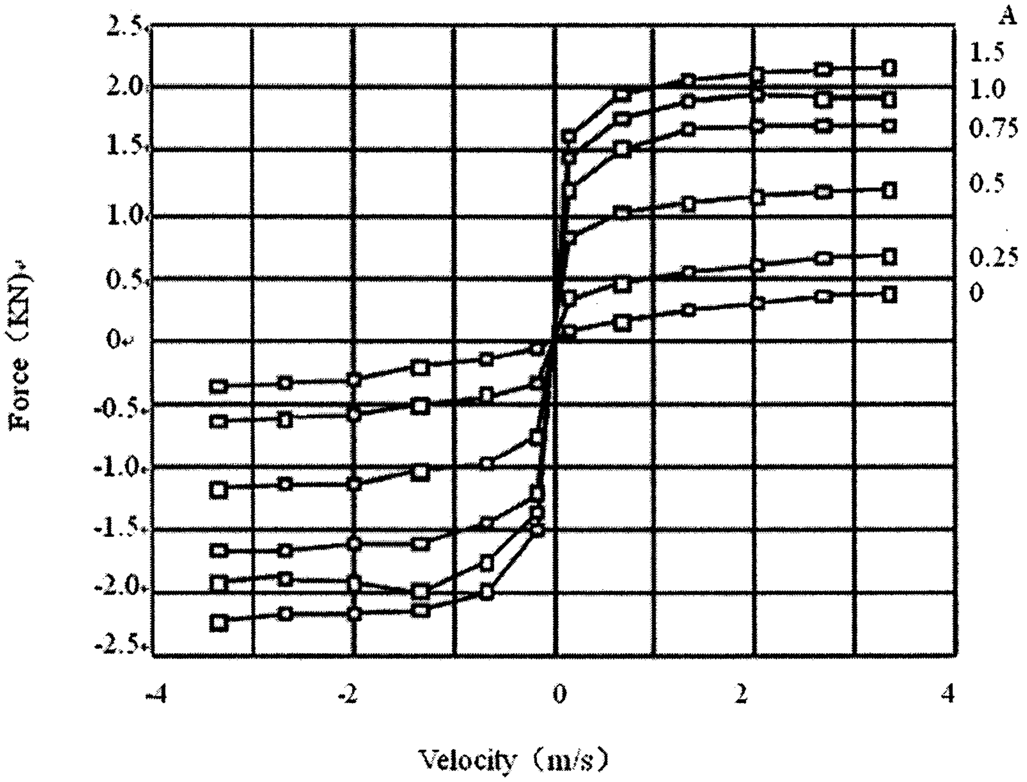

Figure 1.4: Mean *F*-*v* characteristics of a MR-fluid damper as a function of coil current.

Apart from the control current, the *F*-*v* characteristics of a MR-damper depend upon the nature of vibration (frequency and magnitude). Moreover, the *F*-*v* characteristics exhibit considerable hysteresis, which depend upon the nature of vibration, command current and operating temperature [54-57]. The results presented in Figure 1.4 represent the mean *F-v* characteristics corresponding to different piston velocities, assuming negligible hysteresis. Only a few studies have attempted to characterize the hysteretic *F-v* properties of such dampers [6-11], while a theoretical characterization over a wide range of excitation condition has not yet been reported. Considerable efforts, however, have been made to characterize the hysteretic properties of such dampers using regression based models in order to facilitate the development and implementation of an effective controller for realizing desirable controlled variations in the damping force.

The reported models on characterizing the hysteretic properties have been reviewed by Wereley *et al.* [8]. These include linear or viscous damping model, nonlinear Bingham plastic model, nonlinear bi-viscous model and nonlinear hysteretic bi-viscous model, in which the current control property and the effect of excitation are not considered. Among these, the nonlinear hysteresis bi-viscous model considers the hysteresis behavior using the piecewise linear functions, while the model results were correlated with the measured data under a fixed excitation condition and control current. Spencer *et al.* [7] proposed a model combining the Bouc-Wen hysteron with a linear viscous damper and a spring in parallel, which can be formulated by a set of differential equations. The results revealed that the damping force varies with control voltage in a linear manner. Choi *et al.* [6] formulated the hysteretic steady state dynamic characteristics of a MR-fluid damper using an algebraic formulation derived from the experimental data. The formulation comprised of two polynomial functions to match both the positive and negative acceleration curves of the hysteretic *F-v* cycle. The two functions lacked convergence at extreme velocities. The model, however, could describe the steady state dynamic properties of the MR-fluid damper under a specific excitation condition.

Wang *et al.* [64] and Xia [65] employed the neural network techniques to achieve a dynamic model and an inverse model to characterize the hysteretic properties of the MR-damper. The proposed models were considered quite complex and infeasible for implementation.

The vast majority of the above-discussed models do not characterize hysteretic variations in *F-v* characteristics of the MR-damper with continuous variations in the command current and the nature of piston deflection and velocity. The polynomial function model proposed by Choi *et al.* [6] and the extended Bouc-Wen model describe only linear dependence of hysteresis on the current. Moreover, the reported models could be applied to characterize the symmetric motion of the damper in compression and rebound. The vehicle suspension dampers invariably offer asymmetric damping in compression and rebound, while the rebound damping could be 3-5 times the compression damping force to limit the upward velocity of vehicle [2, 33]. Cebon [2] indicated that the vehicle suspension damper must be asymmetric in compression and rebound, which can be easily realized by the conventional passive dampers through valves. Milliken *et al.* [33] suggested that the desirable asymmetry damping-ratio of rebound to compression is about 3 to 5, to achieve better handling and road holding for the vehicle. The variable damping properties in response to changing response and excitation necessitate thorough characterization and the model development under continually varying command current. The resulting model could significantly simplify the controller design task. The asymmetric damping properties of a MR-damper could be realized in many ways. The use of flow limiting valves, similar to those used in conventional hydraulic dampers, could provide a constant level of asymmetry. The development of a control algorithm to modulate the magnitude of current, in response to the direction of piston velocity, could provide asymmetric damping with variable asymmetry factor (ratio of rebounding damping force to that in compression).

1.2.4 Hysteresis rejection control

Considering the superior potentials of the MR-fluid dampers in realizing intelligent vehicle suspension designs, the synthesis of an effective semi-active controller forms the essential objective. The strong hysteresis and force-limiting nonlinearities of the damper, associated with pre-yield at low velocity and post-yield saturation at high velocity, coupled with the need for asymmetric force generation, make this task quite challenging. The consideration of multiple performance objectives would further enhance the challenge for the controller design. These may include the ride or vibration attenuation, shock attenuation or resonant oscillation control, rattle space, road-holding and dynamic tire load performance. A vast number of studies have attempted to characterize the hysteresis behaviour of different materials and systems [16, 66-72], and proposed different control concepts for such systems for improving their tracking performance [73-79]. Khalil [70] presented a thorough analysis of general hysteresis behaviour of systems and demonstrated the adverse effects of hysteresis on the performance. The study showed that the presence of hysteresis could cause a number of undesirable effects, including loss of control, poor robustness, limit cycle, steady-state error, etc. A number of studies have attempted to compensate the hysteretic effect by proposing different hysteresis rejection control schemes.

Tao *et al.* [73] proposed an adaptive control scheme for plants with unknown hysteresis parameters, in which the piecewise linear function method is employed to characterize the hysteretic dynamic system. The hysteretic effect is compensated by the inverse model used in the adaptive-control scheme with unknown parameters. Ge *et al.* [74] proposed a displacement response tracking control scheme for a piezoceramic actuator to disminish the hysteretic effect, in which the traditional PID control scheme is applied to realize the displacement tracking control. Su *et al.* [75] proposed a robust adaptive control scheme for a class of nonlinear systems with unknown backlash-like hysteresis, wherein, the hysteresis is modeled by a time-varying differential equation. The input formulation in the model is simplified to a linear function superimposing a nonlinear function with constraints. A robust adaptive control scheme is thus employed to realize the nonlinear controller synthesis to achieve globally stable and desired tracking performance.

Cruz-Hernandez *et al.* [76] suggested a phase control approach to realize the hysteresis reduction. Gorbet *et al.* [77] proposed the passivity-based control scheme to reduce the hysteresis in smart actuators. Ralph *et al.* [78] developed the inverse compensator control scheme to suppress the hysteresis for high speed nano-positioning system, by cascading the inverse model in the closed-loop system. Corradini *et al.* [79] proposed a control scheme to achieve robust stabilization of nonlinear uncertain plants with backlash or dead zone in the actuator, in which the linear piecewise modeling technique is effectively incorporated with the sliding-mode control law.

The proposed hysteresis rejection control schemes invariably focus on the hysteresis reduction for the Lur'e nonlinear systems, in which hysteresis depends only on the command variable. Moreover, the synthesized controllers invariably belong to the active class of controllers. These schemes cannot be directly applied to a vehicle suspension system with MR dampers, since the controller synthesis for the MR-suspension system inevitably belongs to the semi-active class. Moreover, the hysteresis mechanism associated with a MR-damper is more complex than that of the Lur'e nonlinear system. The hysteresis in the MR-suspension system depends not only on the control current input, but also on the design and operating conditions of the system. For vehicle suspension applications, the control schemes are required to address the asymmetry apart from the hysteresis, which has not yet been attempted. A recent analytical study of an asymmetric conventional hydraulic damper has established that the vehicle sprung mass tends to drift in the downward direction when high rebound damping is applied [1, 33], which could further influence the damper hysteresis and performance.

1.2.5 Controller syntheses for MR-suspension dampers

With the recent emergence of MR fluids and recognition of their potential for achieving variable damping for control of vibration, a number of semi-active control schemes have been synthesized with varying performance objectives [12, 13, 80-86]. The vast majority of these studies focus on a single performance objective involving attenuation of sprung mass vibration, while the asymmetric and hysteretic properties are ignored. Yokoyama *et al.* [12] synthesized a sliding mode controller, in which a "skyhook" model is used as the reference model for tracking control. The "skyhook" control law was initially proposed by Karnopp *et al.* [87] to limit the resonant oscillations of the sprung mass and to achieve improved attenuation of vibration in the isolation range of frequencies. The control law was initially proposed to achieve variable damping in an on-off manner.

The study by Yokoyama *et al.* [12] concluded that the "skyhook" reference model could yield superior vibration isolation performance of the MR-damper when considered in conjunction with a quarter-vehicle model. Lee *et al.* [13] utilized the same "skyhook" control law for a full-vehicle model and concluded that the "skyhook"-based MR-suspension could effectively attenuate the sprung mass resonant vibration. Choi *et al.* [80, 81] applied the PID control law to track the desired damping force for a full-vehicle model, and further proposed a H_∞ controller to realize robustness against sprung mass uncertainties. Lam *et al.* [82] proposed a semi-active control scheme applying the sliding mode control law to generate the desired damping force, where the control voltage is derived from a force feedback loop rather than the "skyhook" control. Hiu *et al.* [83] applied the sliding mode control law to adapt for the load uncertainty in vehicles. Yao *et al.* [84] analyzed the vehicle suspension system based on a scaled quarter-vehicle model comprising a MR-damper, where the Bouc-Wen model was applied for synthesizing the semi-active control, while no attempt was made to account for contributions due to hysteresis. Liao *et al.* [85] utilized the LQG control law with acceleration feedback to realize damper force tracking with reference to an optimal damping force, in which the state variables are estimated from the acceleration responses using the Kalman estimator. Guo *et al.* [86] employed the neural network control strategy including an error back propagation algorithm with quadratic momentum of the multi-layer forward neural networks.

The above reported studies are based upon idealized vehicle models and mean and symmetric *F-v* properties of the MR-damper. These studies invariably focus on a particular control goal for the vehicle suspension, either attenuating the resonance of sprung mass, or adapting the suspension to the loading uncertainty, or optimizing the control index in a cost function, comprising rattle space, sprung mass acceleration and dynamic forces. Moreover, the controllers do not consider the hysteresis compensation and the influences of command signal switching, as well as the asymmetric damping requirement. Besides, the proposed semi-active control polices invariably employ the clipped-optimal algorithm, which is based on the direction of the force error.

1.3 Scope and Objectives of Dissertation Research

From the review of literature, it is evident that a number of intelligent vehicle suspension designs based upon active and semi-active control have evolved during the past 40 years. The implementations of fully-active suspensions, however, have been severely limited due to their high cost and power requirements. The semi-active suspensions with minimal power requirements could offer performance benefits similar to those of the fully-active suspension. The limited bandwidth of the semi-active dampers based upon hydraulic flow modulation has also prohibited their applications. The ER and MR fluids, which exhibit significant variations in their rheological properties, offer attractive potential to realize variable damping with high bandwidth. The MR fluids are considered to be superior to ER fluids due to their low power requirement and high yield strength. A number of designs of the MR-damper have thus evolved in recent years.

The vast majority of these dampers are designed to yield damping forces that are symmetric in compression and rebound, while the control of vehicle vibration and road-holding requires significantly larger damping in the rebound mode. The reported control laws employed for such dampers are mostly based upon particular performance goal and mean F-v characteristics, assuming negligible hysteresis. The F-v properties of such dampers exhibit considerable hysteresis that depends not only on the command current but also on the nature of the response and excitation variables. The presence of hysteresis could deteriorate the tracking performance and thus the overall suspension performance.

The design and synthesis of an intelligent vehicle suspension necessitates consideration of multiple conflicting objectives for the vehicle and hysteresis and asymmetric properties of the damping force. The design and synthesis of a controller for the MR-damper should therefore address a combination of goals: (i) hysteresis rejection to achieve desired tracking performance; (ii) asymmetric damping in compression and rebound to realize a better compromise between the vehicle ride and road-holding performance; (iii) consideration of parameter uncertainties associated with vehicle operations; and (iv) consideration of essential multiple goals, such as ride, rattle space, road-holding and dynamic tire forces transmitted to the pavement.

A hybrid semi-active control (HSC) synthesis may thus be considered to address the above desired goals through development of an intelligent vehicle suspension comprising symmetric MR-damper. The development of such a synthesis would necessitate a thorough characterization of the MR-damper as functions of the command signal, and response and excitation variables. The development of a reliable analytical model of the symmetric and asymmetric damping force, that effectively characterizes the hysteretic damping properties, would thus form the essential basis for the HSC synthesis. Owing to the strong nonlinearities of the MR-damper associated with command current-dependent asymmetry and hysteresis, it is essential to formulate an effective analytical model that would be valid over a wide range of variations in the key variables (current, excitation magnitude and frequency). A control system incorporating an inverse model could then be considered meritorious, since it could be easily deduced from the analytical model for the MR-damper. The current-switching discontinuities associated with the semi-active control tend to cause considerable transient responses and need to be modulated in a continuous manner. HSC synthesis comprising an accurate description of the hysteretic *F-v* characteristics, a smoothing modulation and asymmetric damping force generation controls could be considered desirable to achieve improved suspension performance, hysteresis rejection, and robustness.

1.3.1 Objectives of the dissertation research

The primary objectives of the proposed dissertation research are formulated on the basis of the desired tasks described in the scope of the study. The dissertation objective deals with formulation of the hybrid semi-active controller (HSC) syntheses for realizing intelligent vehicle suspension incorporating hysteresis rejection, continuous current modulation, asymmetric damping force generation, parameter uncertainties, and multiple vehicle performance goals. The specific objectives of the dissertation research are summarized below:

- Characterize hysteretic *F-v* characteristics of a MR-damper in the laboratory under a wide range of command current, and excitation frequency and stroke. Identify salient physical features for describing the hysteresis and force-limiting properties.
- Synthesize a generalized hysteretic model for describing both the symmetric and asymmetric *F-v* properties of the MR-damper and identify the model parameters. Assess the validity of the model over a wide range of applied current and excitation conditions.
- Derive a velocity-based inverse dynamic model for the hysteretic symmetric damping for effectively suppressing the hysteresis of MR-damper by integrating the inverse model control in the HSC synthesis.
- Develop a current modulation (CM) algorithm to realize continuous variations in the drive current for exciting the MR-damper, in order to effectively suppress transient oscillations in responses due to discontinuity in current-switching.
- Develop an asymmetric damping force generation (ADFG) algorithm to realize asymmetric damping force in compression and rebound from the same hardware.
- Synthesize different semi-active control algorithms in conjunction with a "quarter-vehicle" model integrating the current modulation (CM) and ADFG algorithms.
- Define a set of performance measures in view of multi-objective performances of vehicle suspension such as ride, road-holding and suspension rattle space, and define

a set of deterministic and stochastic road excitations for assessing the proposed different control schemes.

- Investigate the contributions due to discontinuities caused by current-switching, and hysteresis and force-limiting nonlinearities of the MR-damper, and assess the performance potentials of higher-order semi-active control policies.
- Evaluate dynamic responses of the proposed "skyhook"-based hi-lo semi-active controller in both symmetric (SCM) and asymmetric control modes (ACM), under deterministic and random excitations.
- Investigate the force-tracking and hysteresis rejection abilities of the proposed "inverse model"-based hi-lo semi-active ACM controller, and propose control laws to improve the force-tracking ability at low velocities.
- Investigate the force-tracking, hysteresis rejection and robust properties of the proposed "inverse model"-based sliding mode semi-active ACM controller.
- Assess relative merits and limitations of the proposed "skyhook"-based hi-lo, "inverse model"-based hi-lo and "inverse-model"-based sliding mode semi-active ACM controllers.
- Develop a hardware-in-the loop (HiL) test and assessment methodology to assess and tune different controller syntheses using a prototype damper subject to different types of excitations.

1.4 Organization of the Dissertation

A thorough review of literature on the properties, modeling and applications of MR-fluid dampers, hysteresis rejection, semi-active and active suspension control strategies, is presented in Chapter 1 to formulate the scope and objectives of the dissertation research.

Chapter 2 presents the experimental methodology and characteristics of a MR-damper measured under wide ranges of drive current, and excitation frequency and stroke. The measured data are analyzed to formulate the modeling considerations. A generalized hysteretic *F-v* model is formulated for describing both symmetric and asymmetric damping characteristics. The model parameters are identified and used to validate the model synthesis over a wide range of operating conditions. An inverse model is further developed for the hybrid semi-active control design to compensate for the hysteresis effects. An asymmetric damping force generation (ADFG) algorithm is proposed to yield asymmetric damping force in compression and rebound while using the symmetric MR-damper.

Four different semi-active control schemes are formulated in Chapter 3 for realizing variable symmetric and asymmetric damping properties of the MR-damper. The hysteretic damper model is integrated to a "quarter-vehicle" model, while an idealized "skyhook" reference model is formulated for the controller syntheses. A continuous current modulation (CM) function is proposed to suppress the switching transient effects, and the asymmetric damping force generation algorithm (ADFG) is proposed to attain asymmetric damping forces in compression and rebound. Higher-order hi-lo control law is also proposed to enhance the control bandwidth. The formulations are also presented for the "inverse model"-based hi-lo semi-active ACM controller for effectively suppressing the hysteresis effects. An "inverse model"-based sliding-mode semi-active ACM controller is further developed to enhance the robustness in view of variations in vehicle load. A modified "skyhook"-based reference model is used as the control target for improving the multi-objective suspension performances of the MR-suspension.

Chapter 4 presents relative evaluations of the proposed "skyhook"-based hi-lo semi-active ACM controller. The influences of hystereis and force-limiting nonlinearities of the MR-damper, and the current-switching discontinuities are investigated. Relative performance characteristics of the four different hi-lo and "skyhook"-based semi-active control policies are analyzed and discussed. The influences of variations in the vehicle operating parameters and controller parameters on the response measures are further analyzed to evaluate the effectiveness of controller synthesis.

The response characteristics of the "inverse model"-based hi-lo and sliding-mode semi-active controllers are evaluated and discussed in Chapters 5 and 6, respectively. The force-tracking and hysteresis rejection abilities are particularly emphasized. Control parameters are varied to improve the force-tracking performance, particularly at low speeds. The performance potentials of the controllers are evaluated under different shock and vibration excitations.

A hardware-in-the-loop (HiL) test platform is described in Chapter 7 for experimental evaluations of the controller syntheses and validations of the proposed hybrid semi-active controller syntheses. A real-time monitor is designed to assess and monitor the responses of the "quarter-vehicle" model with the MR-damper and controller syntheses. A monitor is designed to easily select the excitation, controller synthesis and the output displays. The HiL simulations and tests are performed under different excitations and controller settings for the promising hi-lo synthesis. The experiments are initially performed under constant levels of drive current to validate the proposed MR-damper model and the HiL test technique. Owing to the superior performance of the "skyhook"-based hi-lo semi-active damping in relation to those of the inverse model and sliding mode controllers, the experimental works are limited to the "skyhook"-based hi-lo semi-active damping.

The major conclusions drawn from the study together with the recommendations for further studies are finally summarized in Chapter 8.

CHAPTER 2

CHARACTERIZATION AND MODELING OF A MR-DAMPER

2.1 Introduction

A wide range of magneto-rheological (MR) fluid-based dampers are currently being explored for their potential implementation in various systems, such as vibration control devices and vehicle suspension. A number of analytical and experimental studies have clearly established superior potential performance benefits of the MR-damper in vehicle applications in relation to conventional hydraulic dampers [6-11]. The MR dampers offer high viscous damping corresponding to low velocities in the pre-yield condition, while the post-yield saturation corresponding to high velocities can be characterized by a considerably lower viscous damping coefficient. The requirement of adequate ride, road-holding, handling and directional control stability performance of road vehicles entails variable damping [2, 17, 33], which could be achieved with MR dampers with only minimal power consumption.

The MR-damper is considered to be a continuously controlled semi-active damper, since it offers variable damping force with minimal power requirement, unlike a fully active suspension which could add or remove energy depending upon the demand with the help of an elaborate power supply. The semi-actively controlled MR-fluid dampers offer rapid variations in damping properties in a reliable fail-safe manner, since they continue to provide adequate damping in a passive manner in the event of control hardware malfunction [45]. Although a vast number of semi-active variable damping concepts based upon hydraulic flows modulation and electro-rheological (ER) fluids have been developed, definite advantages of the MR-fluid dampers have been clearly established, such as significantly higher yield stress and wider operating temperature [5-8, 45].

Owing to the rheology of the MR fluid in terms of its shear stress-strain rate behavior, the damper exhibits highly non-linear variations in damping force, attributed to the hysteresis and force-limiting properties of the fluid as functions of intensity of applied magnetic field, and displacement and velocity of the piston. The development of an effective controller for realizing desirable variations in damping requires accurate characterization of hysteretic force-velocity (*F-v*) characteristics of the MR-damper in the pre-yield condition and force saturation in the post-yield condition. In view of its highly non-linear properties, considerable attempts are being made to study their dynamic behavior for model synthesis and for developing effective control algorithms [7, 8, 46, 48].

Spencer *et al.* [7] proposed a damper model on the basis of the Bouc-Wen hysteresis model. The model, however, poses inherent difficulties in predicting essential parameters and in realizing control systems for desired tracking control performance. Bingham plastic model has been proposed assuming rigid material behavior in the pre-yield, while the shear flow in the post-yield is characterized by a viscous damping coefficient [8, 48]. Assuming the material to be plastic in both pre- and post-yield conditions, Stanway *et al.* [46] proposed a nonlinear model, where the pre-yield force is characterized by considerably high viscous damping. On the basis of this model, Wereley *et al.* [8, 48] proposed a nonlinear hysteretic bilinear model by fitting the *F*-*v* characteristics using four parameters: pre- and post-yield viscous damping coefficients, yield force and zero-force velocity intercept.

The above models, however, do not include the effects of continually varying control current. Moreover, hysteretic damping force generated by a MR-damper not only depends upon the intensity of the magnetic field but also upon the excitation frequency and amplitude. This dependence of the hysteretic force on the nature of excitation has not yet been accurately characterized. In this chapter, a series of laboratory tests are performed to characterize the dependence of hysteretic damping force of a MR-damper on the excitation frequency and stroke, and the drive current. The measured data are used to synthesize a generalized hysteretic model of the MR-damper on the basis of a symmetric sigmoid function. The effectiveness of the proposed hysteretic model is demonstrated by comparing the simulation results with the measured data over a wide range of excitation parameters and magnitudes of drive current.

2.2 Experimental Characterization of a MR-Damper

A MR-damper pictorially shown in Figure 2.1 is considered for characterizing its damping properties in the laboratory. The considered damper, designed for automotive applications, could provide a total stroke of 200 mm. The damper is a mono-tube design and comprises floating piston, which separates the MR-fluid and the gas media. The piston is designed with annular orifices, and it comprises electro-magnetic coils to generate magnetic field in response to an applied electric current. The variations in viscous and shear properties of the fluid, caused by the applied magnetic field, yield variations in the damping force, developed by the damper. For this particular damper, a direct current limited to 0.5 A at 12 V served as the command signal for the coils.

Figure 2.1: A pictorial view of a candidate MR-damper [95].

2.2.1 Test apparatus and experimental methodology

The force-velocity (*F-v*) and force-displacement (*F-d*) characteristics of the candidate MR-damper are measured in the laboratory over a wide range of applied currents and excitations. A voltage-to-current circuit was designed to realize different constant levels of current excitations for the coil. Owing to the symmetric design of the damper, the voltage-to-current circuit was initially applied to obtain symmetric *F-v* characteristics in compression and rebound. The candidate MR-damper was installed on an MTS electro-hydraulic vibration exciter between the exciter and a fixed inertial frame through a force transducer. Position (LVDT) and velocity (LVT) sensors were also installed on the exciter to measure the instantaneous position and velocity of the damper piston. The damper was subject to harmonic displacement excitations of different constant amplitudes at selected discrete frequencies to characterize its properties over a wide range of excitations. The force, velocity and displacement data, acquired through a data acquisition board, were directly imported into an Excel worksheet using dynamic data exchange to obtain an on-line display of the hysteretic F-v characteristics. A dual regulated DC power supply was used to supply the command current to the damper. A thermocouple was also mounted on the damper body to monitor the damper temperature. The experimental data under each condition were acquired in the vicinity of a defined temperature range (40±10 °C), so as to suppress the thermal effects in the characterization task. Figure 2.2 illustrates the test apparatus.

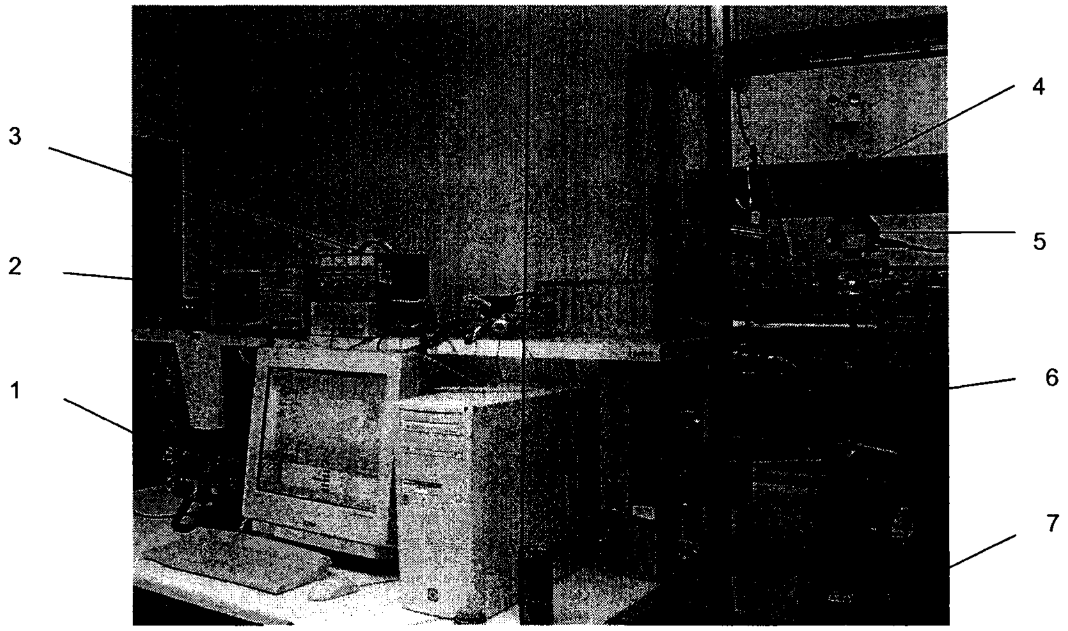

Figure 2.2: A pictorial view of MR-damper test system (1-Servo-controller; 2-Data acquisition; 3-DC power supply; 4-Temperature monitor; 5-Force transducer; 6-MR-damper; 7-Hydraulic actuator).

The hysteretic *F-v* characteristics of the candidate damper, symmetric in compression and rebound, were measured under sinusoidal displacement excitations at several discrete frequencies in the 0 to 15 Hz range, which is considered to represent the range of predominant vehicular motions along the vertical axis. The tests were performed under different constant magnitudes a_m of displacement, ranging from 2.5 to 75 mm, and command current i_d in the 0 to 0.4 A range. A total of 165 tests are performed corresponding to different combinations of frequency (0.1, 0.5, 1.5, 2.5, 5, 7.5, 10, 12.5, and 15 Hz), stroke (2.5, 12.5, 25, 50, and 75 mm), and drive current (0, 0.1, 0.2, 0.3 and 0.4 A). The amplitudes of displacement excitations at higher frequencies were limited to lower values to ensure damper operation within safe velocity limits. Table 2.1 summarizes the test matrix.

The measurements were initially performed under low amplitude excitation at a frequency of 0.1 Hz. The measured force was considered to represent the seal friction, assuming negligible contributions due to MR-fluid damping at extremely low velocities. The damper was then subjected to a selected excitation condition and current using the servo-controller and the voltage-current circuit, respectively. The force, velocity and displacement signals were acquired in the dynamic state as the body temperature approaches 40 °C. The measured signals were displayed in the form of time-histories and Lissajuous curves in *F-v* and *F-d* corresponding to each test condition. The acquired data are subsequently analyzed to characterize important properties of the MR-fluid damper.

Table 2.1: Test matrix.

Amplitude (a_m)	**Current (i_d)**	**Frequency (Hz)**								
		0.1	0.5	1.5	2.5	5	7.5	10	12.5	15
2.5 mm	0	×	×	×	×	×	×	×	×	×
	0.1 A	×	×	×	×	×	×	×	×	×
	0.2 A	×	×	×	×	×	×	×	×	×
	0.3 A	×	×	×	×	×	×	×	×	×
	0.4 A	×	×	×	×	×	×	×	×	×
12.5 mm	0	×	×	×	×	×	×	×	×	
	0.1 A	×	×	×	×	×	×	×	×	
	0.2 A	×	×	×	×	×	×	×	×	
	0.3 A	×	×	×	×	×	×	×	×	
	0.4 A	×	×	×	×	×	×	×	×	
25 mm	0	×	×	×	×	×	×	×		
	0.1 A	×	×	×	×	×	×	×		
	0.2 A	×	×	×	×	×	×	×		
	0.3 A	×	×	×	×	×	×	×		
	0.4 A	×	×	×	×	×	×	×		
50 mm	0	×	×	×	×	×				
	0.1 A	×	×	×	×	×				
	0.2 A	×	×	×	×	×				
	0.3 A	×	×	×	×	×				
	0.4 A	×	×	×	×	×				
75 mm	0	×	×	×	×					
	0.1 A	×	×	×	×					
	0.2 A	×	×	×	×					
	0.3 A	×	×	×	×					
	0.4 A	×	×	×	×					

2.2.2 Force-velocity and force-displacement characteristics

The force-velocity (*F*-*v*) characteristics measured under a few selected excitation conditions are initially analyzed to build an understanding the dynamic behavior of the MR-damper. Figures 2.3 to 2.5 illustrate the measured *F*-*v* characteristics under selected harmonic excitations and drive currents. It should be noted that *F*-*v* loops depicted in these figures follow counterclockwise path with increasing time. The results generally show nearly linear rise in the damping force at low velocities in the pre-yield and force saturation at higher velocities in the post-yield. The results also show strong dependence of damping force hysteresis in the pre-yield condition on the applied current. The damping force increases with increasing drive current in a non-linear manner, and tends to saturate under higher drive current due to the saturation property of the magnetic field, as evident in Figure 2.3.

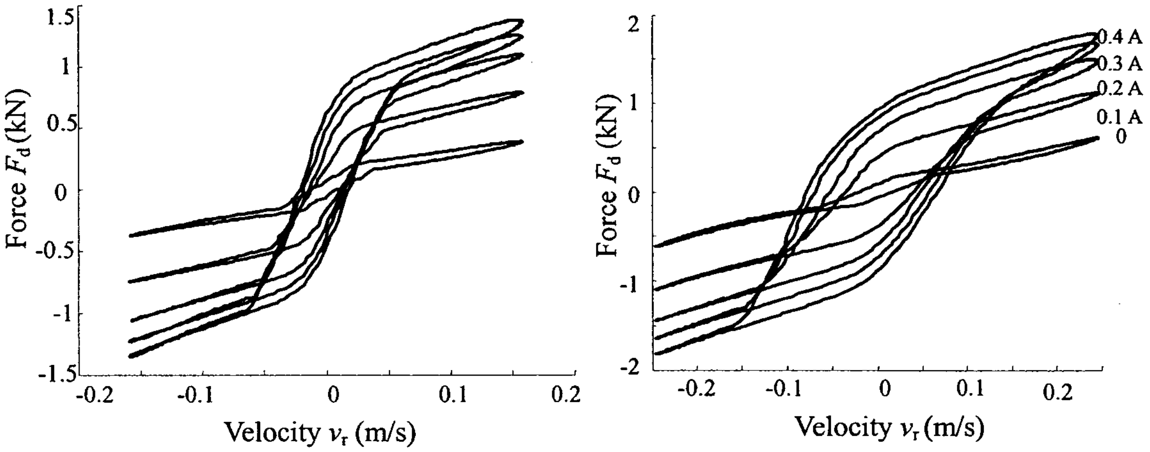

(a) f=0.5 Hz, a_m=50 mm (b) f=1.5 Hz, a_m=25 mm

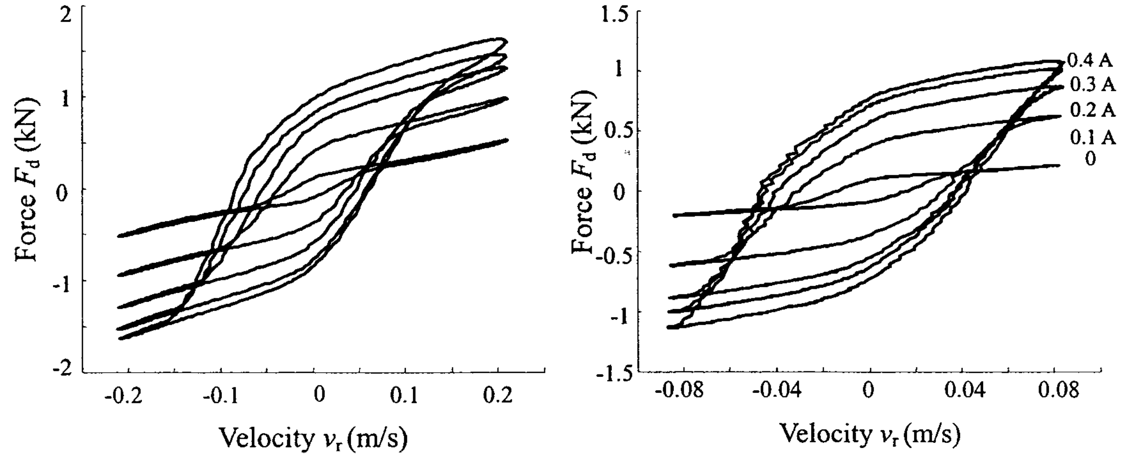

(c) f=2.5 Hz, a_m=12.5 mm (d) f=5 Hz, a_m=2.5 mm

Figure 2.3: Measured F-v characteristics of MR-damper under different drive currents and excitations.

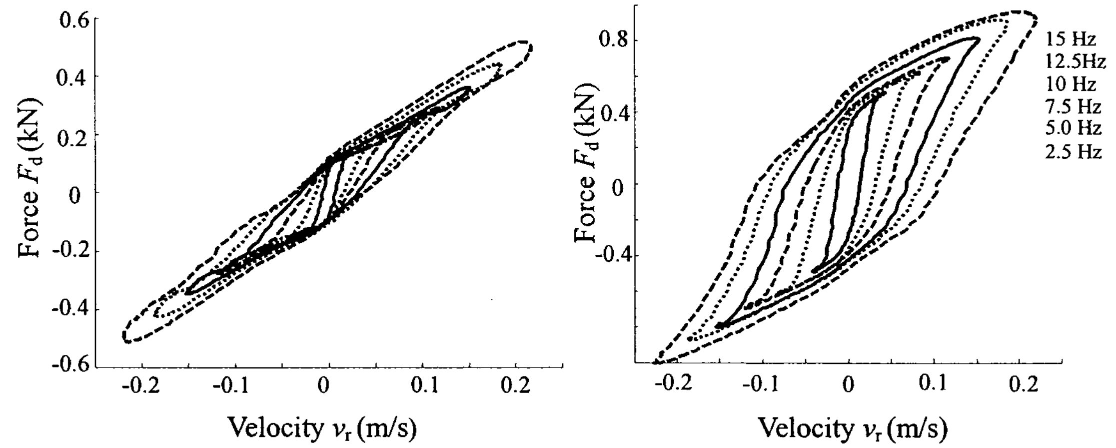

(a) i_d=0 (b) i_d=0.1 A

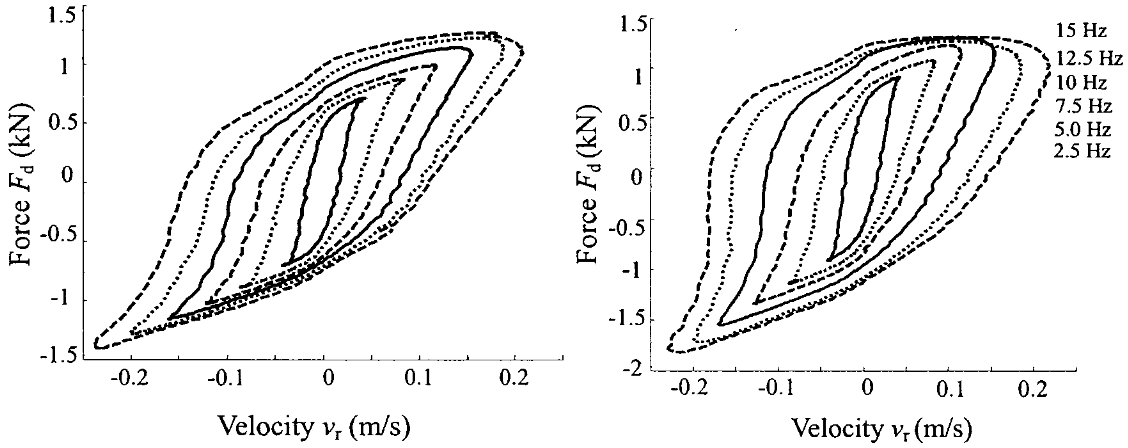

(c) i_d=0.2 A (d) i_d=0.4 A

Figure 2.4: Measured F-v characteristics of MR-damper under different excitation frequencies and drive current (a_m=2.5 mm).

The nonlinear damping properties are further dependent upon excitation frequency and amplitude, as illustrated in Figures 2.4 and 2.5, respectively. Figure 2.4 further shows the damping force dependence on the excitation frequency under varied currents and fixed excitation amplitude. The hysteresis loop increases with increasing frequency in a nearly linear manner for frequencies below 10 Hz. The F-v characteristics exhibit stronger hysteresis at higher frequencies. In the passive mode (i_d=0), damping force varies nearly linearly with velocity, particularly at frequencies above 5 Hz. Application of a higher current ($i_d \geq 0.3$ A) and excitation frequency ($f \geq 10$ Hz) causes asymmetry in the hysteresis loop, as seen in Figure 2.4. Larger hysteresis width in compression could be attributed to possible mixing of gas in the MR-fluid. The results show increase in hysteresis width with the excitation amplitude. The change in the damping coefficient observed at the onset of post-yield tends to diminish under higher excitation in the passive mode (Figure 2.5a).

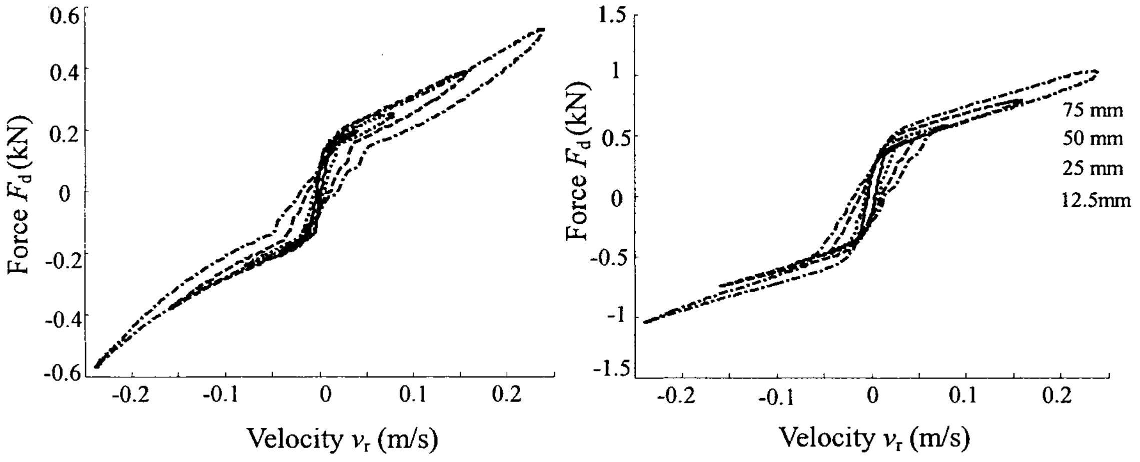

(a) i_d=0

(b) i_d=0.1 A

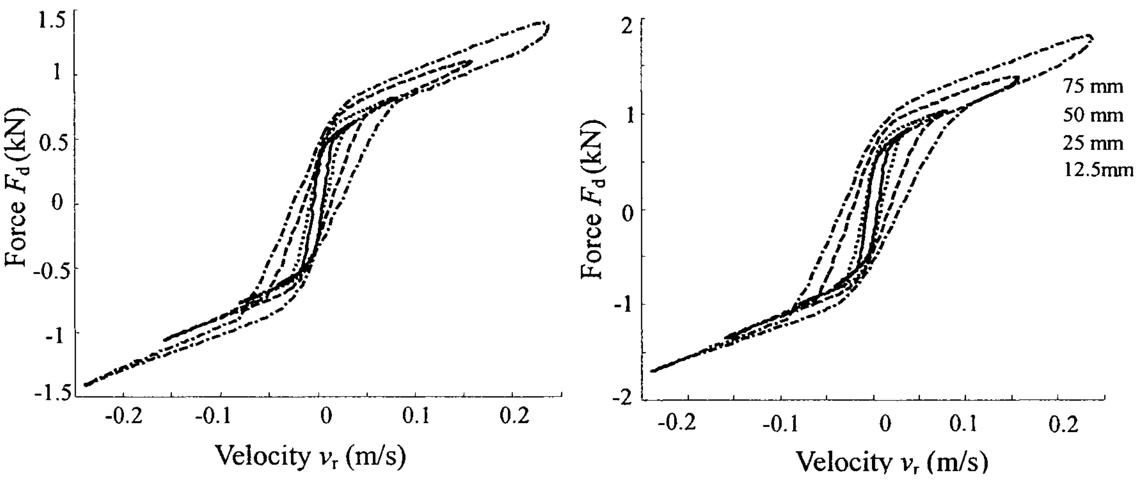

(c) i_d=0.2 A

(d) i_d=0.4 A

Figure 2.5: F-v characteristics measured under different excitation amplitudes and drive current (f=0.5 Hz).

The above experimental results show that the damping properties of the candidate damper strongly depend on the magnitudes of drive current, and excitation frequency and amplitude. The excitation frequency tends to have a strong effect on the force limiting property at higher velocities, particularly when f>5 Hz. On the basis of the observed trends, the essential dynamic behavior of the candidate MR-damper can be summarized as below, which also form the basis for the model synthesis.

Incremental feature: The *F-v* characteristics of a MR-damper can be generally depicted as symmetric bi-nonlinear with significant hysteresis at lower velocities (pre-yield), followed by linearly increasing force at higher velocities (post-yield). A force-limiting behavior is also evident during transition between low and high velocity responses. The behavior is also evident in *F-v* characteristics of typical hydraulic dampers with low-speed bleeds flow and high-speed blow-off valves [1]. The damping force may thus be characterized as an incremental function of velocity in the pre- and post-yield conditions, in which the damping force primarily depends on the relative velocity in the pre-yield stage and on the command current in the post-yield stage. The transition between pre- and post-yield stages occurs around the velocity v_r=0.025 m/s for the candidate damper considered.

Passive behavior: The MR-damper exhibits almost viscous property when zero drive current is applied (passive property), as evident from nearly linear *F-v* curves with relatively small hysteresis as shown in Figures 2.3 to 2.5(a).

Controllable property: The damping force increases considerably with magnitude of drive current. Nearly parallel shift in the measured yield force (force developed at the onset of post-yield saturation) corresponding to either $dv_r/dt<0$ (upper *F-v* curve) or $dv_r/dt>0$ (lower *F-v* curve) can be observed with increasing drive currents, as shown in Figure 2.3. The rate of increase in force magnitude is approximately linear under lower current levels (<0.2 A), which tends to gradually decrease under higher values of applied current (0.2~0.4 A), and a further increase in current (>0.4 A) yields saturation of the damping force. The damping force has strong and weak current dependence properties in the post-yield and pre-yield characteristics of MR-damper at higher and low velocities, respectively. The pre-yield damping force strongly depends on the low damper velocity.

Hysteretic phenomenon: The damper hysteresis progresses along counterclockwise path with increase in time. The upper curve in the *F-v* characteristics reflects force variation under decreasing velocities ($dv_r/dt<0$), while the lower curve corresponds to force under increasing velocities ($dv_r/dt>0$). The mean slope of the hysteretic loop, often referred to the viscous damping coefficient, is dependent upon both the drive current and excitation conditions (frequency and stroke).

Viscous character: Given a drive current, the MR-damper would generally yield nearly identical *F-v* curves under same excitation velocity that may be realized from different combinations of frequency and stroke. The damping force can therefore be expressed as a function of piston velocity and drive current, with appropriate consideration of the force-limiting behavior.

2.3 Characterization of Asymmetric *F-v* Characteristics

The candidate MR-damper is designed to provide symmetric damping force in compression and rebound. The vehicle suspension, however, are designed to realize asymmetric damping to achieve compromise among the conflicting ride, road-holding and directional control performances. It has been suggested that the ratio of rebound damping force to that in compression should be in the 3 to 5 range to realize better suspension performance [33]. For this purpose, an asymmetric damping force generation (ADFG) algorithm is proposed and integrated within the current driver circuit.

2.3.1 Formulation of asymmetric damping force generation algorithm

The asymmetric damping properties of the symmetric candidate damper are realized by limiting the drive current i_d to a lower value i_L during compression, when the relative velocity of the piston is positive ($v_r>0$). The current is switched to a higher value i_H during rebound motion ($v_r<0$). Such an approach, however, would cause transient responses due to switching discontinuities around $v_r=0$. An asymmetric damping force generation (ADFG) algorithm is initially formulated using the on-off control law, in response to direction of damper velocity. The asymmetric current i_s can be expressed as:

$$\begin{aligned} i_s &= \begin{cases} p i_c, & v_r > 0 \\ i_c\ , & v_r \le 0 \end{cases} \quad ; \quad i_L \le i_c \le i_H \\ &= [p(v_r > 0) \cup (v_r \le 0)] i_c \end{aligned} \tag{2.1}$$

where i_c is the control current and p is the asymmetry factor of the drive current in compression and rebound, which can be selected between 0 and 1. The logic function $p(v_r{>}0) \cup (v_r{\le}0)$ results in a lower of p for $v_r{>}0$ or $p{=}1$ for $v_r{<}0$.

The above on-off based asymmetric drive current i_s will invariably cause transient responses due to switching discontinuity near $v_r{=}0$. A smoothing modulation technique is thus developed to realize the on-off based asymmetric drive current in a smooth manner near $v_r{=}0$, while ensuring negligible phase shift. A modified on-off based ADFG algorithm, based upon the arctan function, is thus proposed as:

$$i_d = \mathrm{M_p}(p, \xi, v_r) i_c \tag{2.2}$$

where i_d is the drive current generated on the basis of the baseline current i_c, and the modulating function $\mathrm{M_p}$ is given by:

$$\mathrm{M_p}(p, \xi, v_r) = \frac{1+p}{2} + \frac{2}{\pi}[\mathrm{p}(v_r > 0) \cup (v_r \le 0) - \frac{1+p}{2}] \left| \tan^{-1}(\frac{\xi v_r}{v_m}) \right| \tag{2.3}$$

where $\mathrm{M_p}$ is the multiplier, v_m is peak relative velocity, p is asymmetry factor of drive current ($0{\le}p{\le}1$) and ξ is smoothing factor defining the slope of the *arctan* function ($\xi{>}0$).

The application of the above modulation function yields smooth transition between the i_L and i_H, as illustrated in Figure 2.6. Unlike the traditional filter-based modulation techniques, which could cause appreciable phase shift between the control current and the response velocity, the algebraic *arctan* function used in the proposed modulation function would not yield any phase shift. The proposed ADFG algorithm could be generally incorporated within a controller synthesis to realize the asymmetric suspension damping force with the symmetric MR-damper design. The parameters p and ξ, however, need to be selected to achieve a desirable compromise between the asymmetric damping force ratio (γ), defined as the ratio of damping force in rebound to that in compression, and the degree of smooth transition from i_L to i_H. For the vehicle suspension design with symmetric MR-damper, the parameter $p=0$ would be desirable to realize light compression damping ($i_d=0$) and asymmetric damping force ratio (γ) in the range of 3 to 5. A slightly higher value of ξ would be desirable to attain adequate asymmetric damping force ratio and smooth transition.

The effectiveness of the proposed modulation technique based upon the ADFG algorithm is investigated by comparing its current response with that of the on-off modulator, as shown in Figure 2.7. The figure also shows the symmetric drive current. The results were obtained for sinusoidal variations in the symmetric current, $i_c=0.25+0.2\sin(3\pi t)$ A, $p=0$ and $\xi=2$. The results show the drive currents i_s derived from the on-off control law defined in (2.1) and i_d derived using the proposed ADFG algorithm defined in EQS (2.2) and (2.3). The results clearly show smooth transition in current i_d due to proposed algorithm and it does not cause any phase shift. The results thus suggest that the proposed ADFG algorithm could effectively suppress the transients in the drive current in the vicinity of $v_r=0$.

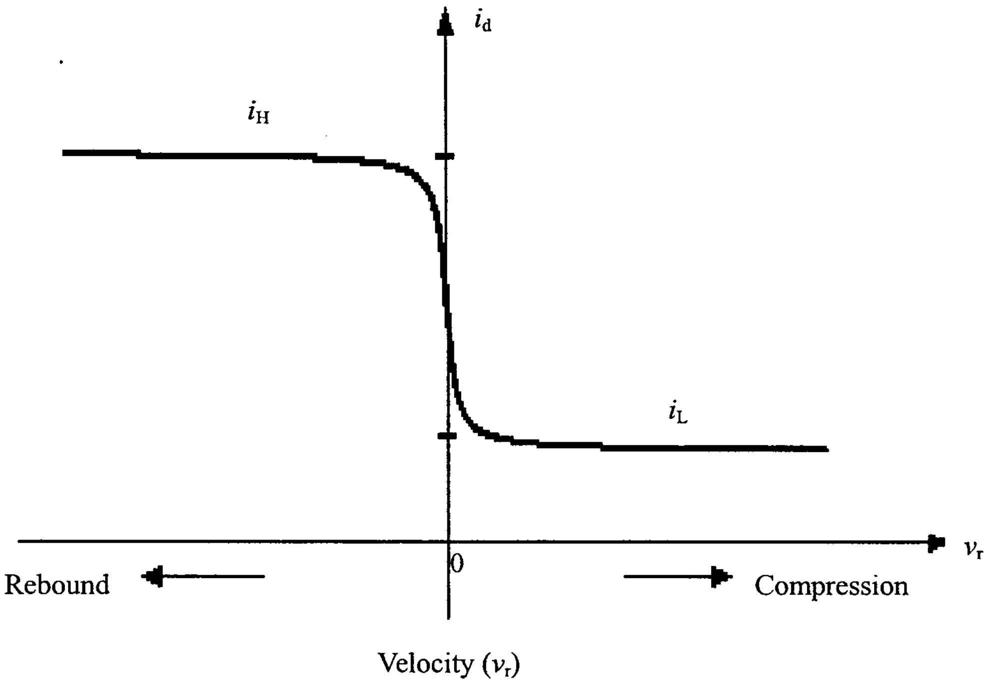

Figure 2.6: Modulation of command current with velocity to achieve asymmetric damping.

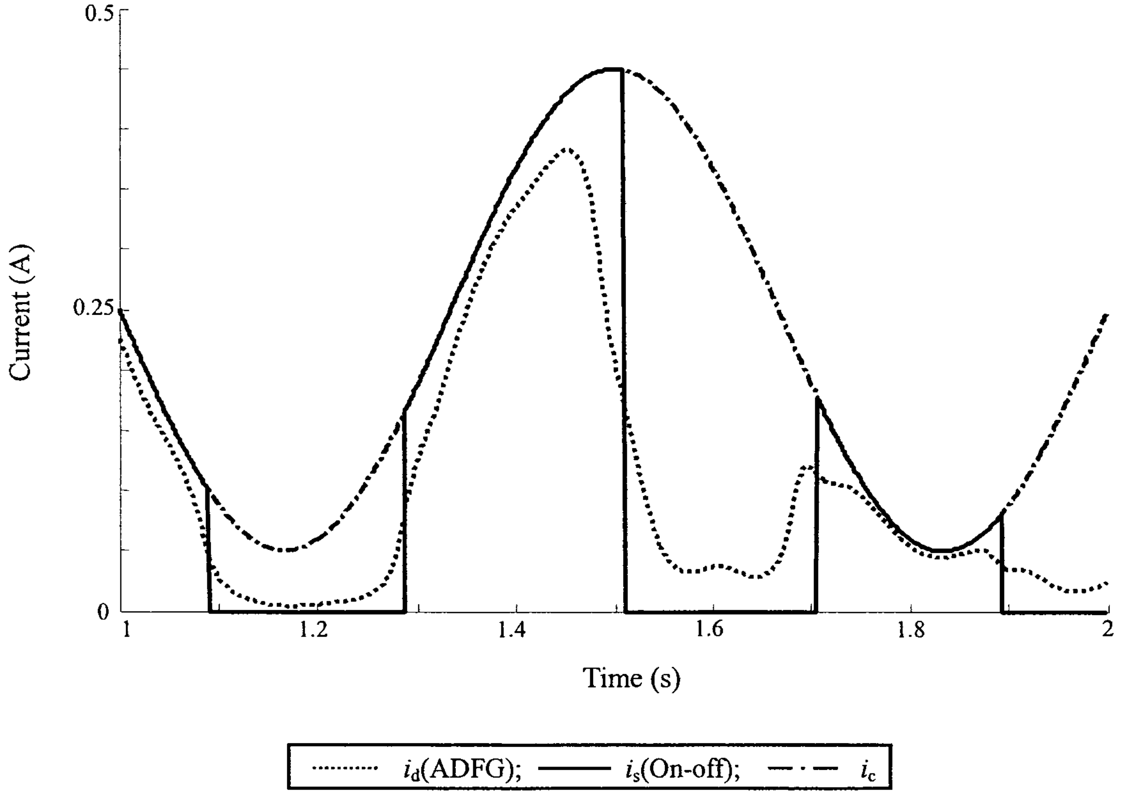

Figure 2.7: Modulation of command current in the symmetric and asymmetric control using on-off and asymmetric damping generation (ADFG) algorithm.

2.3.2 Measurement of asymmetric F-v characteristics

The proposed ADFG algorithm is implemented into the driving current circuit of the experimental setup described in section 2.2.1. The experiments are performed to characterize the asymmetric damping force under the test conditions summarized in Table 2.1, and using p=0 and ξ=2 in the modulation function. This would yield i_L=0 and i_H=i_d. As an example, Figure 2.8 illustrates the measured F-v characteristics corresponding to selected excitation conditions and i_d ranging from 0 to 0.3 A.

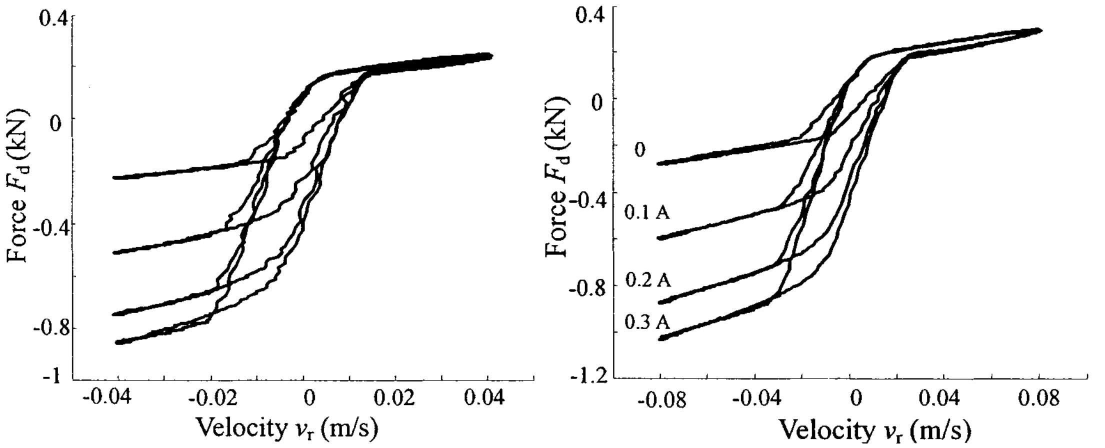

(a) f=0.5 Hz, a_m=12.5 mm (b) f=0.5 Hz, a_m=25 mm

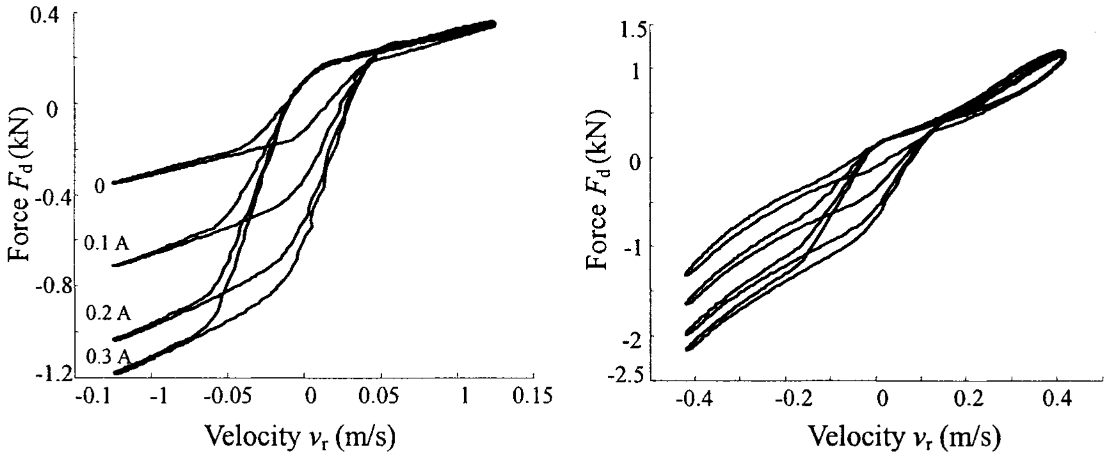

(c) f=1.5 Hz, a_m=12.5 mm (d) f=2.5 Hz, a_m=25 mm

Figure 2.8: Measured asymmetric F-v characteristics of the candidate MR-damper under different control conditions.

The results show that the same candidate damper can provide asymmetric damping force in compression and rebound in a continuous manner. Moreover, the contributions due to switching transients are not evident. The chosen parameters of the modulation function yield asymmetric damping force ratio (γ) in the order of 4, for low velocities. The ratio γ, however, diminishes under higher velocities as observed in Figure 2.8(d). A γ value of approximately 2 is attained under i_d=0.3 A, which is partly attributed to the force limited behavior of the MR-damper. The experimental results, however, clearly demonstrate the effectiveness of the proposed ADFG algorithm.

2.4 Modeling *F-v* Characteristics of Symmetric MR-Damper

The *F-v* characteristics of the MR-damper reveal strongly nonlinear hysteresis and force-limiting property. The hysteresis is a widely known phenomenon commonly encountered in a broad spectrum of physical systems. Structures invariably exhibit hysteresis, especially when the response becomes inelastic [4, 16]. The model synthesis of such systems thus poses a challenging task. In this section, the equivalent characteristic method (ECM) is applied on the basis of experimental data to achieve a model synthesize in the form of a nonlinear algebraic function to fully characterize the hysteretic characteristics of the MR-damper.

A generalized analytical model of hysteretic *F-v* characteristics is subsequently derived for the symmetric and asymmetric MR dampers, so as to describe the variations in damping force as functions of the drive current, and displacement and velocity of the piston. The nonlinear control current dependence of the damping force is characterized by a nonlinear gain function based on the asymmetric sigmoid function, while the hysteron is formulated with a symmetric sigmoid function.

2.4.1 Formulation of symmetric and hysteretic *F*-*v* model

The typical *F*-*v* curve of a MR-damper, corresponding to specific magnitudes of velocity and drive current, can be represented by a general hysteresis loop shown in Figure 2.9. The mean damping curve, frequently used to evaluate the overall system response, can also be easily derived from the loop as shown by the bold curve. The model synthesis can be obtained from the generalized hysteresis loop with appropriate considerations of the features observed from the experimental data. The essential parameters required to formulate the model are described below. Owing to the symmetry, the parameters are described for compression alone ($v_r \geq 0$).

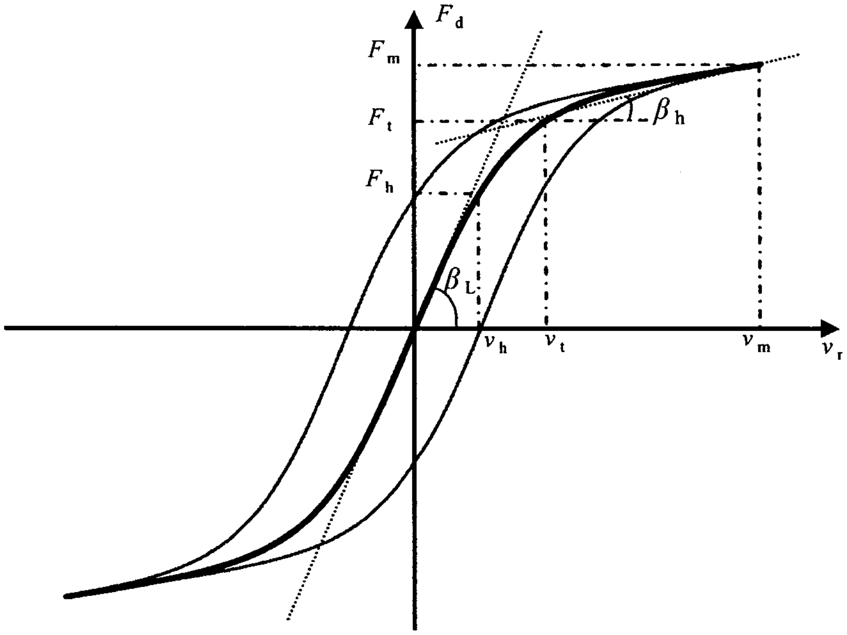

Figure 2.9: Generalized hysteretic *F*-*v* curve (—— Hysteretic, **——** Mean).

F_d, v_r	Damping force and piston velocity derived from the model synthesis, respectively.
v_m	Maximum velocity of the damper piston determined from the excitation frequency and stroke.
F_m	Maximum force developed by the MR-damper corresponding to specified v_m and drive current i_d.
v_h	Zero-force velocity intercept corresponding to the zero damping force under given i_d and excitation condition.
F_h	Zero-velocity force intercept corresponding to the zero velocity under given i_d and excitation condition.
v_t	Transition velocity corresponding to onset of force-limiting property (post-yield condition) leading to linearly increasing force and saturation, as derived from the mean curve.
F_t	Transition force, the mean damping force corresponding to v_t.
β_L	Low velocity slope of the mean F-v curve at v_r=0, representing low speed viscous damping coefficient.
β_h	High velocity slope of the mean F-v curve at v_t, representing high-speed viscous damping coefficient.

2.4.2 Synthesis of the characteristic curves

The family of F-v hysteresis curves for the MR-damper shown in Figures 2.2 to 2.5 can be described by three distinct properties: *saturated hysteresis loop*, *linear rise* and *current-induced rise*. Various curves attained corresponding to different drive current may be considered as amplification of the passive characteristics (i_d=0). A saturated hysteresis loop in the absence of linear rise, $F_s(v_r+v_h)$, can be formulated by the *symmetric sigmoid* function with bi-directional deflection in the lateral axis:

$$F_s(v_r+v_h)=F_t\frac{1-e^{-\alpha(v_r+v_h)}}{1+e^{-\alpha(v_r+v_h)}} \tag{2.4}$$

where v_r is the instantaneous relative velocity of the damper piston and α is a constant used to adjust slope of the hysteresis curve.

The *linear rise* segment of the curves relates to force-limiting property in the post-yield condition that can be expressed by the linear function, $c_\mathrm{v}(v_\mathrm{r})$, often referred to as high velocity damping coefficient:

$$c_\mathrm{v}(v_\mathrm{r}) = 1 + k_\mathrm{v}|v_\mathrm{r}| \tag{2.5}$$

where k_v is a constant describing the influence of excitation condition on the linear rise.

Equations (2.4) and (2.5) yield formulation of a general hysteresis loop shown in Figure 2.9. The hysteretic damping force, F_h, can thus be expressed as a function of v_r, as:

$$F_\mathrm{h}(v_\mathrm{r}) = F_\mathrm{t}\frac{1-e^{-\alpha(v_\mathrm{r}+v_\mathrm{h})}}{1+e^{-\alpha(v_\mathrm{r}+v_\mathrm{h})}}(1 + k_\mathrm{v}|v_\mathrm{r}|) \tag{2.6}$$

2.4.3 Influence of drive current and nature of excitation

The above formulation could provide the hysteretic damping force as a function of v_r alone, while the current dependence of the damping force is not considered. Considering that the *current-induced rise* is a mere shift of the *F-v* curve, the role of drive current in the model synthesis can be introduced as a gain $C_\mathrm{i}(i_\mathrm{d})$ limiting the force to F_t, such that $F_\mathrm{d}(i_\mathrm{d},v_\mathrm{r})=C_\mathrm{i}(i_\mathrm{d})F_\mathrm{h}(v_\mathrm{r})$. The gain function, $C_\mathrm{i}(i_\mathrm{d})$, is derived with systematic considerations of the relationships among F_t, v_h, α and k_v, corresponding to given excitation condition and command current. This requires the derivation of rather complex relationships among various characteristic parameters (F_t, v_h, α, k_v) and excitation conditions, which are described below.

Transient force F_t

The experimental data suggest strong dependence of F_t on the excitation condition v_m and the drive current i_d. F_t increases with increasing excitation velocity, which can be clearly observed from Figures 2.4 and 2.5. The transition force in the passive mode (i_d=0) may thus be formulated as:

$$F_t = \mathrm{F}_0(1+\mathrm{e}^{a_1 v_m}) \tag{2.7}$$

where F_0 denotes the constant base value of F_t taken as the seal friction force, and a_1 is a positive constant used to adjust the rising rate of the exponent v_m.

Furthermore, the hysteron force F_h in passive damping mode (i_d=0) can be thus formulated by combining (2.6) and (2.7) as follows:

$$F_h(v_r) = \mathrm{F}_0(1+\mathrm{e}^{a_1 v_m})\frac{1-\mathrm{e}^{-\alpha(v_r+v_h)}}{1+\mathrm{e}^{-\alpha(v_r+v_h)}}(1+k_v|v_r|) \tag{2.8}$$

where F_h denotes the hysteron force of the MR-damper in the passive damping mode (i_d=0), which depends solely on the damper velocity v_r.

The current dependence of hysteretic force can be described as an amplification of the passive characteristic (i_d=0), as evident in Figure 2.3, which show the nonlinear incremental behavior. As a result, the current-induced rise can be characterized by an asymmetric sigmoid function with a certain bias in the lateral axis.

$$C_i(i_d) = 1+\frac{\mathrm{k}_2}{1+\mathrm{e}^{-a_2(i_d+\mathrm{I}_0)}}-\frac{\mathrm{k}_2}{1+\mathrm{e}^{-a_2 \mathrm{I}_0}},\quad C_i(i_d)\ge 1 \tag{2.9}$$

where C_i is the control gain of the MR-damper, which depends only on the command current i_d ($0 \le i_d \le i_H$), and yields a unit value for the passive damping mode (i_d=0). k_2 and

α_2 are positive constants, and I_0 is an arbitrary constant.

Linear rise coefficient k_v

The analyses of the measured data revealed that the rate of linear rise (β_h) at high velocities increases exponentially with v_m, and is relatively insensitive to i_d. The linear rise coefficient k_v is thus formulated as:

$$k_v = k_1 e^{-a_4 v_m} \tag{2.10}$$

where k_1 and a_4 are positive constants.

Hysteresis slope coefficient α

The damping coefficient (β_L) at low velocities also increases with increasing v_m, and is relatively insensitive to i_d, as shown in Figures 2.3-2.5. The hysteresis slope coefficient α can thus be formulated as a function of v_m:

$$\alpha = a_0/(1+k_0 v_m) \tag{2.11}$$

where a_0 and k_0 are positive constants of the decreasing function α.

Zero-force velocity intercept v_h

Zero force velocity intercept v_h strongly affects the shape of the hysteresis curve, specifically the width of the hysteretic loop, as shown in Figures 2.3 to 2.5. The results show a strong dependence of v_h on the excitation condition v_m, and only slight dependence on the command current i_d. The dependence of v_h on i_d for given values of v_m can be formulated by an asymmetric function similar to that defined for $C_i(i_d)$ in EQ (2.9). The dependence of v_h on v_m for given values of i_d can be described by a linear function in v_m. Furthermore, the sign of v_h can be determined from sgn(dv_r/dt). For $dv_r/dt = 0$, the velocity v_r approaches its maximum value v_m and the two enveloping curves converge. Thus, the zero-force velocity intercept can be formulated as a function of v_m and i_d as:

$$v_h = \mathrm{sgn}(\ddot{x}_r)\mathrm{k}_4 v_m \left(1 + \frac{\mathrm{k}_3}{1+e^{-a_3(i_d+\mathrm{I}_1)}} - \frac{\mathrm{k}_3}{1+e^{-a_3\mathrm{I}_1}}\right) \tag{2.12}$$

where a_3, k_3 and k_4 are positive constants, I_1 is an arbitrary constant, and $\ddot{x}_r = dv_r/dt$ is the relative acceleration of the damper piston.

Equation (2.12) considers the influences of v_m and i_d on v_h. The measured data shown in Figure 2.3, however, suggest relatively small influence of i_d on v_h. As a result, the formulation (2.12) can be simplified upon neglecting the dependence on the current, such that:

$$v_h = \mathrm{sgn}(\ddot{x}_r)\mathrm{k}_4 v_m \tag{2.13}$$

<u>Nature of excitation v_m</u>

The nature of excitation refers to the peak velocity v_m, which is not a directly measurable quantity. It is, however, essential to derive a relationship between the hysteretic force characteristics and v_m, which would enhance the synthesis for implementation over a broad range of operating conditions. The measured data shown in Figures 2.3 to 2.5, illustrates that the damper response is strongly dependent upon the excitation frequency f and stroke a_m. Although these excitation conditions can be equivalently expressed by the maximum velocity for harmonic motion, $v_m=2\pi f a_m$, v_m can not be directly measured in real time, specifically under random excitations. Alternatively, the magnitude of v_m can be estimated from the instantaneous displacement x_r, velocity $\dot{x}_r$ and acceleration $\ddot{x}_r$ of the damper piston, such that:

$$v_{\mathrm{m}} = \sqrt{(\dot{x}_{\mathrm{r}})^2 - \ddot{x}_{\mathrm{r}} x_{\mathrm{r}}} \tag{2.14}$$

where $\dot{x}_{\mathrm{r}} = v_{\mathrm{r}}$ is the instantaneous velocity of the damper piston.

2.4.4 Synthesis of the overall model

The overall model synthesis can be established from the generalized passive hysteresis loop model described in EQ (2.8) by integrating the above formulations describing the nonlinear dependence of the force on the drive current , as formulated in EQ (2.9):

$$F_{\mathrm{d}}(i_{\mathrm{d}}, v_{\mathrm{r}}) = C_{\mathrm{i}}(i_{\mathrm{d}}) F_{\mathrm{h}}(v_{\mathrm{r}}) \tag{2.15}$$

The proposed symmetric and hysteretic *F-v* model described in EQ (2.15) requires identification of a total of 13 parameters (F_0, I_0, I_1, a_0, a_1, a_2, a_3, a_4, k_0, k_1, k_2, k_3, and k_4) from the measured data, when the formulation of v_{h} described in EQ (2.12) is employed. It should be noted that proposed symmetric and hysteretic *F-v* model can be easily simplified to the mean *F-v* model by letting k_4=0 (i.e. v_{h}=0), and the number of parameters to be identified can be reduced form 13 to 9. Besides, the proposed symmetric *F-v* model can be further simplified to decouple the drive current gain and the hysteron functions, and the number of parameters to be identified can be reduced form 13 to 10. Such a simplified model in the decoupled form offers considerable potential benefits, when an inverse model of the symmetric MR-damper is required.

2.5 Formulation of an Inverse Model of the Symmetric MR-Damper

The model synthesis proposed in EQ (2.15) can be easily applied for deriving a velocity-based hysteretic inverse model for the design of controller and implementation.

The model synthesis involving v_h as a function of v_m alone, as described in EQ (2.13), is considered for deriving the inverse model relating the damping force to the command current. On the basis of the generalized model synthesis, defined in EQ (2.15), the current gain C_i can be expressed as:

$$C_i = \frac{F_d(i_d, v_r)}{F_h(v_r)}, \quad C_i \geq 1 \tag{2.16}$$

where C_i is the current control gain of the MR-damper described in EQ (2.9). F_d is the target damping force associated with a particular controller synthesis. F_h is the passive hysteron force of the MR-damper formulated in EQ (2.8) as a function of v_r. The inverse command current i_z can be derived from EQS (2.9) and (2.16), as:

$$\begin{aligned} i_z &= f_d^{-1}(F_d, F_h) \\ &= -I_0 - \frac{1}{a_2}\ln\left\{\frac{(k_2 F_h - F_d + F_h)e^{-a_2 I_0} - F_d + F_h}{(F_d - F_h)(1 + e^{-a_2 I_0}) + k_2 F_h}\right\} \quad ; \quad 0 \leq i_z \leq i_H \end{aligned} \tag{2.17}$$

The above inverse model relates the target damping force F_d to inverse drive current i_z, $0 \leq i_z \leq i_H$. The validity of the inverse model is examined for a given i_d and excitation $x_r(t)$. As an example, i_d and x_r are chosen to vary in a harmonic manner, such that $i_d = 0.25 + 0.2\sin(3\pi t)$ A and $x_r = 2.5\sin(3\pi t)$ cm. The generalized model synthesis defined in EQ (2.15) in conjunction with C_i and v_h defined in EQS (2.9) and (2.13), is solved to compute the drive current i_z on the basis of the computed F_d. The validity of the model is examined by computing the initial current i_d with i_z, as shown in Figure 2.10. The Figure illustrates the error, $e_i = | i_d - i_z |$, and the computed forces, $F_h(v_r)$ and $F_d(i_d, v_r)$. Herein, the MR-damper model operates in mean damping mode to generate in-phase F_d and F_h.

The results show that the proposed hysteretic inverse model can fully recover the drive current i_d without any phase shift, while the damping force F_d remains in phase with the hysteron F_h, which confirms the current function as a mere gain. The hysteretic inverse model can be easily simplified to the mean inverse model by letting $k_4=0$ in EQ (2.12) (i.e. $v_h=0$). The proposed velocity-based inverse model of the symmetric MR-damper could thus be applied in the controller synthesis to realize force-tracking and hysteresis rejection control, which is investigated in the following chapters.

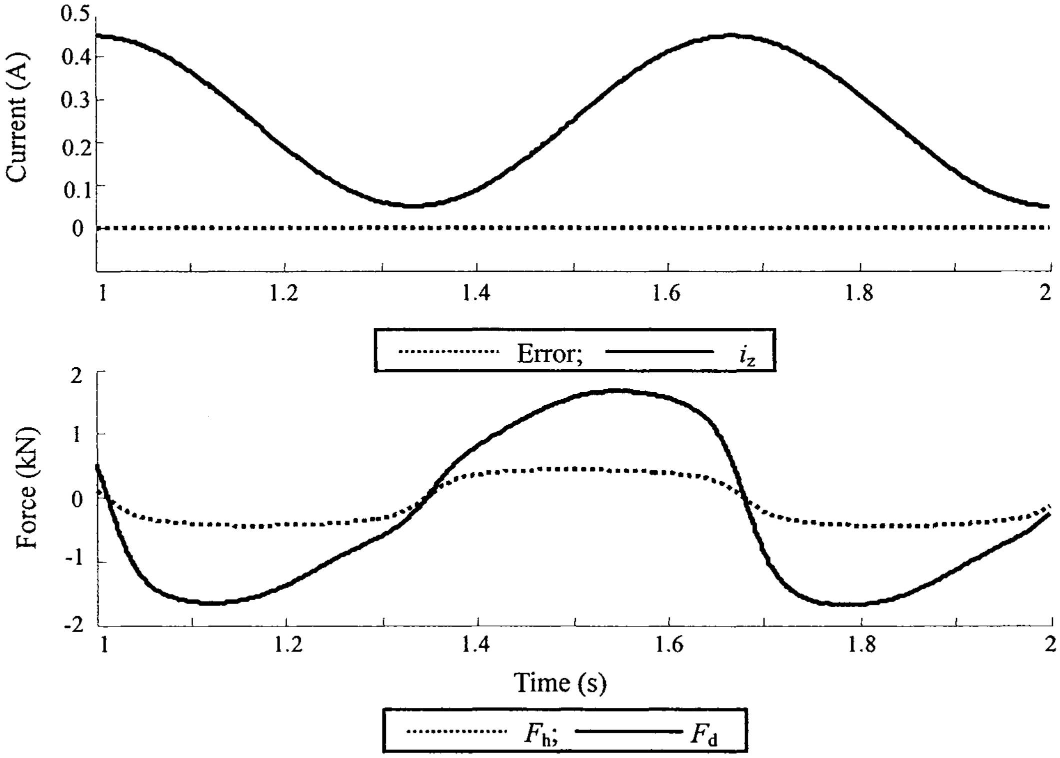

Figure 2.10: Validity of inverse model, and variations in the hysteron and the damping force.

2.6 Asymmetric and Hysteretic F-v Model Formulation

The available test damper provided only symmetric damping force in rebound and compression due to the symmetric nature of the applied current. Furthermore, the reported models of the MR-damper, invariably, characterize the symmetric characteristics as a function of the piston velocity, while the current dependence is mostly ignored [4-7]. The vehicle suspension systems, however, are generally designed with asymmetric damping characteristic to achieve a better compromise among different conflicting performance measures. The conventional suspension dampers provide higher rebound damping to suppress wheel velocity in the upward direction when compared to that in the downward direction [1, 2].

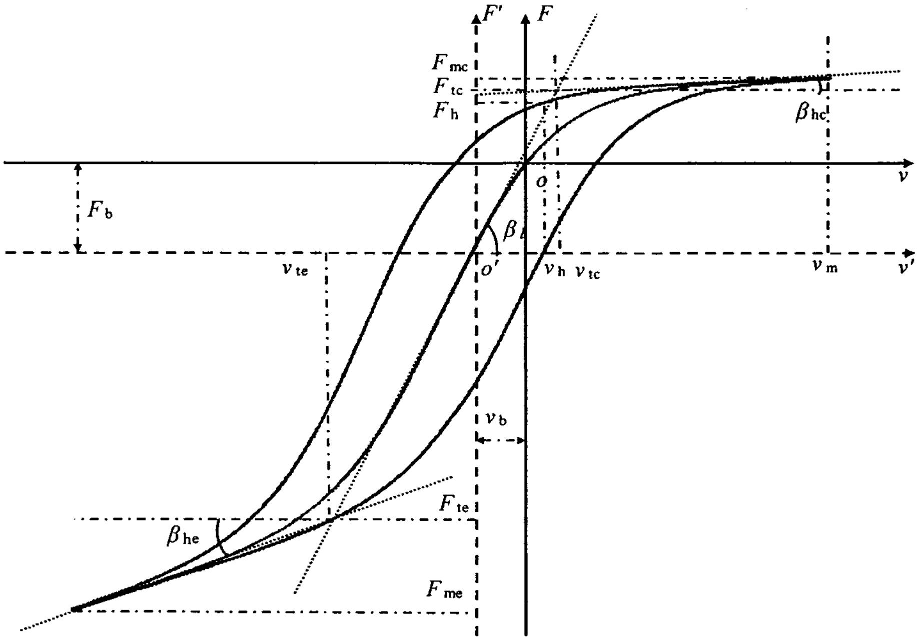

Figure 2.11: A generalized representation of the asymmetric F-v characteristics (—— Hysteresis, —— Mean).

The proposed ADFG algorithm can be conveniently applied to realize asymmetric F-v characteristics from the available symmetric MR-damper. The model synthesis of the symmetric damper, described in section 2.4, can be easily extended to characterize the asymmetric and hysteretic damper properties. The asymmetric and hysteretic F-v

characteristics of a damper, employed in vehicle suspension, can be described by a general asymmetric hysteresis nonlinear curve in the *F-o-v* coordinate system, as shown in Figure 2.11.

The mean damping characteristics, invariably used to evaluate the vehicle response to external excitations, is also shown. The generalized representation shows considerably higher damping force in rebound ($v_r<0$) than that in compression ($v_r>0$). The force is limited in compression as well as in rebound at higher piston velocity, which can be attributed to the force limiting behavior of the MR-damper. Conventional passive dampers also exhibit such force-limiting behavior caused by either single- or multi-stage pressure limiting valves.

The asymmetrically hysteretic *F-v* curve could be also described by two distinct properties: saturated hysteresis loop and linear rise, as discussed in section 2.4 for the symmetric *F-v* curve. The hysteresis loop can be considered to be symmetric by shifting the reference coordinate system from *F-o-v* to *F'-o'-v'*, and the symmetric model can then be applied to construct the asymmetric model. Furthermore, the synthesis of a more general model for asymmetric and hysteretic properties would necessitate the consideration of following characteristic parameters:

v_m	Maximum velocity of the damper piston determined from both the excitation frequency and the stroke.
F_{mc},F_{me}	Maximum damping forces corresponding to v_m developed in compression and rebound, respectively. The asymmetry is further by the factor γ, such that $\gamma=\|F_{me}/F_{mc}\|$.
v_{tc}, v_{te}	Transition velocities in compression and rebound corresponding to onset of

	force-limiting property, respectively, leading to linear post-yield rise and saturation.
F_{tc}, F_{te}	Transition forces in compression and rebound corresponding to v_{tc} and v_{te}, respectively, as determined from the mean curve.
β_{hc}, β_{he}	Slopes of mean curve in the pose-yield representing high speed viscous damping coefficients in compression and rebound, respectively, given by: $\beta_{\mathrm{hj}}=(F_{\mathrm{mj}}-F_{\mathrm{tj}})/(v_{\mathrm{m}}-v_{\mathrm{tj}})$, j=c, e.
β_{L}	Low velocity slope of the mean curve in the pre-yield representing the low speed viscous damping coefficient ($\beta_{\mathrm{L}}=\lvert F_{\mathrm{h}}/v_{\mathrm{r}}\rvert$).
v_{b}, F_{b}	The velocity and force offset with respect to the coordinate system F'-o'-v' of the symmetric curve, respectively.
v_{h}, F_{h}	Zero-force velocity and zero-velocity force intercepts in the F'-o'-v' axis system, as defined in section 2.4.

From the generalized hysteresis loop, depicted in Figure 2.11, the force associated with the saturated symmetric hysteresis loop in the absence of high velocity linear rise, $F_{\mathrm{s}}(v_{\mathrm{r}}+v_{\mathrm{h}})$, is formulated using the symmetric sigmoid function in EQ (2.4). The transition force F_{t} used in the symmetric formulation, however, is the mean of the compression and rebound transition forces, such that $F_{\mathrm{t}}=0.5(F_{\mathrm{tc}}+F_{\mathrm{te}})$. The high velocity linear rise segment of the asymmetric hysteresis curve related to the force-limiting property of the damper, however, differ in compression and rebound. Equation (2.5) is thus modified to incorporate the linear rise in compression and rebound, such that:

$$c_{\mathrm{v}}(v_{\mathrm{r}})=\begin{cases}1+k_{\mathrm{vc}}\lvert v_{\mathrm{r}}\rvert & v_{\mathrm{r}}\geq 0\\ 1+k_{\mathrm{ve}}\lvert v_{\mathrm{r}}\rvert & v_{\mathrm{r}}<0\end{cases} \tag{2.18}$$

where k_{vc} and k_{ve} are constants describing the effect of excitation condition on the linear rise in compression and rebound, respectively.

The asymmetric model synthesis is then derived upon integrating the velocity and force offsets (v_b and F_b) into the symmetric synthesis. The shifting of the symmetric axis system F'-o'-v' to the asymmetric axis F-o-v, and integrating the current function C_i defined in EQ (2.9), yields:

$$F_d(v_r, i_d) = \begin{cases} C_i(F_t \dfrac{1-e^{-a(v_r+v_h+v_b)}}{1+e^{-a(v_r+v_h+v_b)}} - F_b)(1+k_{vc}|v_r|) & v_r \geq 0 \\ C_i(F_t \dfrac{1-e^{-a(v_r+v_h+v_b)}}{1+e^{-a(v_r+v_h+v_b)}} - F_b)(1+k_{ve}|v_r|) & v_r < 0 \end{cases} \tag{2.19}$$

The above equation can characterize the asymmetric and hysteretic force-velocity characteristics of the MR-damper, presented in Figure 2.8. The model involves feature parameters (F_t, F_b, v_h, v_b, a, k_{vc}, k_{ve}) that are dependent not only on the nature of excitation (frequency and amplitude), but also on the drive current i_d. The transition force F_t, the current dependent function C_i, , the constant a, and the zero-force velocity intercept v_h are identical to those formulated in EQS (2.7), (2.9), (2.11) and (2.12), respectively. The force and velocity offsets are related to the peak velocity and drive current in the following manner:

$$F_b = k_5\, C_i\, F_t \quad \text{and} \quad v_b = k_6 v_m \tag{2.20}$$

where k_5 and k_6 are constants.

The high velocity linear rise coefficients in rebound and compression, k_{ve} and k_{vc}, are also related to the peak piston velocity:

$$k_{ve} = k_{1e} e^{-a_4 v_m} \qquad k_{vc} = k_{1c} e^{-a_4 v_m} \tag{2.21}$$

The proposed asymmetric and hysteretic F-v model requires identification of a total of 16 parameters (F_0, I_0, I_1, a_0, a_1, a_2, a_3, a_4, k_0, k_{1c}, k_{1e}, k_2, k_3, k_4, k_5, k_6) from the measured data. The proposed asymmetric hysteresis model can be easily simplified to yield mean asymmetric *F-v* model of the MR-damper by letting $k_4=0$ ($v_h=0$). The model can also be simplified to yield symmetric *F-v* characteristics by letting $k_5=k_6=0$ and $k_{1c}=k_{1e}$. The damping force characteristics in the passive mode can also be derived by letting $k_2=0$, $k_3=0$, $a_2=0$, $\alpha_3=0$, $I_0=0$ and $I_1=0$. Consequently, the proposed asymmetric *F-v* model can be regarded as a generalized hysteretic *F-v* model for both symmetric and asymmetric MR dampers to characterize the damping characteristics as function of the applied current and excitation condition.

2.7 Parameter Identification and Model Validation

The generalized model synthesis in conjunction with the measured data for the symmetric and asymmetric damping characteristics are used to identify the model parameters. In order to characterize the damping properties over wide ranges of applied current and excitation condition, a cost function is formulated to incorporate the squared errors corresponding to different test conditions:

$$U=\sum_{l=1}^{\mathrm{L}}\sum_{k=1}^{\mathrm{K}}\sum_{j=1}^{\mathrm{J}}[F(i_{\mathrm{d}},v_{\mathrm{r}})_{j,k,l}-F_{\mathrm{d}}(i_{\mathrm{d}},v_{\mathrm{r}})_{j,k,l}]^2 \tag{2.22}$$

where $F_{(j,k,l)}$ is the magnitude of measured damping force corresponding to j^{th} coordinate of the hysteron loop, k^{th} current and l^{th} frequency. $F_{\mathrm{d}(j,k,l)}$ is the corresponding damping force computed from the model. J, K and L define the levels of data points, currents and frequencies considered in the squared sum error function U.

The error function is derived upon considering the steady-state responses over a single cycle. A total of 360 data points are considered within each hysteresis loop derived for 5 different levels of current (K=5: 0, 0.1, 0.2, 0.3, and 0.4 A) and different excitation frequencies, for the symmetric *F-v* model parameter identification. The consideration of these frequencies for a given excitation magnitude provide a reasonable range of the piston velocity. The optimization function available within the MATLAB optimization toolbox (*fminunc*) is used to solve the minimization problem defined in EQ (2.22).

Owing to the strong dependence of the hysteretic forces in the symmetric and asymmetric modes on the peak velocity and thus the excitation frequency, the error minimization was performed for two different ranges of excitation frequencies, for the symmetric *F-v* model parameter identification. The different model parameters are thus identified for the low and high frequency ranges in the 0.5 to 5 Hz and 5 to 15 Hz, respectively. A total of 4 different frequencies (J=4: 0.5, 1.5, 2.5 and 5 Hz) were considered for low frequency excitation, while those for the high frequency involved 5 different frequencies (J=5: 5, 7.5, 10, 12.5 and 15 Hz). For the asymmetric model, the parameter identification was limited to the low frequency only (J=2: 0.5 and 1.5), and 4 different levels of current were considered (K=4: 0, 0.1, 0.2 and 0.3).

Tables 2.2 and 2.3 summarize the parameters of the symmetric and asymmetric models identified from the measured data. The results presented for the symmetric model show that parameters related to the current dependence of the damping force (k_2, a_2, I_0), width of the hysteresis loop (k_3, a_3, I_1), transition force (a_1) and high velocity linear rise (k_1, a_4) are strongly influenced by the excitation frequency range. The low velocity behavior is relatively insensitive to the excitation frequency. This is evident from comparable values of the seal friction force (F_0) and low velocity rise parameter (a_0) under the two frequency ranges. The results presented for the asymmetric model show that parameters related to the low velocity behavior is almost the same as those of the symmetric model at low frequency range, which are the seal friction force (F_0), low velocity rise parameter (a_0) and hysteresis width parameter (k_4).

Table 2.2: Identified symmetric model parameters of the candidate MR-damper.

Parameter	**Frequency (Hz)**		**Parameter**	**Frequency (Hz)**	
	0.5-5	**5-15**		**0.5-5**	**5-15**
a_0	992.985	988.967	k_0	125.987	177.249
a_1, $(m/s)^{-1}$	5.197	4.477	k_1	11.2	9.486
a_2, A^{-1}	7.258	12.757	k_2	9.244	4.355
a_3, A^{-1}	6.635	10.137	k_3	9.186	17.781
a_4, $(m/s)^{-1}$	7.504	5.501	k_4	-0.119	-0.156
I_0, A	0.079	-0.082	F_0, N	68.506	70.921
I_1, A	0.267	0.165			

Table 2.3: Identified asymmetric model parameters of the candidate MR-damper.

Parameter	**Asymmetry**	**Parameter**	**Asymmetry**
a_0	995.499	k_{1c}	16.877
a_1, $(m/s)^{-1}$	1.417	k_{1e}	4.673
a_2, A^{-1}	5.225	k_2	10.61
a_3, A^{-1}	2.441	k_3	10.666
a_4, $(m/s)^{-1}$	2.383	k_4	-0.125
I_0, A	0.268	k_5	0.269
I_1, A	1.131	k_6	0.453
k_0	177.51	F_0, N	79.92

2.7.1 Validation of the symmetric and hysteretic model

The proposed symmetric and hysteretic F-v model is further analyzed under a wide range of excitation conditions and magnitudes of drive current. The simulation results are compared with the measured data to evaluate the effectiveness of the proposed model. The comparisons generally showed reasonably good agreements between the model results and the test data over the entire range of test conditions considered, with the exception of those attained at high frequencies. Figures 2.12-2.14 show comparisons of simulation results in terms of F-v characteristics with the measured data under a number of the test conditions, as examples, to demonstrate the validity of the proposed model. Figure 2.12 illustrates the comparisons under different drive currents (i_d=0 to 0.4 A) and two different excitation conditions (f=1.5 and 2.5 Hz; a_m=12.5 mm).

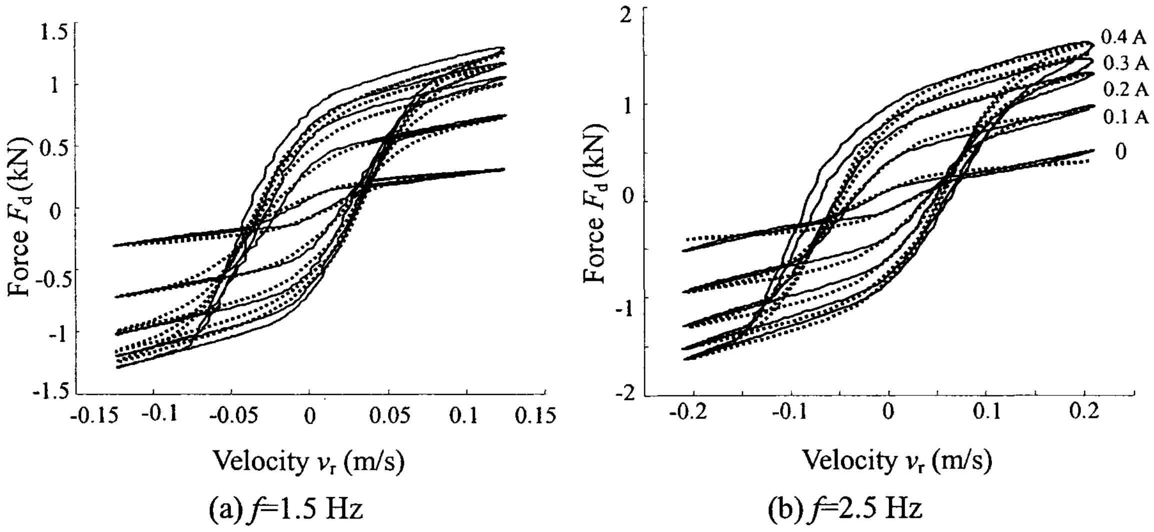

(a) f=1.5 Hz (b) f=2.5 Hz

Figure 2.12: Comparisons of symmetric model results with the measured data under different applied currents and excitation frequencies (a_m=12.5 mm).

Figure 2.13 shows comparisons of results under different excitation amplitudes in the 2.5 to 50 mm range, and frequencies in the 0.5 to 2.5 Hz range, while the applied current is held fixed (i_d=0.2 A). The results show reasonably good agreements between the measured data and the model results, irrespective of the applied current and excitation conditions within the lower frequency range.

Figure 2.14 illustrates the comparison of the model responses corresponding to higher frequency excitations with the measured data. The figure illustrates the model validity over the entire range of applied current (i_d=0 to 0.4 A) and excitation frequencies in the 5 to 15 Hz range, while the displacement amplitude is held as 2.5 mm. The model results follow trends similar to those observed in the measured data, correlate reasonably well with the measured data under lower currents and excitation frequencies. The model results, however, exhibit sharp jumps near the extreme velocities, particularly under high currents ($i_d \geq 0.3$ A).

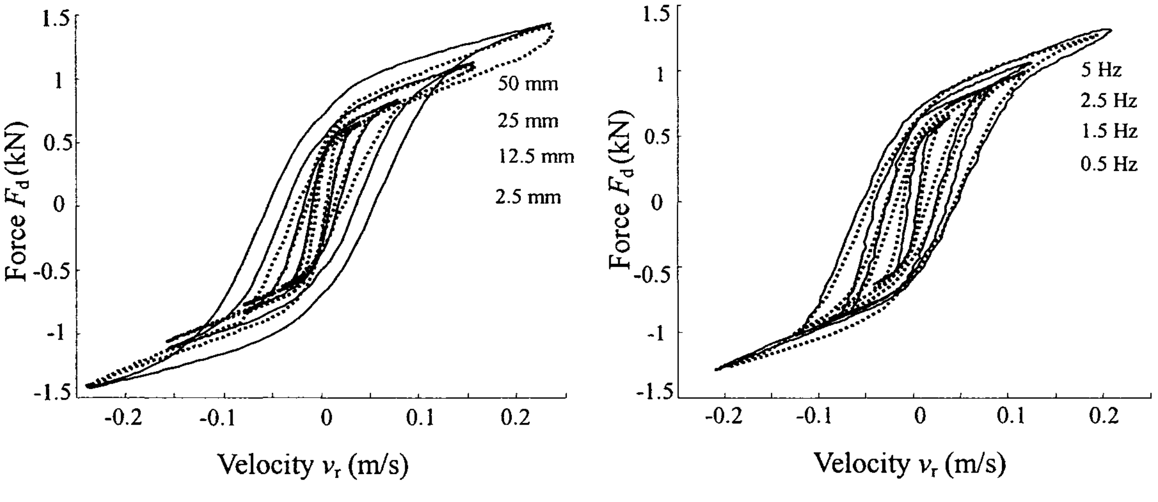

Figure 2.13: Comparisons of symmetric model results with the measured data for fixed current (i_d=0.2 A) under: (a) different excitation amplitudes, f=0.5 Hz; and (b) different frequencies, a_m=12.5 mm.

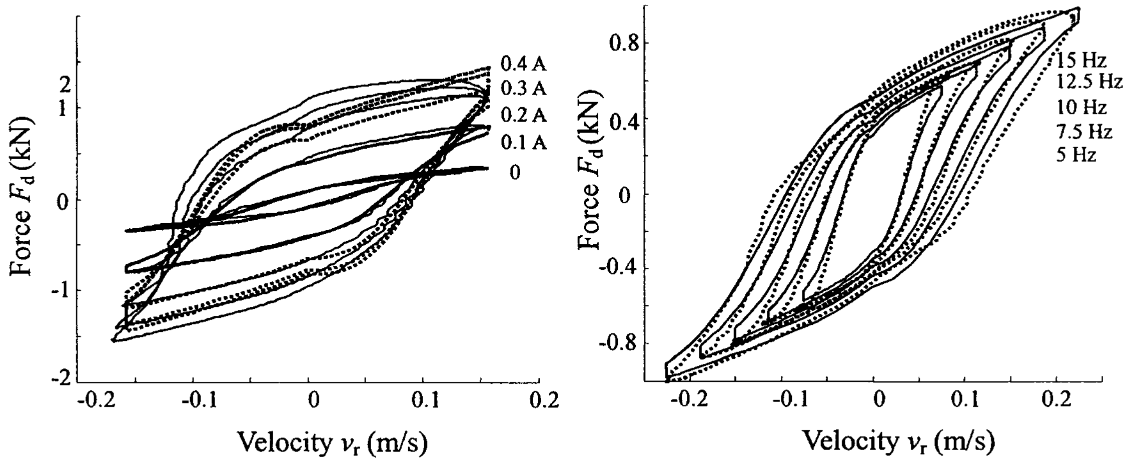

(a) (b)

Figure 2.14: Comparisons of symmetric model results with the measured data under higher frequency excitation functions of: (a) applied current, f=10 Hz, a_m=2.5 mm; and (b) excitation frequency, i_d=0.1 A, a_m=2.5 mm.

2.7.2 Validation of the asymmetric and hysteretic model

The proposed asymmetric and hysteretic F-v model is further analyzed under selected ranges of excitations and drive currents. The simulation results are compared with the measured data to demonstrate the validity of the proposed model. Figure 2.15 illustrates the comparisons of the model results with the measured data under different drive currents (i_d=0 to 0.4 A) and low frequency excitations (f=0.5 and 1.5 Hz; a_m=12.5 and 25 mm).

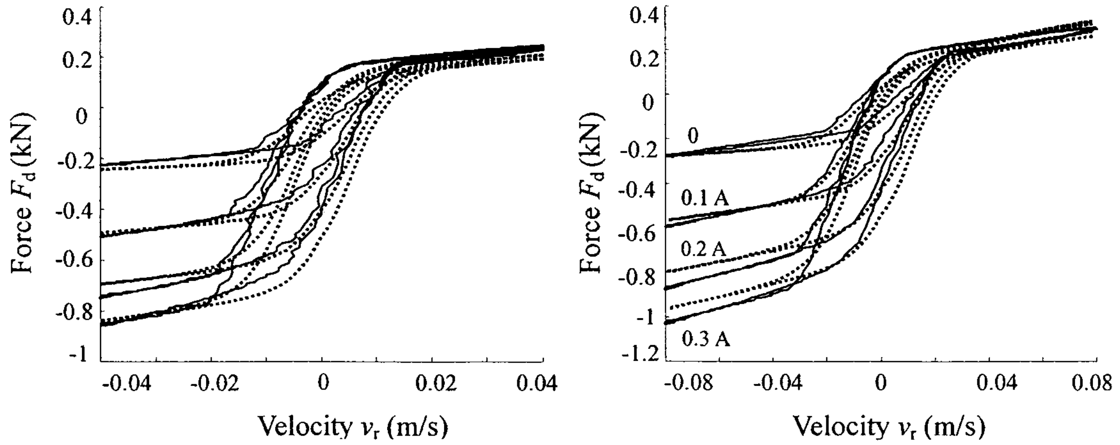

(a) f=0.5 Hz, a_m=12.5 mm (b) f=0.5 Hz, a_m=25 mm

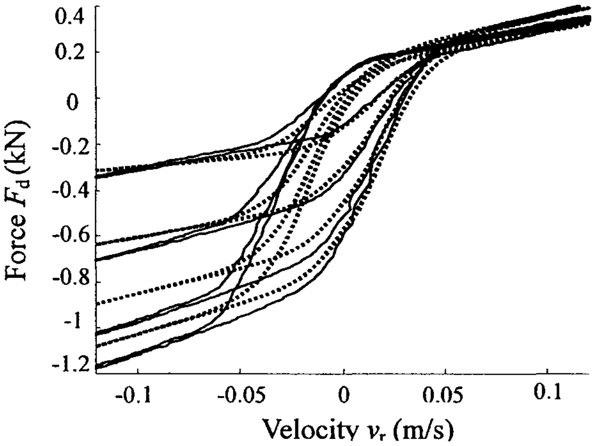

(c) f=1.5 Hz, a_m=12.5 mm

Figure 2.15: Comparisons of symmetric model results with the measured data under low frequency excitations and applied current.

The comparisons of model results with the measured data generally show reasonably good agreements between the model results and the test data over the range of test conditions considered.

2.8 Summary

Extensive laboratory measurements were performed to characterize the symmetric and asymmetric hysteresis force properties of a MR-damper under a wide range of drive current and excitation conditions (frequency and stroke). An asymmetric damping force generation (ADFG) algorithm is proposed to generate the asymmetric damping force in compression and extension for the symmetric MR-damper. A generalized model and an inverse dynamic model are proposed to characterize the hysteretic *F*-*v* characteristics of the controllable symmetric and asymmetric MR dampers. The essential features of the model are derived on the basis of the measured force-displacement, force-velocity and seal friction properties attained under a wide range of excitation conditions. The model formulation is systematically realized on the basis of the fundamental force generation mechanism, observed qualitative trends and the measured data.

The global model synthesis is realized upon integration of components describing the excitation and current dependent hysteretic linear rise in the pre-yield condition, force limiting in the post-yield condition, zero-force velocity intercept, zero-velocity force intercept and yield force corresponding to onset of saturation. Simulations are performed to assess the effectiveness of the proposed model synthesis and results obtained under wide range of simulation conditions are compared with those obtained from the measured data. The results show reasonably good agreements between the simulation results and the measured data, irrespective of the excitation conditions and control current. It is thus concluded that the proposed model can effectively describe the nonlinear steady state hysteretic dynamic properties of the controllable MR damper and can thus be effectively used to design optimal semi-active controller for implementation in vehicle suspension.

CHAPTER 3

SYNTHESES OF SEMI-ACTIVE MR-DAMPER CONTROLLERS

3.1 Introduction

The automotive suspensions are designed to satisfy several conflicting requirements, such as adequate ride quality, road holding, and handling and control characteristics within limited rattle space. A vast number of semi-active and active suspension systems have thus been explored to generate variable forces in response to varying excitations and to achieve better compromise among the various conflicting performance requirements [3, 4, 18, 19]. Studies on variable damping concepts using conventional hydraulic dampers have established that such dampers can effectively track the force that could be generated by a fully-active force generator when the force is of dissipative nature. Although the cost and hardware complexities associated with such dampers are considerably lower, the performance is limited due to low bandwidth and switching transients [4, 31, 32, 41-44].

Upon recognizing the high potentials of recently developed MR dampers, a number of control concepts for such dampers have been explored in recent years [12, 13, 80-86]. As stated earlier, the MR-damper offers high viscous damping corresponding to low velocities in the pre-yield condition, while the post-yield saturation at higher velocities can be characterized by a considerably lower viscous damping coefficient. Such damping properties are considered to be well suited for vehicle suspension applications to achieve satisfactory compromise among the various conflicting requirements [5, 6, 13, 57-61]. The development of an effective controller for realizing desirable variations in damping requires not only an accurate characterization of hysteretic *F-v* characteristics in the pre-yield and force saturation in the post-yield, but also effective control algorithms. The reported studies, however, invariably consider damping properties that are symmetric in compression and rebound, and negligible hysteresis. The vehicle suspensions are designed to provide highly asymmetric damping in compression and rebound to ensure adequate tire-road interactions [1, 33].

In this chapter, symmetric and asymmetric hysteretic models of MR dampers, formulated in Chapter 2, are employed to a single vehicle model to synthesize and evaluate different control algorithms. Three different controller syntheses are developed in a systematic manner, involving "skyhook"-based hi-lo, "inverse-model"-based hi-lo and "inverse-model"-based sliding-mode semi-active controllers. A set of performance measures is also defined to carry out relative evaluations of the controller synthesis under harmonic, transient and random road excitation signals.

3.2 Development of a Quarter-Vehicle Model

The performance potentials of the MR-damper and the controller can be conveniently investigated using a simplified "quarter-vehicle" model. Such models involving linear or nonlinear component properties have been widely used to evaluate different suspension concepts and can provide relatively good agreements of ride, tire load and rattle space performances [12, 19, 23, 82-84, 97]. Assuming negligible contributions due to roll and pitch motions of the sprung and unsprung masses, the vertical dynamics of the vehicle can be characterized by a two-degree-of-freedom (DOF) shown in Figure 3.1.

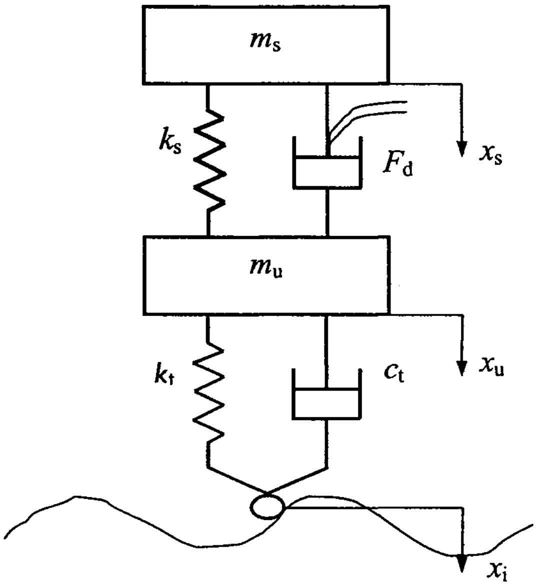

Figure 3.1: Two-DOF "quarter-vehicle" model.

The sprung and unsprung masses of the vehicle are represented by rigid bodies of masses m_s and m_u, respectively. While the suspension spring is characterized by its constant stiffness k_s, the tire is modeled by its stiffness and viscous damping constants (k_t and c_t), assuming point-contact with the undeformable road surface. The suspension damping force developed by the MR-damper F_d is derived from EQ (2.15) as a function of the drive current i_d and relative velocity across the damper. The equations of motions for the vehicle model can be expressed as:

$$\begin{cases} m_s\ddot{x}_s + F_k + F_d - m_s g = 0 \\ m_u\ddot{x}_u + F_T - F_k - F_d - (m_s + m_u)g = 0 \end{cases} \tag{3.1}$$

where x_s and x_u are the displacement coordinates of sprung and unsprung masses, respectively. $F_k = k_s(x_s - x_u + \Delta x_s)$ is the restoring force developed by the suspension spring, and $\Delta x_s = m_s g/k_s$ is the static deflection of the suspension spring. F_T is the dynamic force due to tire, given by:

$$F_T = \begin{cases} k_t(x_u + \Delta x_u - x_i) + c_t(\dot{x}_u - \dot{x}_i); & x_u + \Delta x_u - x_i > 0 \\ 0 & ; \; x_u + \Delta x_u - x_i < 0 \end{cases} \tag{3.2}$$

where x_i is the displacement excitation at the tire-road interface, $\Delta x_u = (m_s + m_u)g/k_t$ is the static deflection of the tire and g is acceleration due to gravity.

The above tire force model also incorporates the possible loss of contact with the road surface under extreme road inputs. The term F_d in EQ (3.1) is damping force developed by the MR-damper as described in EQ (2.15):

$$F_d = f_d(i_d, v_r); \quad 0 \le i_d \le i_H \tag{3.3}$$

where $v_r = \dot{x}_s - \dot{x}_u$ is the relative velocity across the MR-damper motion.

3.2.1 Generalized formulation of MR-damper force

Owing to the symmetric design of the MR-damper, the damper may be operated in either the passive or symmetric control mode. The passive damping mode refers to constant damping force characteristics, where i_d assumes either a zero value or a constant value ($i_d \le i_H$). The resulting damping force, developed in an open-loop manner, can thus be expressed using EQS (2.8) and (2.15), such that:

$$F_d = f_d(i_d, v_r); \quad i_d = 0 \quad \text{or} \quad i_d = \text{constant} \tag{3.4}$$

The reported studies have invariably proposed controller design with $i_d \ge 0$, which yields symmetric variation in the damping force, in compression and rebound, such that:

$$F_d = f_d(i_d, v_r); \quad 0 \le i_d \le i_H \tag{3.5}$$

The above mode of operation would yield symmetric variation in damping force in compression and rebound in a closed-loop manner, as a function of the command current i_d and relative velocity response v_r.

The asymmetric damping force generation (ADFG) algorithm, formulated in EQ (2.3), could be applied to derive asymmetric force in compression and rebound, such that:

$$F_{\mathrm{d}} = f_{\mathrm{d}}(i_{\mathrm{d}}, v_{\mathrm{r}}); \quad 0 \le i_{\mathrm{d}} = \mathrm{M}_{\mathrm{p}}(p, \xi, v_r) \le i_{\mathrm{H}} \tag{3.6}$$

where $\mathrm{M}_{\mathrm{p}}(p, \xi, v_{\mathrm{r}})$ is the ADFG multiplier, which is a function of sign of velocity and the asymmetry factor p ($0 \le p < 1$). A value of $p=0$ would yield largest asymmetry in the damping force by letting $i_{\mathrm{d}}=0$ when $v_{\mathrm{r}}=0$. The multiplier modulates the drive current i_{d} in an asymmetric manner on the basis of the controller current i_{c}. In the above formulation, ξ is chosen to suppress the effects of discontinuity near $v_{\mathrm{r}}=0$.

3.3 Generalized Formulation of Drive Current

Depending upon the mode of operation (passive, symmetric and asymmetric), the command current may assume either constant or varying values. Furthermore, the variations in the command current are dependent on the controller design. The control current in hi-lo or on-off semi-active control would generally modulate between the lower and upper limits on the basis of a condition or logic function. The variation in the control current is thus generally expressed as:

$$i_{\mathrm{c}} = \begin{cases} i_{\mathrm{z}}; & \text{if} \quad z_{\mathrm{c}} < 0 \\ 0; & \text{if} \quad z_{\mathrm{c}} \ge 0 \end{cases} \tag{3.7}$$

where z_{c} is the logic switching condition for the semi-active controller, and i_{z} is the control current derived from the controller synthesis, which varies in an active manner.

For symmetric control mode, the controller current could serve as the drive current ($i_{\mathrm{d}}=i_{\mathrm{c}}$). Such a formulation, however, causes discontinuity near $z_{\mathrm{c}}=0$ and thus undesirable transient dynamic responses of the suspension dampers. Asymmetric variations in the command current in a continuous manner can be realized by integrating the ADFG multiplier M_p, as described in EQ (3.5). This algorithm allows for suppressing the transient oscillations caused by abrupt variations in i_c, as described in section 2.3. In addition to the variation i_c, the discontinuity in the condition function employed in a controller synthesis could also cause transient oscillations in the system responses. A continuous variation in the condition function within an algorithm may be realized by employing a function similar to ADFG algorithm to the condition function. A continuous modulation (CM) algorithm is thus proposed to minimize the effects of discontinuity in the controller current, EQ (3.7), such that:

$$\mathrm{M}_c(p_c, \xi_c, z_c) = \frac{1+p_c}{2} + \frac{2}{\pi}\left[p_c(z_c \geq 0) \cup (z_c < 0) - \frac{1+p_c}{2}\right]\left|\tan^{-1}(\xi_c z_c)\right| \qquad (3.8)$$

where $\mathrm{M}_c(p_c, \xi_c, z_c)$ refers to the CM multiplier, p_c is the asymmetry factor used in the semi-active controller synthesis ($0 \leq p_c < 1$), and ξ_c is the smoothing factor ($\xi_c > 0$). The logic function $p_c(z_c \geq 0) \cup (z_c < 0)$ defines a lower value of p_c when $z_c > 0$ or $p_c = 1$ when $z_c < 0$. A zero value of p_c would yield continuous variation in the controller current i_c between the defined extreme limits (0 to i_z).

As an example, Figure 3.2 illustrates the variations in controller current i_c, derived from the on-off controller defined in EQ (3.7) in conjunction with CM function M_c, where the condition function is varied in a harmonic manner. The results show the effect of variations in the asymmetry factor p_c and the smoothing factor ξ_c. A lower value of ξ_c yields more continuous and smooth variation in i_c, and may cause greater error in the controller current. A zero value of p_c causes variation within the extreme limits of the controller current (0 to i_z), while a higher value of p_c would permit modulation from the lower to higher limit (hi-lo).

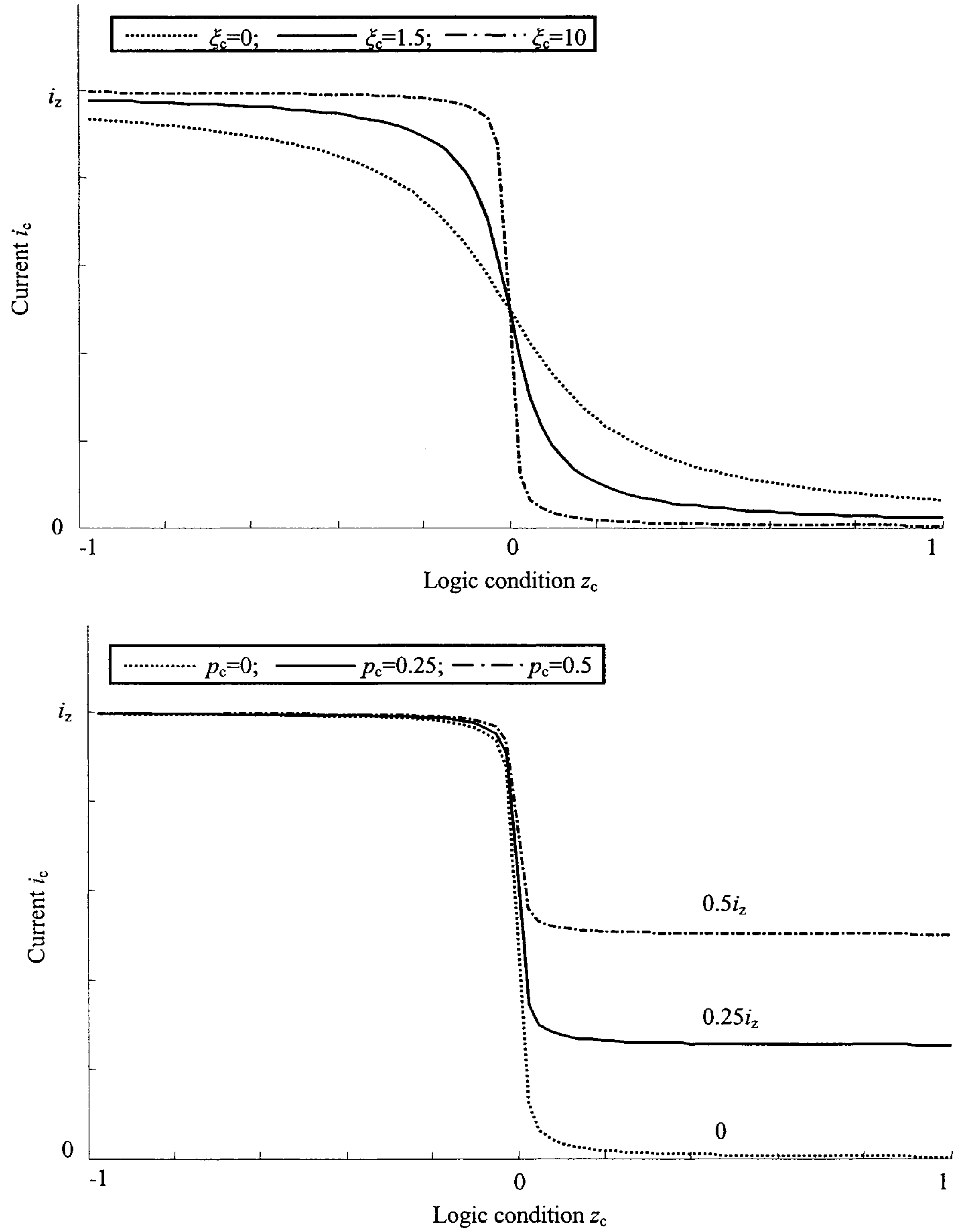

(b) Hi-lo: ξ_c=10, p_c=0, 0.25, 0.5

Figure 3.2: Continuous variations in the controller current of on-off or hi-lo control algorithm, and the effects of smoothing and asymmetry factors.

For on-off type of semi-active control, a higher value of ξ_c and zero value of p_c would be desirable. The drive current i_d, as defined in EQS (3.5) and (3.6), can then be related to i_z through the multiplier of the ADFG and CM functions, such that:

$$i_d = M_p(p,\xi,v_r)M_c(p_c,\xi_c,z_c)i_z\ ; \qquad 0 \le i_d \le i_H \tag{3.9}$$

3.4 Syntheses of Semi-Active MR-Suspension Controllers

Three different semi-active control algorithms are synthesized for the "quarter-vehicle" model with an MR-damper. These syntheses are based upon the well-known "skyhook", "inverse model" and "sliding-mode" controllers. The different controller syntheses are formulated using the symmetric and asymmetric damping modes and integrated within the "quarter-vehicle" MR-suspension model.

3.4.1 Formulation of skyhook based reference model

Controller synthesis for the MR-suspension under varying excitations and load conditions could be realized by formulating target functions on the basis of a reference model. Model reference adaptive control techniques have been widely applied for adaptive controller design under varying disturbances or excitations [12, 70, 82, 97]. For vehicular suspension applications, an idealized suspension performance model is frequently defined in accordance with defined performance measures in synthesizing a controller, where the idealized model serves as the target function for the controller [12, 82, 97]. A "skyhook" damper suspension model is chosen to serve as the reference model in this study, as it can provide superior vibration isolation within reasonable rattle space, and thus the dynamic tire load and road holding performance [12, 82, 97].

The "skyhook" control concept proposed by Karnopp *et al.* [87], which considers the damper with a fixed inertial reference, as shown for the "quarter-vehicle" model in Figure 3.3(a). It has been shown that the robustness of the "skyhook"-based sliding mode controller can be enhanced by light additional passive damping, particularly under load uncertainties. Lam *et al.* [82] thus proposed a modified "skyhook" damping, which integrates an additional passive viscous damper in parallel with the suspension spring, as shown in Figure 3.3(b).

The equations of motion for the modified model are formulated as:

$$\begin{cases} m_{s0}\ddot{x}_s + F_k + F_s + F_v - m_{s0}\,g = 0 \\ m_{u0}\ddot{x}_u + F_T - F_k - F_v - (m_{s0} + m_u)g = 0 \end{cases} \tag{3.10}$$

where m_{s0} is the nominal sprung mass of the reference model. F_s and F_v are damping forces generated by the "skyhook" and viscous damper, respectively, with damping coefficients c_s and c_0, given by:

$$F_s = c_s\dot{x}_s;\ \text{and}\ F_v = c_0(\dot{x}_s - \dot{x}_u) \tag{3.11}$$

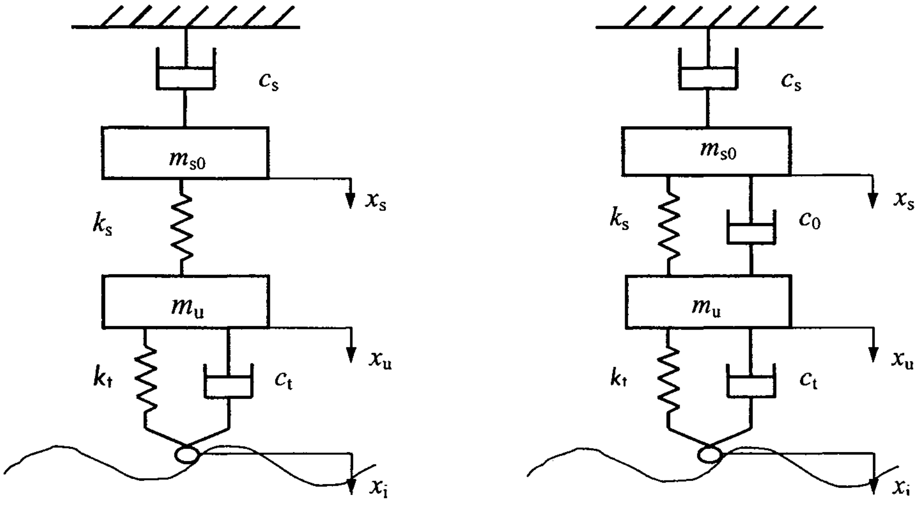

(a) (b)

Figure 3.3: "Quarter-vehicle" model with (a) "Skyhook" damping [87]; (b) Modified "skyhook" damping [82].

The reference model responses are derived upon considering the nominal model parameters: m_{s0}=563 kg; m_u=90 kg; k_s=57 kN/m; c_s=6.75 kNs/m; k_t=285 kN/m; and c_t=100 Ns/m. These parameters yield sprung and unsprung mass natural frequencies as, $f_{n\text{-}s0}\approx1.5$ Hz and $f_{n\text{-}u0}\approx10$ Hz; and static deflection as, $\Delta x_{s0}\approx9.67$ cm and$\Delta x_{u0}\approx2.24$ cm. The value of the viscous damping coefficient is chosen to achieve desirable reference model responses.

Figure 3.4 illustrates the reference model frequency responses in terms of selected performance measures that are defined in section 3.6. These include: the acceleration transmissibility of the sprung (T_{as}) and unsprung (T_{au}) masses; normalized dynamic tire force, referred to as the dynamic load coefficient (DLC); and relative suspension deflection transmissibility (T_{dr}).

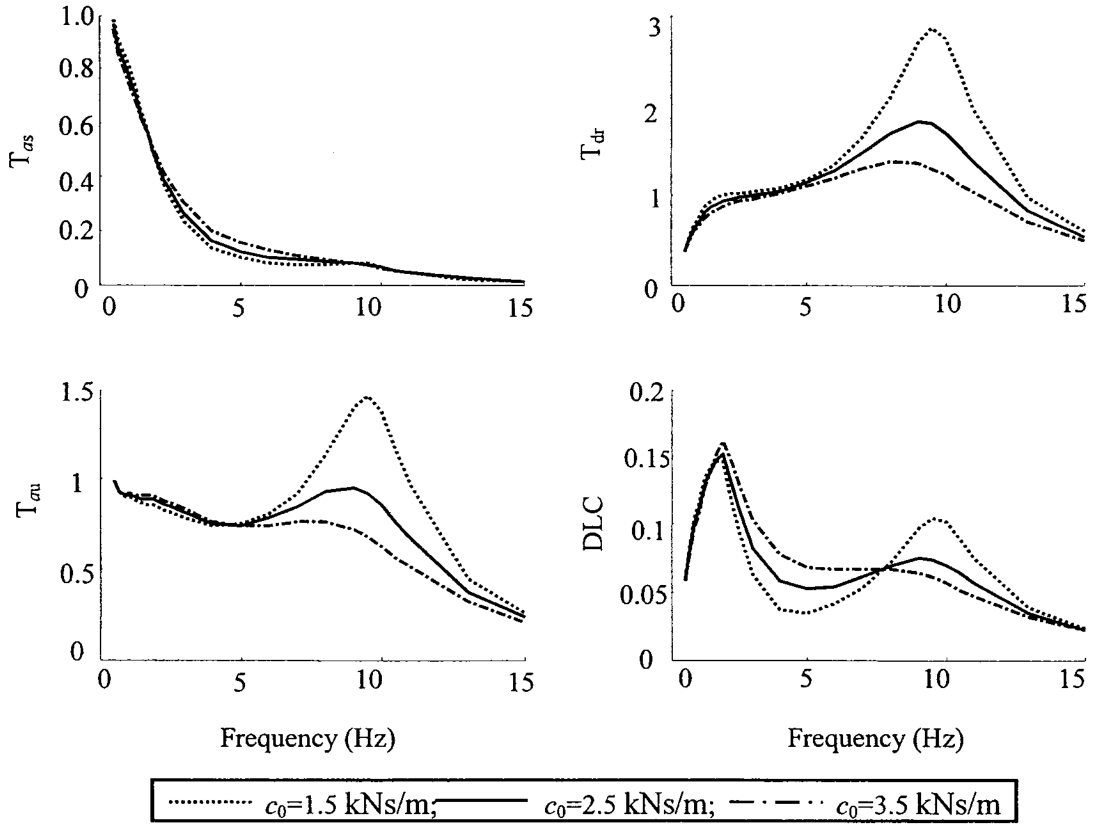

Figure 3.4: Frequency response characteristics of modified "skyhook"-based reference model as a function of the viscous damping.

The results show the influence of variations in c_0 on the selected measures. The results show that the sprung mass acceleration transmissibility response of the reference model is relatively insensitive to variations in c_0. The peak DLC due to tire force in the vicinity of the sprung mass resonance also remains unaffected by variations in c_0. The suspension relative motion, the DLC due to tire force and unsprung mass acceleration transmissibility around the unsprung mass resonance, however, could be significantly reduced by selecting a higher additional viscous damping. Too high a viscous damping, however, could cause overdamped unsprung mass deflection mode. Viscous damping of c_0=2.5 kNs/m is thus selected for the reference modified "skyhook" model, which could provide reasonable unsprung mass deflection and rattle. The model and its responses are used in the later section, as the target functions for synthesizing the sliding-mode controller for the MR-damper suspension.

3.4.2 Hi-lo based controller synthesis

A number of studies have demonstrated superior performance potentials of vehicle suspension with "skyhook" damping in realizing the multi-objective performances goals [12, 22, 82, 87, 97]. The implementation of the "skyhook" damping, however, is quite challenging due to fixed inertial reference of the damper. Karnopp *et al.* [87] proposed control law to realize damping force in a "skyhook" manner, which has been widely explored in many studies [12, 22, 40, 82, 97]. It was proposed that the magnitude of mass acceleration could be reduced by reducing the damping force, when the sprung mass velocity ($\dot{x}_s$) is out of phase with the damper relative velocity across the suspension spring. The "skyhook" damping scheme, proposed by Karnopp *et al.* [87] can thus be expressed as:

$$F_{\mathrm{d}} = \begin{cases} c_{\mathrm{s}}\dot{x}_{\mathrm{s}}; & \text{if} \quad \dot{x}_{\mathrm{s}}(\dot{x}_{\mathrm{s}} - \dot{x}_{\mathrm{u}}) > 0 \\ 0\ ; & \text{if} \quad \dot{x}_{\mathrm{s}}(\dot{x}_{\mathrm{s}} - \dot{x}_{\mathrm{u}}) < 0 \end{cases} \tag{3.12}$$

The above control scheme yields high damping force when the sprung mass velocity is in phase with the relative velocity across the suspension spring. The damping force is suppressed otherwise. The damping force modulation in the on-off manner, however, yields discontinuity in the damping force near $\dot{x}_{\mathrm{s}}(\dot{x}_{\mathrm{s}} - \dot{x}_{\mathrm{u}}) \approx 0$ and transient responses of the sprung and unsprung masses [40]. Moreover, the control concept can be applied only for damping force symmetric in compression and rebound. The idealized "skyhook" control law could also cause instability due to zero damping force in the "off" state, which can be easily verified by employing the stability theory for the linear systems [70]. Furthermore, the measurement of absolute velocity of the sprung mass also poses many difficulties [40].

Alternatively, Rakheja *et al.* [40] proposed an on-off control scheme based upon the directly measurable relative displacement ($x_{\mathrm{r}}= x_{\mathrm{s}}-x_{\mathrm{u}}$) and relative velocity ($\dot{x}_{\mathrm{r}}$) of the sprung mass with respect to the unsprung mass. It was suggested that the magnitude of sprung mass acceleration could be reduced by suppressing the damping force, when the damping force (F_{d}) is in phase with the suspension spring force (F_{k}). Owing to the linear relationship of F_{d} and F_{k} with the relative velocity and displacement, respectively, the on-off damping algorithm was proposed as:

$$F_{\mathrm{d}} = \begin{cases} c_{\mathrm{s}}(\dot{x}_{\mathrm{s}} - \dot{x}_{\mathrm{u}}); & \text{if} \quad x_{\mathrm{r}}\dot{x}_{\mathrm{r}} < 0 \\ 0 \qquad ; & \text{if} \quad x_{\mathrm{r}}\dot{x}_{\mathrm{r}} \geq 0 \end{cases} \tag{3.13}$$

The above control laws have been implemented with conventional hydraulic dampers involving flow modulation devices. The MR-damper can be conveniently operated in the on-off or hi-lo modes by modulating the controller current i_c on the basis of the condition function comprising the responses of the sprung and unsprung masses. Four different control algorithms are formulated in this study to realize the modulation of controller current in an on-off manner. It should be noted that the on-off current modulation would yield hi-lo damping force variation, where the low damping mode corresponds to the passive damping force due to MR-damper (i_d=0). The proposed control schemes, formulated on the basis of the condition function functions proposed by Karnopp *et al.* [87] and Rakheja *et al.* [40], are expressed as:

$$
\begin{aligned}
&\text{Policy I:} && i_c = \begin{cases} k_c|\dot{x}_s|; & \text{if} \quad \dot{x}_s\dot{x}_r > 0 \\ 0\ ; & \text{if} \quad \dot{x}_s\dot{x}_r \le 0 \end{cases} \\
&\text{Policy II:} && i_c = \begin{cases} k_c|\dot{x}_r|; & \text{if} \quad \dot{x}_s\dot{x}_r > 0 \\ 0\ ; & \text{if} \quad \dot{x}_s\dot{x}_r \le 0 \end{cases} \\
&\text{Policy III:} && i_c = \begin{cases} k_c|\dot{x}_r|; & \text{if} \quad x_r\dot{x}_r < 0 \\ 0\ ; & \text{if} \quad x_r\dot{x}_r \ge 0 \end{cases} \\
&\text{Policy IV:} && i_c = \begin{cases} k_c|x_r|; & \text{if} \quad x_r\dot{x}_r < 0 \\ 0\ ; & \text{if} \quad x_r\dot{x}_r \ge 0 \end{cases}
\end{aligned}
\tag{3.14}
$$

where k_c represents the control gain of the proposed hi-lo semi-active policies.

In the above formulation, the policy I, based upon the "skyhook" control concept, would yield controller current proportional to magnitude of the sprung mass velocity $\dot{x}_s$. Higher current and thus the damping force is realized when the absolute sprung mass velocity is in phase with the relative velocity, as proposed by Karnopp *et al.* [87]. Unlike the originally proposed control scheme, the policy I would yield non-zero damping force, when $\dot{x}_s \dot{x}_r \le 0$. The control policy II also employs the identical switching function but generates controller current proportional to the relative velocity. Owing to the difficulties associated with measurement of sprung mass velocity, the policies III and IV are formulated on the basis of directly measurable x_r and $\dot{x}_r$, as proposed in [40]. The controller currents are generated in proportion to the relative velocity and displacement, respectively, when the condition function warrants higher damping force $\dot{x}_s \dot{x}_r \le 0$.

The discontinuity in the controller current in the proposed switching schemes can be effectively suppressed by introducing the continuous modulation (CM) function, formulated in section 3.3. The asymmetric damping force generation (ADFG) algorithm, derived in section 2.3.1, can be further integrated to realize asymmetric damping force in compression and rebound. The proposed modulation schemes are further generalized by introducing an exponent n of the control velocity $\dot{x}_s$ or $\dot{x}_r$, or displacement x_r, which is referred as the order of the controller. The modulation schemes comprising the CM and ADFG functions are thus formulated as:

$$\begin{aligned}
&\text{Policy I:} && i_z = k_c|\dot{x}_s|^n; \quad z_c = -\dot{x}_s\dot{x}_r \\
&\text{Policy II:} && i_z = k_c|\dot{x}_r|^n; \quad z_c = -\dot{x}_s\dot{x}_r \\
&\text{Policy III:} && i_z = k_c|\dot{x}_r|^n; \quad z_c = x_r\dot{x}_r \\
&\text{Policy IV:} && i_z = k_c|x_r|^n; \quad z_c = x_r\dot{x}_r
\end{aligned} \tag{3.15}$$

where i_z is the control current derived from a control synthesis and is related to the drive current i_d through the CM and ADFG functions and the condition function z_c, such that:

$$i_{\mathrm{d}} = \mathrm{M_p}(p,\xi,v_{\mathrm{r}})\mathrm{M_c}(0,\xi_{\mathrm{c}},z_{\mathrm{c}})i_{\mathrm{z}}\ ;\quad 0 \le i_{\mathrm{d}} \le i_{\mathrm{H}} \tag{3.16}$$

In the above formulation, p_c is chosen as 0 to realize lowest drive current (i_d=0), while a negative value of condition function z_c yields high current. Symmetric and asymmetric modulations of the current are realized by letting p=1and p=0, respectively, in the ADFG function, $M_P(p, \xi, v_r)$. The exponent n is chosen to further suppress the effects of discontinuity around $z_c \approx 0$. A unity value of n corresponds with the control policies defined in EQ (3.14). A higher value of the exponent ($n \geq 2$) would yield nonlinear variation in i_z with either $\dot{x}_s$ or $\dot{x}_r$ or x_r. Considering that the magnitudes of absolute and relative velocities and displacement of sprung mass of a vehicle are generally well below 1 m/s and 1 m, a higher exponent would help realize lower value of current in the "lo" state, particularly $\dot{x}_s$ or $\dot{x}_r$ or x_r are near zero. This would further ensure smoother switching of the current. Figure 3.5 illustrates a general structure of the MR-damping control schemes, compromising the CM and ADFG functions together with the modulation schemes.

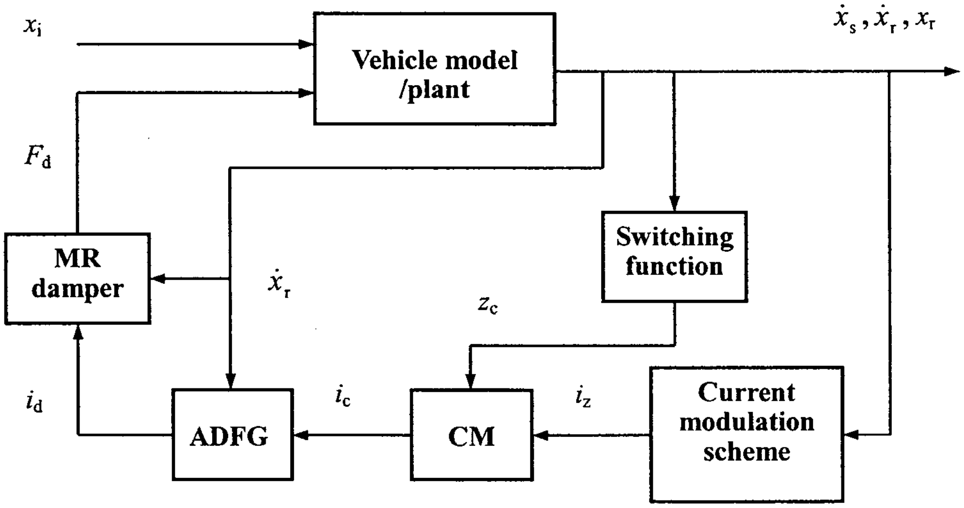

Figure 3.5: Schematic of general structure of the hi-lo MR-damping control scheme.

3.4.3 Inverse model based hi-lo controller synthesis

A number of studies have employed inverse model (IM) control algorithm to achieve desired force in accordance with defined target functions [65, 78]. The inverse model control techniques are known to be quite complex for nonlinear plants. The hysteretic inverse model of a MR-damper, derived on the basis of the generalized synthesis in section 2.5, can be applied to realize force tracking on the basis of inverse model control. A few recent studies have implemented force tracking control of MR dampers using conventional feedback control techniques, where the drive current is generated in response to the magnitude of the error between the damping force F_d and the target force F_c ($F_e = |F_d - F_c|$) [12, 80-84]. Such feedback control techniques yielded poor force tracking for the semi-active control of MR dampers due to contribution of the absolute error, and the presence of hysteresis. The utilization of the inverse model control law in conjunction with a reliable inverse model of the MR-damper can not only realize enhanced tracking of the desired force, but can also suppress the contribution due to hysteresis nonlinearity of the MR-damper.

An "inverse model"-based hi-lo semi-active controller for the MR-damper is formulated using the hysteretic inverse model described in EQ. (2.17). A modified on-off damping law is further used to define the target force, proposed by Alanoly *et al.* [44]. On the basis of the on-off control law, proposed by Rakheja *et al.* [40], it has been suggested that the sprung mass acceleration can be suppressed by selecting the magnitude of the damping force equal to that of the spring force, when the two forces oppose each other. The damping force should be suppressed when it acts in the direction of the spring force. By letting $F_d = F_k$, when

$x_r\dot{x}_r<0$, the inverse model, defined in EQ (2.17), yields:

$$i_z = f_d^{-1}(F_k, F_h);\quad z_c = F_h F_k = x_r \dot{x}_r \tag{3.17}$$

In the above formulation, F_h is the passive hysteron force of the MR-damper, defined in EQ (2.8). The current i_z is derived from the inverse model and the condition function z_c. The drive current i_d is then generated in response to i_z using the CM, ADFG and the condition functions, as described in EQ (3.16).

Figure 3.6 illustrates the structure of the proposed "inverse model"-based hi-lo semi-active control of the MR-suspension, in which the suspension spring force F_k serves as the desirable damping force, and the inverse model converts F_k to the control current i_c by employing CM algorithm. The current i_d is generated using "inverse model"-based hi-lo semi-active in conjunction with CM and ADFG functions. Both the symmetric (SCM) and asymmetric (ACM) damping force control modes may be realized by letting p=1and p=0, respectively. The structure also employs the condition function that allows for the damping force F_d to track the spring force F_k, when the two forces oppose each other. Alternatively, the damper operates in the passive mode (i_d=0).

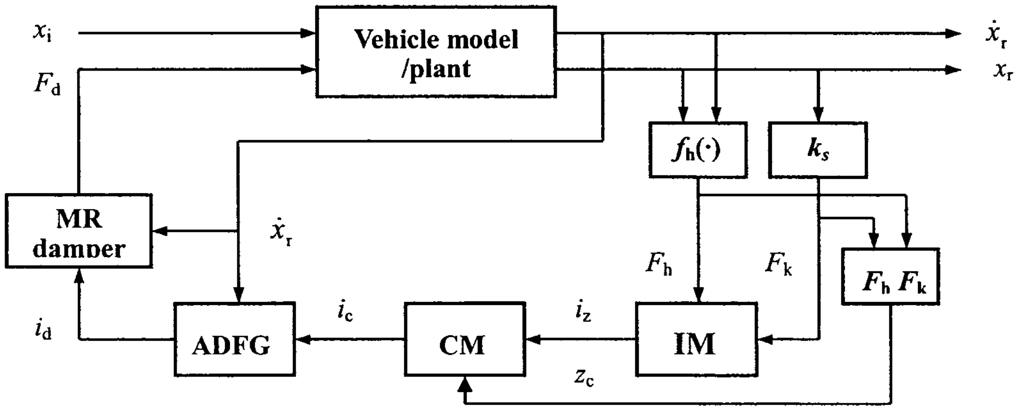

Figure 3.6: Schematic diagram of "inverse model"-based hi-lo semi-active MR-suspension.

The proposed controller structure does not involve minimization of the force error that has been employed in the reported studies [12, 80-84]. Moreover, it employs feedback from the directly measurable relative displacement and relative velocity.

3.4.4 Inverse model based sliding mode controller synthesis

The nonlinear control problem invariably encounters discrepancies between the actual plant and the mathematical model developed for controller design, which may be due to un-modeled dynamics, uncertainty of system parameters or the idealized approximation of the complex plant behavior [70, 73, 75, 79, 100]. The system parameter uncertainty can have adverse effects on the performance of the controller. The control approach involving the robust controller design on the basis of a reference model is thus considered desirable [12, 42, 70, 75-77]. The sliding-mode (SM) control technique offers enhanced robustness and provides a systematic approach for maintaining the stability and performance in the presence of modeling imprecision [12, 82, 97, 100].

The robustness of the semi-active MR-suspension controller design is vital in view of the multi-objective performance requirements and extreme potential variations in the excitations and vehicle loading. The uncertainties due to road excitations, speed and load thus form the primary challenge for design of an intelligent vehicle suspension. A number of studies have investigated performance characteristics of active and semi-active vehicle suspension employing the sliding-mode control approach [12, 82, 97]. Lam *et al.* [82] and Yokoyama *et al.* [12] proposed a MR-suspension control synthesis using the SM control law to generate the desired damping force by integrating a force feedback loop to regulate the control voltage. The proposed semi-active controller, however, resulted in poor force tracking in the presence of damper hysteresis.

In this study, the sliding mode control law is employed in conjunction with a modified "skyhook"-based reference model that is constructed on the basis of the model described in section 3.4.1. The reference model serves as the nominal control target, while the inverse model control is applied to reduce the effects of hysteresis. Owing to the variations in the vehicle load, the sprung mass (m_s) is considered as the uncertain parameter, and the desirable force F_c derived from the sliding mode control synthesis serves as the target force for the MR-damper. The proposed "inverse-model"-based sliding mode semi-active controller in conjunction with the inverse model control of the MR-damper can help realize improved tracking of the desired force, and suppress the contributions due to hysteretic nonlinearity of the MR-damper. The controller synthesis is realized in two stages. The initial stage involves the formulation of the target force (F_c) using the SM control approach together with the "skyhook"-based reference model. The second stage generates the semi-active drive current (i_d) on the basis of the IM control law that employs the CM and ADFG functions, as described in sections 3.3 and 2.3.1, respectively.

Assuming constant tire properties, the road roughness uncertainty can be adequately reflected in the unsprung mass deflection response. The reference model, described in section 3.4.1, could thus be further simplified as a single-DoF system comprising c_0. Figure 3.7 illustrates the single-DoF reference model together with the "quarter-vehicle" model employing the MR-damper.

The differential equation describing the motion x_{s0} of the nominal sprung mass m_{s0} of reference model can be expressed as:

$$m_{s0}\ddot{x}_0 + c_0(\dot{x}_{s0} - \dot{x}_u) + c_s\dot{x}_{s0} + k_s(x_{s0} - x_u) = 0 \tag{3.18}$$

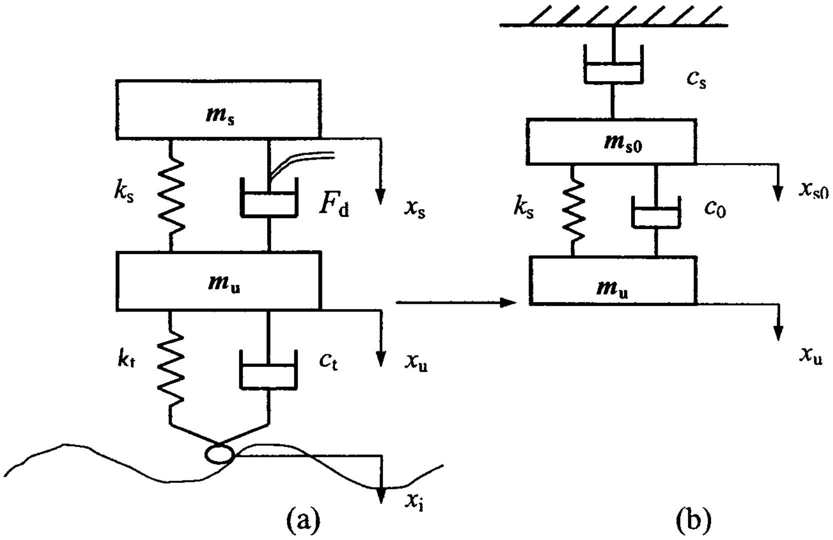

Figure 3.7: (a) "Quarter-vehicle" model; and (b) Modified "skyhook"-based reference model.

The sliding mode control law is employed on the basis of the motion of the sprung mass of the plant (quarter-vehicle) to track the nominal sprung mass motion of the reference model. Herein, the sliding surface is defined as:

$$s = \dot{e}_s(t) + \lambda e_s(t) \tag{3.19}$$

where $e_s(t)$ and $\dot{e}_s(t)$ define the position and velocity errors, respectively, such that, $e_s(t) = x_s(t) - x_{s0}(t)$, $\dot{e}_s(t) = \dot{x}_s(t) - \dot{x}_{s0}(t)$. λ is a positive constant referred to as the sliding surface slope, which plays an important role to ensure that the magnitude of position error diminishes as $t \rightarrow \infty$. The rate of convergence of the error strongly depends on the choice of λ. The strategy of the sliding mode control is to force the system trajectories towards the manifold s=0 in finite time, and to maintain the trajectories around the same manifold. The dynamic responses of the system on the sliding surface are represented by a reduced-order model, given by:

$$\dot{e}_{\mathrm{s}} = -\lambda e_{\mathrm{s}} \tag{3.20}$$

The sliding condition $s\dot{s} < 0$ should ensure the state to move toward and reach the sliding surface. Consideration of $V = s^2/2$ as a Lyapunov function candidate for $\dot{s}$ yields:

$$\dot{V} = s\dot{s} \tag{3.21}$$

Equations (3.18) and (3.19) yield following expression for $\dot{s}$:

$$\begin{aligned} \dot{s} &= \ddot{e}_{\mathrm{s}} + \lambda \dot{e}_{\mathrm{s}} \\ &= -\frac{k_{\mathrm{s}}}{m_{\mathrm{s}}}(x_{\mathrm{s}} - x_{\mathrm{u}}) - \frac{F_{\mathrm{d}}}{m_{\mathrm{s}}} - \ddot{x}_{\mathrm{s0}} + \lambda \dot{e}_{\mathrm{s}} \end{aligned} \tag{3.22}$$

Substitution for $\dot{s}$ in EQ (3.21) yields:

$$\dot{V} = \left[-\frac{k_{\mathrm{s}}}{m_{\mathrm{s}}}(x_{\mathrm{s}} - x_{\mathrm{u}}) - \ddot{x}_{\mathrm{s0}} + \lambda \dot{e}_{\mathrm{s}} - \frac{1}{m_{\mathrm{s}}} F_{\mathrm{d}} \right] s \tag{3.23}$$

The control input or target force F_{d} is assumed as:

$$F_{\mathrm{d}} = F_{\mathrm{d0}} - K\,\mathrm{sgn}(s) \tag{3.24}$$

where K is the sliding mode control gain, and the sgn(·) function yields a value of -1 or 1 when (·)<0 or (·)>0, respectively. Consequently, EQ (3.23) can be rewritten as:

$$\dot{V} = \left[-\frac{k_{\mathrm{s}}}{m_{\mathrm{s}}}(x_{\mathrm{s}} - x_{\mathrm{u}}) - \ddot{x}_{\mathrm{s0}} + \lambda \dot{e}_{\mathrm{s}} - \frac{1}{m_{\mathrm{s}}}(F_{\mathrm{d0}} - K\,\mathrm{sgn}(s)) \right] s \tag{3.25}$$

The uncertainty in the sprung mass m_{s} is expressed in terms of a positive constant β, such that:

$$\frac{1}{\beta} \le \frac{m_{\mathrm{s}}}{m_{\mathrm{s0}}} \le \beta \tag{3.26}$$

By letting $\nabla m = m_s - m_{s0}$, the mass uncertainty can be further expressed as:

$$\frac{1}{m_s} = \frac{1}{m_{s0}} - \frac{\nabla m}{m_{s0}(m_{s0} + \nabla m)} \tag{3.27}$$

Equation (3.25) can then be rewritten as:

$$\dot{V} = [-\frac{k_s}{m_{s0}}(x_s - x_u) - \ddot{x}_{s0} + \lambda \dot{e}_s - \frac{1}{m_{s0}} F_{d0}$$

$$+ \frac{\nabla m}{m_{s0}(m_{s0} + \nabla m)}(F_{d0} + k_s x_s - k_s x_u) + \frac{1}{m_{s0} + \nabla m} K \operatorname{sgn}(s) s \tag{3.28}$$

The nominal target force F_{d0} in EQ (3.24) is then set as:

$$F_{d0} = -\mathrm{k}_s(x_s - x_u) - m_{s0}\ddot{x}_{s0} + m_{s0}\lambda \dot{e}_s \tag{3.29}$$

Consequently, EQ (3.28) becomes:

$$\dot{V} = \left[\frac{\nabla m}{m_{s0}(m_{s0} + \nabla m)}(F_{d0} + k_s x_s - k_s x_u) + \frac{1}{m_s + \nabla m} K \operatorname{sgn}(s) \right] s \tag{3.30}$$

The components of control input F_{d0} and K in EQ (3.2) should be configured to ensure:

$$\dot{V} \le -\varphi |s| \tag{3.31}$$

where φ is a positive constant referred to as the sliding condition gain.

Equations (3.30) and (3.31) yields:

$$\left[\frac{\nabla m}{m_{s0}(m_{s0} + \nabla m)}(F_{d0} + k_s x_s - k_s x_u) + \frac{1}{m_{s0} + \nabla m} K \operatorname{sgn}(s) \right] s \le -\varphi |s| \tag{3.32}$$

Considering that $|\operatorname{sgn}(s)| \le 1$ and $\frac{1-\beta}{\beta} \le \frac{\nabla m_s}{m_{s0}} \le \beta - 1$, the above equation can be manipulated to yield the control gain K as:

$$K = m_{s0}\beta\varphi + (\beta - 1)(|F_{d0}| + k_s|x_s| + k_s|x_u|) \tag{3.33}$$

Consequently, the target damping force F_c is obtained from EQS (3.24) (3.29) and (3.33), wherein F_d is replaced by F_c in EQ (3.24) from point of view of the controller synthesis.

Remark: Since the sliding mode control law will exhibit chattering problem when $s \geq 0$, which may result in poor tracking performance, and could excite un-modeled high-frequency dynamics. The sign function *sgn*(·) in EQ (3.24) is thus replaced by the saturation function $sat(s/\varepsilon)$ to effectively diminish the chattering [70]. The function $sat(s/\varepsilon)$ takes values of s and $sgn(s)$ when $|s| \leq \varepsilon$ and $|s| > \varepsilon$, respectively. The EQ (3.24) is thus rewritten as:

$$F_c = F_{d0} - K\,\mathrm{sat}(s/\varepsilon) \tag{3.34}$$

Figure 3.8 illustrates the schematic diagram of the proposed "inverse model"-based sliding mode semi-active controller, in which the modified "skyhook"-based reference model serves as the desired suspension framework for tracking the sprung mass position x_s to x_{s0} of the reference model. Similar to the "inverse model"-based hi-lo semi-active control design, presented in the previous section, the desirable damping force F_c is converted to the drive current i_d using the inverse model together with the ADFG and CM algorithms, as described in EQ (3.16). The semi-active logic condition z_c is that the damping force F_d tracks the desirable force F_c when it acts in phase with F_h. The controller suppresses the drive current to permit the damper operation in the passive mode (i_d=0), when F_c and F_h act in the opposite directions. The proposed "inverse model"-based sliding mode semi-active controller is thus formulated as:

$$i_z = f_d^{-1}(F_c, F_h);\quad z_c = -F_h F_c \tag{3.35}$$

where the drive current i_d is generated in response to i_z using the CM, ADFG and the condition functions, as described in EQ (3.16). Furthermore, the symmetric and asymmetric (SCM and ACM) damping modes can be realized by letting p=1and p=0, respectively.

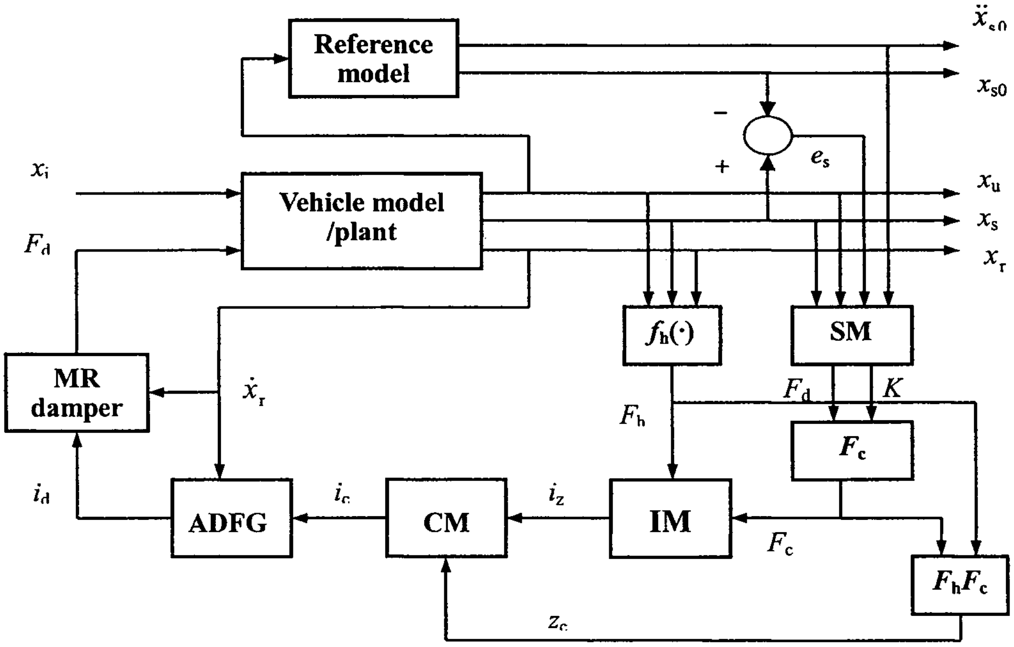

Figure 3.8: Schematic representation of "inverse model"-based sliding mode semi-active MR-suspension controller structure.

3.5 Characterization of Excitations

3.5.1 Deterministic excitation

Road vehicles invariably encounter different road profiles, which are random in nature. The suspension performance is strongly influenced by the road roughness and the frequency contents of the surface roughness. The vibration isolation performance of a vehicle suspension is strongly influenced by the magnitude and frequency contents of the excitations at the tire-road interface. The fundamental behavior of the vehicle suspension can be generally evaluated in terms of its frequency response characteristics under harmonic excitations of the form:

$$x_{\mathrm{i}} = a_{\mathrm{m}} \sin(2\pi f \, \mathrm{t})\,(\mathrm{m}) \tag{3.36}$$

where a_{m} is the displacement amplitude and f is the frequency of excitation.

Harmonic excitations of constant amplitude are frequently applied to study the frequency responses of the suspension and vehicle models. Such excitations, however, cause high acceleration at higher frequencies and thus high inertial forces and saturation of the suspension components, under nonlinear properties are considered. It is desirable to limit the displacement excitation at the tire-road interface at higher frequencies. In this study, fundamental responses of the "quarter-vehicle" model employing different MR-damping controller syntheses are evaluated under two-stage harmonic excitations in order to limit the acceleration due to high frequency excitations, such that:

$$x_i = \begin{cases} a_{\mathrm{m}} \sin(2\pi f \, \mathrm{t}) & f \le f_{\mathrm{T}} \\ a_{\mathrm{m}} (f_T / f) \sin(2\pi f \, \mathrm{t}) & f > f_{\mathrm{T}} \end{cases} \tag{3.37}$$

The above formulation yields constant displacement excitation at lower frequencies ($f \le f_{\mathrm{T}}$) and constant acceleration excitation at higher frequencies ($f > f_{\mathrm{T}}$). The transition frequency f_{T} is chosen as 2.1 Hz, which closely resembles the $\sqrt{2}\, f_{\text{n-s0}}$. Different magnitudes of displacement amplitudes (1.5, 2.5 and 3.5 cm) are also chosen for the analyses, while the upper frequency is limited to 15 Hz.

The shock isolation properties of a vehicle suspension are also evaluated under a deterministic rounded pulse excitation, given by [40]:

$$x_i = 0.25 a_m e^2 (\mu \varpi_0 t)^2 e^{-\mu\omega_0 t} \quad ; \qquad \mu = 1, 2, 3 \cdots, \tag{3.38}$$

where a_m is peak magnitude of the rounded pulse excitation, ω_0 is the fundamental frequency and μ is the pulse severity parameter.

A higher value of μ would cause higher shock severity and acceleration due to excitation. The shock isolation properties of the vehicle model are evaluated under the rounded pulse excitation of different amplitudes (a_m=2, 3.5 and 5 cm), severity (μ=1, 2 and 3) and fundamental frequency (ω_0=10.4 and 20.8 rad/s). Figure 3.9 illustrates the time histories of the rounded pulse excitations of varying severity parameters and peak magnitudes. The duration time of the rounded pulse excitation can be estimated by $\tau_s=3\pi/(\mu\omega_0)$, which is inverse proportional to the parameters μ and ω_0.

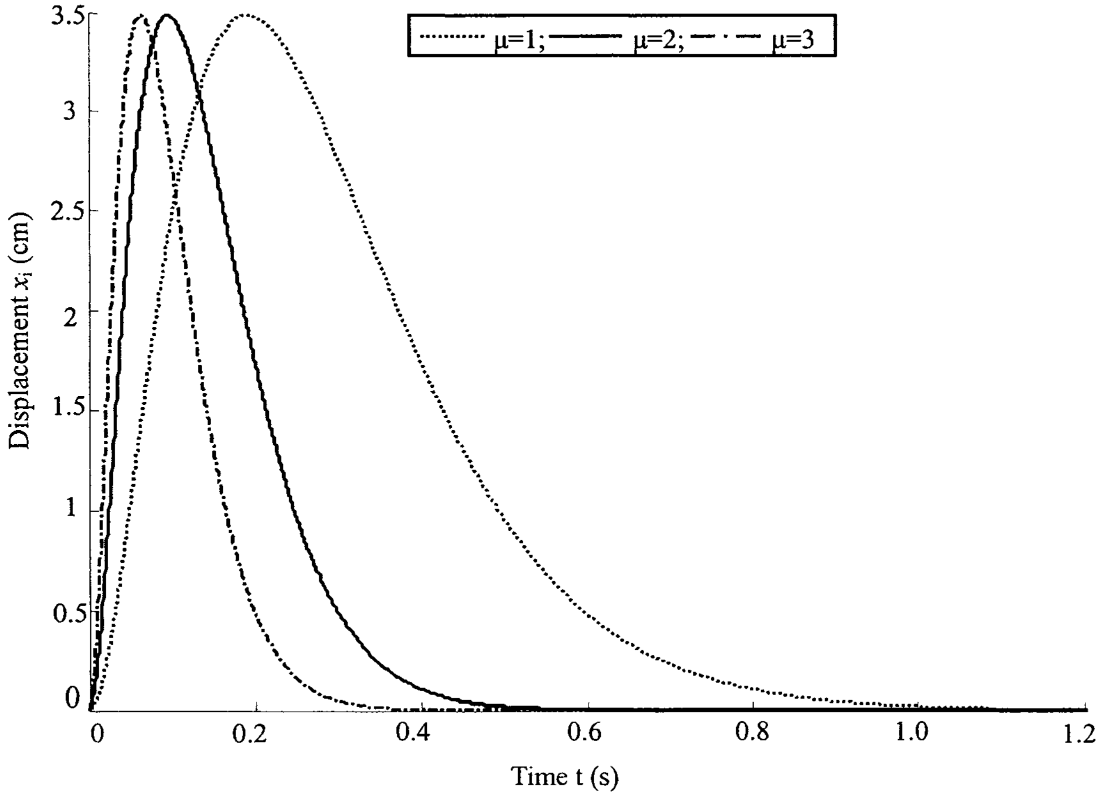

(a) a_m=3.5 cm; ω_0=10.4 rad/s

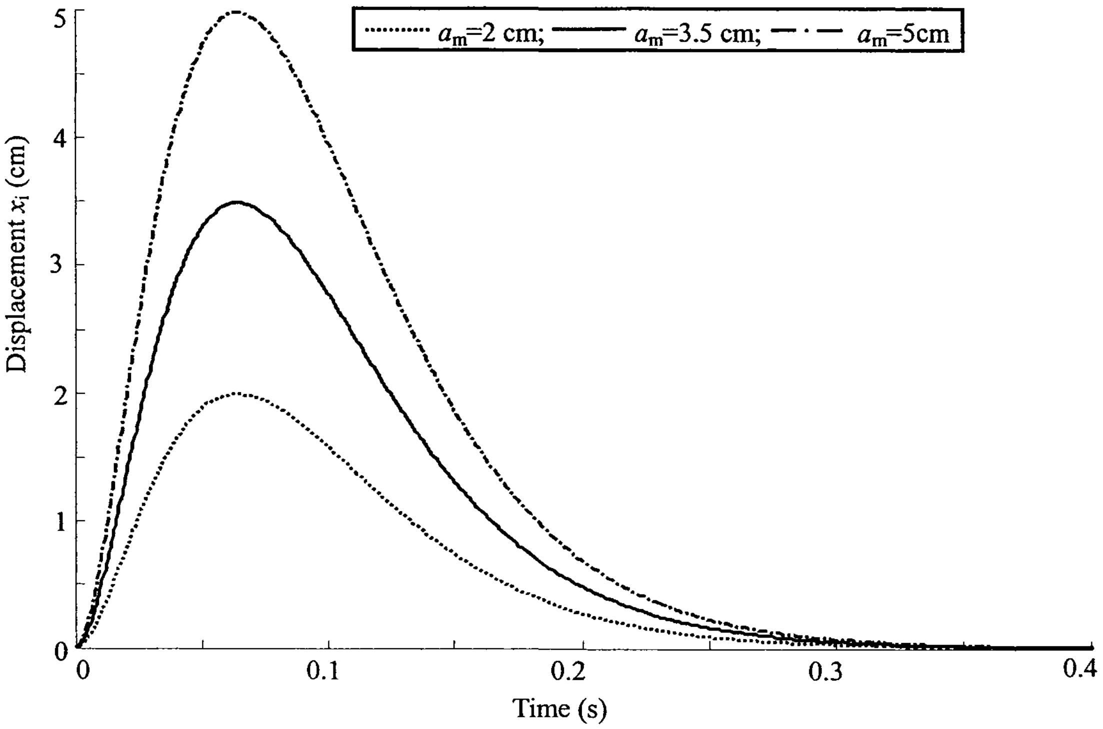

(b) μ= 3; ω_0=10.4 rad/s

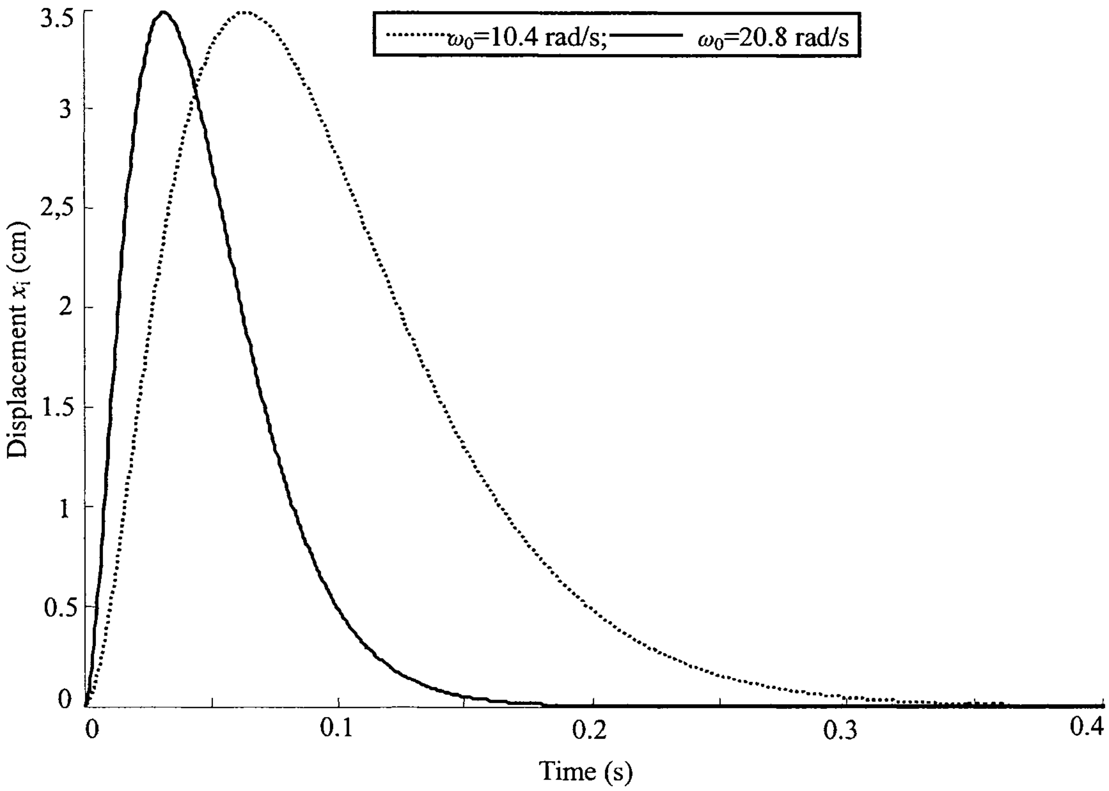

(c) a_m=3.5 cm; μ= 3

Figure 3.9: Rounded pulse displacement excitation: (a) Variation in pulse severity; (b) Variation in peak displacement; and (c) Variation in fundamental frequency.

3.5.2 Random road excitation

The performance characteristics of a vehicle suspension are strongly dependent upon the magnitude and frequency components of the excitations due to randomly rough roads. Apart from the deterministic excitations, the performance characteristics of the vehicle suspension thus must be evaluated under representative excitations arising from roads with randomly distributed surface roughness. The reported roughness data of different roads in Canada [98] are considered for the analyses of MR-suspension dampers employing different controller syntheses. The elevations of three different roads reported over a length of approximately 500 m at intervals of 0.3 m are considered, which have been classified as smooth, medium-rough and rough on the basis of their roughness index [98, 99]. The analyses of the filtered roughness data revealed peak elevations of the selected roads in the order of 4, 7.5 and 15 mm, which are termed as smooth, medium-rough and rough, respectively.

Fast Fourier Transform (FFT) technique is employed to derive the spatial spectra of the three road profiles, as shown in Figure 3.10 (a). The spectral densities of the road displacements in the frequency domain are further evaluated at two different speeds 50 and 100 km/h, which are presented in Figures 3.10(b) and (c). The result illustrates that the predominant wavelength frequencies of the different road profiles are in the range of 0-2 cycle/m, and magnitudes of the spatial PSDs increase with increasing the road roughness. The results also illustrate that the magnitudes of PSDs of the different road profiles slightly decrease with increasing the vehicle speed.

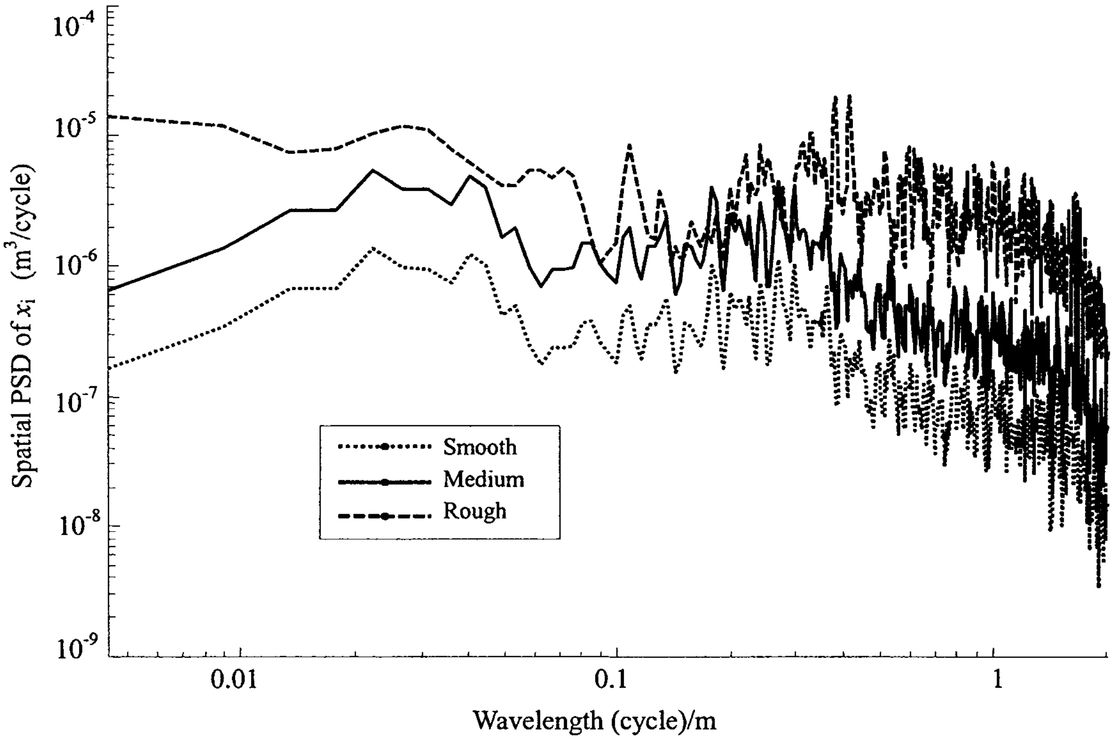

(a) Spatial PSD of varied road profiles

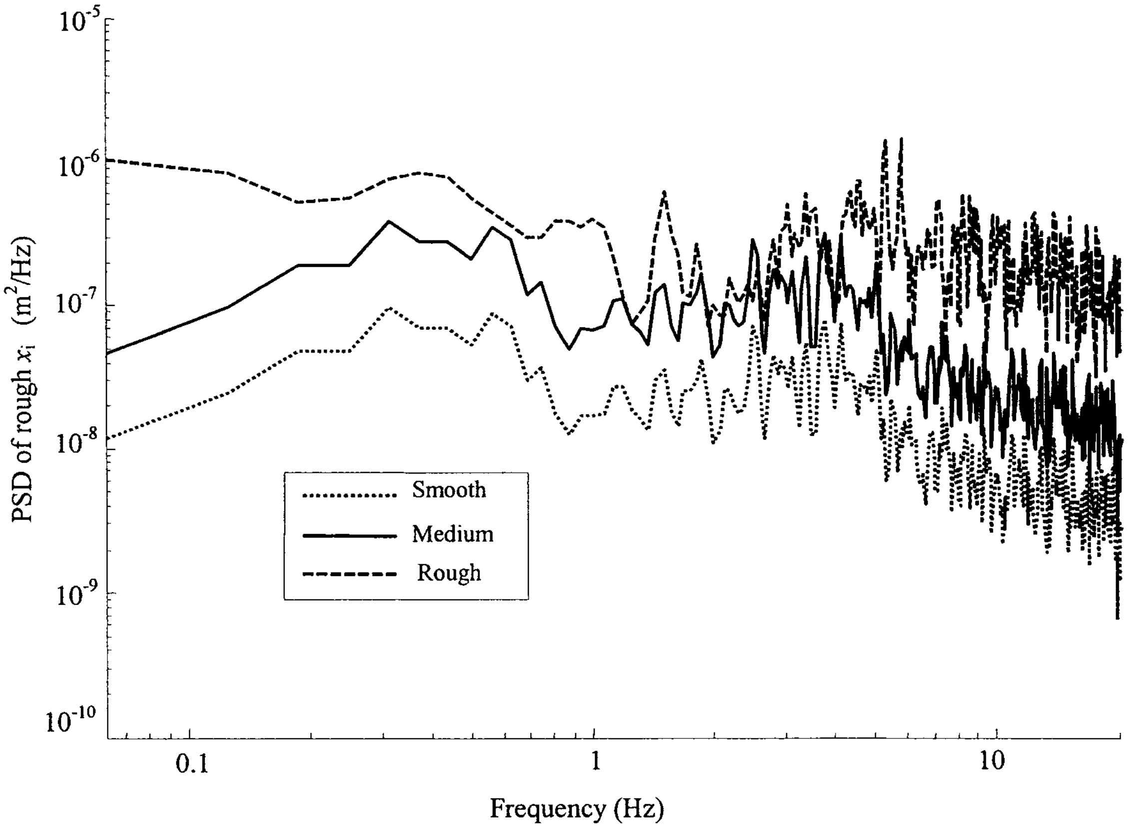

(b) PSDs of varied road profiles (50 km/h)

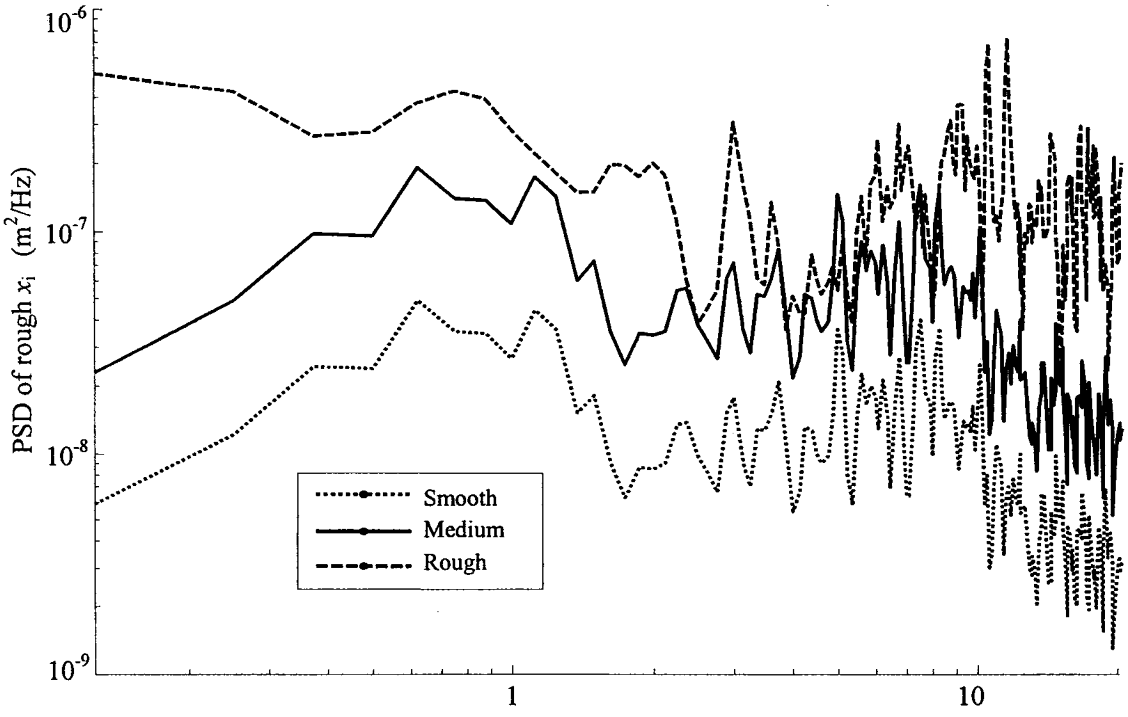

(c) PSDs of different road profiles (100 km/h)

Figure 3.10: Analyses of road profile spectrum and influence of vehicle speed.

3.6 Performance Measures

The analysis of the "quarter-vehicle" model under deterministic and random excitation could yield a wide range of performance measures related to ride, road-holding, dynamic tire loads and suspension working space. The selection of the performance measures depends on the objective of the suspension design. The present study of the semi-active MR-damping suspension focuses on these distinct performance measures relevant to the ride quality, dynamic tire loads transmitted to the pavement and the suspension working space. These performance measures are evaluated from time histories of the sprung and unsprung mass responses, and the tire force. The methodologies for evaluating these performance measures are described in the following sub-section.

3.6.1 Ride performance measures

The ride performance of a vehicle suspension is invariably evaluated in terms of the acceleration of sprung mass acceleration. A vast number of studies have established that the human rider perception to vibration is directly related to the magnitude and frequency components of the transmitted acceleration [1-3, 17, 23-25, 28, 34, 35]. The vertical acceleration responses of the sprung mass of the "quarter-vehicle" model are evaluated under deterministic as well as random road excitation.

The ride dynamic responses of the suspension to harmonic excitation, described in EQ (3.37), are evaluated in terms of acceleration transmissibility, T_{as}. The transmissibility describes the frequency response of the suspension system including the resonant transmissibility and the degree of vibration isolation. Owing to the nonlinear properties of the MR-damper, the acceleration transmissibility is defined as the ratio of the RMS acceleration of the sprung mass corresponding to a given frequency of excitation to that due to excitation at the same frequency, such that:

$$T_{as}(f) = \frac{a_s(f)}{a_i(f)} \tag{3.39}$$

where $a_s(f)$ and $a_i(f)$ are the RMS values of accelerations of the sprung mass and the excitation, respectively, corresponding to excitation frequency f, evaluated from:

$$a_s = \sqrt{\frac{1}{T}\int_0^T \ddot{x}_s^2(t)\,dt}\ ; \qquad \text{and} \qquad a_i = \sqrt{\frac{1}{T}\int_0^T \ddot{x}_i^2(t)\,dt} \tag{3.40}$$

where T is the duration of the dynamic acceleration signals.

The shock isolation performance of the suspension system is evaluated in terms of shock displacement (SDR_s) and shock acceleration (SAR_s) ratios. The SDR_s and SAR_s are defined as the ratios of peak response (displacement/acceleration) to the peak excitation variable, given by:

$$SDR_s = \frac{\max[\, x_s(t)]}{\max[\, x_i(t)]}; \qquad \text{and} \qquad SAR_s = \frac{\max[\, \ddot{x}_s(t)]}{\max[\, \ddot{x}_i(t)]}; \; 0 \le t \le T_L \tag{3.41}$$

where T_L is the duration of the shock excitation and response in the analyses.

The ride performance characteristics under random road excitation are evaluated in terms of power spectral density (PSD) of the sprung mass acceleration. The spectra evaluated for medium-rough and rough road excitations at different forward speeds permit for assessments in terms of the magnitude as well as frequency components of the responses.

3.6.2 Tire force measures

The variations in the dynamic tire force relate to the road-holding and handling performance of the vehicle suspension. Apart from these, the tire forces transmitted to the road surface also relate to the road friendliness of the vehicle, particularly when freight vehicles are involved [1-3, 17, 20, 24, 25]. The variations in the tire forces also relate to the wheel hop tendencies, which can be assessed in terms of unsprung mass acceleration. Under harmonic excitations, the performance measure is defined in terms of unsprung mass acceleration transmissibility, given by:

$$T_{a_u}(f) = \frac{a_u(f)}{a_i(f)} \tag{3.422}$$

where $a_u(f)$ is the RMS acceleration of the unsprung mass corresponding to excitation frequency *f*, given by

$$a_u=\sqrt{\frac{1}{T}\int_0^T \ddot{x}_u^2(t)\,dt} \tag{3.43}$$

Under shock excitations, the tire force variation performances are evaluated in terms of shock displacement (SDR_u), shock acceleration (SAR_u) and deviation in peak tire force (DTR) ratios, derived from:

$$SDR_u=\frac{\max[\,x_u(t)]}{\max[\,x_i(t)]}; \qquad SAR_u=\frac{\max[\,\ddot{x}_u(t)]}{\max[\,\ddot{x}_i(t)]};\ 0\le t\le T_L;$$

$$\text{and } DTR=\frac{\left|F_{T(peak)}-F_{T0(peak)}\right|}{(m_{s0}+m_u)g} \tag{3.44}$$

where $F_{T0(peak)}$ is the peak magnitude of the shock tire force response corresponding to the nominal sprung mass.

Under random excitations, the variation in tire forces are frequently evaluated in terms of dynamic load coefficient (DLC), defined as the ratio RMS tire force to the mean tire force, such that:

$$DLC=\frac{F_{Trms}}{\bar{F}_t} \tag{3.45}$$

where $\bar{F}_t$ is the mean tire force, which equals $(m_s+m_u)g$, and F_{Trms} is the RMS tire force.

The tire force transmissibility, the ratio of RMS tire force to the static, is also evaluated to study the road-holding property of the suspension as a function tire excitation frequency. The tire force transmissibility can also be termed as DLC corresponding to a given excitation frequency, such that:

$$DLC(f)=\frac{F_{Trms}(f)}{\bar{F}_t} \tag{3.46}$$

3.6.3 Suspension travel measures

The suspension working space, as determined from the relative displacement response across the suspension, poses severe constraints on the suspension design. Moreover, the ride and working space responses form two conflicting measures of the suspension performance. A hard and well-damped suspension would yield lower relative deflection but high sprung mass acceleration. A soft and lightly damped suspension, on the other hand, causes superior vibration isolation at the expense of excessive suspension deflection. The performance assessments of vehicle suspensions thus necessitate evaluations of both the ride as well as suspension deflection responses [1-3, 24, 25].

The frequency response characteristics of the suspension deflection can be conveniently evaluated under harmonic excitation in terms of relative displacement transmissibility, T_{dr}, given by:

$$T_{dr}(f) = \frac{a_r(f)}{a_i(f)} \tag{3.47}$$

where $a_r(f)$ is the RMS suspension displacement corresponding to excitation frequency f, given by:

$$a_r = \sqrt{\frac{1}{T}\int_0^T \ddot{x}_r^2(t)\,dt} \tag{3.48}$$

The shock response of the suspension system is evaluated in terms of peak relative displacement ratio (RDR):

$$\text{RDR} = \frac{\max[\,x_r(t)]}{\max[\,x_i(t)]} \tag{3.49}$$

Under random road excitation, the deflection response of the suspension system is evaluated in term of PSD of the relative displacement of the sprung mass with respect to the unsprung mass.

3.7 Summary

A "quarter-vehicle" model of a road vehicle is formulated comprising the MR-damper model defined in the previous chapter. A reference model is proposed on the basis of the "skyhook" damping to derive the target responses for the synthesis of sliding mode controller. Four different on-off- and "skyhook"-based hi-lo control policies are formulated to achieve semi-active modulation in the drive current of the MR-damper. The continuous modulation (CM) and asymmetric damping force generation (ADFG) algorithms are integrated within the control policies to minimize the effects of switching transients, and to realize the damping forces in the symmetric as well as asymmetric modes. Another two different controller syntheses are formulated based on the inverse model and sliding mode controls of the damping force. The sliding mode semi-active controller integrates the inverse model control and offers enhanced robustness on vehicle loading uncertainties. The different deterministic and random excitations of the suspension systems using measures related to ride, tire-force variations and suspension working space. The formulations derived in this chapter are analyzed in the following chapters to assess the relative performance characteristics of different control algorithms.

CHAPTER 4

PERFORMANCE ANALYSES OF HI-LO SEMI-ACTIVE DAMPING

4.1 Introduction

A number of studies have demonstrated strong performance potentials of on-off and "skyhook" damping suspensions [12, 40, 82, 87, 91]. It has been suggested that the on-off and "skyhook"-based damping within a vehicle suspension can help realize better compromise among various conflicting performance requirements, namely the ride quality, rattle space and road-holding. The on-off control, however, could cause high sprung mass acceleration due to the associated switching discontinuity. Furthermore, the ideal "skyhook" control law could cause instability due to zero damping force in the off state [70]. The MR-damper, however, would continue to provide light damping in its passive mode during the off-state, and thereby circumvent the potential instability. The light passive mode damping in the off-state further permits the damping force variation in a hi-lo manner. The effects of switching discontinuity can also be minimized by ensuring damping modulation in a continuous manner using the modulation function proposed in the previous chapter. Moreover, the damping force asymmetric in compression and rebound can also be realized using the asymmetric damping force generation (ADFG) algorithm proposed in the previous chapter.

The performance characteristics of a vehicle suspension employing semi-active hi-lo variation in the damping force depend upon many factors. These include the condition function that determines the state of damping, limiting values of drive current and thus the damping force, mode of modulation (rate of switching), control algorithm, damping force hysteresis and saturation, and the control objectives. In this chapter, the effects of damping force hysteresis and saturation on the response characteristics are analyzed under selected excitations. Four different on-off and "skyhook"-based hi-lo algorithms were formulated to realize damping force variations using different condition functions, damping force generation schemes, and the exponent of controller. The performance characteristics of these four control policies presented in the previous chapter are evaluated under deterministic as well as stochastic excitations at the tire-road interface. The response characteristics of the "skyhook"-based hi-lo semi-active controller are further focused on evaluation in terms of the defined performance measures. The sensitivity of the performance measures to variations in operating conditions, such as speed, excitation magnitude and load, are assessed under selected excitations. The response characteristics are evaluated with symmetric as well as asymmetric damping force in compression and rebound. The relative controller synthesis performances in minimizing the hysteresis effects are further assessed.

4.2 Influence of MR-Damper Nonlinearities

The strong hysteresis and force-limiting nonlinearities of the MR-damper, as observed from the measured force-velocity characteristics may cause undesirable effects on the dynamic performance of the vehicle suspension, particularly when a semi-active controller is employed. These may include limit cycle and larger steady-state error [70-76, 79]. Moreover, such nonlinearities may cause large magnitude transient responses, which could be harmful to the damper and electronic circuit hardware. Apart from the damper nonlinearities, the current-switching nonlinearity, inherent to a semi-active control synthesis coupled with the force hysteresis, could cause large magnitude transients in the sprung mass acceleration.

The effect of damping force hysteresis on the responses could be conveniently assessed using the "quarter-vehicle" model employing damper models based on mean as well as hysteretic F-v characteristics. The vehicle model employing mean and hysteretic damping force formulations are evaluated assuming two different passive damping modes realized using i_d=0 and 0.2 A. Figure 4.1 illustrates comparisons of dynamic responses of the vehicle model employing mean and hysteretic damping force models, while the drive current is held as 0.2 A. The results are presented under a 1.5 Hz harmonic excitation of 2.5 cm amplitude. The results presented in terms of variations in the passive damping force (F_d), relative velocity (v_r), and sprung and unsprung mass acceleration (a_s and a_u) responses suggest relatively small effects of hysteresis, The presence of hysteresis, however, yields slightly larger magnitudes of relative velocity and acceleration responses. The force-limiting nature of the damping force tends to cause higher frequency oscillations in a_u. The magnitude of such oscillations is further amplified under light damping (i_d=0), as shown in Figure 4.2. The results suggest that the magnitudes of sprung and unsprung mass accelerations and the oscillations in a_u due to force-limiting property of the MR-damper can be reduced by selecting higher drive current and thus the damping force.

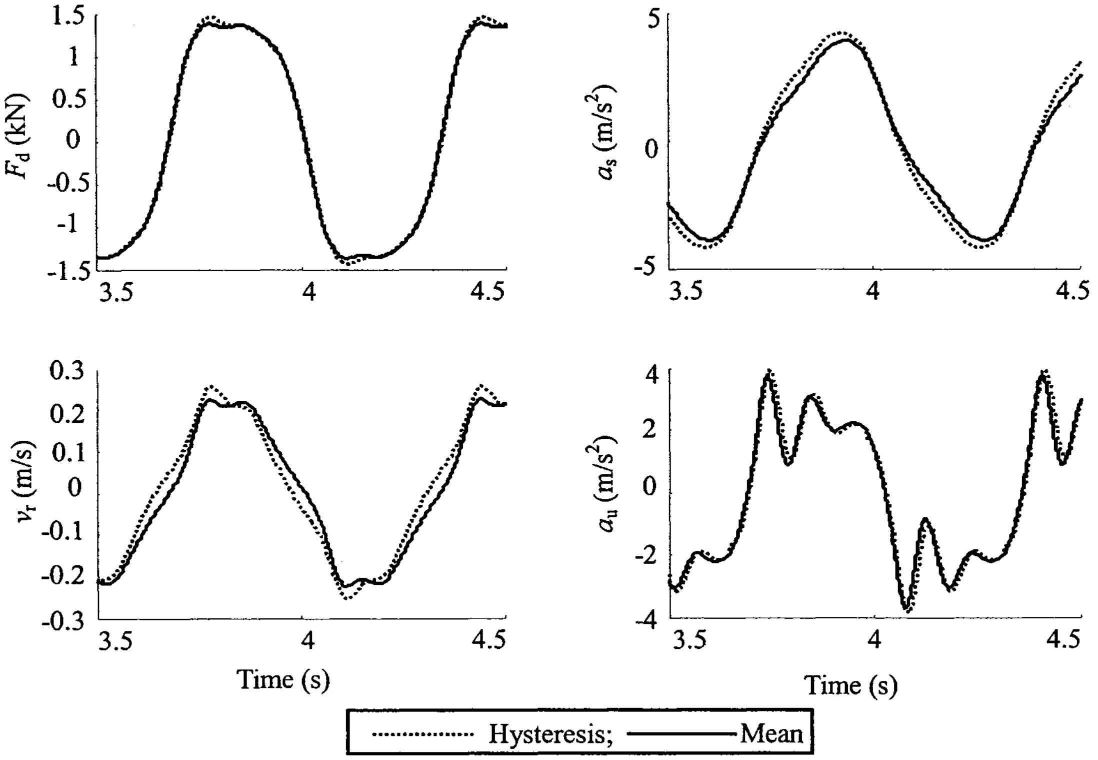

Fig. 4.1: Comparisons of responses of the "quarter-vehicle" model employing mean and hysteretic damping force models (i_d=0.2 A; f=1.5 Hz; a_m=2.5 cm).

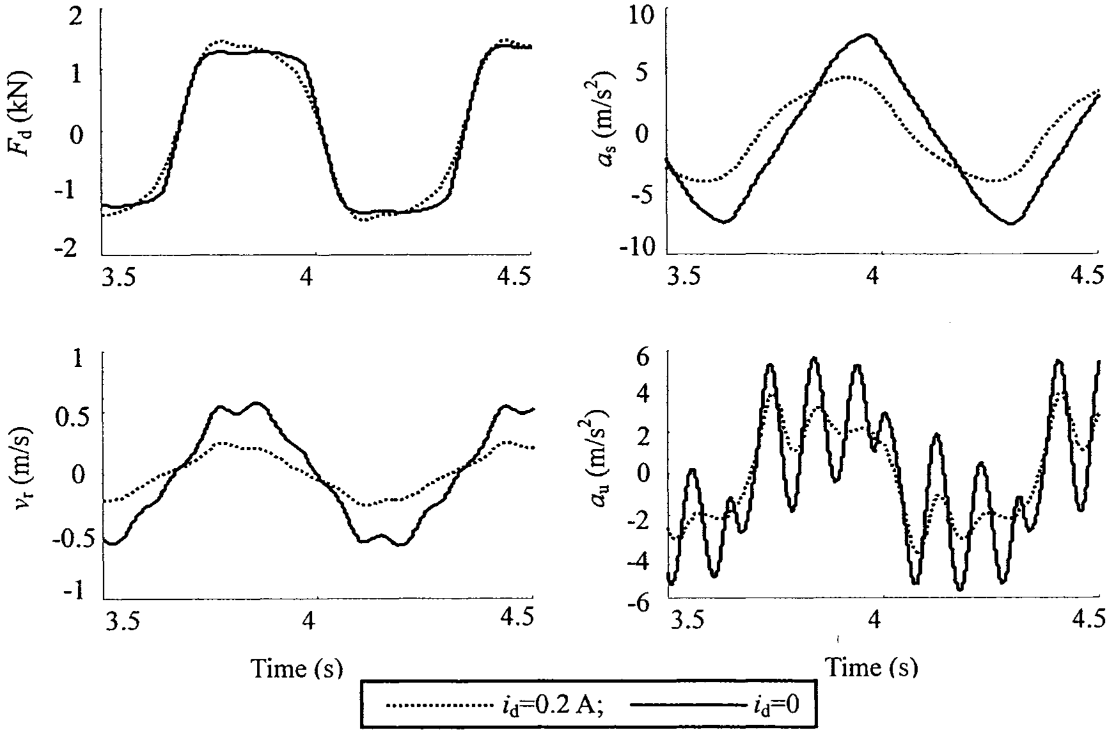

Fig. 4.2: Influence of damping force magnitude (drive current) on the responses of the "quarter-vehicle" model with damping hysteresis (i_d=0 and 0.2 A; f=1.5 Hz; a_m=2.5 cm).

Unlike the open-loop passive damping of the MR-suspension, the semi-actively controlled damper may yield more significant influences due to damper hysteresis, which are partly attributed to switching nonlinearity. As an example, the effect of damping hysteresis on the suspension responses are evaluated for the on-off control algorithm formulated in EQ (2.1), which yields asymmetric variation in the drive current in response to the direction of the velocity. The on-off controller yields a high value of constant current (i_d=i_H) when v_r<0 (compression), and switches to the lower limit (i_L=0) when v_r≥0 (rebound), as shown in Figure 2.6. The dynamic responses obtained for both the mean and hysteretic damping force models under a harmonic excitation are compared in Figure 4.3. The results presented in terms of F_d, i_d, a_s and a_u show significant influence of the damping hysteresis on all the response quantities. The presence of hysteresis causes larger magnitude transient peaks in damping force and acceleration responses, which occur in the vicinity of current switching (v_r≈0). The consideration of the mean damping force model yields continuous variations in responses, suggesting insensitivity to current switching nonlinearity.

The above results suggest that the force-limiting nonlinearity of the MR-damper would cause self-exciting oscillations in the dynamic response of the unsprung mass, under both the passive as well as on-off damping modes. Such oscillations could be observed with mean and hysteretic damping models, and may be effectively reduced by increasing the upper limit of the force. The hysteresis nonlinearity has insignificant influence on the responses of the MR-damper in its passive mode. The on-off variations coupled with the damping hysteresis, however, result in significantly large magnitude transient variations in the damping force and acceleration responses around the current switching instants. The controller design for the MR-damper thus necessitates considerations of the damping force hysteresis and force-limiting nonlinearities. The transient peaks could be suppressed by ensuring the continuous modulation in the drive current, and by introducing current variation based upon higher order of response variations, as discussed in section 3.4.2.

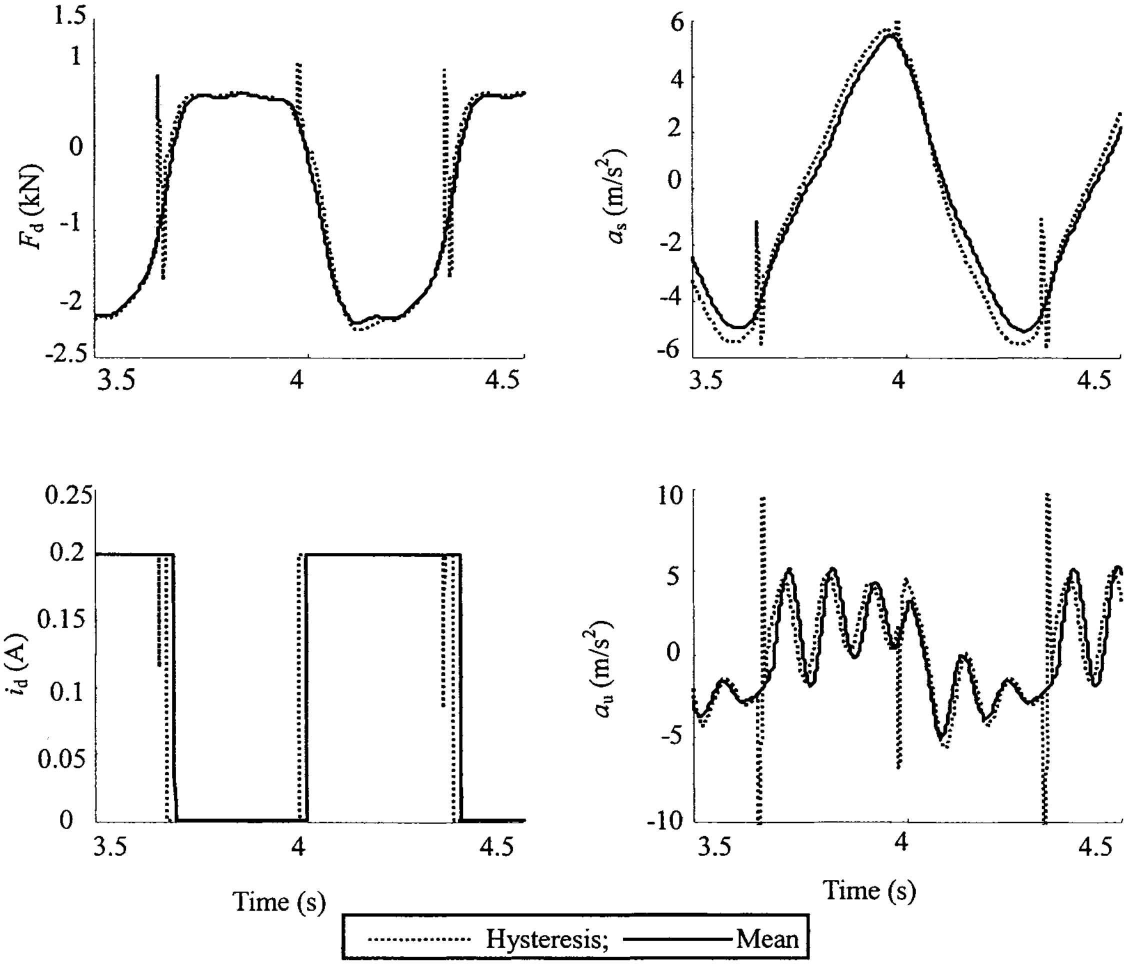

Fig. 4.3: Comparisons of responses of “quarter-vehicle” model employing on-off control with mean and hysteretic damping force models (i_L=0; i_H=0.2 A; f=1.5 Hz; a_m=2.5 cm).

4.3 Response Analyses of Hi-Lo Semi-Active Suspension Damper

The response characteristics of different hi-lo damping policies, formulated in EQ (3.15), are investigated in conjunction with the "quarter-vehicle" model to assess their relative performance potentials. The continuous modulation and ADFG algorithms are used to minimize the effects of switching discontinuities, while the preliminary assessments are conducted for the symmetric damping modulation (SCM). Four hi-lo schemes are referred to as policy I to policy IV, respectively. The policy I employs the condition function based on the skyhook control ($z_c = \dot{x}_s v_r$), while the drive current is varied in proportion to the sprung mass velocity using the exponent or order n=2. The policy II employs the same condition function, but modulates the current in proportion to the relative velocity (n=2). The policy III employs identical modulation of current but utilizes the condition function based on directly measurable relative portion and velocity ($z_c = x_r v_r$). The final IV involves current modulation on the basis of relative portion (n=2) on the basis of the condition function $z_c = x_r v_r$.

4.3.1 Relative analyses of different hi-lo damping modulation policies

The response characteristics of the "quarter-vehicle" model employing nonlinear MR-damper, described in EQ (2.15), and the proposed hi-lo modulation schemes are evaluated under harmonic excitations. The responses are presented in terms of selected performance measures, namely time-histories of damping force, drive current, sprung and unsprung mass accelerations, and frequency response characteristics. For relative analyses, control gains of the four schemes are chosen as 3, 10, 10 and 300, respectively, to ensure identical peak value of the drive current about (i_d=i_H=0.5 A) under selected excitation magnitude. Time variations in the responses are evaluated under a 2.5 cm amplitude harmonic excitation at a frequency of 1.5 Hz. The frequency response characteristics are analyzed in the 0.5 to 15 Hz range under varying excitation magnitudes, as described in section 3.5. Both the continuous modulation (CM) and ADFG algorithms are applied to reducing the switching effects using p=1, ξ=4.5, p_c=0 and ξ_c=10 for the SCM model. The controller order is chosen as 2 to realize smooth variations in the drive current.

Figure 4.4 presents comparisons of time variations in F_d, i_d, a_s and a_u responses of the "quarter-vehicle" model employing the four different hi-lo damping modulation policies in SCM. The dynamic responses under harmonic excitations (a_m=2.5 cm; f=1.5 Hz) illustrate the response variations, and modulation in the drive current and damping force. The results suggest that the modulation scheme I based upon the "skyhook" damping concept [87] yields relative smooth variations in the drive current and damping force. The control scheme IV based upon modulation of current in proportion to relative deflection response causes large variations in F_d and i_d near the switching instants. This is attributed to high gain (k_c=300) employed in this control, which is required to compensate for lower magnitude of the relative deflection response. All the control policies cause current modulation between the set limits (i_L=0; i_H=0.5 A) in a continuous manner, with the exception of scheme IV that causes transient variation in i_d in the vicinity of $z_c \approx 0$. The schemes II and III involving modulation in i_d on the basis of v_r response yield continuous variation in both F_d and i_d, but cause high frequency oscillations around the switching, which are more evident in the unsprung mass acceleration response. These are partly attributed to relatively larger gain used for the two schemes (k_c=10), and in-part due to the condition function based upon relative position and velocity ($z_c=x_rv_r$). It should be noted that this condition function relies upon the constant phase relationship between the relative position and velocity responses [40]. The presence of damping hysteresis tends to distort the phase relationship and thus contributes to high frequency oscillations in the responses near $z_c\approx0$. The magnitudes of high frequency oscillations in responses could be suppressed by reducing the control gain. This would, however, limit the upper limits of i_d and F_d, and yield relatively higher resonant response.

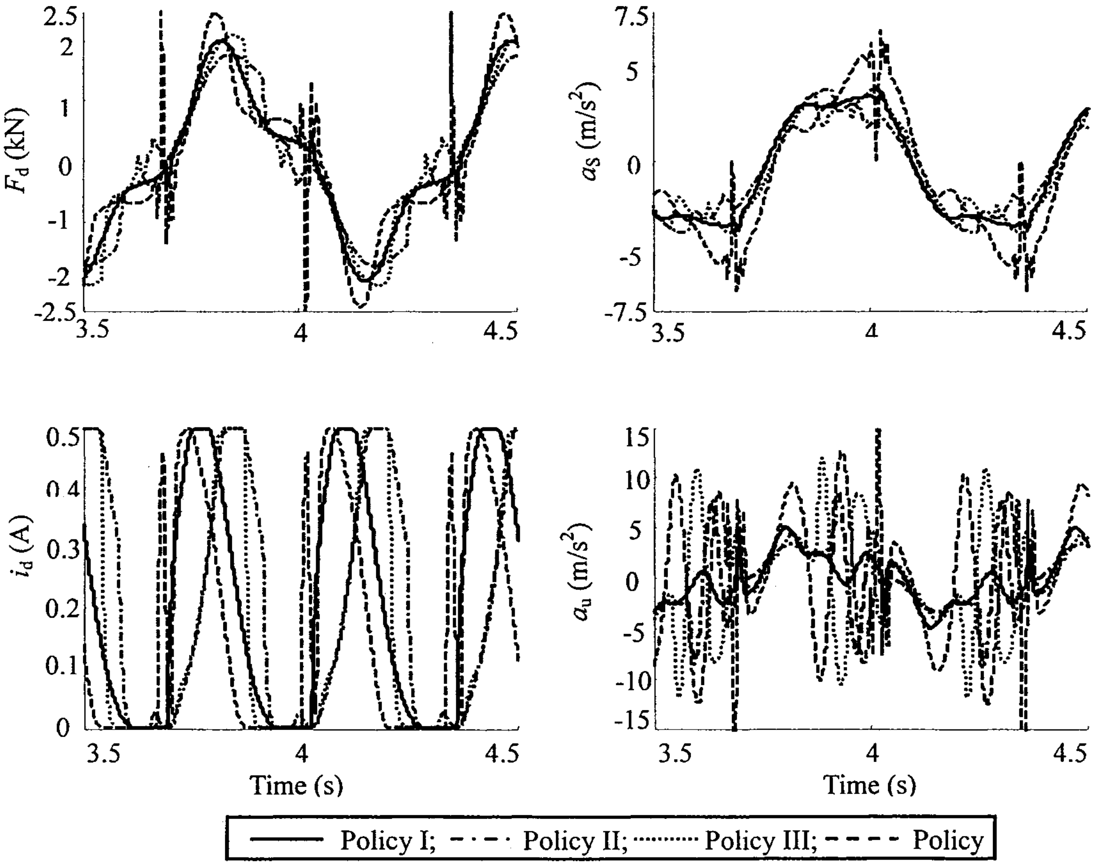

Figure 4.4: Comparison of time-histories of the "quarter-vehicle" model responses employing four different hi-lo damping modulation schemes (SCM: a_m=2.5 cm; f=1.5 Hz).

The frequency response characteristics of the "quarter-vehicle" model with the four different hi-lo MR-damper control configurations are compared in Figure 4.5. The responses are presented in terms of sprung and unsprung mass accelerations (T_{as}, T_{au}), relative displacement ratio (T_{dr}), and dynamic variation in the tire force (DLC). The results show that the scheme I based upon "skyhook" modulation of the current yields significantly lower resonant acceleration responses, and better attenuation of sprung mass acceleration in the higher frequency range. This is attributed to relatively higher magnitude of $\dot{x}_s$ and thus i_d and F_d due to this control policy. The lower damping due to policy IV related to relative displacement response yields highest resonant response but improved vibration attenuation in the ride frequency range, similar to that of policy I. Both the schemes also yield relative small variations in the dynamic tire forces suggesting better road-holding potential as evident form lower DLC response in majority of the frequency range. Both the schemes also yield higher relative displacement response near the unsprung mass resonant frequency.

The results attained from the preliminary analyses suggest that the hi-lo scheme I based upon the "skyhook" damping concept can yield improved resonance control, vibration isolation and dynamic tire force performance. Moreover, the associated condition function and current modulation tend to reduce the contributions due to switching discontinuities and damping hysteresis. The performance potentials of the MR-damper suspension based upon this hi-lo control policy are thus further investigated in both the symmetric and asymmetric control modes.

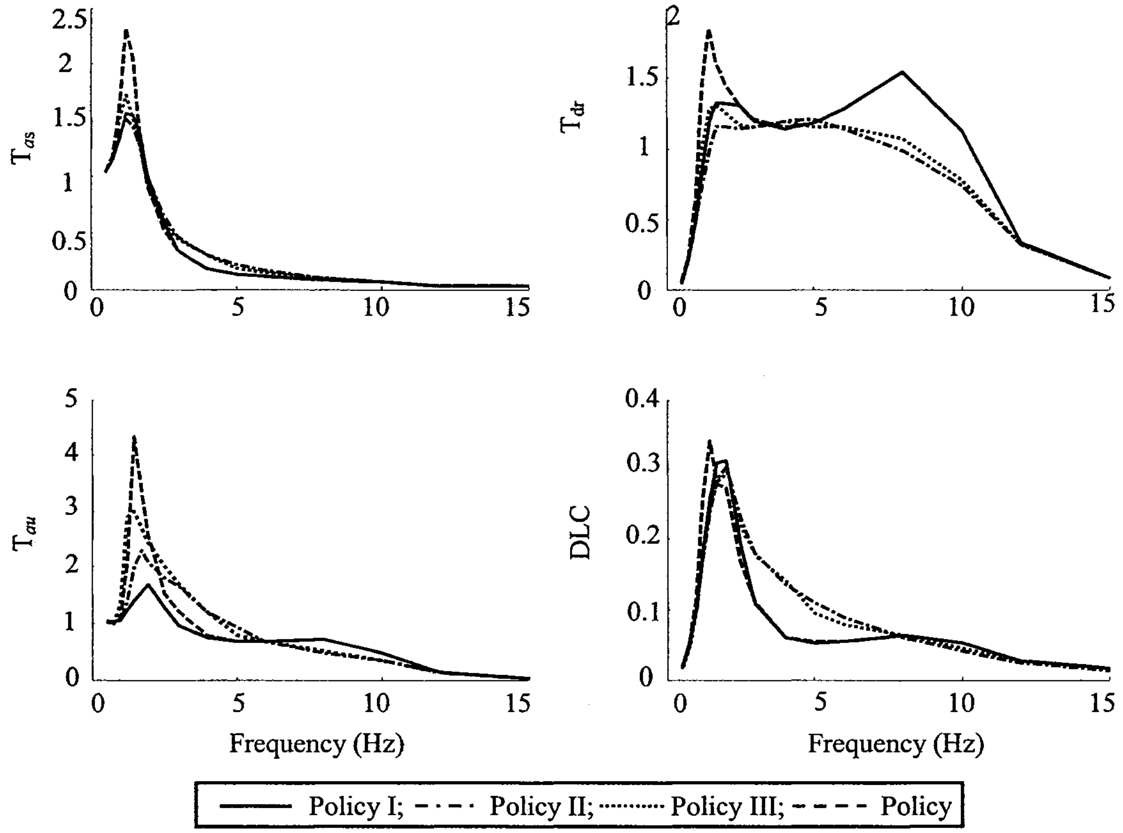

Figure 4.5: Comparison of frequency responses of the "quarter-vehicle" model employing four different hi-lo damping modulation schemes (SCM).

4.3.2 Response analyses of symmetric and asymmetric damping modes

As stated earlier, the suspension dampers in vehicular applications are usually designed to yield asymmetric variations in damping forces in compression and rebound, to achieve improved handling and road holding performance [1, 33]. The proposed "skyhook"-based hi-lo semi-active MR-suspension in the SCM can also yield asymmetric variation in damping force in compression and rebound by letting the smoothing parameter p=0 in the ADFG formulation as described in EQ (3.16). The relative performance characteristics of the "skyhook"-based hi-lo semi-active controller in the SCM and ACM are evaluated by comparing the responses in both time and frequency domains. The controller parameters are selected as n=2, k_c=3, p_c=0, ξ_c=10, ξ=4.5, and p=1 for SCM and p=0 for the ACM.

Figures 4.6 and 4.7 show time histories and selected responses in dynamic and frequency response characteristics, respectively, of the "quarter-vehicle" model employing "skyhook"-based hi-lo semi-active damping in SCM and ACM. The results suggest that the chosen control parameters could yield asymmetric damping force ratio in the order of 2.4 in the ACM, under harmonic excitation at 1.5 Hz (a_m=2.5 cm). The corresponding power consumption is reduced by nearly 50% as observed from variations in i_d in Figure 4.6, when compared to that for the SCM. The lower limit of the non-zero drive current in ACM during compression (F_d>0) is attributed to ADFG smoothing function (ξ=4.5). The results show the asymmetric damping modulation causes slightly higher magnitudes of the tire force (F_T), sprung mass deflection and acceleration (x_s and a_s), relative displacement (x_r) responses during the compression cycle, when compared to those observed in SCM. The light damping in the compression mode also yields asymmetric variations in the sprung mass displacement and relative displacement responses about their static equilibria. This may cause a drift in the sprung mass responses, which has also been reported in a few studies [1, 33, 40]. The damping force modulation in both SCM and ACM tend to excite resonant oscillations of the unsprung mass, even though the excitation frequency is close to the sprung mass resonance. The unsprung mass acceleration response thus exhibits oscillations near 1.5 Hz and 10 Hz, as seen in Figure 4.6.

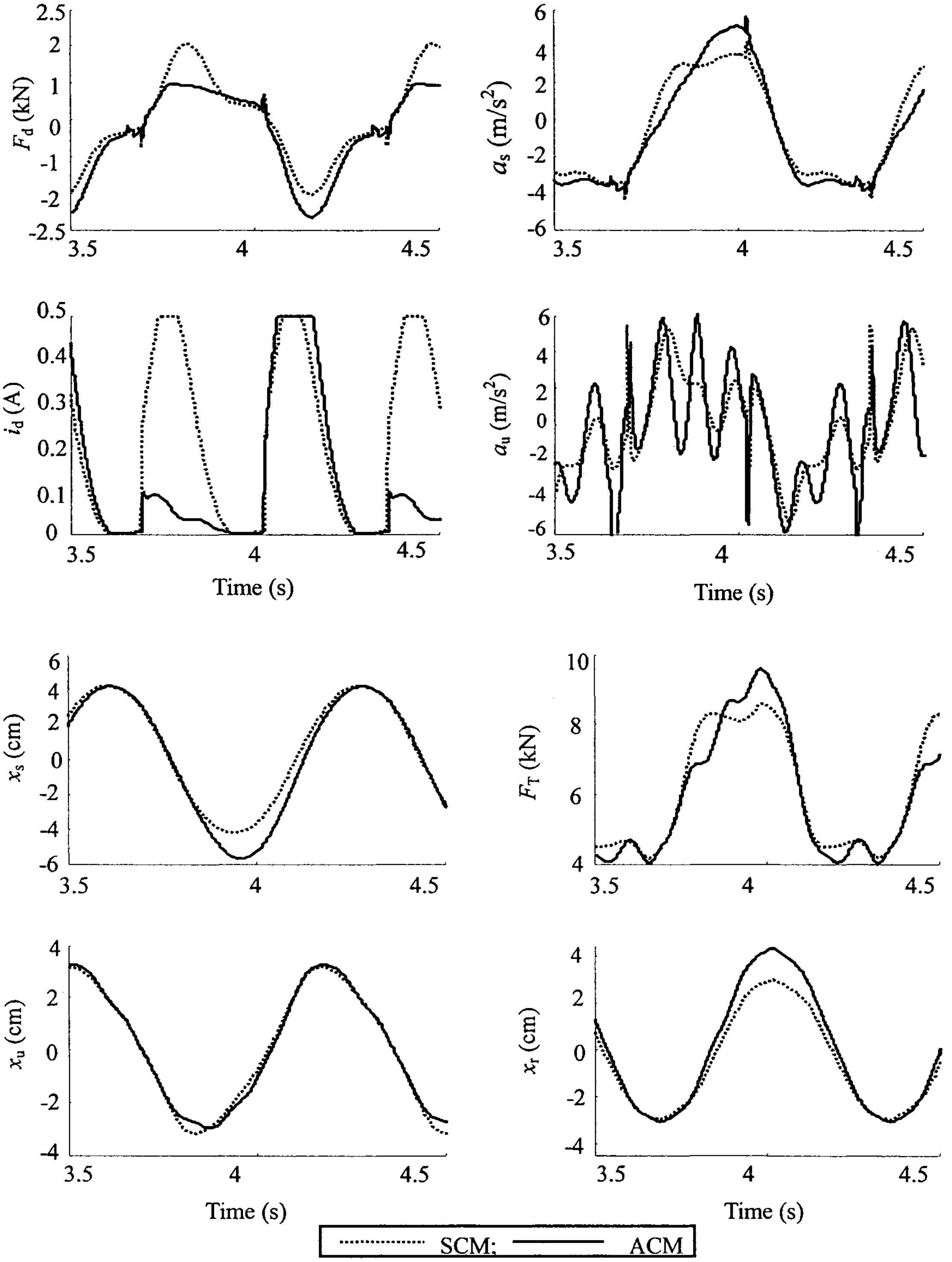

Figure 4.6: Comparisons of time-histories of responses of the "quarter-vehicle" model employing "skyhook"-based hi-lo semi-active modulation in damping force (policy I) in the symmetric as well as asymmetric control modes (SCM and ACM).

The frequency response characteristics of the "quarter-vehicle" model with the "skyhook"-based hi-lo semi-active damping in SCM and ACM are compared in Figure 4.7. The responses are evaluated under constant amplitude excitation (a_m=1.5 cm) in the 0.5 to 15 Hz frequency range to emphasize the wheel hop response at higher frequencies. Owing to its light compression damping, the ACM damping variations cause slightly larger resonant responses in a_s and x_r, when compared to the SCM, as observed from the frequency responses presented in Figure 4.7. The ACM variations, however, yield lower magnitudes of variations in the dynamic tire force (DLC) and transmitted accelerations at frequencies above the sprung mass resonant frequency. The results suggest that the damping modulation in ACM could yield improved road-holding performance by limiting the unsprung mass acceleration and tire force variation at higher frequencies.

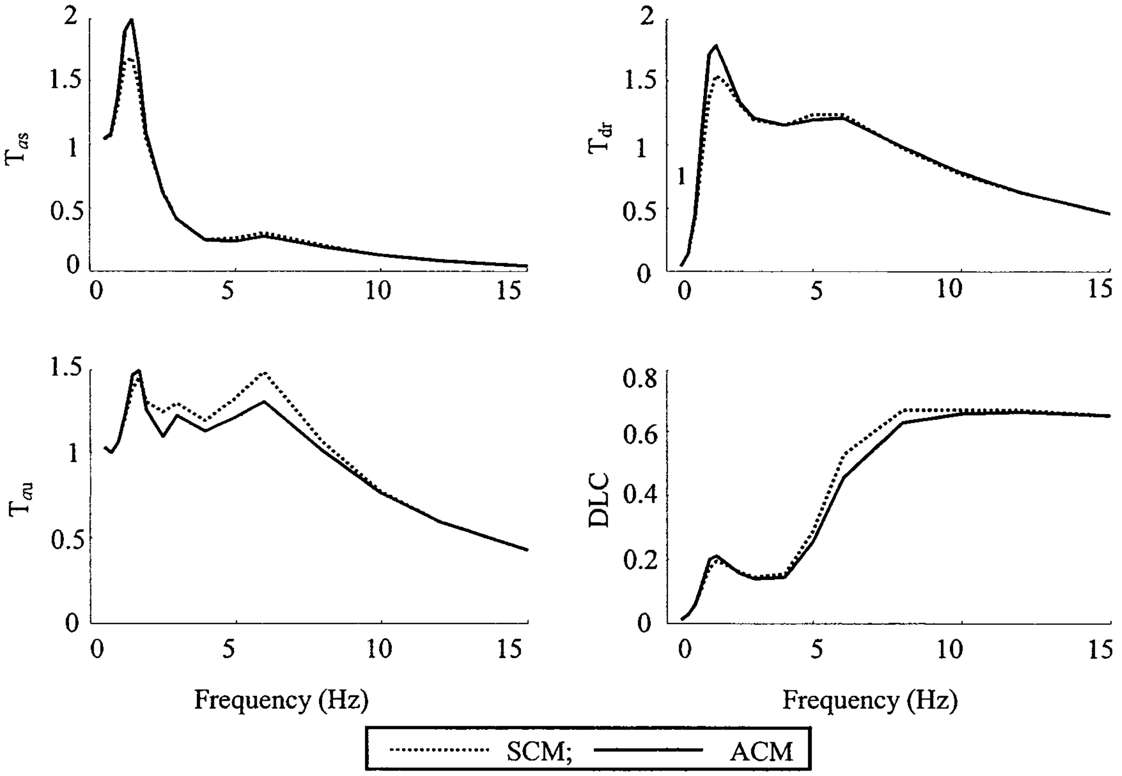

Figure 4.7: Comparison of frequency response characteristics of "skyhook"-based hi-lo semi-active MR-damping in symmetric and asymmetric control modes (SCM and ACM).

A vast number of studies have analyzed the performance characteristics of vehicle suspensions employing passive, active and semi-active damping mechanisms [3, 36, 40-42]. These studies have invariably suggested that a semi-active suspension could yield superior performance than a passive suspension. Moreover, the performance benefits could be comparable to that of a "fully-active" suspension. The harmonic responses of the proposed "skyhook"-based hi-lo semi-active MR-suspension in the ACM are thus compared to those for the passive MR-suspension to demonstrate its potential performance gains. The analyses are performed for two different damping modes (i_d=0 and 0.1 A) and the asymmetric semi-active control mode (ACM). The controller parameters are selected as n=2, k_c=3, p_c=0, ξ_c=10, ξ=4.5 and p=0. The analyses for both damper modes are also performed under transient and stochastic excitations at the tire-road interface, and the results are discussed in the following sections.

Response to Harmonic Excitations

Figure 4.8 presents comparisons of time-histories of dynamic responses of asymmetric semi-active and the passive damping modes, under a 2.5 cm harmonic excitation at a frequency of 1.5 Hz. Light constant damping corresponding to i_d=0 yields lager magnitudes of a_s, a_u, x_s, x_r and F_T. An increase in the passive mode damping by selecting i_d=0.1 A tends to reduce the peak magnitudes considerably. The corresponding change in the damping force, however, is small due to lower relative velocity response. The results suggest that a higher damping force is desirable for limiting resonant responses. A higher damping, however, would be expected to yield poor vibration transmission in the isolation region. The responses of the "skyhook"-based hi-lo semi-active ACM damping show current modulation in the 0 to 0.5 A range, which yields considerably higher damping force in rebound. The compression mode damping force tends to be lower than that observed for the passive mode. The sprung and unsprung acceleration magnitudes tend to be comparable or lower than those attained for i_d=0.1 A and i_d=0, respectively. The peak unsprung mass acceleration response, however, is lowest under higher value of passive damping (i_d=0.1 A). The "skyhook"-based hi-lo semi-active ACM damping causes lower magnitudes of sprung mass displacement and tire force, while the magnitude of unsprung mass displacement remains nearly insensitive to mode of damping.

The "skyhook"-based hi-lo semi-active ACM damping yields superior sprung mass acceleration transmissibility (T_{as}) and variations in the tire force in vast majority of the frequency range, as seen in Figure 4.9. The figure shows the comparisons of frequency response characteristics under harmonic excitations in the 0.5 to 15 Hz range with varying displacement amplitude. Both the passive modes of damping yield higher resonant values of T_{as} and DLC, while the responses corresponding to i_d=0 approach those of the semi-active damping at frequencies above 2.5 Hz. The results thus suggest that the proposed semi-active damping can help achieve resonant control and better vibration attenuation in the important ride frequencies. The rattle space response of the semi-active ACM damping is comparable to that of the higher frequency range. A higher value of passive damping, however, is desirable to limit the unsprung mass acceleration response in the higher frequency range.

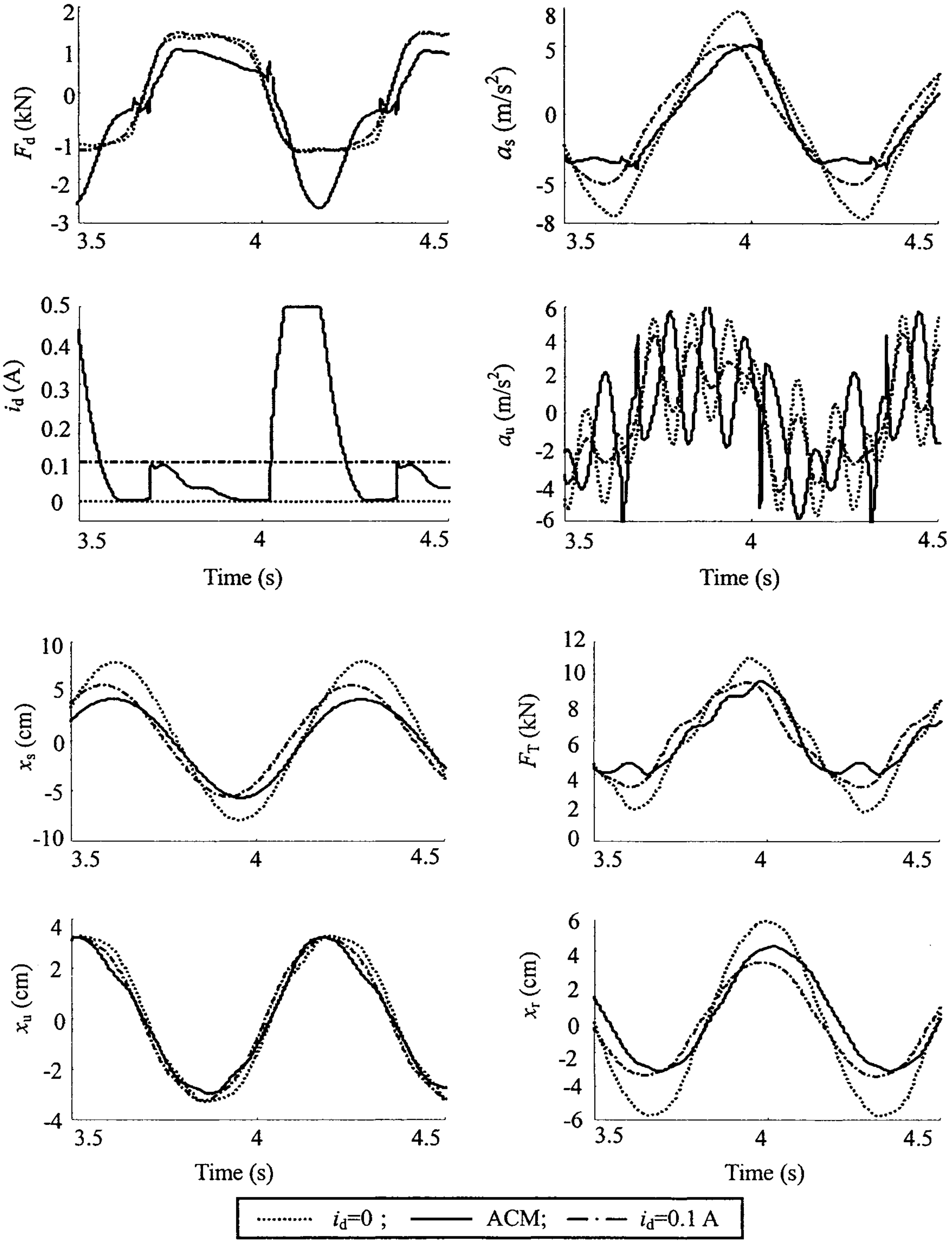

Figure 4.8: Comparison of time-histories of responses of the "quarter-vehicle" model with passive (i_d=0; i_d=0.1 A) and "skyhook"-based hi-lo semi-active ACM damping (a_m=2.5 cm; f=1.5 Hz).

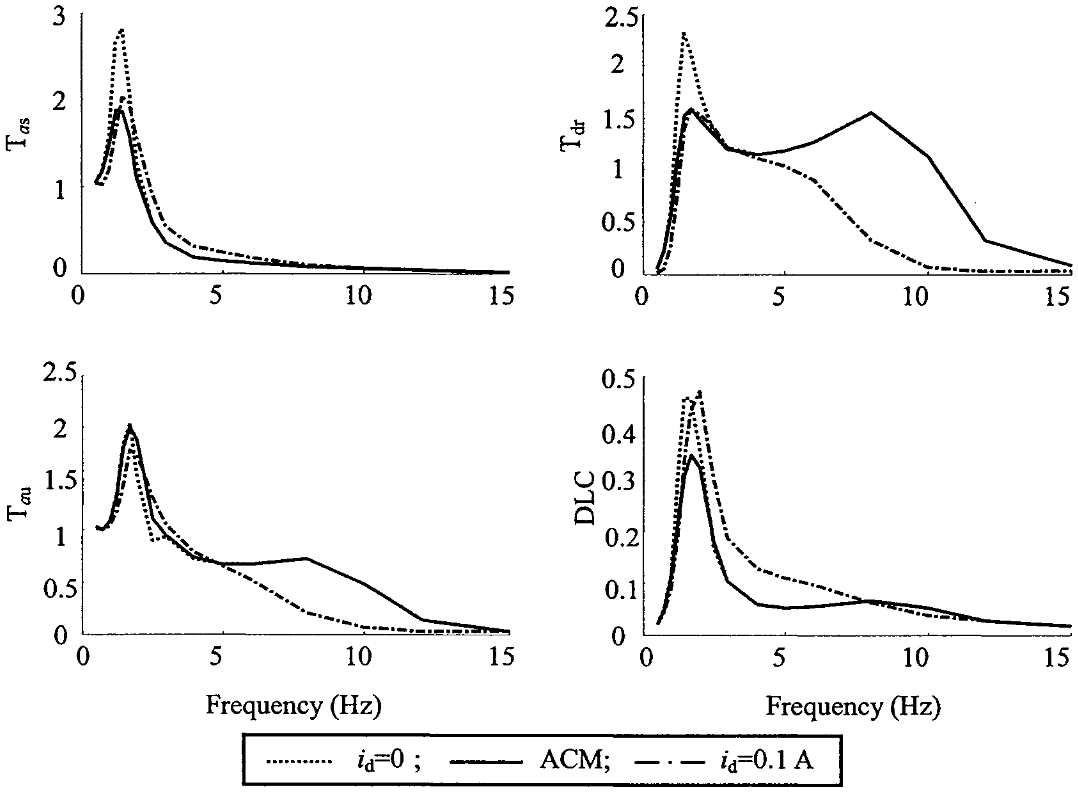

Figure 4.9: Comparison of frequency response characteristics of the "quarter-vehicle" model with passive (i_d=0; i_d=0.1 A) and "skyhook"-based hi-lo semi-active ACM damping.

Responses to a Rounded Pulse Excitation

The relative transient response characteristics of passive and semi-active ACM damping properties are also evaluated under a rounded pulse excitation (μ=3, ω_0=10.4 rad/s and a_m=5 cm). Figure 4.10 illustrates the transient responses in terms of F_d, i_d, a_s, a_u, x_s, x_u, F_T and x_r. The "skyhook"-based hi-lo semi-active ACM damping algorithm yields high current when v_r<0 and thus high rebound mode damping. The light compression and high rebound mode damping forces due to the semi-active damper help to limit not only the peak magnitudes of a_s and x_s, but also enhance the rate of decay of oscillations. The higher rate of decay due to semi-active damping is particularly evident in the sprung mass

(a_u and x_u) and tire force (F_T) responses.

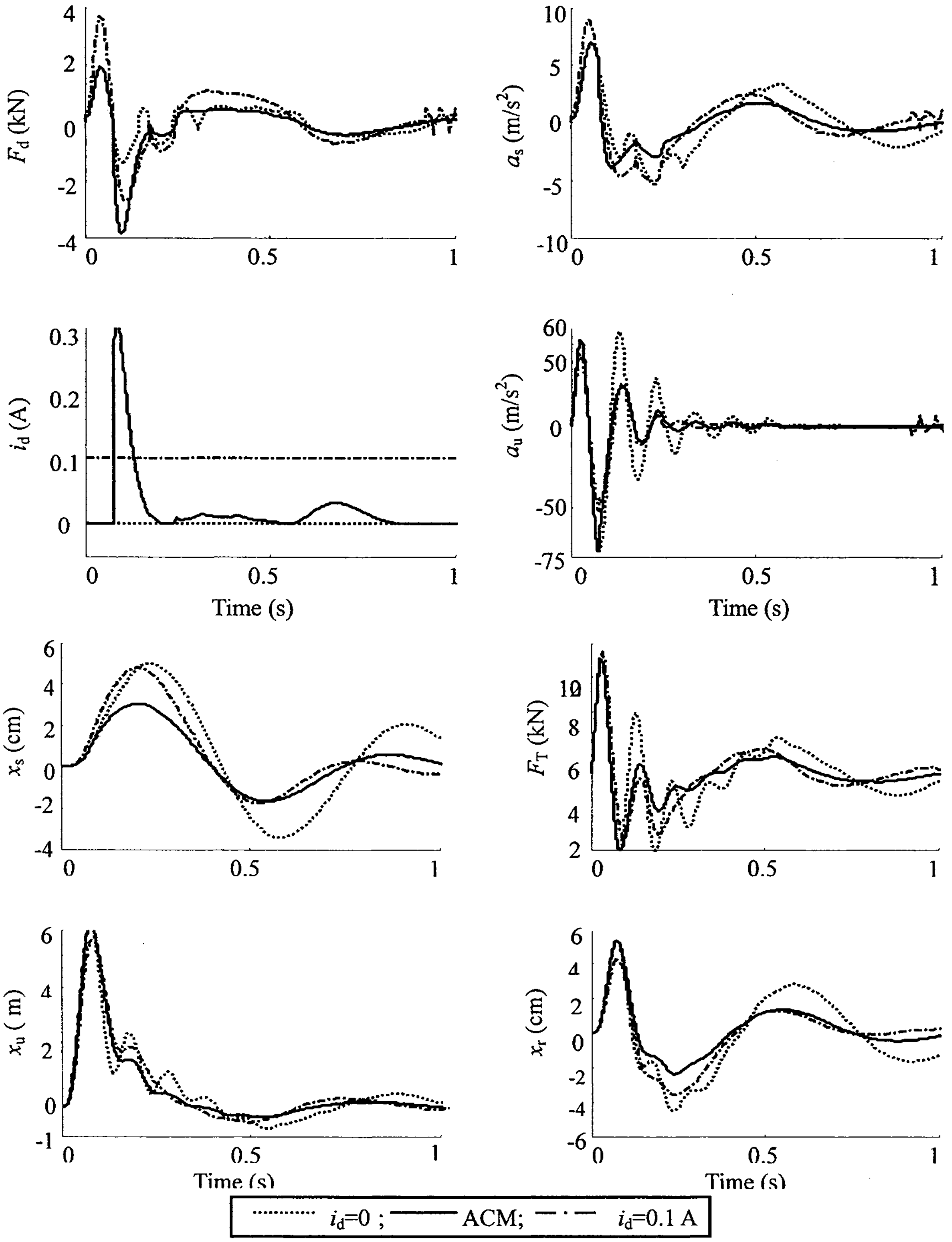

Figure 4.10: Comparisons of transient response characteristics of "quarter-vehicle" model with passive (i_d=0; i_d=0.1 A) and "skyhook"-based hi-lo semi-active ACM damping.

The results illustrate that a higher passive damping (i_d=0.1 A) also yields rapid rate of decay, while the peak magnitudes of sprung mass responses are considerably larger. Light passive damping (i_d=0), on the other hand, yields lower peak value of a_s, but higher peak values of x_s and considerably lower rate of decay. From the results, it can be concluded that the "skyhook"-based hi-lo semi-active ACM damping variations can help realize the benefits of both the lower and higher passive mode damping, in limiting the peak responses and rate of decay.

Responses to a Random Road Excitations

The response characteristics of the proposed "skyhook"-based hi-lo semi-active ACM damping variations are further evaluated under randomly distributed road excitation. The analyses are performed for excitation arising from the rough road, as described in section 3.5, and forward speed 50 km/h. The equations of motion for the "quarter-vehicle" model together with those for the "skyhook"-based hi-lo semi-active damping in the asymmetric mode are solved under the roughness profile of the road. The time variations in the responses are expressed in the frequency domain using FFT techniques. The selected response measures are expressed in terms of their respective power spectral density (PSD), evaluated using sampling frequency of 512, frequency resolution of 0.0625 Hz and bandwidth of 256 Hz. Figure 4.11 shows comparisons of damping force (F_d), sprung and unsprung mass accelerations (a_s, a_u), suspension relative travel (x_r) and dynamic tire force (F_T) responses of the quarter-vehicle model employing both passive MR-damping and "skyhook"-based hi-lo semi-active ACM damping.

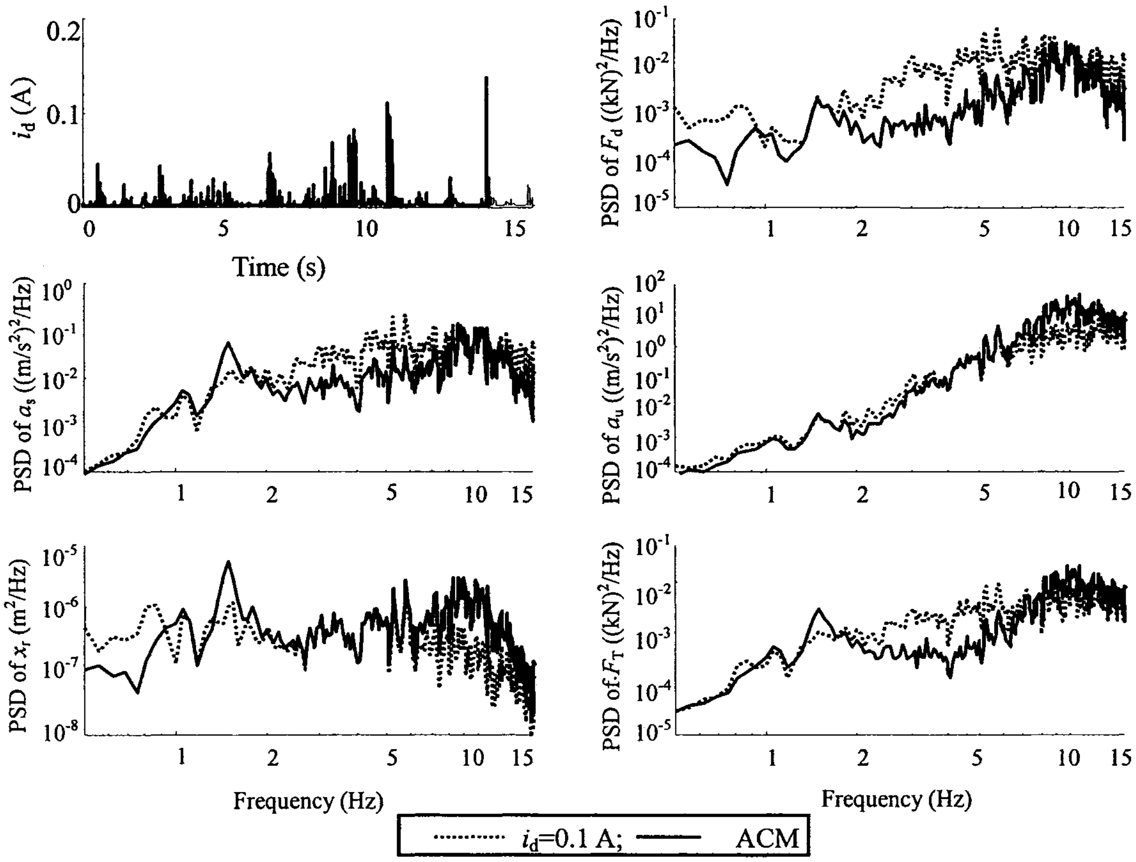

Figure 4.11: Comparisons of random responses of the "quarter-vehicle" model with passive and "skyhook"-based hi-lo damping variations in ACM.

The passive mode damping is realized upon setting i_d=0.1 A, while the results are presented in terms of PSD of the response variables. The Figure also illustrates drive current variations in the semi-active synthesis. The results show that the passive mode damping force is generally considerably higher that the semi-active damping force in majority of the frequency range, even though a relatively small drive current (i_d=0.1 A) is chosen. The PSD of sprung mass acceleration in the vicinity of the sprung mass resonance thus tends to be lower for the passive mode damping, while the response in the ride frequency range (2-8 Hz) is considerably larger than that of the semi-active MR-damping. The high passive mode damping also causes higher unsprung mass acceleration in the low frequency range (below 4 Hz) and higher levels of tire force PSD in the ride frequency range.

The corresponding suspension relative motion response in the passive mode, however, tends to be comparable with that of the semi-active damping at frequencies below 7 Hz, but lower at higher frequencies. The dynamic load coefficients due to tire force were further computed for both damping mechanisms. The results revealed comparable values of DLC of 0.111 for the fixed higher damping and 0.138 for the semi-active ACM damping. The results suggest that "skyhook"-based hi-lo semi-active damping control in the asymmetric mode can provide superior ride performance in the resonant and ride frequency ranges. Moreover, the semi-active ACM damping variations yield lower unsprung mass acceleration and dynamic tire force variations, and thus offer potential for improved road holding and road-friendliness. The semi-active damping variations also yield suspension travel comparable to that due to passive damping in the lower frequency range, where the displacement tends to be high.

4.4 Influence of Variations in Operating Parameters

The road vehicles inevitably encounter wide variations in operating conditions, such as variations in operating load (m_s), forward speed (V) and road roughness. Such variations strongly influence the suspension performance [20, 35, 40, 82, 98, 99]. Passive vehicle suspensions with fixed properties are frequently design for nominal operating conditions and could yield significantly different performance under varying road and load conditions. The control parameters of semi-active suspensions, in a similar manner, are also formulated for a defined set of operating conditions and may not yield superior performance when operating variables are varied [20, 98, 99]. Adaptive control concepts in semi-active suspension have also been proposed to enhance the suspension performance over a range of operating conditions [21, 22, 29, 81]. A number of studies have suggested that a controller synthesis should exhibit adequate robustness over a range of operating speed, load and excitation conditions. The robustness of the proposed "skyhook"-based hi-lo semi-active ACM damping formulation is investigated under variations in operating load, speed and road conditions. The analyses are performed under harmonic, transient and stochastic excitations, described in section 3.5, and responses are evaluated in terms of selected measures described in section 3.6. The "skyhook"-based hi-lo semi-active ACM controller parameters are selected as: n=2, k_c=3, p_c=0, ξ_c=10, p=0 and ξ=4.5.

4.4.1 Variations in operating mass

The effective sprung mass of a road vehicle load may vary depending upon the number of passengers and the load being transported. The influences of variations in the sprung mass on the selected performance measures are evaluated by varying the sprung mass by ±25% around the nominal value, m_{s0}=563 kg. The resulting masses of 422 and 703 kg yield sprung mass natural frequencies of 1.3 and 1.7 Hz, and suspension defections of 7.25 cm and 12.1 cm, respectively. The corresponding static tire deflections are computed as 1.76 and 2.73 cm, respectively. Figure 4.12 illustrates comparisons of time-histories of dynamic responses due to different values of m_s when subject to 2.5 cm harmonic excitation in the vicinity of the nominal sprung mass resonant frequency (1.5 Hz).

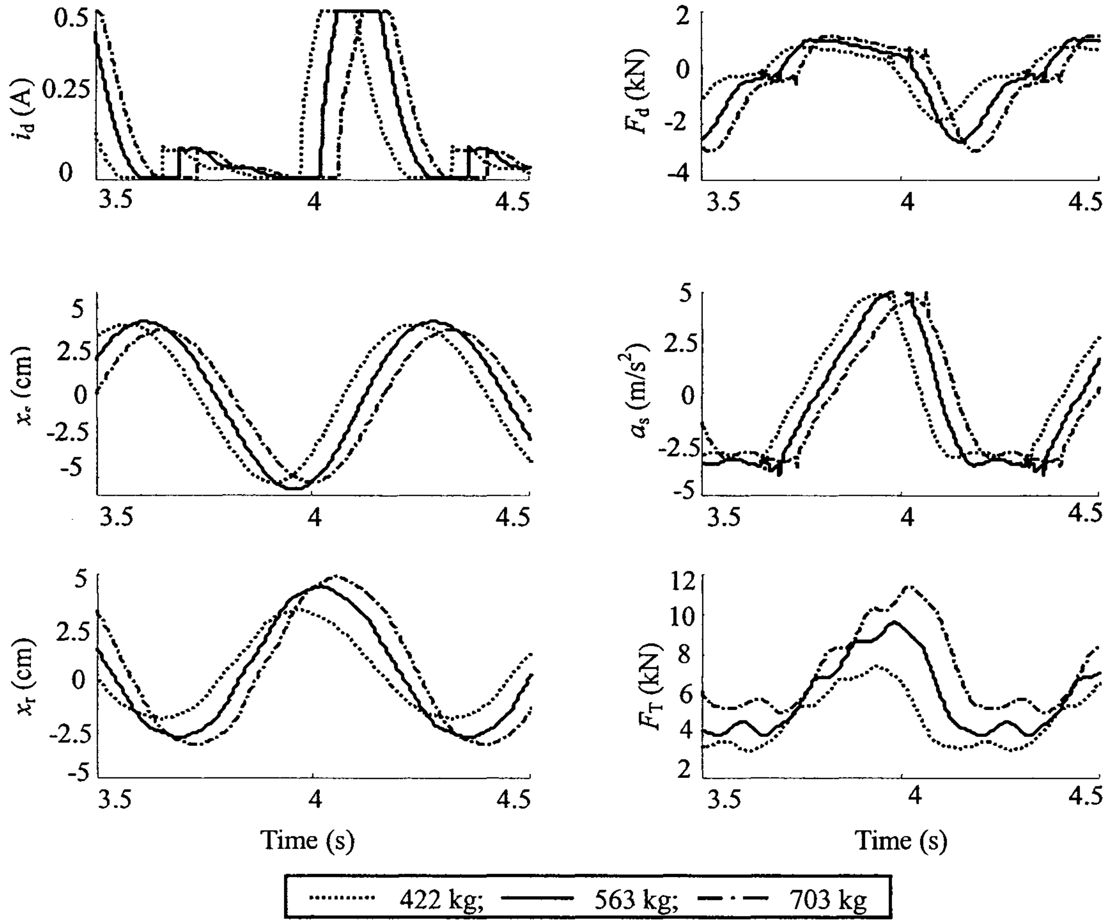

Figure 4.12: Influence of sprung mass variation on the time-histories of harmonic responses of the "skyhook"-based hi-lo semi-active ACM damping controller.

The variations in the absolute and relative velocity responses of the sprung mass cause the current modulations to occur at different instants. For a lighter sprung mass, the current modulation to higher value occurs earlier than that for the nominal mass, and the magnitude of the corresponding damping force is relatively smaller, particularly in the rebound mode. The peak magnitudes of sprung mass responses (a_s and x_s), however, remain almost insensitive to variations in m_s. It should be noted that variations in m_s yield variations in effective damping ratio and the sprung mass natural frequency. The proposed "skyhook"-based hi-lo semi-active ACM damping modulation, however, exhibits reasonably high robustness to such variations. The mean and amplitude of the tire force increase with increasing sprung mass. A lower mass yields considerably smaller magnitude of the tire force and rattle space. The higher sprung mass causes higher tire force and suspension travel, while the relative changes small in relation to those of the nominal sprung mass.

Figure 4.13 illustrates the influence of variations in m_s on the frequency response characteristics of the "quarter-vehicle" model employing the proposed "skyhook"-based hi-lo semi-active ACM synthesis. The results are presented in terms of sprung and unsprung mass acceleration (T_{as}, T_{au}), and relative displacement (T_{dr}) ratios, and DLC due to the tire force, while the excitation employs varying displacement amplitudes with frequency. The results show only slight variations in T_{as}, T_{au} and T_{dr} in the lower frequency range. An increase in m_s causes slightly higher magnitudes of T_{as} and T_{dr}, which is mostly attributed to lower effective damping ratio with higher mass. A lower mass, on the other hand, yields lower peak magnitudes of T_{as} and T_{dr}. The unsprung mass acceleration transmissibility in the vicinity of the sprung mass resonance, however, decreases slightly with increasing mass. The responses in the vicinity of the unsprung mass resonance, however, remain insensitive to variations in m_s. The DLC due to tire force exhibits significant variations due to changes in m_s. Owing to its definition, the DLC increases with decreasing vehicle weight. The lower mass thud yields higher DLC response in the entire frequency range. The responses to harmonic excitations, shown in

Figures 4.12 and 4.13, generally suggest high robustness of the proposed "skyhook"-based s hi-lo semi-active ACM damping synthesis to variations in the sprung mass.

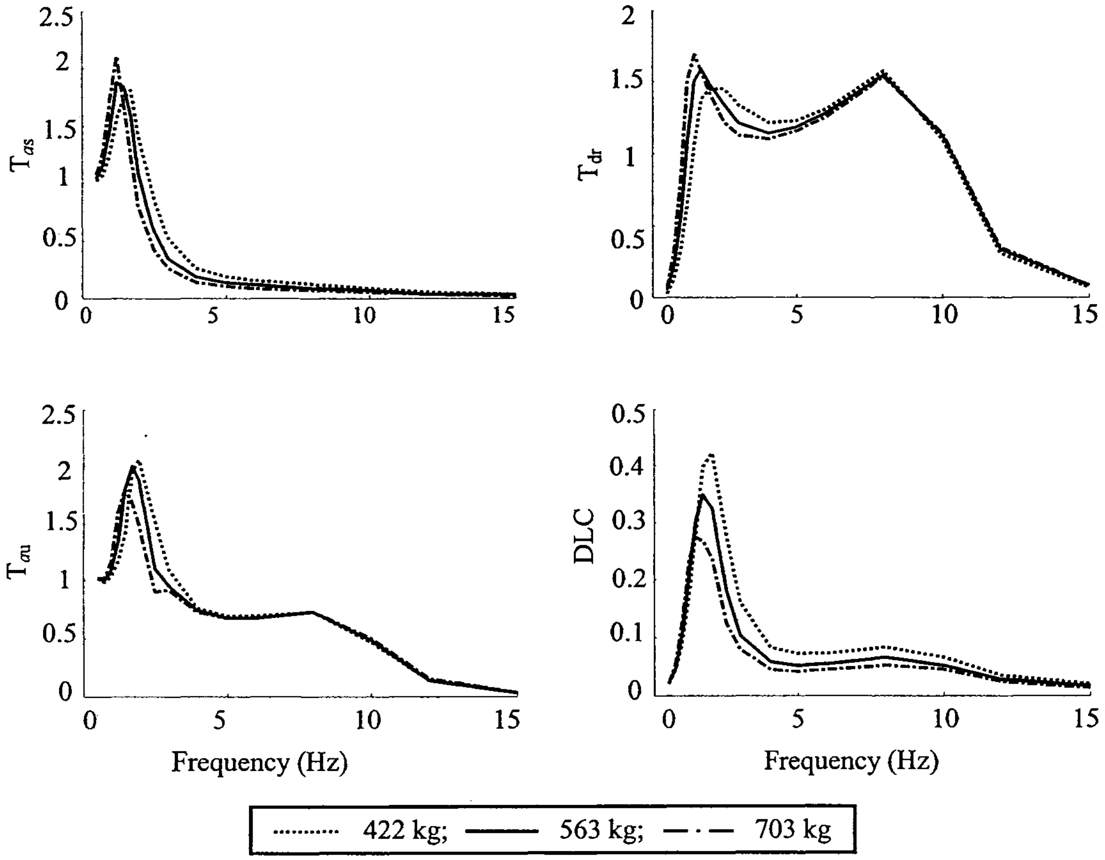

Figure 4.13: Influence of sprung mass variation on the frequency response characteristics of the "skyhook"-based hi-lo semi-active ACM damping controller.

The influences of sprung mass variations on the transient responses to a rounded pulse excitation (μ=3, ω_0=10.4 rad/s and a_m=3.5 cm) are illustrated in Figure 4.14. The results are also summarized in terms of the performance measures described in section 3.6, namely the shock displacement ratios of the sprung and unsprung masses (SDR$_s$ and SDR$_u$), shock acceleration ratios (SAR$_s$ and SAR$_u$), suspension relative displacement ratio (RDR) and deviation in peak tire force ratio (DTR). The variations in the sprung mass cause considerable changes in the peak drive current during rebound, but only minimal change in the peak damping force could be observed. A lower sprung mass causes higher drive current in rebound due to higher sprung mass velocity, as evident from the sprung mass acceleration response shown in Figure 4.14. The peak damping force, however, varies only slightly due to force-limiting nonlinearity of the MR-damper. The tire force responses exhibit shifts along the magnitude axis with varying sprung mass, which is attributed to variations in the mean tire force.

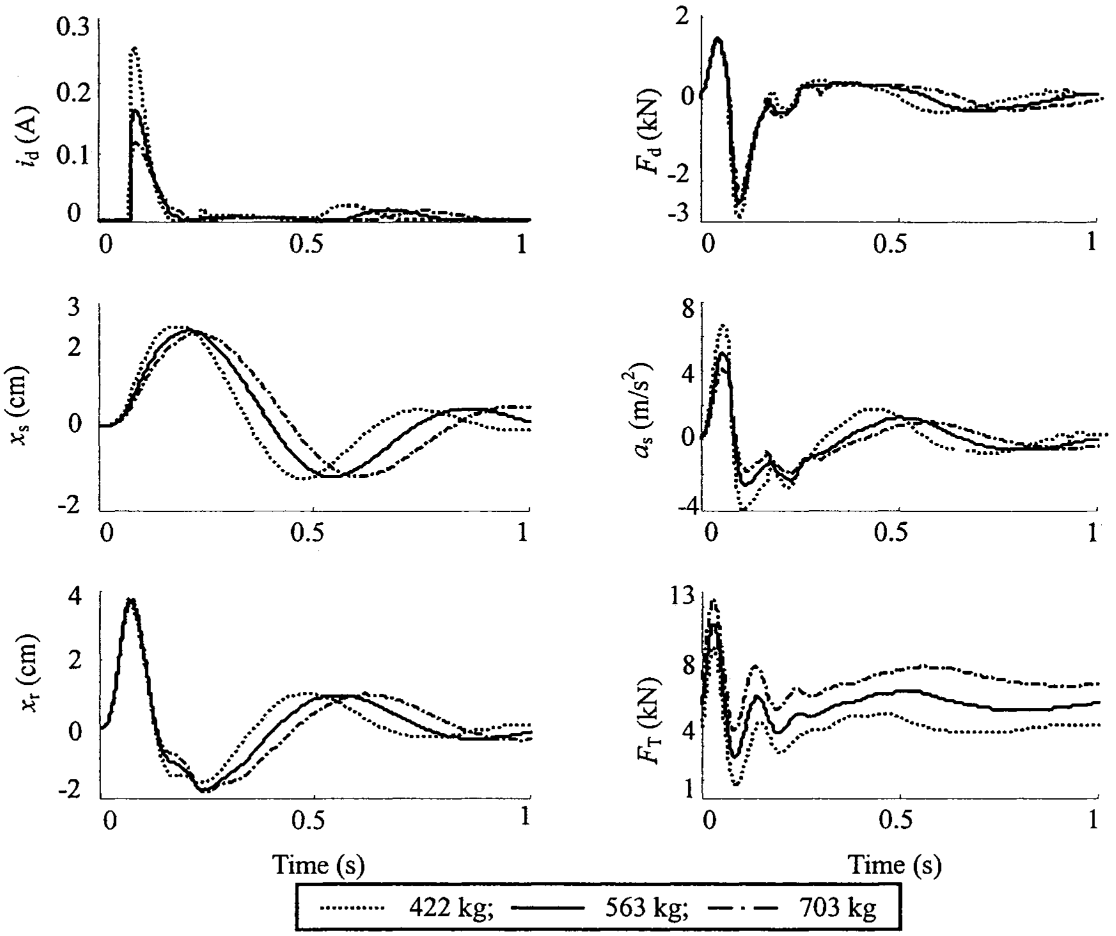

Figure 4.14: Influence of sprung mass variations on the transient responses to a rounded pulse excitation.

The transient response measures summarized in Table 4.1 also show relatively small influence of sprung mass variation on the deviation in the peak tire force. The normalized peak force increases is in the order of 26%, when sprung mass is decreased by 25%. The peak tire force deviation, however, decreases by 29%, when the sprung mass is increases by 25%. The results also show that the peak suspension travel (RDR), sprung mass displacement ratio (SDR_S) and unsprung mass acceleration and displacement ratios (SAR_u and SDR_u) remain insensitive to variations in m_S. The sprung mass shock acceleration ratio (SAR_s), however, increases by 32% when m_S is reduced by 25%, and it decreases by 21% when m_S is increased by 25%.

Table 4.1: Influence of sprung mass variations on the transient response measures.

m_s (kg)	SDR_s	SAR_s	SDR_u	SAR_u	RDR	DTR
422	0.71	0.25	1.17	1.92	1.13	0.26
563	0.71	0.19	1.17	1.92	1.13	0
703	0.71	0.15	1.17	1.92	1.13	0.29

The influences of variations in m_S on the suspension performance are also evaluated under stochastic excitations due to rough road, while the speed is held constant as 50 km/h. The relative responses of the "quarter-vehicle" model employing the proposed semi-active ACM synthesis are evaluated in terms of PSD of F_d, a_s, a_u, x_r and F_T, and time variations in i_d, while the sprung mass is varied by ±25%.

The results show higher drive current for the lower mass (m_s=422 kg) due to high sprung mass motion and thus damping force demand (Figure 4.15). The comparisons of damping forces, corresponding to different operating masses, however, exhibit only minimal differences. This is attributed to two factors: saturation nonlinearity of the MR-damper; and controller property in limiting the motion of a heavier sprung mass and thus the damping force demand. Comparable magnitudes of damping forces for all these measures also yielded comparable responses of the model in terms of PSD. The sprung mass acceleration response of the "skyhook"-based hi-lo semi-active damping is lower in the important ride frequency range with increasing sprung mass. The relative displacement and tire force responses in the low frequency range increase with sprung mass. The DLC due to tire force tends to be lower for heavier operating mass, which is attributed to its definition. The DLC due to tire forces increases from 0.114 to 0.176, when the sprung mass is increased by 67%.

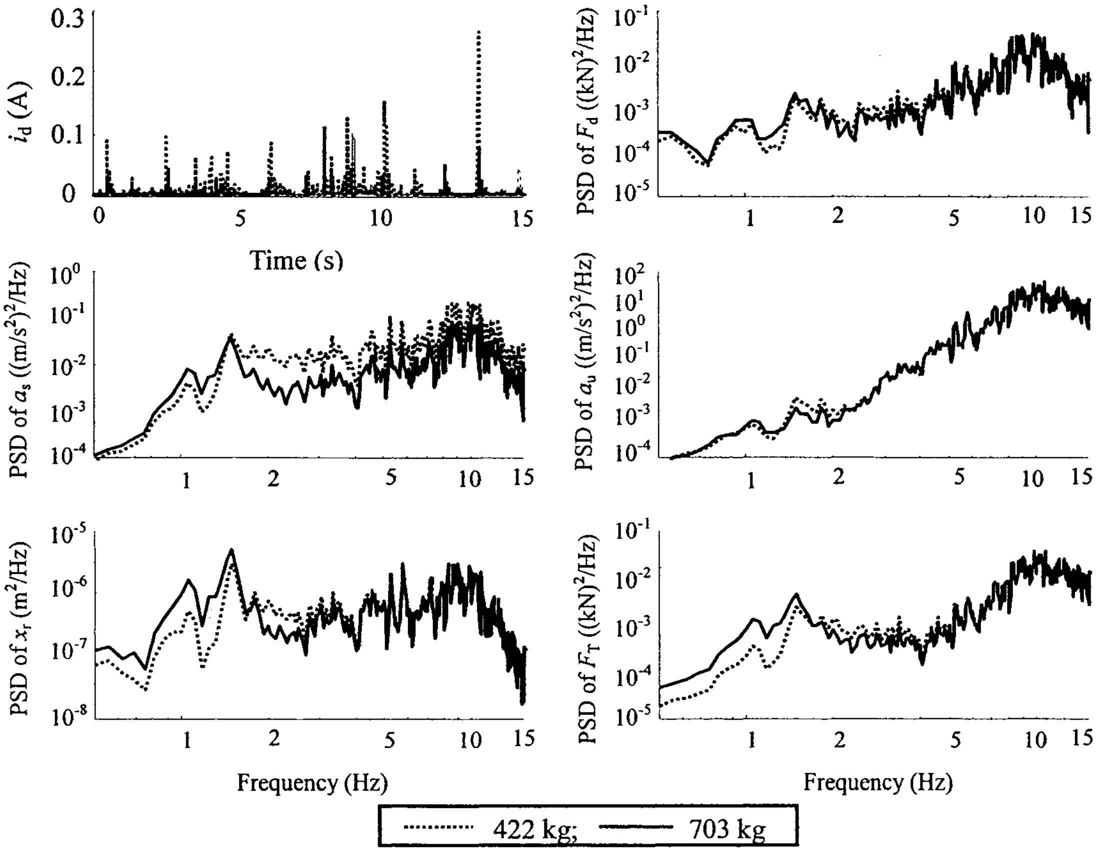

Figure 4.15: Influence of sprung mass variations on the random response characteristics of "quarter-vehicle" model employing "skyhook"-based hi-lo semi-active damping in ACM.

The above analysis results illustrate that the proposed "skyhook"-based hi-lo semi-active MR-suspension in ACM has superior robustness on vehicle load parameter uncertainty, for the different road profiles of harmonic, transient and random excitations.

4.4.2 Variations in operating speed

Variations in operating speed of a vehicle alter the magnitude and frequency components of road excitation, and thus influence the suspension performance in a highly significant manner. The sensitivity of the proposed "skyhook"-based hi-lo semi-active ACM controller is evaluated under different speeds. Two different speeds (50 and 100 km/h) are considered for the analyses, which are performed for transient and random excitations. For transient excitations, the pulse duration T is varied to account for variations in speed. Assuming a constant wavelength (w=4.5 m), the pulse durations related to fundamental frequency ω_0 in EQ (3.38) corresponding to speeds of 50 and 100 km/h, are taken as 0.64 s and 0.32 s, respectively. These result in ω_0=10.4 and 20.8 rad/s, respectively. The corresponding rounded pulse displacement variations have been shown in Figure 3.9(c). Figure 4.16 illustrates the influences of vehicle speed variations on the transient responses of quarter-vehicle model employing skyhook-based hi-lo semi-active ACM damping due to MR-damper. The excitation parameters due to pulse excitation are chosen as: μ=3 and a_m=3.5 cm. The results show that an increase in vehicle speed to 100 km/h causes relatively smaller drive current due to shorter pulse duration. The damping force, however, tends to be generally higher than that observed at 50 km/h, due to higher relative velocity.

The peak sprung mass acceleration response at a speed of 100 km/h is relatively larger than that at 50 km/h. This is attributed to higher severity of the pulse excitation at 100 km/h, as evident in Figure 3.9(c). The acceleration response at 100 km/h also exhibits oscillation of considerably larger magnitudes that occur near the unsprung mass resonant frequency. Relatively higher wheel hop motion at 100 km/h is also evident from the tire force and the controlled damping force responses. The peak sprung mass displacement, however, tends to be smaller due to considerably higher rebound mode damping at 100 km/h.

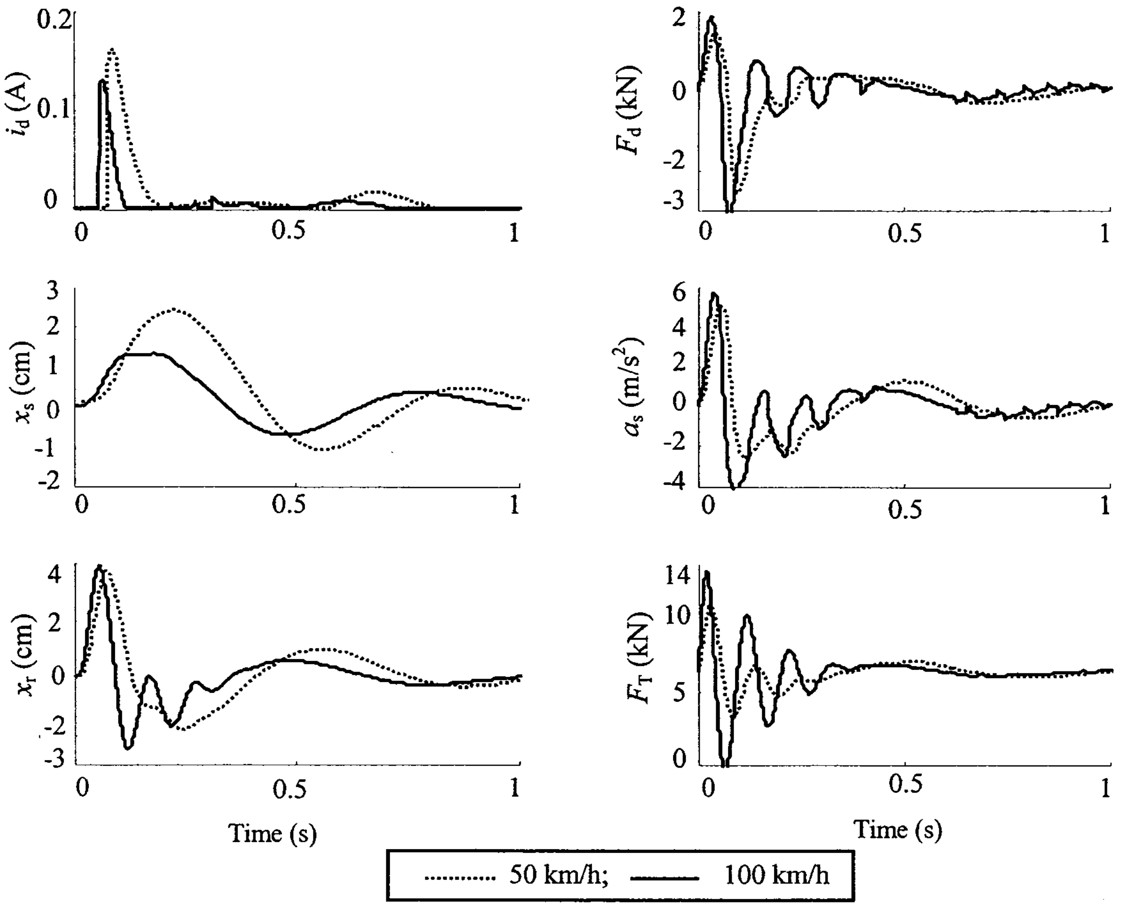

Figure 4.16: Influence of vehicle speed variations on the transient responses to a rounded pulse excitation.

The transient response measures summarized in Table 4.2 also show relatively larger deviation in the peak tire force, normalized with respect to the nominal value at 50 km/h. The peak force deviation (DTR) is in the order of 42%, when vehicle speed is increased by 100%, which most likely would present an extreme case of vehicle passing a rounded pulse shaped bump at such a high speed. The results also show that the unsprung mass and relative displacement ratios (SDR_u and RDR) remain relatively insensitive to variations in speed. However, the sprung mass shock displacement and acceleration ratios (SDR_s and SAR_s) decrease and increase by 42% and 74%, respectively, and the unsprung mass acceleration ratio (SAR_u) decreases by 69%, when speed is increased to 100 km/h.

Table 4.2: Influence of vehicle speed variations on the transient response measures.

V (km/h)	**SDR_s**	**SAR_s**	**SDR_u**	**SAR_u**	**RDR**	**DTR**
50	0.71	0.19	1.17	1.92	1.13	0
100	0.41	0.05	1.17	0.60	1.14	0.42

Figure 4.17 illustrates the influences of variations in vehicle speed on the response characteristics of the "quarter-vehicle" model employing the proposed semi-active ACM synthesis, when subject to random road excitation and variation. An increase in the vehicle speed causes higher frequency components of the road profile as observed form Figures 3.10(b) and 3.10(c). The results show that the higher roughness magnitude at low speed of 50 km/h causes higher sprung mass oscillation and thus poses greater demand for the damping force. The variation in drive current magnitude thus tends to be higher for the 50 km/h operation, when compared to that for 100 km/h. The PSD of damping force corresponding to lower speed, however, is slightly higher due to force saturation

nonlinearity and asymmetric modulation effects of the controller. The higher damping force yields only slightly higher sprung and unsprung mass acceleration response in the ride frequencies range. The influence of vehicle speed on the tire force and suspension travel response PSD's are also observed to be small, as seen in Figure 4.17. The DLC due to tire force at 100 km/h increases slightly to 0.142 compared to 0.138 at 50 km/h. Results thus further show relatively high robustness of the controller synthesis in view of vehicle speed variations.

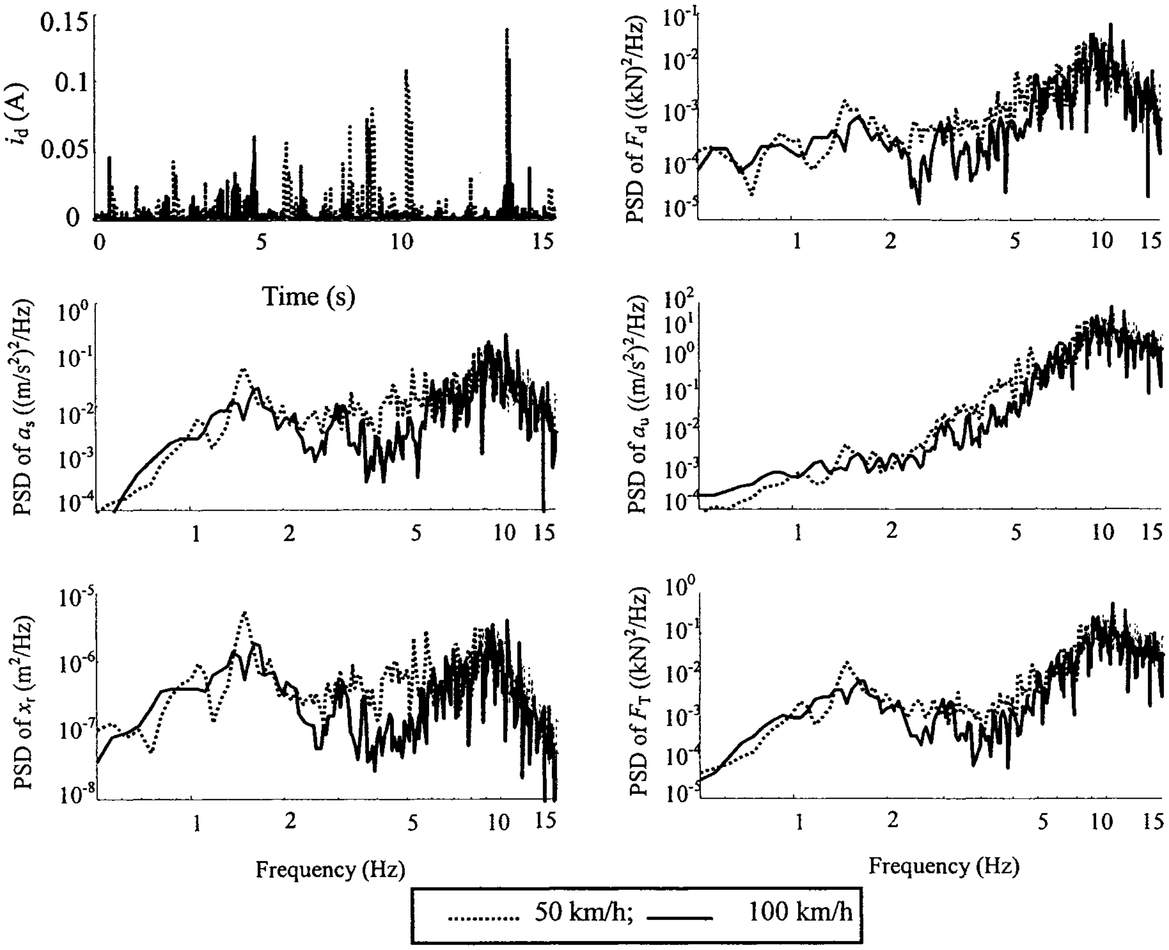

Figure 4.17: Influence of vehicle speed variations on the PSD characteristics of responses to a rough random excitation.

4.4.3 Variations in road roughness

Apart from vehicle speed variations, the road vehicles invariably encounter large variations in magnitudes of road surface roughness. The effect of such variation can be conveniently evaluated by considering different amplitudes of deterministic excitation. For randomly varying road profiles, the analyses are performed for two different road profiles: (i) medium-rough; and (ii) rough road profile, as discussed in section 3.5.2. The influences of excitation magnitude on the frequency response characteristics of the “quarter-vehicle” model employing the “skyhook”-based hi-lo semi-active ACM damping control are evaluated by considering two different types of harmonic excitations: (i) constant frequency (1.5 Hz) excitation of three different displacement amplitudes (a_m=1.5, 2.5 and 3.5 cm); and (ii) swept frequency excitation with same these different displacement amplitudes at frequencies below 2.1 Hz, and constant acceleration at frequencies above 2.1 Hz (2.61, 4.35 and 6.09 m/s^2). The transient response characteristics of the controller synthesis are evaluated under different peak displacements due to rounded pulse excitation (a_m=2, 3.5 and 5 cm), while all other parameters are held constant (μ=3 and ω_0=10.4 rad/s). The corresponding rounded pulse displacement variations have been shown in Figure 3.9(b). Figure 4.18 illustrates the influence of variations in harmonic excitation amplitude on responses of the “quarter-vehicle” model. Considering that the selected excitation frequency lies in the vicinity of the sprung mass natural frequency, the responses represent the resonant behaviour of the vehicle model with semi-active damping.

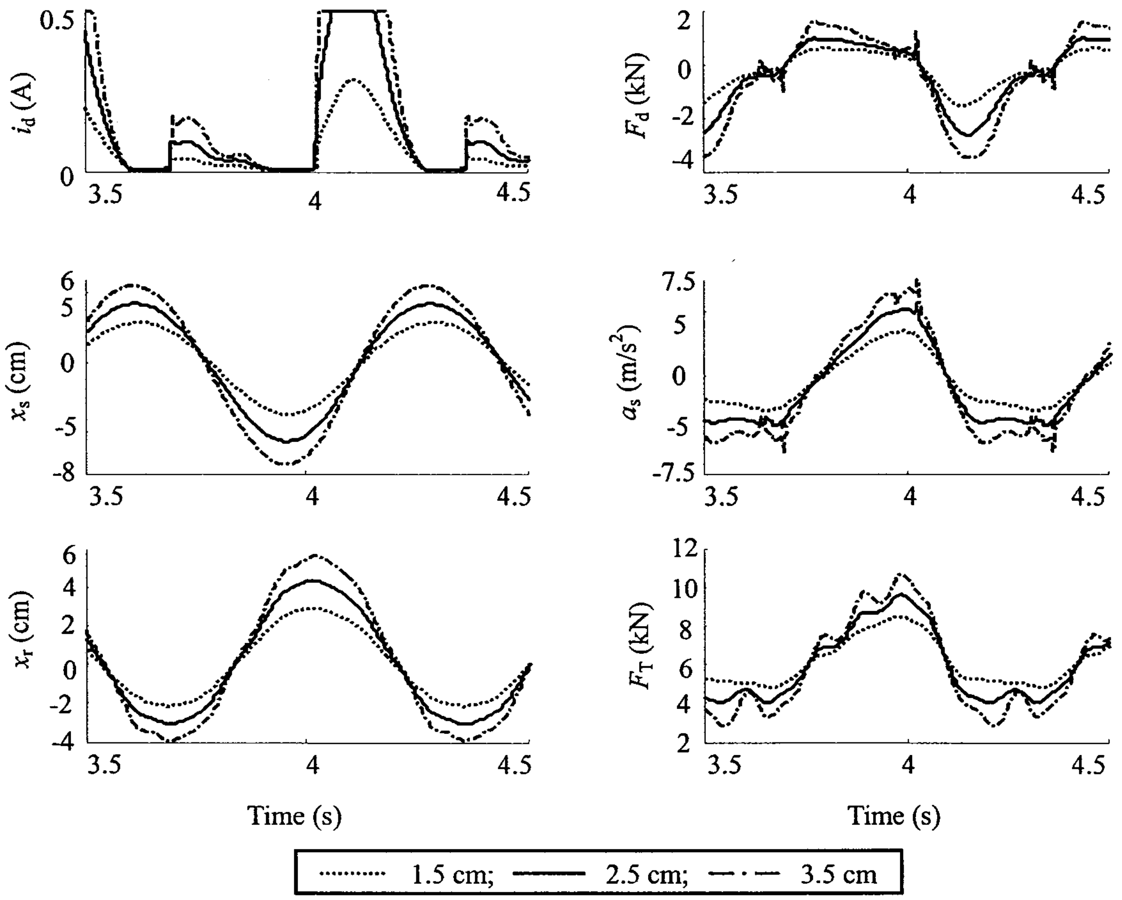

Figure 4.18: Influence of variations in the harmonic excitation magnitude (f=1.5 Hz) on the response characteristics of the "quarter-vehicle" model employing "skyhook"-based hi-lo semi-active ACM damping controller.

An increase in excitation magnitude causes higher sprung mass displacement and acceleration response, and thus poses increased demand on the damping force. The drive current increases considerably, when excitation amplitude is increased from 1.5 to 2.5 cm, and approaches the limiting value during rebound. A further increase in excitation magnitude to 3.5 cm results in only slight increase in i_d in the rebound mode, but relatively larger increase in compression mode. Relatively larger changes in compression damping force could thus be observed with varying excitation amplitude. Higher magnitude excitation not only yields higher resonant responses of sprung and unsprung mass accelerations and tire force, it also excites the unsprung mass resonance mode a_s observed from as and F_T responses. This is attributed to the pronounced effects of switching discontinuity and hysteresis under higher excitations. This is evident from relatively sharp variations in i_d under higher excitations, particularly in the rebound mode. The proposed semi-active controller synthesis with continuous modulation and ADFG functions tends to approach the on-off manner of modulation under higher excitations. Alternative smoothing function or higher order of controller may thus be desirable under such conditions.

Figure 4.19 illustrates the influence of variations in a_m on the frequency response characteristics of the "quarter-vehicle" model employing the proposed "skyhook"-based hi-lo semi-active ACM synthesis. The results are presented in terms of T_{as}, T_{au}, T_{dr}, and DLC, similar to those analyses presented in Figure 4.13 for variations in the sprung mass. The results show only slight variations in sprung mass acceleration transmissibility response (T_{as}). The peak resonant transmissibility increases only slightly with increasing excitation magnitude, while the response in the ride frequency range is nearly insensitive to harmonic excitation magnitude. Higher excitation magnitudes, however, cause significantly higher unsprung mass acceleration and thus the tire force responses in the vicinity of the sprung and unsprung resonant frequencies. The suspension relative displacement response also increases with increasing excitation magnitude, particularly around the resonant frequencies. The frequency response characteristics suggest poor performance of the proposed semi-active asymmetric damping under higher harmonic excitations. The limited performance is mostly attributed to the limited damping force bandwidth of the MR-damper considered in the study. The drive current ($i_d \leq 0.5$ A) and thus the damping force rapidly approach their limiting values, when excitation amplitude is increased, as observed in Figure 4.18. The robustness of the controller synthesis in view of excitation magnitude variations can be improved by enhancing the damping bandwidth and thus the upper current limit of the MR-damper.

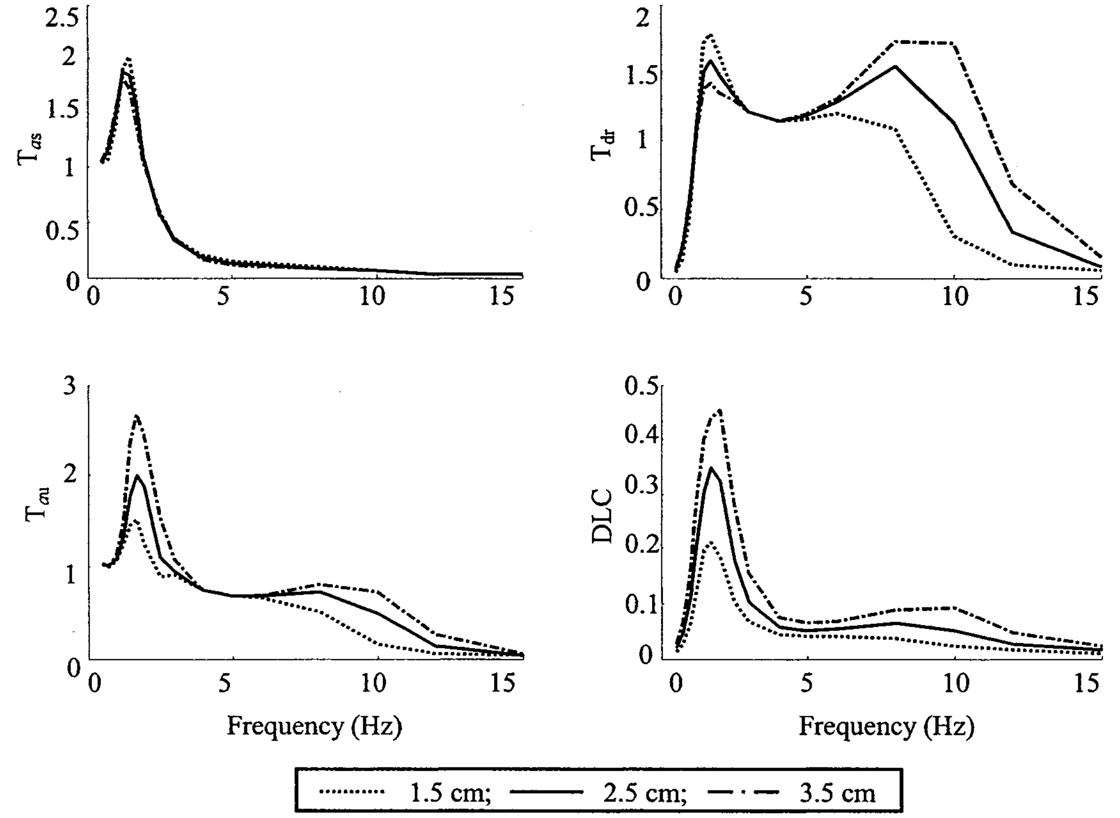

Figure 4.19: Influence of variations in amplitude of harmonic excitation on the frequency response characteristics of the "skyhook"-based hi-lo semi-active ACM damping controller.

Figure 4.20 illustrates the influences of rounded pulse displacement amplitude on the transient responses of the "quarter-vehicle" model employing proposed semi-active controller synthesis. The results show that the drive current increases significantly with increasing pulse displacement, as observed for the harmonic excitation, in response to resulting higher sprung and unsprung mass displacements. Owing to higher severity due to higher displacement pulse excitation, the sprung mass peak displacement and acceleration, and peak tire force responses increase. As discussed in case of the harmonic excitations, the suspension robustness to varying transient excitations could be improved by increasing the damping bandwidth of the MR-damper.

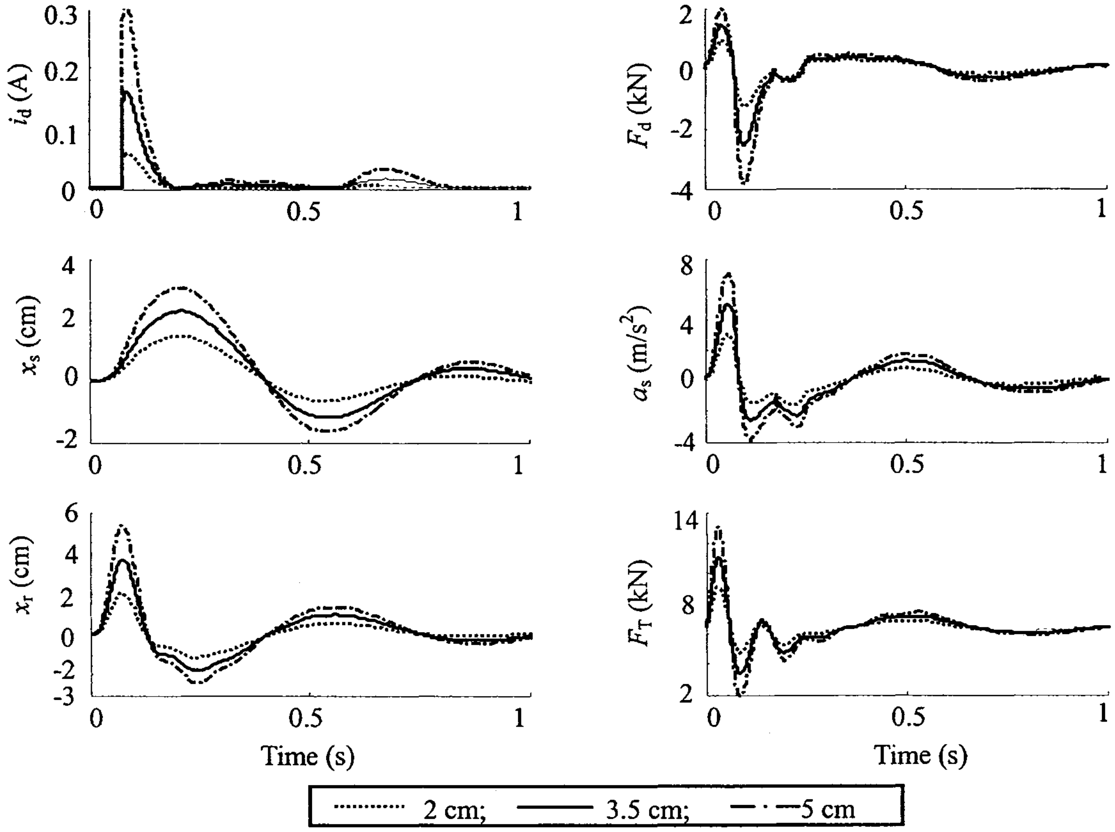

Figure 4.20: Influence of variations in rounded pulse displacement on the "quarter-vehicle" model responses with "skyhook"-based hi-lo semi-active damping control.

The summary of the shock response measures presented in Table 4.3, however, demonstrate superior robustness of the controller synthesis. The transient response measures show relatively smaller deviations in the peak tire force. The peak force deviation (DTR) increases and decreases in the order of 29%, respectively, when peak displacement amplitudes of the rounded pulse excitation are increased and decreased by 43%. The results also show that the corresponding sprung mass displacement ratio (SDR_s) increases and decreases by 5.6% and 9.9%, while the sprung mass acceleration ratio (SAR_s) remains insensitive to variation in the peak excitation magnitude. Moreover, the unsprung mass shock displacement and acceleration (SDR_u and SAR_u) and relative displacement (RDR) ratios generally decrease by 6% and 3.4%, 10% and 15%, and 1.8% and 0.9%, respectively, when peak displacement amplitudes of the rounded pulse excitation are decreased and increased by 43%, respectively,.

Table 4.3: Influence of variations in peak pulse displacement on the transient response measures.

a_m (cm)	SDR_s	SAR_s	SDR_u	SAR_u	RDR	DTR
2.0	0.75	0.19	1.10	1.72	1.10	0.29
3.5	0.71	0.19	1.17	1.92	1.13	0
5.0	0.64	0.19	1.21	1.64	1.12	0.29

Figure 4.21 illustrates the influence of variations in the random road roughness on the performance characteristics of the vehicle model with “skyhook”-based hi-lo semi-active controller. The medium-rough and rough random road excitations at vehicle speed of 50 km/h, as shown in Figure 3.10 (b), are employed, and PSD’s of responses of F_d, a_s, a_u, x_r and F_T and time variations in i_d are presented for the analyses. The results show that the magnitudes of PSD of the responses for the rough road excitation are larger than those for the medium-rough road excitation around both sprung and unsprung mass natural frequencies. This is attributed to the larger displacement excitation magnitude. The

responses of a_s, a_u and F_T for the rough road excitation are comparable to those attained under the medium rough road excitation in the ride frequency range (2-5 Hz). The DLC due to tire force for the rough road excitation increases significantly to 0.138, compared to 0.045 for medium-rough road excitation.

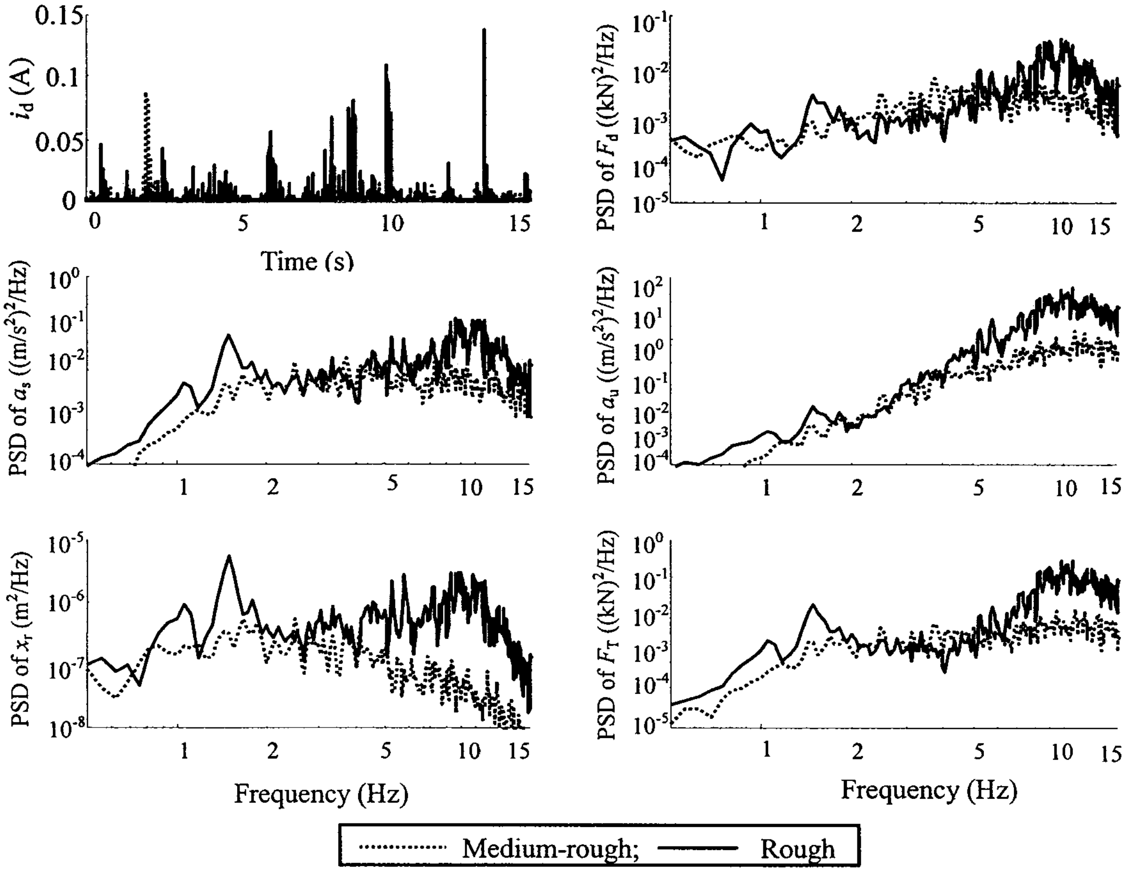

Figure 4.21: Influence of road roughness variations on the PSD of response characteristics of the "quarter-vehicle" model with the "skyhook"-based hi-lo semi-active ACM damping controller (V=50 km/h).

The results further illustrate that the proposed "skyhook"-based hi-lo semi-active ACM controller could offer superior ride and vibration isolation suspension performance and better robustness on the road roughness variations. Furthermore, as discussed in case of the harmonic and rounded pulse transient excitations, the suspension robustness to varying random roughness excitations could be further improved for suppressing the sprung and unsprung mass resonances by increasing the damping bandwidth of the MR-damper.

4.5 Influence of Variations in Controller Parameters

The performance characteristics of a semi-active damping controller are strongly dependant upon its control parameters. In case of the proposed "skyhook"-based semi-active ACM controller, two key control parameters would affect the modulation of the drive current and thus the damping force variations. These include the controller gain k_c and order n that directly relate to the drive current in response to the condition functions, as described in EQ (3.15). The variations in these parameters could help realize better performance and robustness of the proposed synthesis. The influences of variations in these parameters are thus investigated on the vehicle model responses to deterministic as well as random excitations. The analyses are performed considering identical values for the continuous modulation and ADFG functions, i.e. p=0, ξ=4.5, p_c=0 and ξ_c=10.

4.5.1 Controller gain (k_c)

The controller gain parameter (k_c) plays an important role in regulating the magnitude of drive current for MR-damper to realize desirable variations in the damping force in an asymmetric manner. Three different values of the controller gains (k_c=0.5, 1.5 and 3) are considered for the analyses, and the relative response characteristics are evaluated to identify a desirable controller gain, while the controller order is held as 2.

Figure 4.22 illustrates a comparison of time-histories of responses (i_d, F_d, a_s, a_u, x_r and F_T,) attained for different values of k_c, when subject to 2.5 cm harmonic excitation at 1.5 Hz. The resulting responses are considered to describe the resonant behaviour of the suspension system.

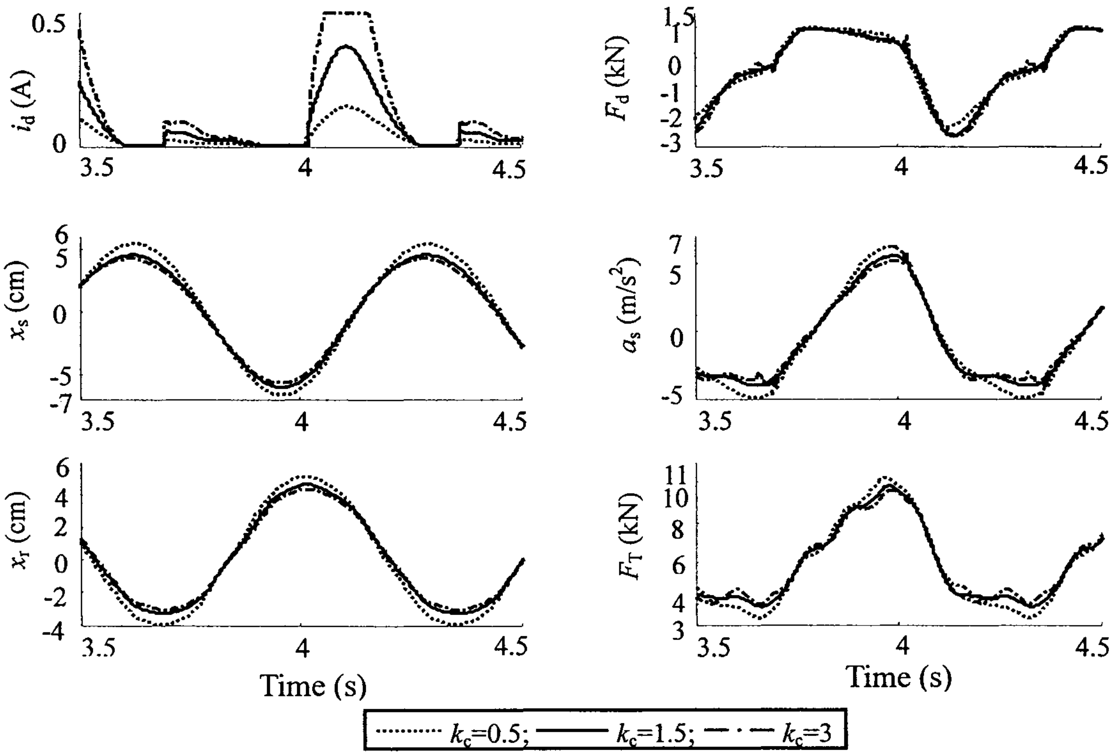

Figure 4.22: Influence of control gain variations on the harmonic responses of the "skyhook"-based hi-lo semi-active ACM damping controller (f=1.5 Hz, a_m=2.5 cm).

The resonant responses show that a lower controller gain yield considerably lower current in accordance with the formulation in EQ (3.15). The corresponding relative velocity response, however, increases, which is evident from slightly higher relative displacement response. The damping force corresponding to lower gain (k_c=0.5), however, is similar to that obtained for higher gains (k_c=1.5 and 3). This is attributed to two factors: (i) the saturation nonlinearity of the MR-damper, particularly in the rebound mode; and (ii) higher relative velocity corresponding to lower control gain. The compression mode damping force, however, tends to be slightly lower for the lower gain. Owing to only slight variations in the damping force, the different values of controller gain yielded only slight variations in the resonant response magnitude. This is evident from comparable magnitudes of x_s, a_s, x_r and F_T. The results thus exhibit superior robustness of the controller synthesis in view of the resonant responses.

Figure 4.23 illustrates the influence of variations in k_c on the frequency response characteristics of the "quarter-vehicle" model employing the proposed semi-active ACM synthesis. The results are presented in terms of T_{as}, T_{au}, T_{dr}, and DLC, under harmonic excitations of varying displacement amplitudes in the 0.5 to 15 Hz frequency range.

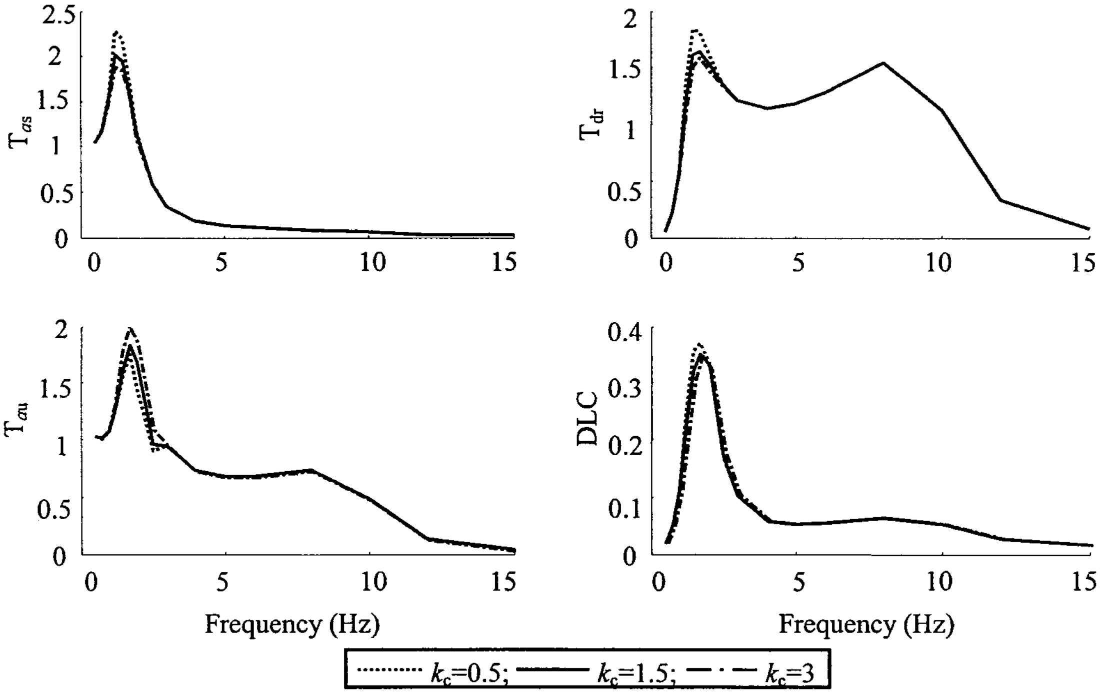

Figure 4.23: Influence of control gain variations of harmonic excitation on the frequency response characteristics of the "skyhook"-based hi-lo semi-active ACM damping controller.

The results show variations in the control gain variation affect the frequency characteristics only slightly. The influences are evident only in the vicinity of the sprung mass natural frequency. Such variations are attributed to lower drive current and comparison mode damping force of the controller with lower gain. An increase in the controller gain does not offer any significant gain due to saturation nonlinearity of the MR-damper and the current limit.

Figure 4.24 illustrates the influence of control gain variations (k_c=0.5, 1.5 and 3) on the transient responses to rounded pulse excitations (μ=3, a_m=3.5 cm and ω_0=10.4 rad/s). The influence of controller gain on the transient response is similar to those observed under swept harmonic excitations. A lower control gain yields lower drive current, as observed under harmonic excitations. The damping force, however, is only slightly smaller in the compression mode, while the rebound damping force remains insensitive to k_c and i_d. The lower compression damping corresponding to lower controller gain (k_c=0.5) causes slightly magnitudes of sprung mass displacement and accelerations, as shown in the Figure. The relatively high insensitivity of the controller synthesis to variations in the gain are further evident from the measures of the shock response predicted in Table 4.4.

Table 4.4: Influence of control gain variations on the transient response measures.

k_c	**SDR$_s$**	**SAR$_s$**	**SDR$_u$**	**SAR$_u$**	**RDR**	**DTR**
0.5	0.88	0.19	1.71	1.92	1.13	0
1.5	0.74	0.19	1.71	1.92	1.13	0
3.0	0.71	0.19	1.17	1.92	1.13	0

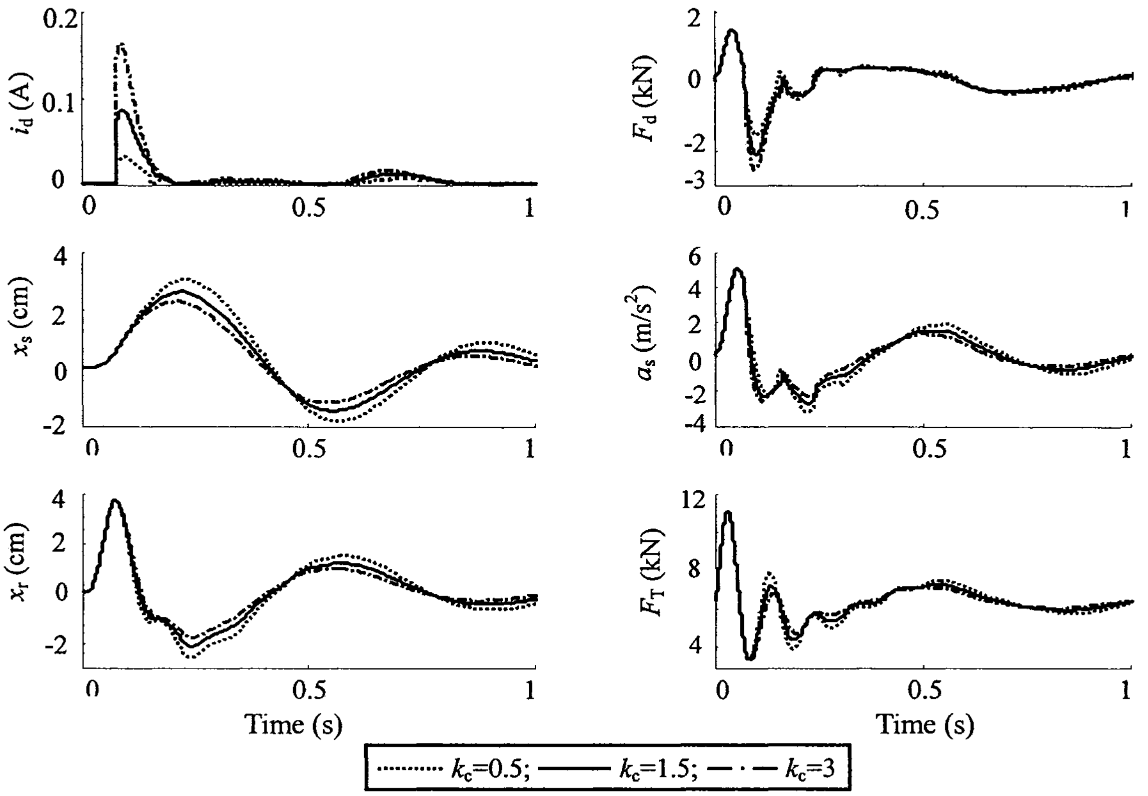

Figure 4.24: Influence of control gain variations on the transient responses to a rounded pulse excitation.

The high robustness of the controller under varying control gains is also observed from the vehicle responses to excitations arising from the random rough road. Figure 4.25 illustrates comparisons of random responses of the "quarter-vehicle" model employing the proposed semi-active ACM synthesis for different controller gains. Owing to only negligible variations in the PSD of responses, the results are presented for only two values of the gain (1.5 and 3). The results show identical PSD's of the F_d, a_s, a_u, x_r and F_T for both controller gains. The DLC values due to tire force also remain identical (0.138) for both controller gains. The lower controller gain, however, yields considerably lower drive current, when compared to that caused by higher gain. The damping forces due to both gains, however, are comparable, as observed and discussed for harmonic and transient excitations.

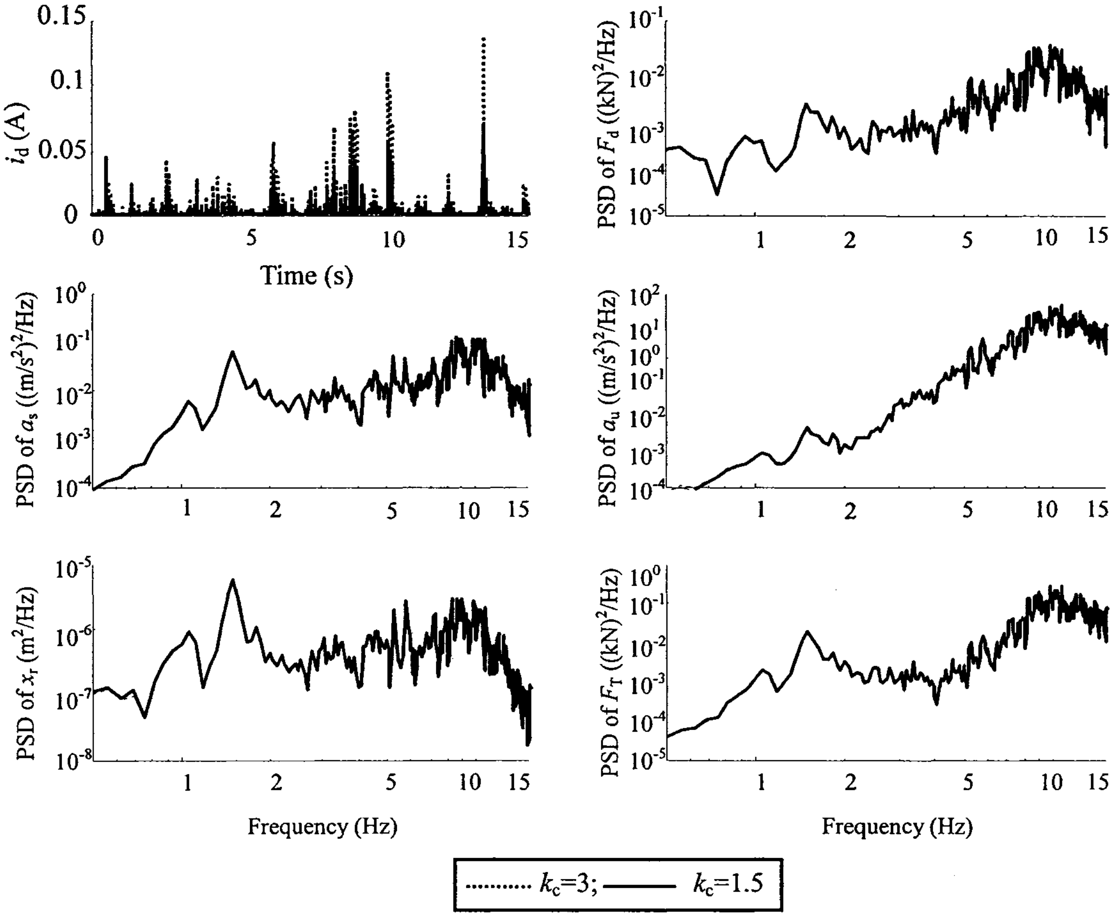

Figure 4.25: Influence of control gain variations on the PSD of responses of the vehicle model under rough random excitations (V=50 km/h).

The results illustrate that the proposed "skyhook"-based hi-lo semi-active ACM controller yields superior multi-objective suspension performance and better robustness on the control gain variations.

4.5.2 Controller order (n)

The order parameter (n) of the controller plays an important role in suppressing the effects of switching discontinuities, as described in section 3.3.1. A higher order controller yield more continuous modulation in damping force, when compared to that caused by linear controller (n=1) invariably employed in the reported studies [40, 87,]. The performance characteristics of the proposed "skyhook"-based hi-lo semi-active ACM controller are evaluated using different orders of the controller (n=1, 2 and 3) to study the effect of the controller order. The control gain parameter for the analyses is chosen as k_c=3.

Figure 4.26 illustrates a comparison of time-histories of responses for different values of the order n, when subject to 2.5 cm harmonic excitation at 1.5 Hz. The results show that a low order (n=1) controller yields rapid variations and considerable discontinuities in the drive current. The drive current in the rebound mode rapidly approaches the limiting value, and exhibits discontinuous switching in the compression mode. The corresponding damping force also exhibits discontinuities during compression cycle and force saturation in the rebound cycle. A higher order (n=3) exhibits more continuous variation in i_d, although the rebound mode force approaches saturation. The order, however, yields slightly higher sprung mass displacement and acceleration, and relative displacement response. The order n=2 is thus considered to offer a reasonably good compromise in realizing adequate damping in a continuous manner. The low order controller yields high magnitude oscillations in the acceleration response and higher tire force during the compression cycle. The peak responses, however, do not show a significant influence of the controller order.

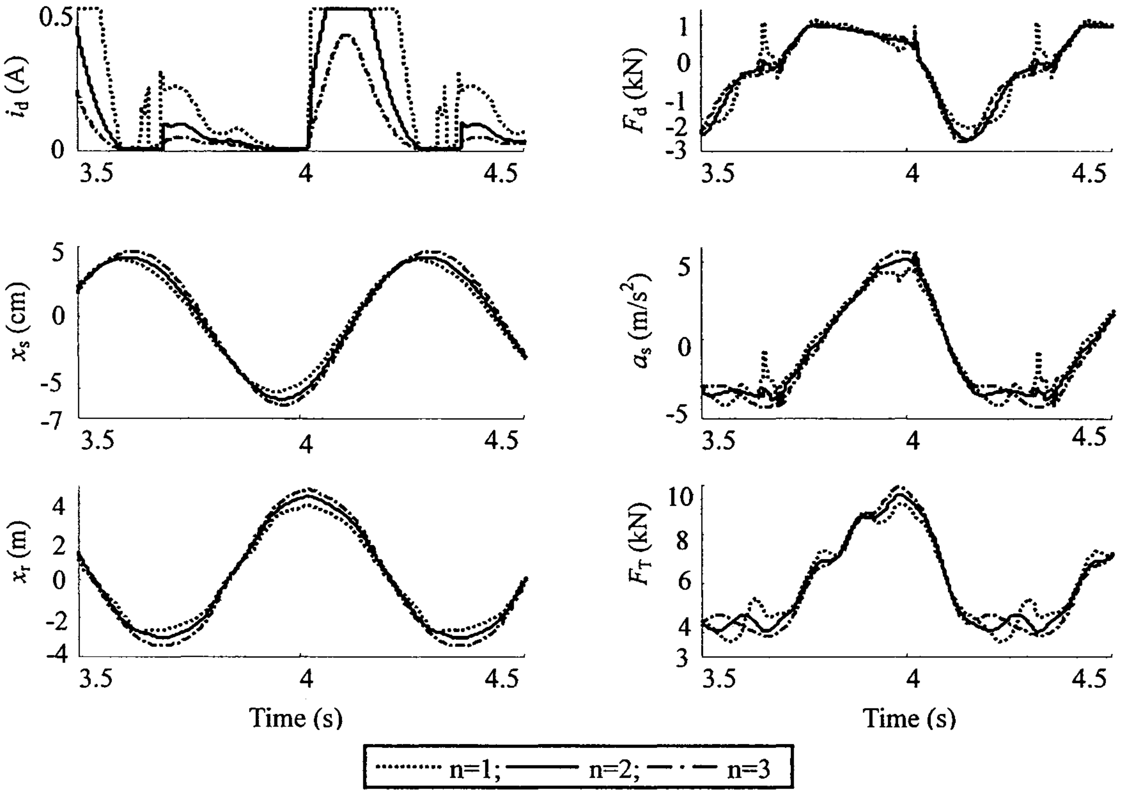

Figure 4.26: Influence of controller order on the responses of the "skyhook"-based hi-lo semi-active ACM damping controller to a harmonic excitation (f=1.5 Hz, a_m=2.5 cm).

The influence of variations in the order of the controller is also evaluated in terms of frequency response characteristics of the "quarter-vehicle" model employing the proposed semi-active ACM synthesis. The results are presented Figure 4.27 in terms of T_{as}, T_{au}, T_{dr}, and DLC, when the model subject to harmonic excitations with varying displacement amplitudes. The rapid variation in i_d and thus high damping force due to the low order controller helps to limit the resonant transmissibility of the sprung mass acceleration (T_{as}), relative displacement (T_{dr}) and tire force. The associated discontinuity in damping force, however, yields significantly higher unsprung mass acceleration transmissibility. A higher order controller yields slightly higher resonant responses due to its lower compression mode damping force. The frequency response characteristics of the highest order controller (n=3) are generally comparable with those of the second order (n=2) controller.

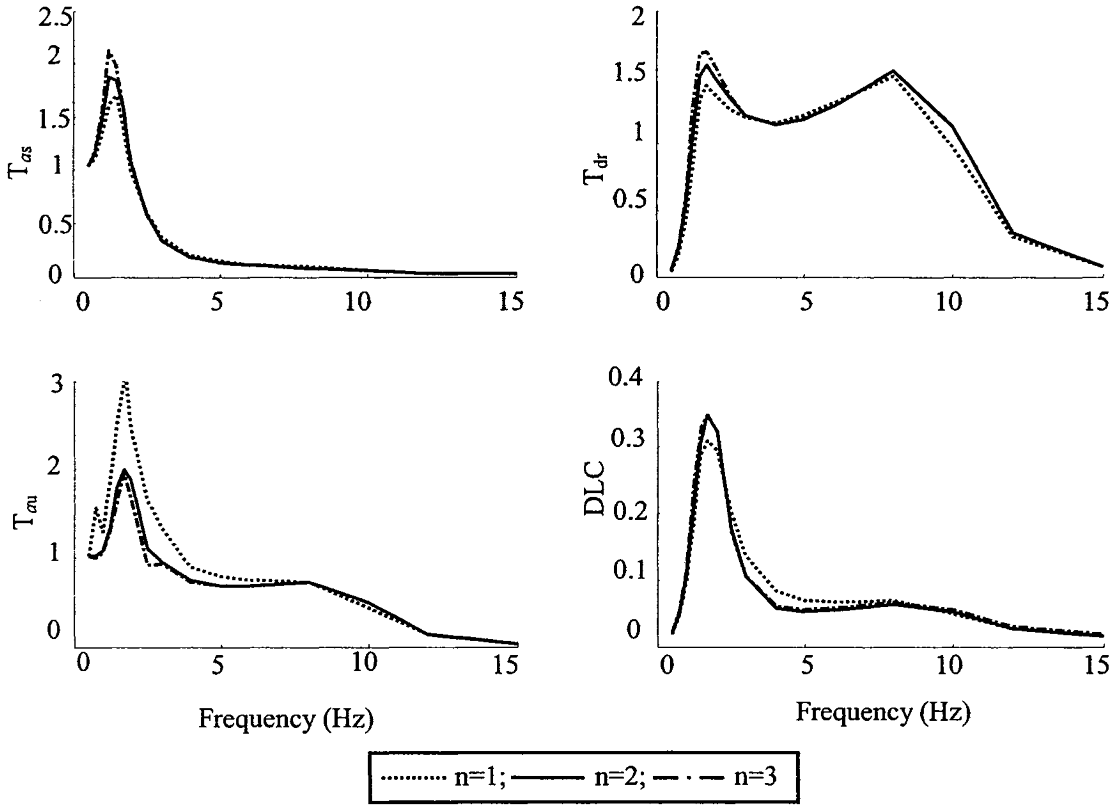

Figure 4.27: Influence of controller order variations on the frequency response characteristics of the “skyhook”-based hi-lo semi-active ACM damping controller.

The results suggest the proposed “skyhook”-based hi-lo semi-active ACM controller with n≥2 is desirable for realizing improved dynamic responses in a continuous manner with relatively good robustness. A linear controller, on the other hand, would yield undesired oscillations in the acceleration responses.

Figure 4.28 illustrates the influences of control order variations (n=1, 2 and 3) on the transient responses to a rounded pulse excitation with peak displacement of 3.5 cm. The results show trends that are similar to those observed from the frequency response characteristics. The linear order controller (n=1) yields rapid and extreme variations in i_d during both the compression as well as rebound portions of the cycle. The rebound mode damping force thus tends to be considerably higher than those attained for higher order controllers. The higher damping yields lower peak displacement of the sprung mass, while the acceleration response exhibits high amplitude oscillations attributed to the switching discontinuities in i_d. The peak responses to rounded pulse excitation exhibit negligible sensitivity to the order of the controller, with the exception of sprung mass displacement. The higher order controller (n=3), however, exhibits lower rate of decay of the relative displacement and tire force responses. The results again suggest that n=2 offers a good compromise to realize damping variations in a continuous manner.

The transient response measures summarized in Table 4.5 also show little deviation in the peak responses, with the exception of SDR_s. The peak tire force deviation (DTR), sprung mass acceleration (SAR_s), unsprung displacement and acceleration (SDR_u and SAR_u) and relative displacement (RDR) ratios remain insensitive to variations in the controller order. The sprung mass displacement ratio (SDR_s), however, decreases and increases by 35% and 20%, when the order is decreased to 1 or increased to 3, respectively.

Table 4.5: Influence of controller order variations on the transient response measures.

n	SDR_s	SAR_s	SDR_u	SAR_u	RDR	DTR
1	0.85	0.18	1.17	1.92	1.13	0
2	0.71	0.19	1.17	1.92	1.13	0
3	0.46	0.18	1.17	1.92	1.13	0

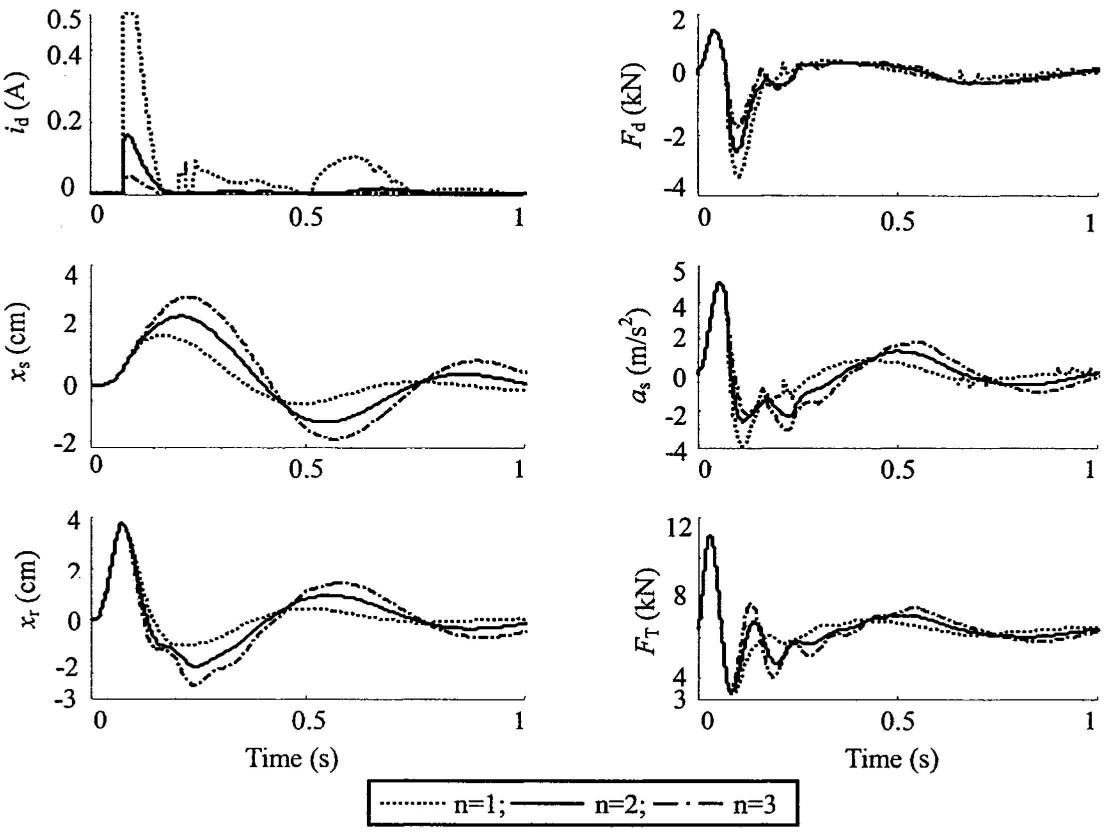

Fig. 4.28: Influence of controller order variations on the transient responses to a rounded pulse excitation (μ=3, a_m=3.5 cm and ω_0=10.4 rad/s).

The influence of variation in the order of the controller is also evaluated from the model responses to random rough road excitation. The analyses are performed for the rough road excitation and vehicle speed of 50 km/h. Figure 4.29 illustrates comparisons of PSD of the model in terms of responses of F_d, a_s, a_u, x_r and F_T together with time variation in i_d for two different controller orders (n=1 and 2). It should be noted that the random response are limited to only two values of the order to ensure clarity of presentation of the results. This controller, however, yields higher damping force only at low frequencies, which is attributed to lower relative velocity response at low frequencies. The PSD's of sprung mass acceleration, relative displacement and tire force responses thus tend to be slightly smaller in the lower frequency range for the low order controller. The responses at frequencies above 2 Hz show negligible effects of the controller order. The results show that the low order controller (n=1) yields considerably higher variation in i_d as observed under deterministic excitations. The unsprung mass acceleration response exhibits insensitivity to the controller order. A comparison of results with the frequency response (T_{au}) in Figure 4.27 may appear to be contradictory. It should be noted that the employed randomly rough road excitation may compromise in sufficient energy in the low frequency response to cause extreme discontinuity in the drive current and thus high magnitude of unsprung mass acceleration in the vicinity of the sprung mass resonance.

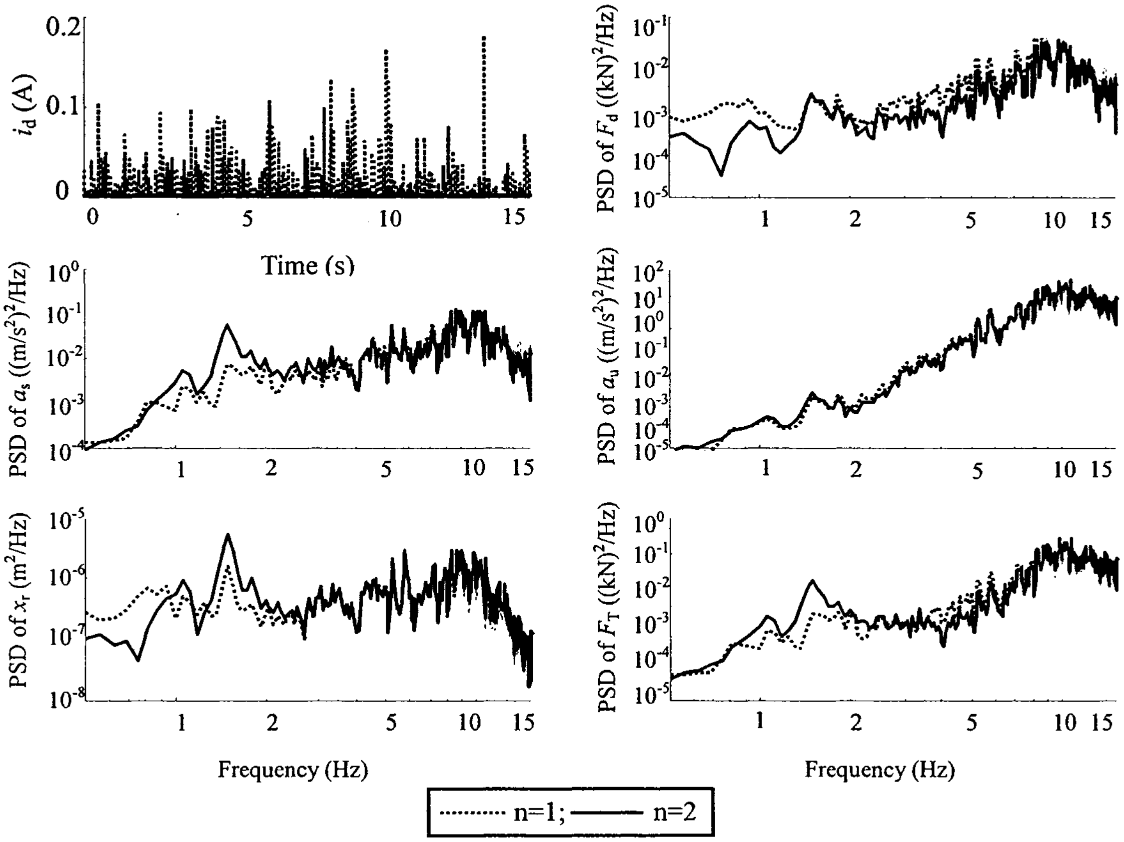

Figure 4.29: Influence of variations in the controller order on the PSD of responses of the "quarter-vehicle" model to rough road excitations.

4.6 Summary

The effects of damping force hysteresis and saturation on the response characteristics of the "quarter-vehicle" model are analyzed under selected excitations. Four different hi-lo algorithms together with the condition functions are formulated to realize damping force variations using different damping force generation schemes and the controller order. The relative response characteristics of the proposed algorithms are evaluated in terms of defined performance measures under harmonic, transient and random excitations. The results show that the proposed "skyhook"-based hi-lo semi-active MR-suspension of the second-order and in the asymmetric mode (ACM) could yield relatively superior dynamic responses to meet the multi-objective suspension performance requirements. The sensitivity of the semi-active suspension performance to variations in operating conditions and controller parameters are further evaluated under harmonic, transient and random excitations. The results of the analyses are summarized below.

- The force hysteresis and saturation nonlinearities of an MR-damper have significant influences on the performance of vehicle suspension with MR-damper. The force saturation in the post-yield at higher velocities could cause strong oscillations in the unsprung mass acceleration response, irrespective of the open- or closed-loop operation of the MR-suspension. The hysteresis property of the MR-damper would invariably yield transient oscillations in the damping force, and sprung and unsprung mass acceleration responses, when the semi-active control scheme is utilized.
- The proposed "skyhook"-based hi-lo semi-active control syntheses involving drive current modulation in response to the sprung mass velocity offers superior vibration attenuation, tire force and rattle space performance, when compared to those of other control synthesis formulated in the study.
- The response oscillations and transients of a controlled MR-suspension, caused by the force hysteresis and saturation nonlinearities of an MR-damper, can be effectively reduced by employing the proposed continuous modulation (CM) and asymmetric

damping force generation (ADFG) functions and by integrating an exponent in the controllers (high controller order).

- The utilization of ADFG in the controller synthesis can help realize asymmetric damping forces in compression and rebound form symmetric MR-damper design.
- The proposed "skyhook"-based hi-lo semi-active MR-suspension in ACM has desirable robust control performance with respect to variations in the operating parameters, such as load, speed and road roughness. Relatively high robustness is also demonstrated for variation in the controller parameters, namely the controller gain and order, under deterministic harmonic and transient excitations, and random road excitations.

The proposed controller is further evaluated through laboratory experiments using the hardware-in-the-loop test simulation technique. The experimental results are used to demonstrate the validity of the controller synthesis in Chapter 7.

CHAPTER 5

PERFORMANCE ANALYSES OF INVERSE MODEL BASED HI-LO SEMI-ACTIVE DAMPING

5.1 Introduction

A number of studies have implemented force tracking control of MR dampers using conventional feedback control techniques, where the drive current is generated in response to the magnitude of the absolute error between the damping force F_d and the target force F_c [12, 80-84]. Such feedback control techniques generally revealed poor force tracking for the semi-active control of MR dampers due to contribution of the absolute error, and presence of hysteresis. As stated in section 3.3.3, some studies have demonstrated strong performance potentials of controller syntheses involving the inverse model to achieve desired force in accordance with defined target functions [65, 78]. The semi-active control scheme in conjunction with a reliable inverse model of the MR-damper can suppress the undesired effects of hysteretic nonlinearity of the MR-damper and thus enhance tracking of the desired force.

An inverse model of the MR-damper was proposed by Xia [65] using neural network technique. However, the proposed scheme concerns only with synthesis of the inverse model uncoupled with controller synthesis. An "inverse model"-based hi-lo semi-active damping control synthesis has been formulated in section 3.4.3. Similar to the drive current formulations of the hi-lo policies, the proposed "inverse model"-based hi-lo semi-active algorithm is also modulated to yield symmetric or asymmetric damping forces using the proposed asymmetric damping force generation (ADFG) algorithm, so as to effectively reduce the effects of current-switching discontinuity.

To eliminate the effects of the hysteresis nonlinearities in MR dampers, the proposed "inverse model"-based hi-lo semi-active control algorithm is formulated to directly yield the drive current in EQS (3.16) and (3.17), based upon the on-off control law [40, 44] and the proposed continuous modulation (CM) and ADFG functions. The proposed "inverse model"-based hi-lo semi-active control scheme suggests that the magnitude of sprung mass acceleration could be reduced by suppressing the damping force, when the damping force (F_d) is in phase with the suspension spring force (F_k). The control condition is to realize $F_d \approx F_k$ using the inverse model of MR-damper, when the condition, $z_c = F_h F_k < 0$ and $i_d = 0$ when $z_c \geq 0$. The merit of the proposed on-off semi-active concept lies in its simpler implementation with measurable relative displacement and velocity. The control structure with the inverse model is shown in Figure 3.5. Based on the advantage of the proposed MR-damper model, as formulated in EQ (2.15), the inverse model can be easily constructed without using any model approximation techniques.

In this chapter, the hysteresis effect reduction and force-tracking property of the proposed "inverse model"-based hi-lo semi-active controller are thoroughly investigated. The analyses are performed for the "quarter-vehicle" model employing both the mean and hysteretic inverse models, as described in section 2.5, under deterministic as well as stochastic excitations at the tire-road interface. The sensitivity of the performance measures to variations in operating conditions, such as speed, excitation magnitude and load, is also investigated. The results illustrate that the proposed "inverse model"-based hi-lo semi-active ACM controller can not only realize the multi-objective performances of ride, road-holding and working space of an intelligent vehicle suspension design, but can also effectively suppress the hysteresis effects of a MR-damper.

5.2 Hysteresis Effects and Force-Tracking Properties

As stated earlier, the proposed "inverse model"-based hi-lo semi-active control algorithm has potentials for eliminating the hyteresis effects of the MR-damper. The hysteresis compensation ability is thus assessed thorough analyses of the "quarter-vehicle" model employing the mean as well as hysteretic damping properties of the MR-damper and the corresponding inverse models. The proposed hysteretic MR-damper model formulated in EQ (2.15) can be easily simplified to yield mean F-v model by letting k_4=0 in EQ (2.12) (i.e. v_h=0). In a similar manner, the proposed hysteretic inverse model of MR-damper formulated in EQ (2.17) can be simplified to its mean inverse model in hyateresis or mean damping mode by letting k_4=0 in EQ (2.12). Moreover, the force-tracking ability of the proposed "inverse model"-based hi-lo semi-active controller is further investigated by considering the pre- and post-yield characteristics of the MR-damper at low and high velocities, as characterized in section 2.2.2. For this purpose, the controller parameters are chosen as: p_c=0, ξ_c=50 for the continuous modulation (CM) function, and p=1 and ξ=10 for the ADFG function in the symmetric damping control (SCM), while p=0 is chosen for the asymmetric control mode (ACM).

The equations of motion for the "quarter-vehicle" model, EQ (3.1), are solved in conjunction with inverse model, EQ (2.17), under harmonic excitations to derive the drive current on the basis of the condition function z_c. The target damping force is derived from the resulting suspension spring force, as proposed in [40, 44]. The hysteresis effects are initially investigated by considering ADFG function in the symmetric mode using p=1 and ξ=10, while harmonic excitation at 1.5 Hz is considered.

Figures 5.1 to 5.3 present the time-histories of dynamic responses in terms of drive current (i_d), relative velocity (v_r), damping force (F_d), hysteron force (F_h) and the target force (F_k) of the "quarter-vehicle" model employing mean as well as hysteresis models. The responses derived using mean damper and mean inverse models are presented in Figure 5.1. The responses derived upon consideration of hysteretic MR-damper model with mean and hysteretic inverse models are presented in Figure 5.2 and 5.3, respectively. The time-histories of responses suggest continuous modulations in drive current and thus the damping and hysteron forces, when mean MR-damper and inverse models are considered (Figure 5.1). The results attained for the hysteretic MR-damper model coupled with mean inverse model exhibit large magnitude transients in the vicinity of $v_r \approx 0$, which is attributed to larger hysteresis near zero velocity and switching. The presence of high magnitude transients in damping force are mostly caused by the mean inverse model. Such transients can be partly suppressed when the hysteretic inverse model is considered, as shown in Figure 5.3. The results thus suggest that the "inverse model"-based upon MR-damping hysteresis could offer considerable advantages in compensating for the effects of hysteretic nonlinearity, and thus improve the force-tracking performance.

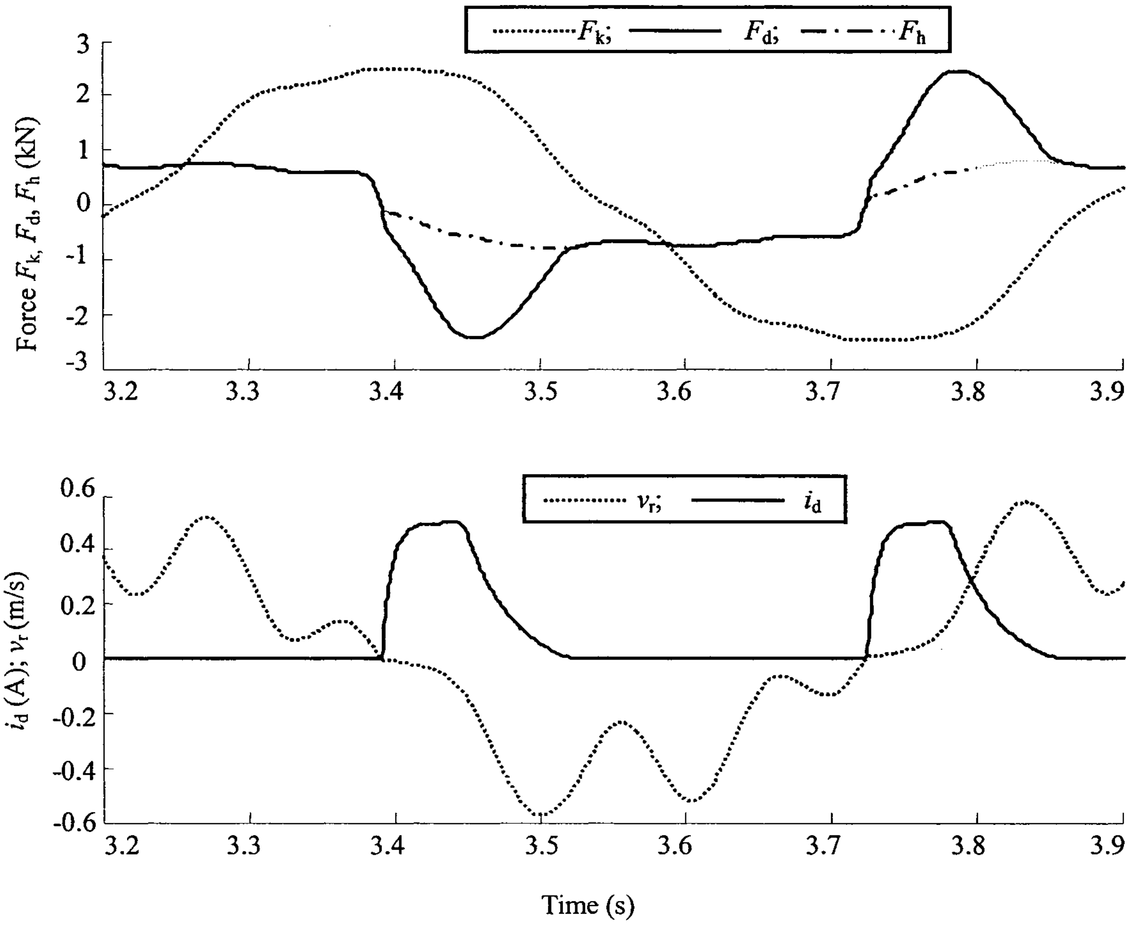

Figure 5.1: Response characteristics of "quarter-vehicle" model employing mean damping and mean "inverse model"-based hi-lo semi-active SCM controller (f=1.5 Hz; a_m=2.5 cm).

The results further show the variations in drive current and force-tracking performance of the proposed synthesis in response to the condition function. The drive current i_d is reduced to zero, when damping force exists ($F_h F_k<0$) to realize the force-tracking $|F_d| \approx |F_k|$. Such variations in i_d are evident in Figures 5.1 to 5.3, irrespective of the models employed. The variations in i_d, however, are continuous in time, when mean models are considered. The results also show relatively poor force-tracking performance, particularly in the pre-yield, when relative velocity is small (e.g. t≈3.4 s in Figure 5.1), although i_d approaches a higher values. Poor force tracking is also evident in Figures 5.2

and 5.3 for the hysteretic model. The magnitude of F_d, however, approaches that of the target force F_k, when relative velocity increases towards force saturation nonlinearity. This, as an example, can be generally observed over $3.45 \leq t \leq 3.52$. It can be concluded that the proposed controller can yield satisfactory forcing-tracking ability only at higher velocities, while the forcing-tracking ability at low velocities is severally limited mostly due to low pre-yield damping forces developed by the MR-damper. The measured characteristics of the MR-damper, presented in section 2.2.2, clearly show that the damping force is relatively insensitive to the drive current in the pre-yield.

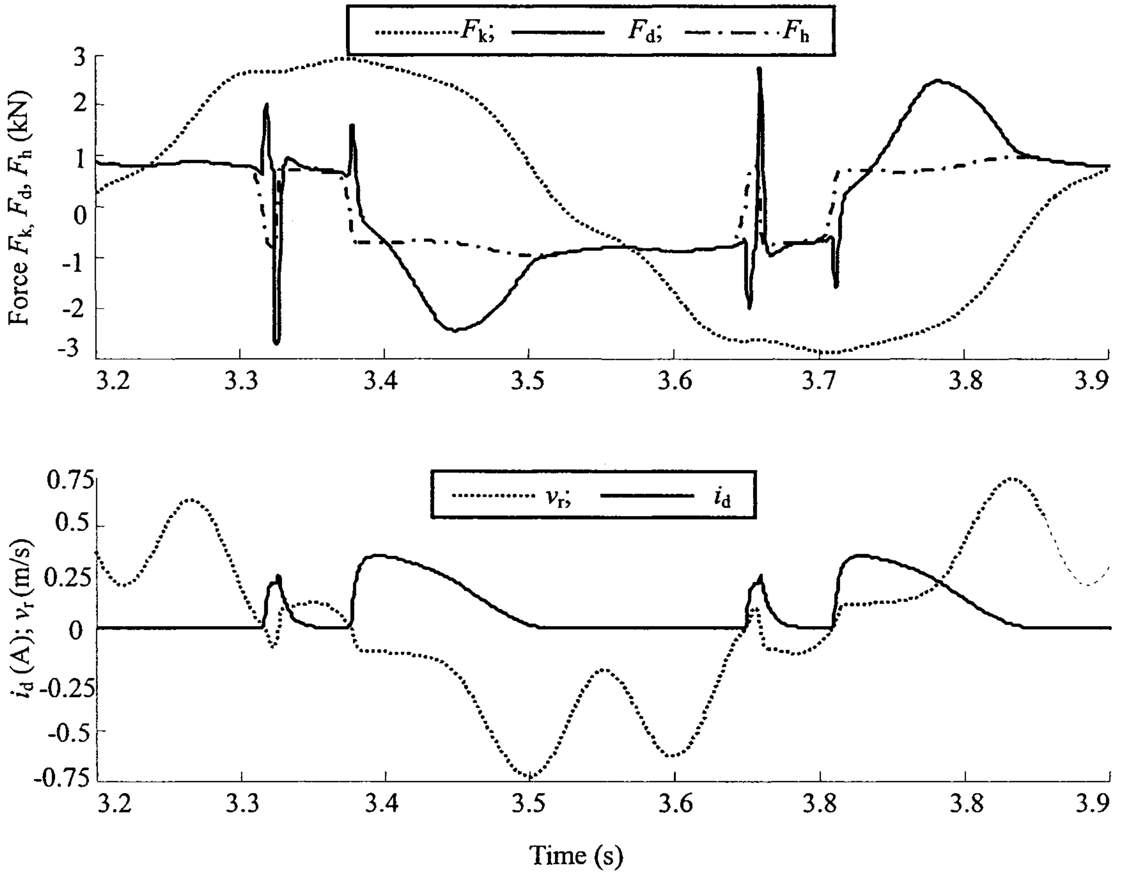

Figure 5.2: Response characteristics of the “quarter-vehicle” model employing hysteretic MR-damper and mean inverse models (f=1.5 Hz; a_m=2.5 cm).

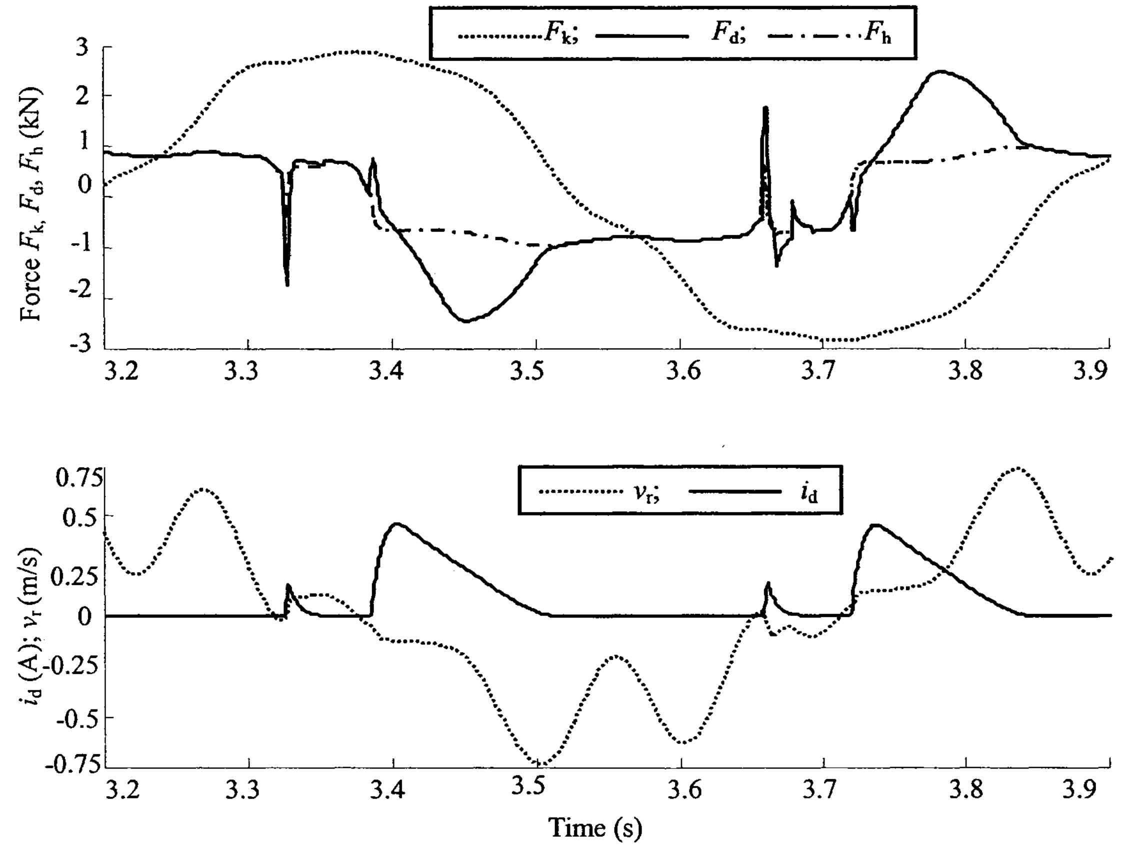

Figure 5.3: Response characteristics of the "quarter-vehicle" model employing hysteretic MR-damper and hysteretic inverse models (f=1.5 Hz; a_m=2.5 cm).

The above analyses, however, clearly show the potential performance benefits of the "inverse model"-based control in suppressing the contribution due to hysteresis effects. Consideration of the mean model of MR-damper would yield superior force-tracking performance of the controller and thus improve suspension performance, which may not be realizable in practice. This is also evident from the results presented in Figure 5.1 to 5.3. The consideration of mean damping and inverse models yields peak steady-state relative velocity in the order of 0.6 m/s, which is considerably smaller than 0.75 m/s attained with hysteretic models. It is also evident that the force-tracking performance in the vicinity of low velocity can be enhanced by increasing the pre-yield damping force through adequate damper design.

The response characteristics of the "quarter-vehicle" model employing hysteretic MR-damper and inverse models are further investigated in the SCM and ACM control to study their relative performance potentials. Figure 5.4 shows the time-histories of selected responses of the "quarter-vehicle" model employing "inverse model"-based hi-lo semi-active damping mode in SCM and ACM, under harmonic excitation at 1.5 Hz. The results suggest that the chosen control parameters could yield asymmetric damping force ratio in the order of 2.5 in the ACM, as observed for the hi-lo control synthesis. The corresponding power consumption is reduced by nearly 50% as observed from variations in i_d in Figure 5.4, when compared to that in the SCM. The lower limits of the non-zero drive current (i_d) in ACM during compression as well as rebound, when compared to those in SCM are attributed to the ADFG smoothing function (ξ=10). It should be noted that the current in the compression mode should be ideally zero for the ACM control.

The results show nonzero current of small peak value (i_d<0.1 A; F_d>0), which is attributed to hysteresis effect. The results also show that asymmetric damping modulation causes slightly higher magnitudes of the sprung mass acceleration (a_s), and lower magnitudes of unsprung mass acceleration (a_u) during the compression cycle, when compared to those observed in SCM. The ACM control, however, helps to suppress the transients slightly better than the SCM control. Moreover, the drive current in ACM leads that in SCM, which is mostly due to slight variations in the associated condition functions. Both SCM and ACM controls tend to excite resonant oscillations of the unsprung mass, even though the excitation frequency is close to the sprung mass resonance. The peak magnitudes of the unsprung mass oscillations, however, are considerably lower with asymmetric damping. The ACM control would thus yield improved road-holding performance of the suspension.

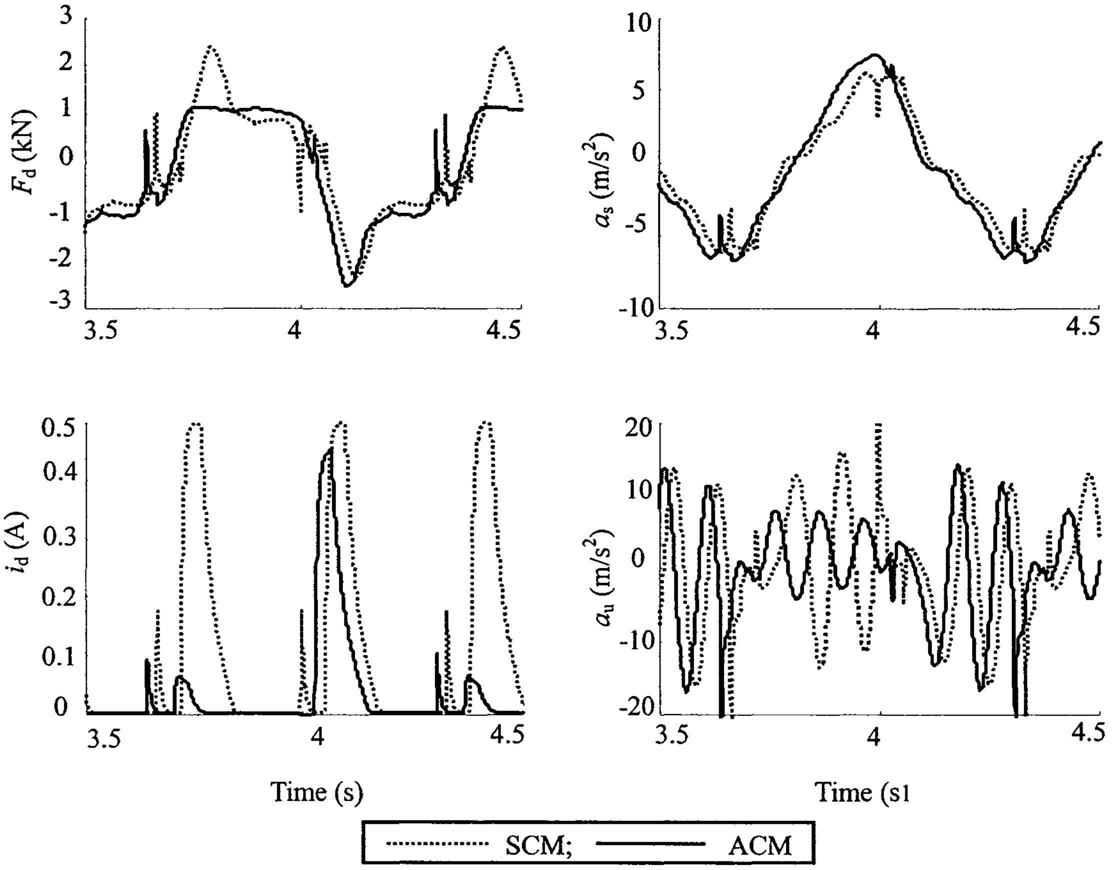

Figure 5.4: Comparisons of dynamic responses of the "quarter-vehicle" model employing "inverse model"-based hi-lo semi-active modulation in damping force in the symmetric as well as asymmetric control modes (SCM and ACM).

Owing to relatively better performance of the "inverse model"-based control employing asymmetric mode damping (ACM), the analyses are performed to study the contributions due to hysteresis for the ACM control. Figure 5.5 shows comparisons of selected dynamic responses (i_d, F_d, a_s and a_u) of the "quarter-vehicle" model employing the "inverse model"-based hi-lo semi-active ACM controller together with mean as well as hysteresis damping and mean inverse models. The results clearly show strong transients due to hysteresis effects, as observed for the SCM control in Figures 5.1 to 5.3. The consideration of hysteretic inverse model yields improved compensation of the hysteresis effects. Although the hysteretic models yield significantly higher peak current in rebound, the corresponding sprung mass acceleration responses for mean as well as hysteretic models are comparable. This is attributed to saturation nonlinearity of the MR-damper.

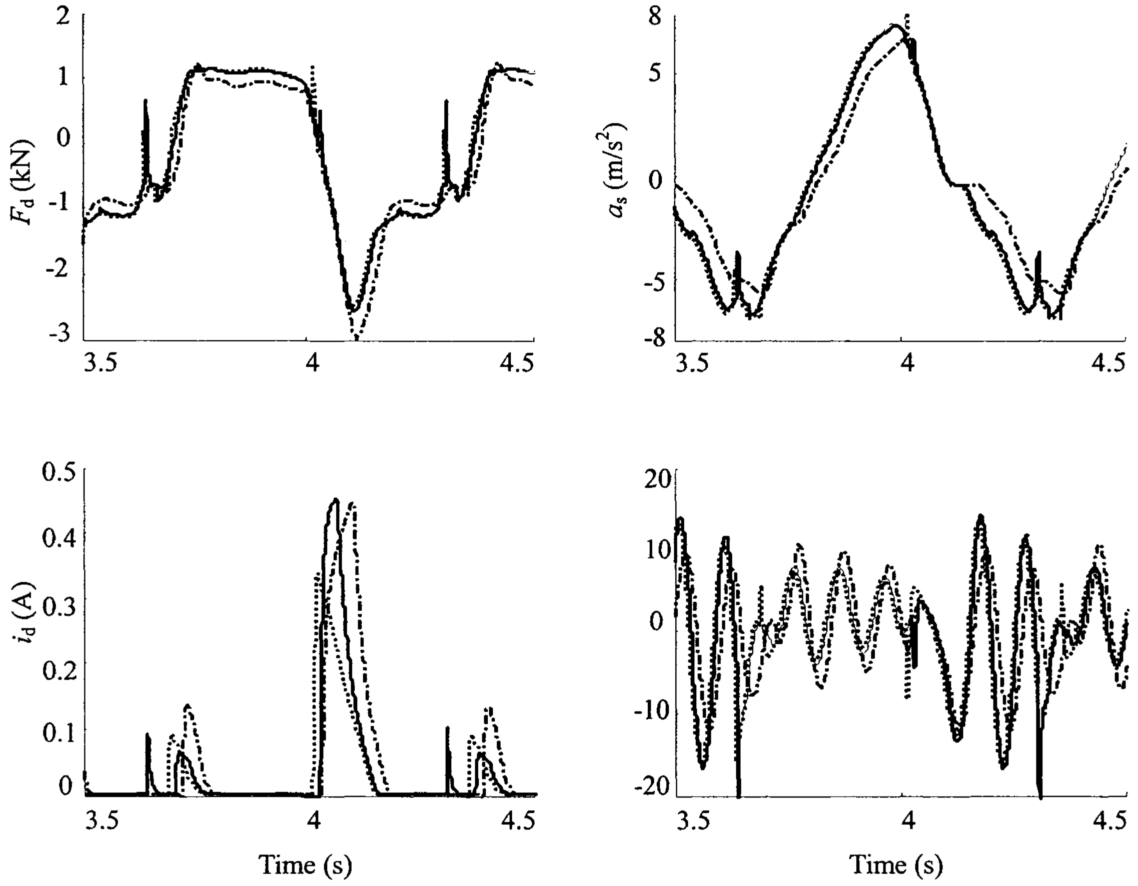

Figure 5.5: Comparisons of dynamic responses of the "quarter-vehicle" model employing the "inverse model"-based hi-lo semi-active ACM controller with mean and hysteresis damping and inverse models (············ mean damping & inverse model; ——— hysteretic damping & inverse model; —·—· hysteretic damping & mean inverse model).

5.3 Enhancement of Force Tracking Property for Inverse Model Based Control

The above results suggest poor force-tracking performance of the proposed "inverse model"-based hi-lo semi-active damping control, which is attributed to low pre-yield damping force of the candidate MR-damper. The force-tracking performance could be enhanced through adequate design of the MR-damper that would yield lager pre-yield damping force at low velocities. The pre-yield damping coefficient of the candidate MR-damper is thus varied by introducing a force gain k_d on the passive hysteron force F_h, which also yields higher post-yield damping force. The influence of the given value on the force-tracking ability and thus the responses are evaluated for the "inverse model" based hi-lo semi-active control in the asymmetric mode. Three different values of the gain (k_d=1, 2 and 2.5) are employed for the analyses, where k_d=1 refers to the nominal damping force properties of the candidate MR-damper considered in this study.

Figure 5.6 illustrates the time-histories of selected responses of the "quarter-vehicle" model employing "inverse model"-based hi-lo semi-active ACM control as a function of the force gain k_d, under 2.5cm harmonic excitation at 1.5Hz. The results show comparisons of the damping force (F_d), drive current (i_d), sprung and unsprung mass accelerations (a_s, a_u), sprung and unsprung mass displacements (x_s, x_u), relative displacement (x_r) and tire force (F_T), attained using the three different values of the force gain. The results suggest a higher force gain yields improved suspension performance in view of a_s, a_u, x_s, x_r and F_T, which can be attributed to improved force-tracking performance. The higher damping force permits reducing the force error between the target spring force and damping force.

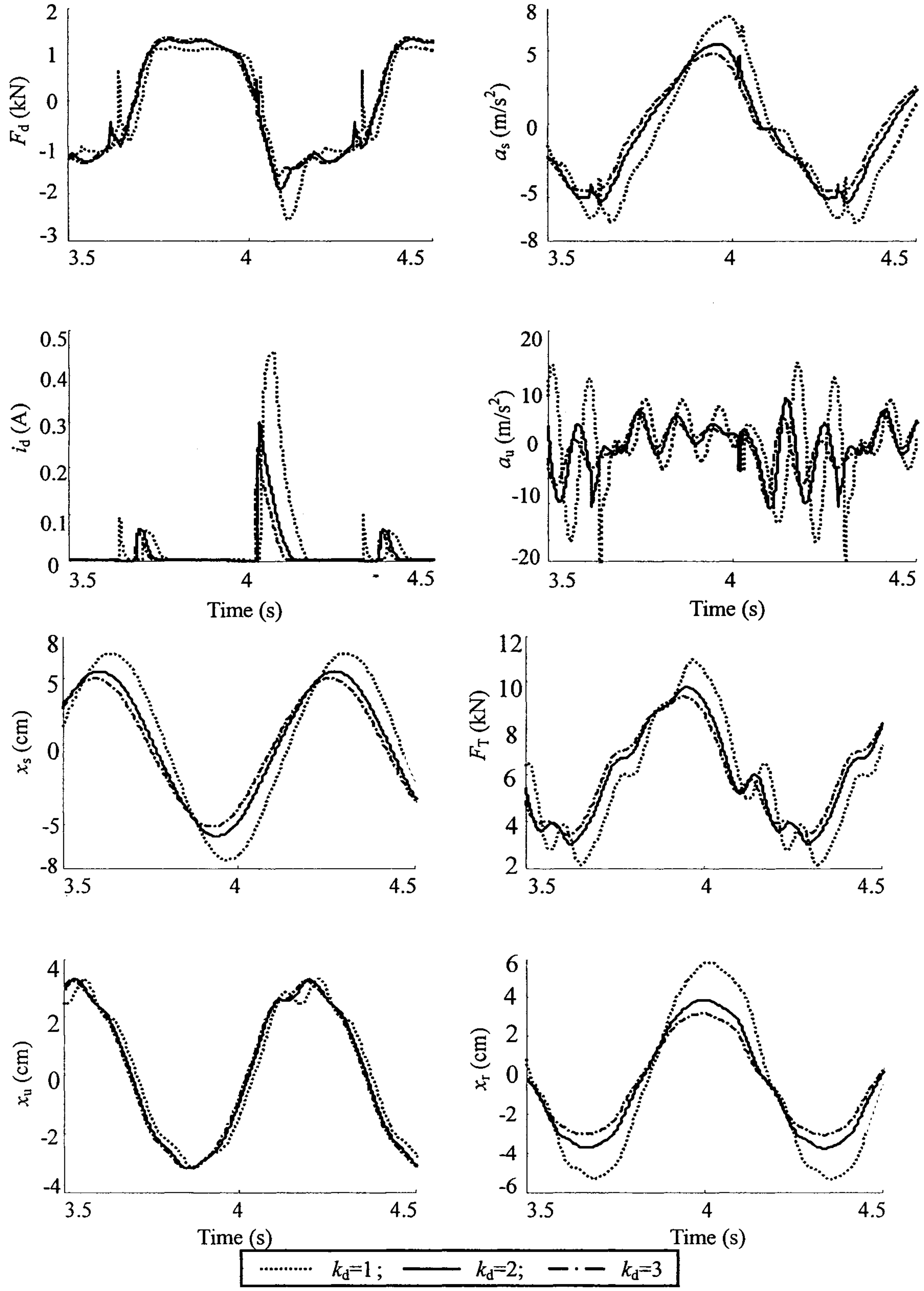

Figure 5.6: Comparisons of responses of the "inverse model"-based hi-lo damping scheme with different force gains (f=1.5 Hz; a_m=2.5 cm).

The results from Figure 5.6 further show that the magnitude of drive current (i_d) in compression and rebound decreases with increasing value of k_d, due to larger passive damping, while the resulting damping force increases only slightly in compression, and thus improved force-tracking property of the controller. Moreover, high passive damping force due to MR-damper tends to suppress the transient effects of hysteresis and switching more effectively.

The influence of force gain is further investigated on the frequency response characteristics of the "quarter-vehicle" model with "inverse model"-based hi-lo semi-active damping in ACM. The response characteristics are evaluated under varying amplitude of harmonic excitations in the 0.5 to 15 Hz frequency range, as described in section 3.6, while the force gain is varied form 1 to 2.5. The frequency response presented in terms of sprung and unsprung mass acceleration transmissibility (T_{as}, T_{au}), relative displacement transmissibility (T_{dr}) and DLC due to tire force are presented in Figure 5.7. The peak acceleration and relative displacement transmissibility decrease significantly with higher force gain, while the sprung mass acceleration response increases in the mid-ride frequencies region. The most significant performance gain due to high damping force is evident in the unsprung mass acceleration response, while DLC due to tire force increases slightly in the 1.5 to 7.5 frequency range. On the basis of the results presented in Figures 5.1 to 5.7, it is suggested that an alternate damper design would be desirable to achieve improved force-tracking performance. Subsequent response analyses are thus performed assuming the force gain of 2.5.

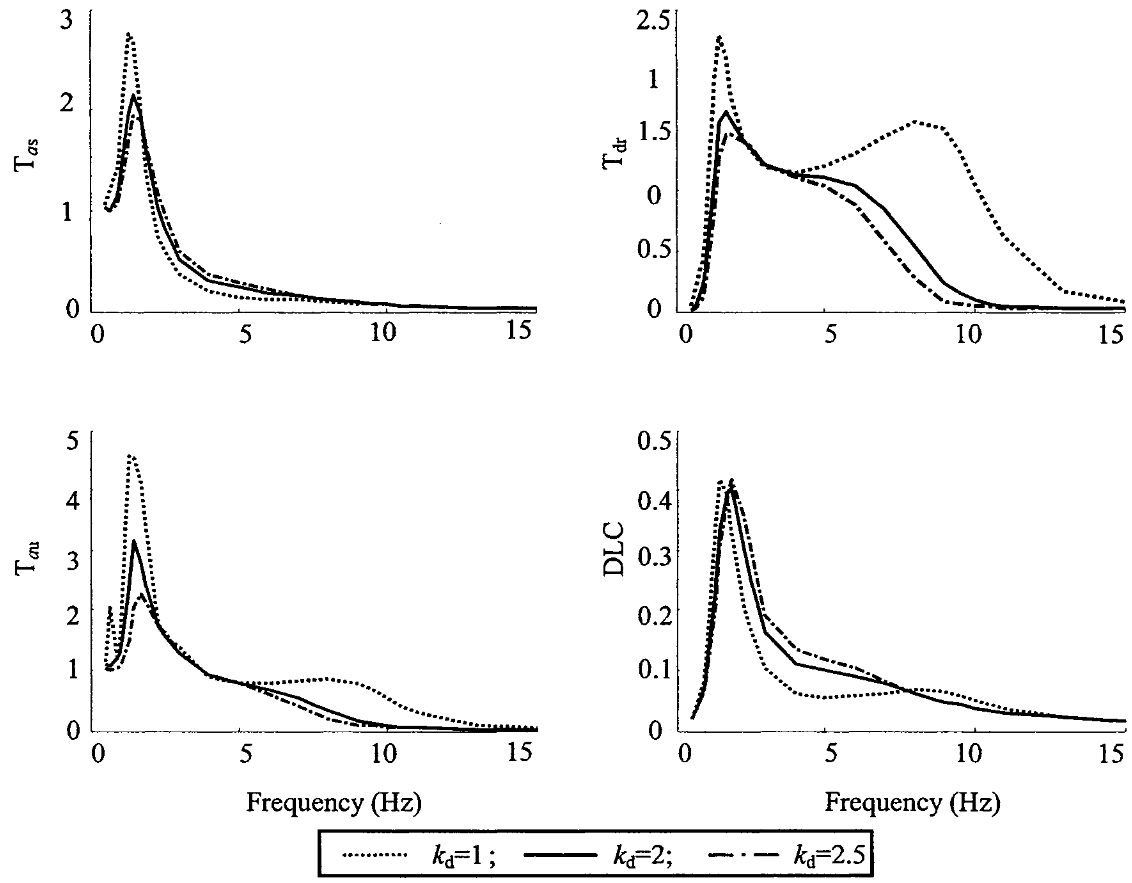

Figure 5.7: Comparisons of frequency response characteristics of the "quarter-vehicle" model employing "inverse model"-based hi-lo damping modulation scheme (ACM) and different force gains.

5.4 Response Analyses

The response characteristics of the proposed "inverse model"-based hi-lo semi-active ACM damping with force gain of 2.5 are evaluated under harmonic, transient and random excitations. The responses are compared with those attained for two different passive damping modes (i_d=0 and 0.1 A) for the candidate MR-damper, to demonstrate the relative performance gains of the proposed "inverse model"-based hi-lo semi-active controller.

Response to Harmonic Excitations

Figure 5.8 presents comparisons of time-histories of dynamic responses of the asymmetric "inverse model"-based hi-lo semi-active and the passive damping modes, under a 2.5 cm harmonic excitation at a frequency of 1.5 Hz.

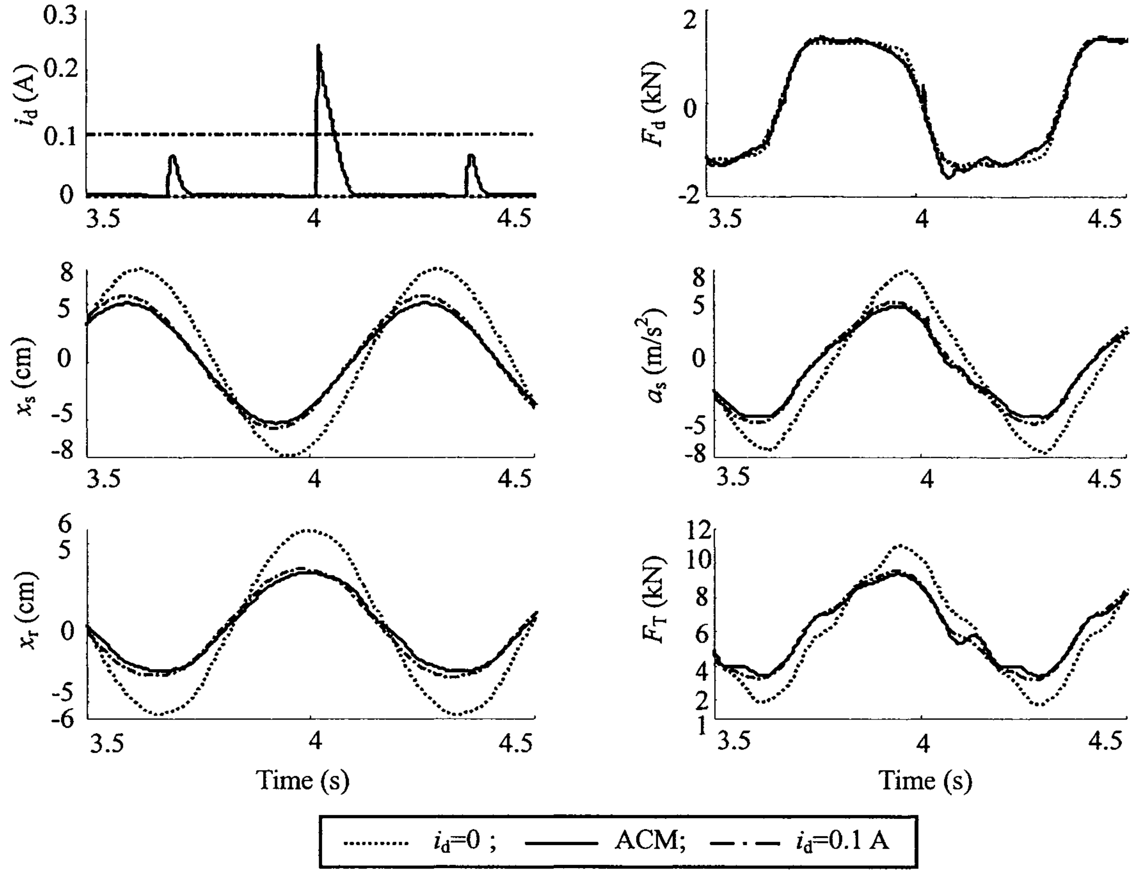

Figure 5.8: Comparisons of time-histories of responses of "quarter-vehicle" model with passive (i_d=0; i_d=0.1 A) and "inverse model"-based hi-lo semi-active ACM damping (a_m=2.5 cm; f=1.5 Hz).

The results show that the semi-active ACM damping mode effectively reduces the peak magnitudes of x_s, a_s, x_r, and F_T, when compared to those attained under light and higher passive damping modes (i_d=0 and 0.1 A). The results suggest that a higher damping force is desirable for limiting resonant responses. The responses of the "inverse model"-based hi-lo semi-active ACM damping show current modulation is well below 0.1 A in the compression cycle, while the current approaches 0.35 A in the rebound mode to generate high rebound damping force.

Figure 5.9 further presents comparisons of the frequency response characteristics of the asymmetric "inverse model"-based hi-lo semi-active damping with those attained for the passive damping modes, under varying displacement amplitude harmonic excitations in the 0.5 to 15 Hz range.

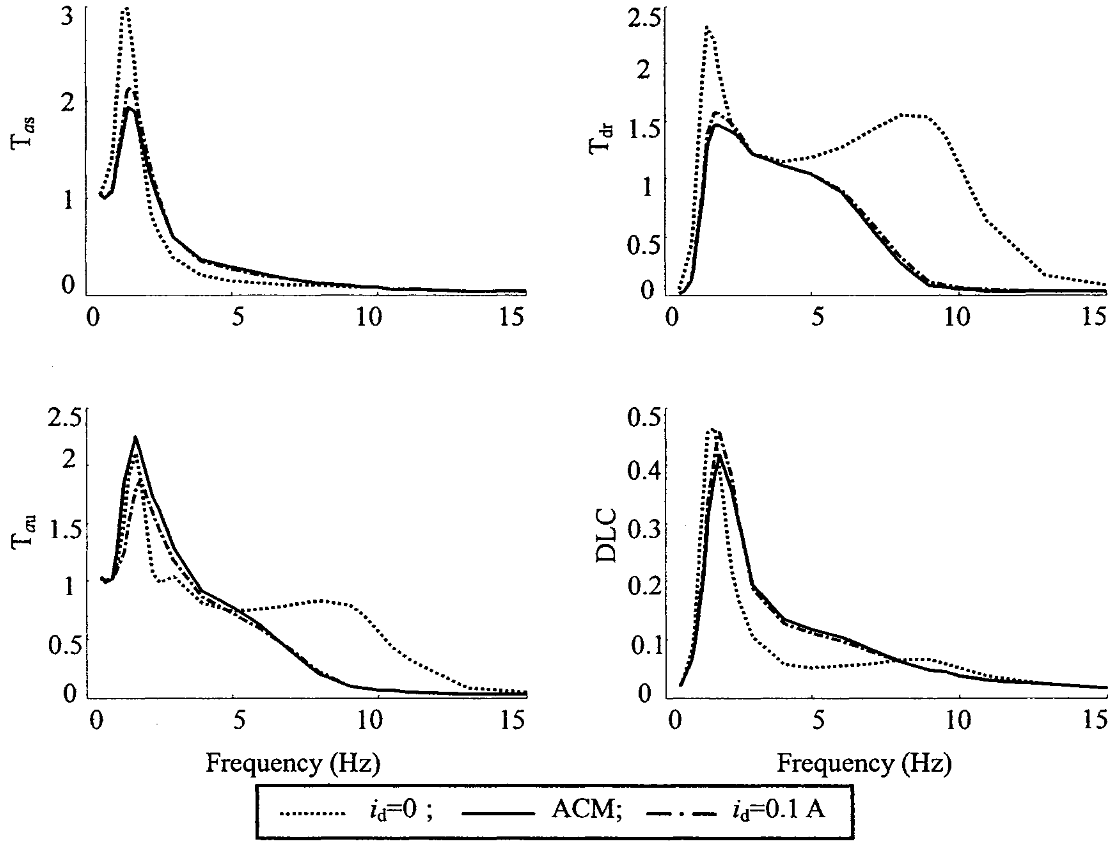

Figure 5.9: Comparisons of frequency responses of the "quarter-vehicle" model with passive (i_d=0; i_d=0.1 A) and "inverse model"-based hi-lo semi-active ACM damping.

The results show that both the passive damping modes yield higher resonant magnitudes of T_{as}, T_{dr} and DLC. Light passive mode damping yields significantly higher unsprung mass acceleration near the unsprung mass resonance but slightly lower response near the sprung mass resonance. The "inverse model"-based hi-lo semi-active damping yields improved resonance control but slightly higher transmission in the important ride frequencies. The suspension rattle space requirements, however, could be considerably reduced with the proposed "inverse model"-based force-tracking algorithm. The proposed semi-active control can thus be considered to offer better compromise between the conflicting performance requirements.

Responses to Rounded Pulse Excitations

The relative transient response characteristics of the passive and "inverse model"-based hi-lo semi-active ACM damping properties are further evaluated under a rounded pulse excitation (μ=3, ω_0=10.4 rad/s and a_m=5 cm). Figure 5.10 illustrates comparisons of the transient responses in terms of i_d, F_d, x_s, a_s, x_r and F_T. The "inverse model"-based hi-lo semi-active ACM and higher passive damping (i_d=0.1 A) yield rapid rate of decay and effectively reduce the peak amplitudes of x_s and x_r. Light passive damping (i_d=0), on the other hand, yields lower peak value of a_s, but higher peak values of x_s and considerably lower rate of decay. By further comparing the results with those for the "skyhook"-based hi-lo damping analyses presented in Figure 4.10, it is found that the "inverse model"-based hi-lo semi-active controller yields larger peak magnitude of a_s in compression than the "skyhook"-based hi-lo semi-active controller, due to the higher force gain used in the "inverse model"-based hi-lo damping synthesis. Oscillations are in the drive current and thus the damping force and sprung mass acceleration responses of the inverse model controller are observed as the relative displacement or target force diminishes. The drive current exceeds 0.1 A only for short durations in rebound, while the semi-active damping force is comparable with the passive force corresponding to 0.1 A for the excitation considered. The semi-active damping variations, however, cause slightly high rate of decay, as observed from the responses in terms of a_s, x_s, x_r and F_T. Owing to the intermittent current caused by the semi-active damper, the proposed controller would require considerably lower power.

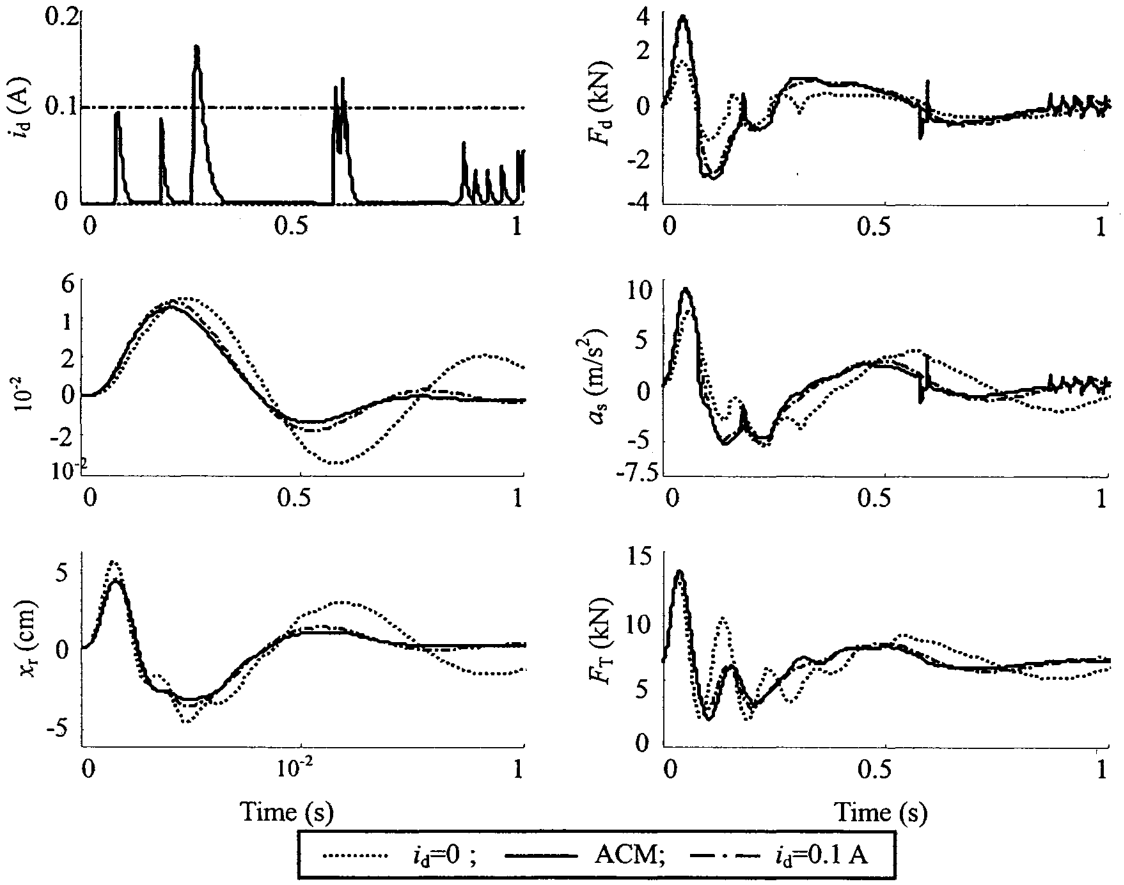

Figure 5.10: Comparisons of transient response characteristics of "quarter-vehicle" model with passive (i_d=0; i_d=0.1 A) and "inverse model"-based semi-active ACM damping.

Responses to Random Road Excitations

The proposed "inverse model"-based hi-lo semi-active ACM damping variation is further evaluated under the randomly distributed rough road excitation, assuming constant forward speed of 50 km/h, as shown in Figure 3.10(b). The response characteristics are evaluated in terms of power spectral density (PSD) of selected responses described in section 3.6. Figure 5.11 shows the comparisons of PSD of responses of F_d, a_s, a_u, x_r and F_T, and time variations in i_d of the "quarter-vehicle" model with the low passive (i_d=0) and "inverse model"-based hi-lo semi-active ACM damping modes. The results show that the "inverse model"-based hi-lo damping controller yields significantly higher damping force than the low passive mode damping (i_d=0) in the entire frequency range. This is attributed to the passive damping force gain used in the "inverse model"-based hi-lo damping formulation.

The resulting high damping force tends to suppress the sprung mass acceleration near the resonant frequency but causes considerably higher acceleration responses in the ride frequency range. From the result, it is concluded that high damping force gain is essential to achieve improved force-tracking ability, while the suspension performance deteriorates. The results illustrate that the proposed "inverse model"-based hi-lo semi-active controller offers superior performance for control of resonant vibration of sprung mass. The vibration attenuation and road-holding performances in the ride frequency range (2-7 Hz), however, show poor performance when compared to that of the fixed low passive damping MR-suspension, as evident form the PSD responses of a_s and F_T. The suspension travel and unsprung mass acceleration responses for the semi-active damping, however, are comparable with the fixed low passive damping in the ride frequency range. This is due to the higher passive hysteron force (k_d=2.5) property for the chosen

MR-damper in the semi-active controller synthesis. The DLC value due to dynamic tire force of the semi-active ACM damping mode is in the order of 0.113, which is slightly lower than 0.139 due to that with the fixed low passive damping mode.

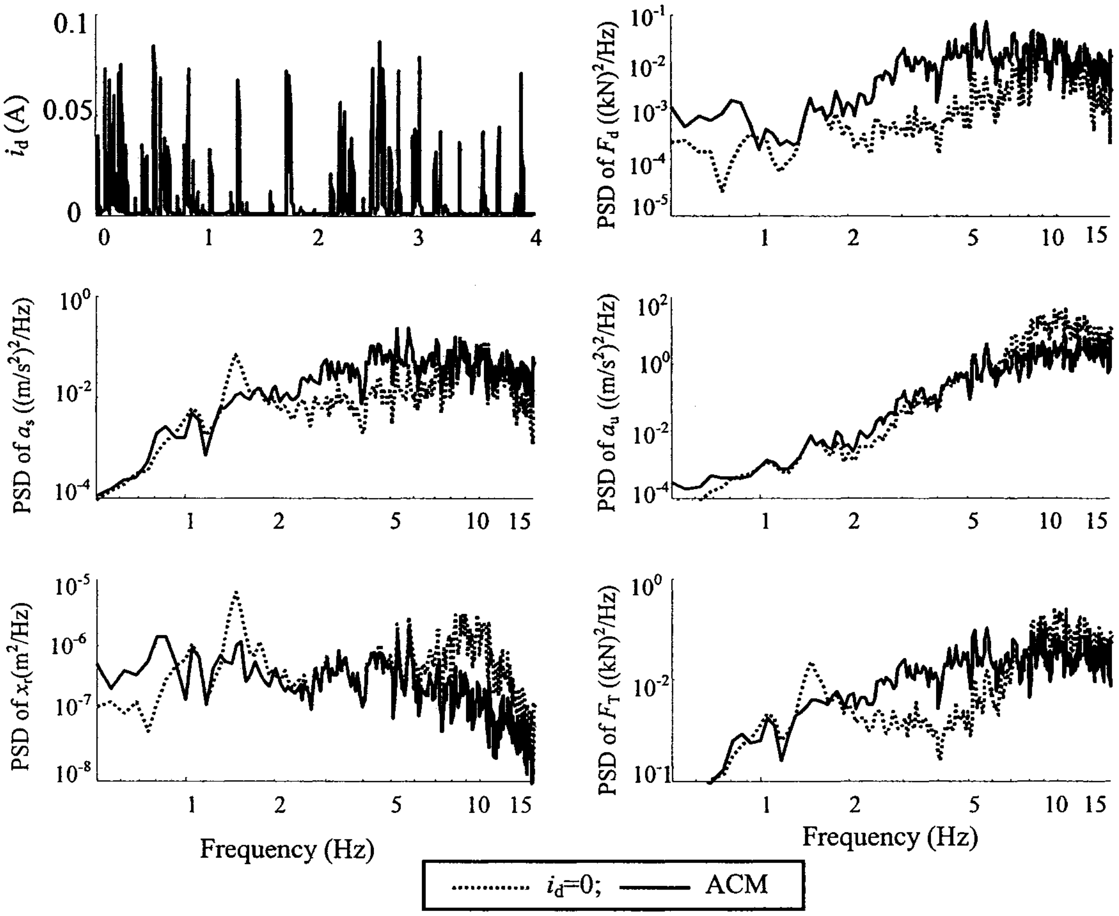

Figure 5.11: Comparisons of PSD of responses of the MR-suspension with the proposed "inverse model"-based hi-lo semi-active controller and passive damping under random excitations (V=50 km/h).

The above analysis results illustrate that the proposed "inverse mode"-based hi-lo semi-active ACM damping mode could achieve superior dynamic response and multi-objective suspension performances than the low or higher passive MR-damping modes.

5.5 Influence of Variations in Operating Parameters

The force-tracking and performance characteristics of the "quarter-vehicle" model with "inverse model"-based hi-lo damping in ACM are evaluated considering variations in operating load (m_s), forward speed (V) and road roughness. A controller synthesis should exhibit adequate robustness over a range of operating speed, load and excitation conditions. The results attained from the analyses are used to examine the robustness of the proposed "inverse model"-based hi-lo semi-active ACM damping formulation. The influences of variations in operating parameters on selected response measures are evaluated under harmonic, transient and stochastic excitations, while a constant force gain of 2.5 is employed to realize satisfactory force-tracking performance. For the analyses, the controller parameters are chosen as: p_c=0, ξ_c=50, p=0, and ξ=10 for the continuous modulation (CM) and ADFG functions.

5.5.1 Variations in operating mass

The influence of variations in operating load is by ±25% of the nominal value of 563 kg. Figure 5.12 illustrates the influence of sprung mass variations on the responses of the "inverse model"-based hi-lo semi-active ACM controller, under 2.5 cm excitation at 1.5 Hz. The responses are considered to describe the resonant behaviour of the system. The variations in the sprung mass cause variations in natural frequency and responses. The resulting variations in the spring and hysteron forces yield changes in the condition function, which causes the drive current switching at different instants. A lower sprung mass yields higher natural frequency and lower spring force magnitude that serves as the target force. Consequently, the damping force magnitude tends to be lower, when compared to that for the nominal mass. The magnitude of the damping force tends to increase with increasing sprung mass. The sprung mass displacement and acceleration amplitudes thus remain comparable to those attained with the nominal mass. The response magnitudes, however, decrease when sprung mass is lowered due to shift in the natural frequency. The relative displacement and tire force increase with increasing sprung mass due to higher tire deflections.

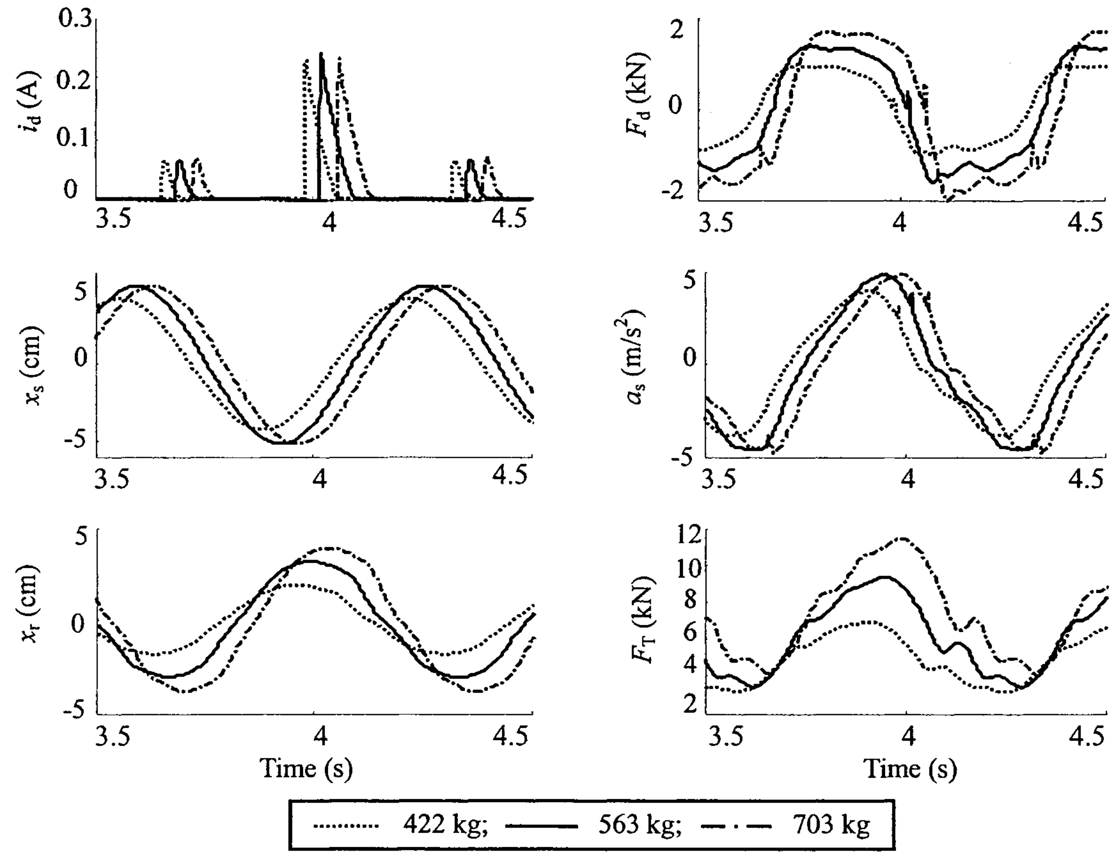

Figure 5.12: Influence of sprung mass variations on the time-histories of harmonic responses of the “inverse model”-based hi-lo semi-active ACM damping controller.

The influence of variations in m_s is also presented on the frequency response characteristics of the “quarter-vehicle” model employing the proposed semi-active ACM synthesis, as shown in Figure 5.13. An increase in the sprung mass yields lower resonant frequency of the sprung mass. The peak magnitude of T_{as}, however, varies only slightly due to higher damping force generated in response to higher spring force, as observed in Figure 5.12. Owing to lower resonant frequency, the acceleration response in the ride frequency range tends to be lower for the higher mass. Same trends are also evident in the unsprung mass acceleration, relative displacement and DLC responses.

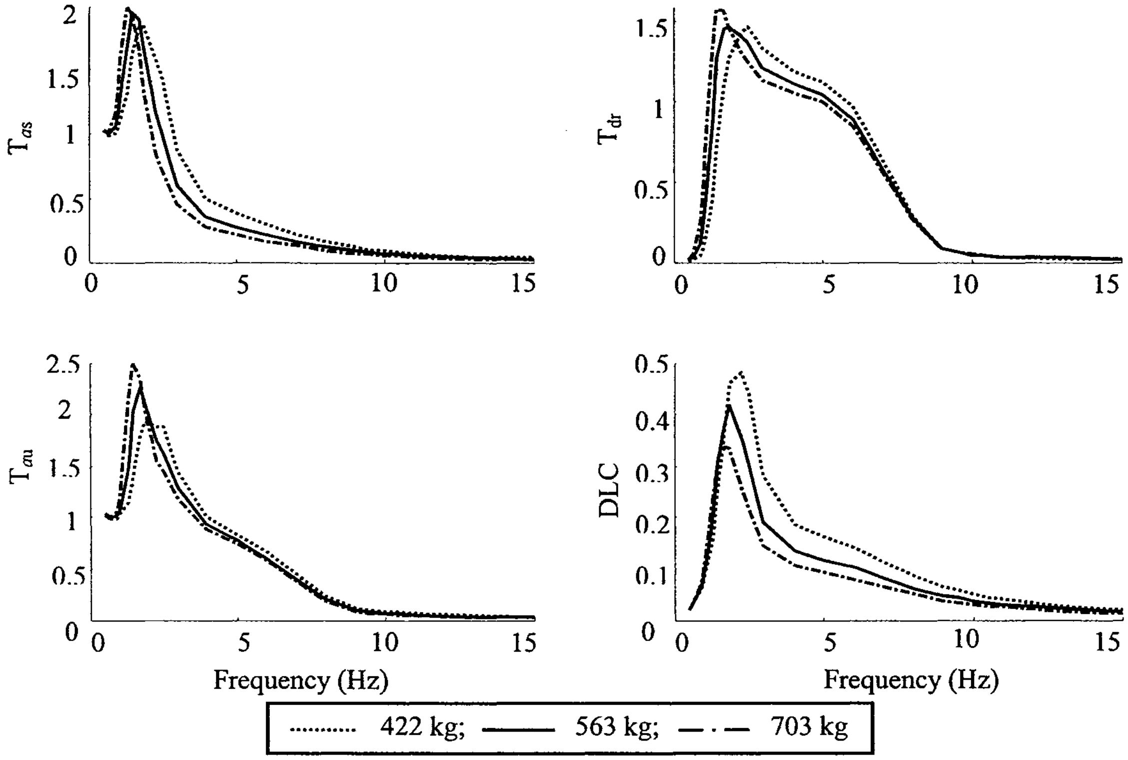

Figure 5.13: Influence of sprung mass variations on the frequency response characteristics of the "inverse model"-based hi-lo semi-active ACM damping controller.

The results from Figure 5.13 further shows that the peak resonant magnitudes of T_{as} and T_{dr} remain insensitive to the sprung mass variations, while the peak magnitudes of T_{au} and DLC around the sprung mass natural frequency increase slightly with increasing m_s. The responses in the vicinity of the unsprung mass resonance, however, remain insensitive to variations in m_s, with the exception of DLC, which exhibits significant variations due to changes in m_s. Owing to its definition, the DLC increases with decreasing vehicle weight. The responses to harmonic excitations, shown in Figures 5.12 and 5.13, generally suggest high robustness of the proposed "inverse model"-based hi-lo semi-active ACM damping synthesis to variations in the sprung mass.

The influences of sprung mass variations on the transient responses to a rounded pulse excitation (μ=3, ω_0=10.4 rad/s and a_m=3.5 cm) are illustrated in Figure 5.14. The influences of sprung mass variations on the transient responses are similar to those observed for the "skyhook"-based hi-lo semi-active controller presented in Figure 4.14. The results suggest that the "inverse model"-based damping control remain relatively insensitive to the sprung mass variations, particularly during the duration of the shock pulse. This, trend, however, was not evident in the "skyhook"-based hi-lo control, which revealed extreme variations in the drive current with varying sprung mass. The magnitudes of sprung mass displacement and acceleration decrease with increasing sprung mass, and reveal high sensitivity to sprung mass variations. The relative displacement response also exhibits only slight sensitivity to sprung mass, while the tire force exhibits bias, as observed for the "skyhook"-based hi-lo control.

The transient response measures for the sprung mass variations are also summarized in Table 5.1. The results show only slight influences of sprung mass variations on the deviations in the peak tire force, unsprung mass responses (SDR_u and SAR_u), and relative displacement ratio (RDR). The peak force deviations (DTR) decreases and increases by

18% and 14%, when the sprung mass is decreased and increased by 25%, respectively. The sprung mass shock displacement ratio (SDR$_s$) and acceleration ratio (SAR$_s$) increase with decreasing sprung mass. The SDR$_s$ increases and decreases by 13% and 9.9%, while the sprung mass acceleration ratio (SAR$_s$) increases and decreases by 32% and 12%, when m_s is decreased and increased by 25%, respectively.

Table 5.1: Influence of sprung masses variations on the transient response measures.

m_s (kg)	**SDR$_s$**	**SAR$_s$**	**SDR$_u$**	**SAR$_u$**	**RDR**	**DTR**
422	1.03	0.33	1.16	1.24	0.86	0.18
563	0.91	0.25	1.14	1.24	0.86	0
703	0.82	0.20	1.14	1.24	0.86	0.14

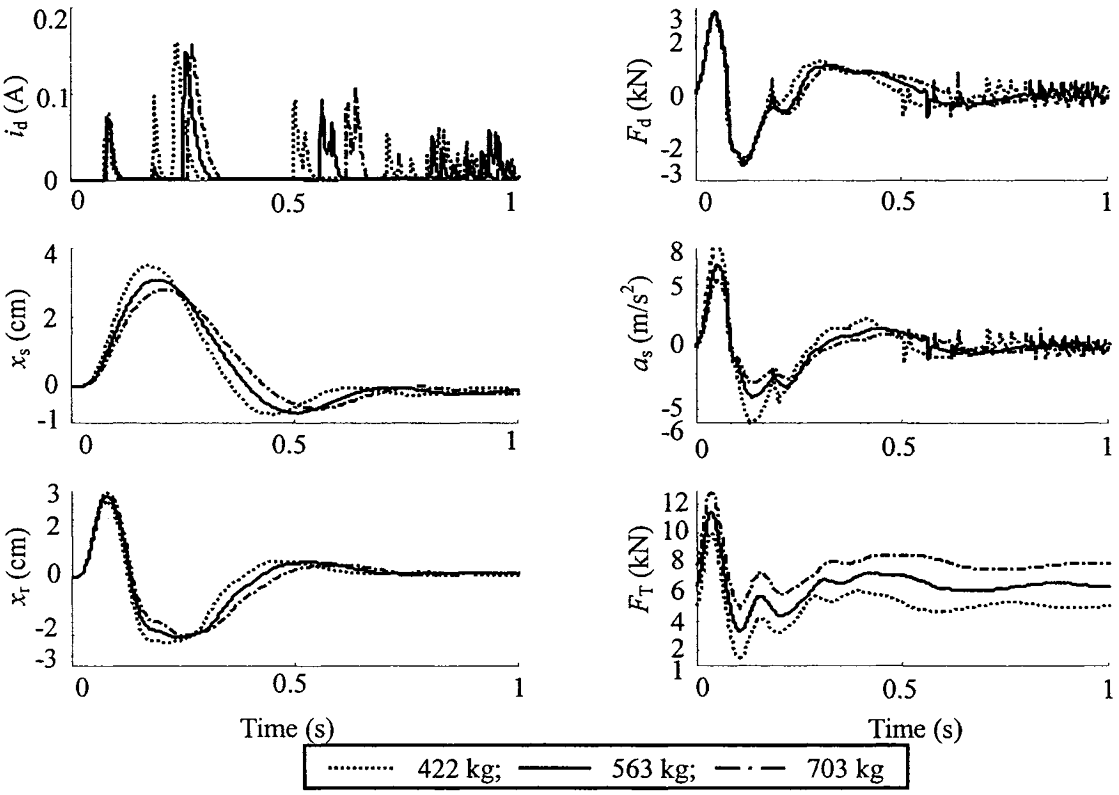

Figure 5.14: Influence of sprung mass variations on the transient responses to a rounded pulse excitation.

Figure 5.15 illustrates the influence of variations in m_s on the response characteristics of the "quarter-vehicle" model employing the proposed semi-active ACM synthesis, under excitations arising from a rough road. Figure illustrates comparisons of PSD of F_d, a_s, a_u, x_r and F_T responses due to two extreme sprung masses (422 and 703 kg). Figure also illustrates time variations in drive current, which tend to vary considerably but do not exceed 0.1 A for both masses. The influence of sprung mass variations on the responses are similar to those obtained using the "skyhook"-based hi-lo semi-active controller, shown in Figure 4.15.The magnitudes of PSD of a_u, however, are considerably lower than those deduced for the "skyhook"-based hi-lo semi-active controller, which is attributed to high force gain used in the inverse model-based hi-lo semi-active controller.

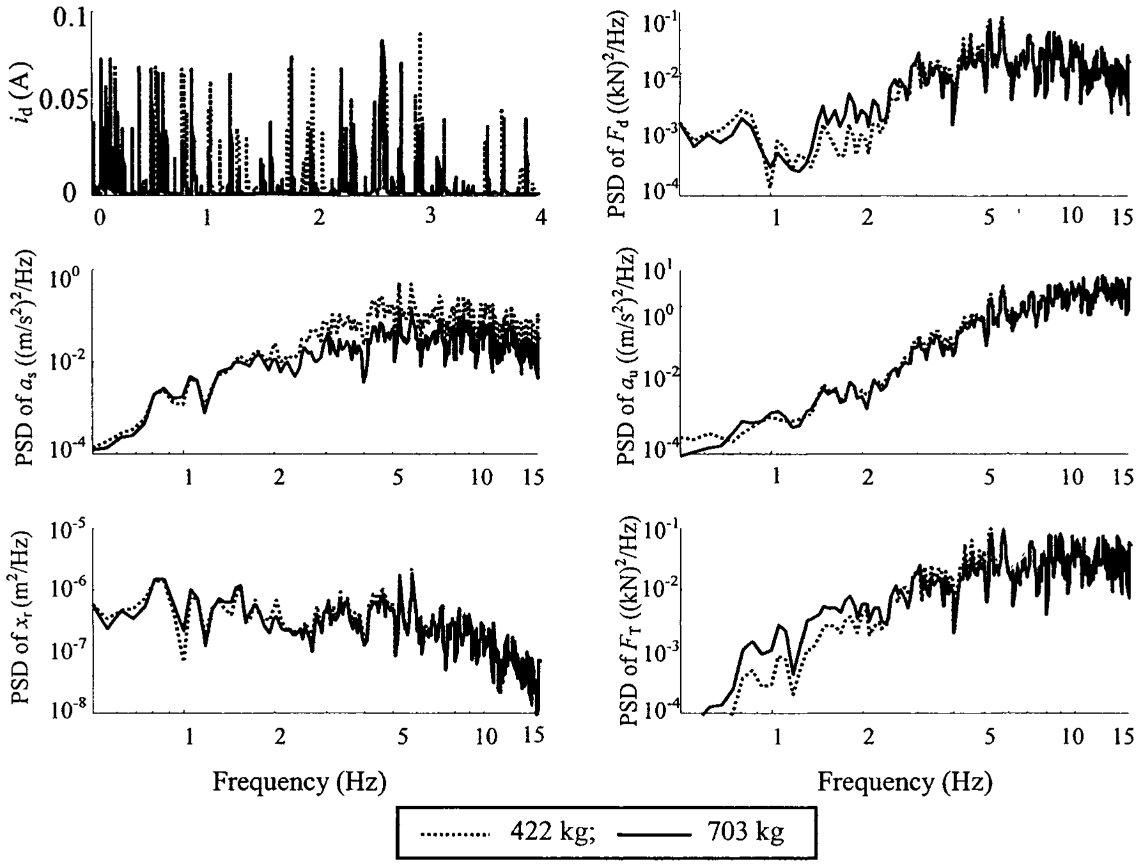

Figure 5.15: Influence of sprung mass variations on the PSD characteristics of responses to a rough random excitation.

Figure 5.15 further illustrates that the unsprung mass acceleration and relative displacement responses exhibit relatively small sensitivity to sprung mass variations, as observed under harmonic and transient excitations. The sprung mass acceleration response, however, increases with decreasing mass at higher frequencies. This is attributed to high damping force developed by the "inverse model"-based hi-lo control. The DLC due to tire force increases from 0.091 to 0.147 for the "inverse model"-based hi-lo semi-active damping, when m_s is increased from 422 to 703 kg. The corresponding increase "skyhook"-based hi-lo semi-active damping was observed from 0.114 to 0.176.

5.5.2 Variations in operating speed

The influence of vehicle speed on the response measures is investigated by considering two different speeds, 50 and 100 km/h. Figure 5.16 illustrates the influence of speed on the responses to the rounded pulse excitation. The vehicle speed shows significant influences on all the responses, as observed from the responses of the "skyhook"-based hi-lo semi-active damping control, shown in Figure 4.16. Operation at a higher speed (V=100 km/h) results in higher demand on the damping force, and yields higher peak acceleration but lower sprung mass displacement. Higher damping force yields relatively faster decay in absolute and relative displacement responses, while it causes oscillations in the damping force and sprung mass acceleration. Similar trends were also observed with the "skyhook"-based hi-lo semi-active damping control. The tire force also exhibits higher magnitude oscillations under higher speed, while the magnitudes are significantly smaller when compared to those obtained with the "skyhook"-based hi-lo control. This is attributed to considerably higher damping force of the inverse model control.

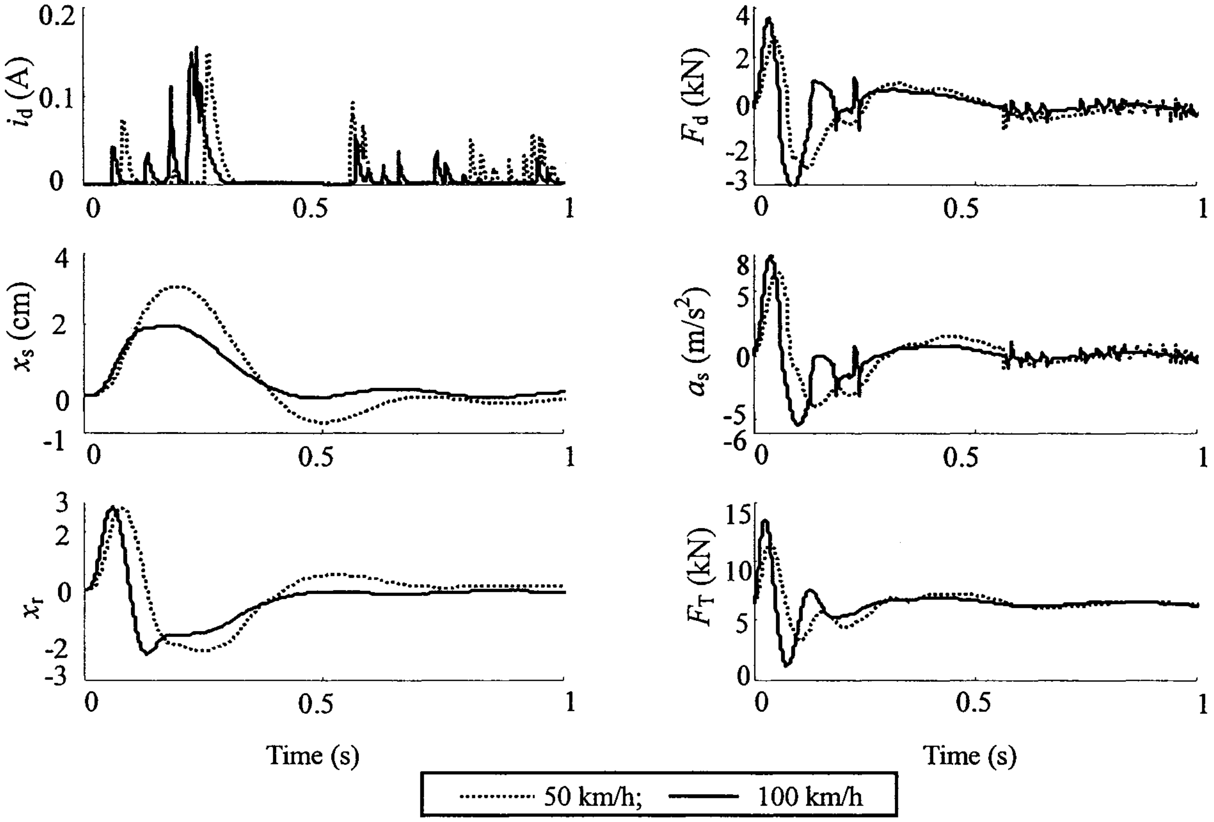

Figure 5.16: Influence of vehicle speed variations on the transient responses to a rounded pulse excitation (μ=3, ω_0=10.4 rad/s and a_m=3.5 cm).

Table 5.2 summarizes the influence of speed on the transient response measures. The results show relatively larger deviation in the peak tire force (DTR). The peak force deviation (DTR) increases in the order of 37%, when vehicle speed is increased by 100%, which is the extreme case when vehicle passes over a rounded pulse shock profile at such a high speed. The results also show that the unsprung mass and relative displacement ratios (SDR_u and RDR) remain insensitive to variations in speed. The sprung mass displacement and acceleration ratios (SDR_s and SAR_s) and the unsprung mass acceleration ratio (SAR_u) decrease by 42%, 76% and 54%, respectively, when speed is increased from

50 to 100 km/h.

Table 5.2: Influence of vehicle speed variations on the transient response measures.

V (km/h)	$\mathrm{SDR_s}$	$\mathrm{SAR_s}$	$\mathrm{SDR_u}$	$\mathrm{SAR_u}$	RDR	DTR
50	0.91	0.25	1.14	1.24	0.86	0
100	0.57	0.06	1.13	0.48	0.86	0.37

The influences of operating speed variations on the stochastic response characteristics are evaluated for the "quarter-vehicle" model employing the proposed inverse model-based hi-lo semi-active ACM synthesis. Figure 5.17 illustrates the comparisons of PSD of F_d, a_s, a_u, x_r and F_T and time variations in i_d, attained for the two operating speeds considered.

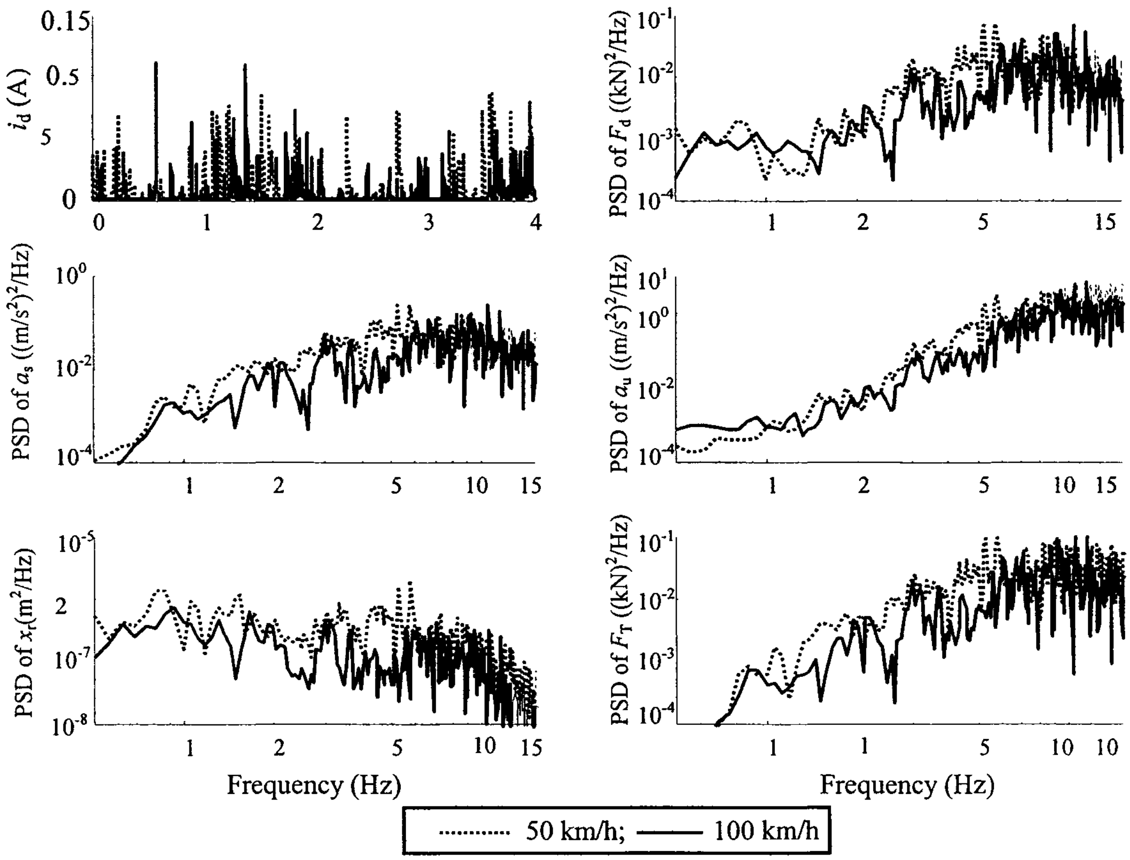

Figure 5.17: Influence of vehicle speed variations on the response characteristics of responses to a rough road random excitation.

The results illustrate that the influence of speed on the random responses are similar to those obtained with the "skyhook"-based hi-lo semi-active damping control, shown in Figure 4.17. The influence on the tire force, however, forms an exception, which tends to decrease with vehicle speed, while the relative change is considerably larger for the "inverse model"-based hi-lo control. An increase in vehicle speed yields slightly lower PSD magnitudes of all responses in vast of the frequency range. The DLC due to tire force at 100 km/h increases slightly to 0.114, compared to 0.113 at 50 km/h. The results thus show relatively high robustness of the controller synthesis in view of vehicle speed variations.

5.5.3 Variations in road roughness

As discussed in section 4.4.3, the road vehicles invariably encounter large variations in magnitudes of road surface roughness, apart from the vehicle speed variations. The different road roughness profiles strongly affect the vibration transmitted to the vehicle, and thus affect the dynamic response and the suspension performances of the suspension system. The sensitivities of the responses to varying excitations are evaluated under different magnitudes of harmonic, transient and random road excitations.

Figure 5.18 illustrates comparisons of time-histories of responses under harmonic excitations of different amplitudes (a_m=1.5, 2.5 and 3.5 cm) at 1.5 Hz. The results show tendencies similar to the "skyhook"-based hi-lo semi-active damping control, shown in Figure 4.18. The variations in excitation magnitude yield only slight changes in the peak drive current, while the switching durations remain identical. Increasing magnitude, however, yields higher magnitude of the spring force and thus the target force. The peak damping force due to "inverse model"-based hi-lo control thus increases with excitation magnitude. This trend was not evident in the "skyhook"-based hi-lo control, where the current rapidly approaches its limiting value. Despite the higher damping force, the amplitudes of sprung mass (x_s and a_s) and tire force (F_T) responses increase considerably with increasing excitation amplitude. The results thus suggest that the resonant response of the "inverse model"-based semi-active damping is highly sensitive to variations in the excitation magnitude.

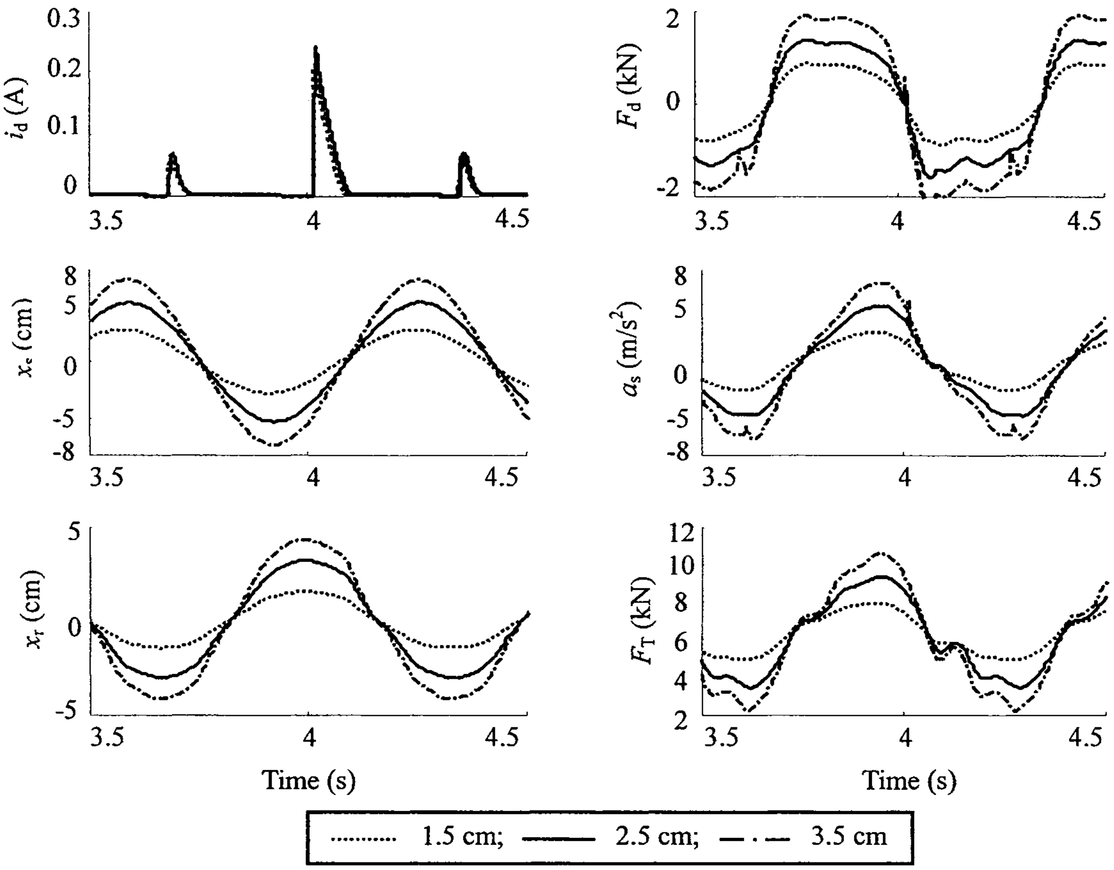

Figure 5.18: Influence of variations in the amplitude of harmonic excitation on responses of the "inverse model"-based hi-lo semi-active ACM damping controller (f=1.5 Hz).

Figure 5.19 illustrates the influence of variations in peak displacement amplitude

(a_m=1.5, 2.5 and 3.5 cm) of harmonic excitations on the frequency response characteristics of the "quarter-vehicle" model employing the proposed semi-active ACM synthesis. The results presented in terms of T_{as}, T_{au}, T_{dr}, and DLC show relatively small variations in T_{as} and T_{au}. The variations in peak displacement of excitation yield only slight changes in the peak values of T_{as} and T_{dr}.

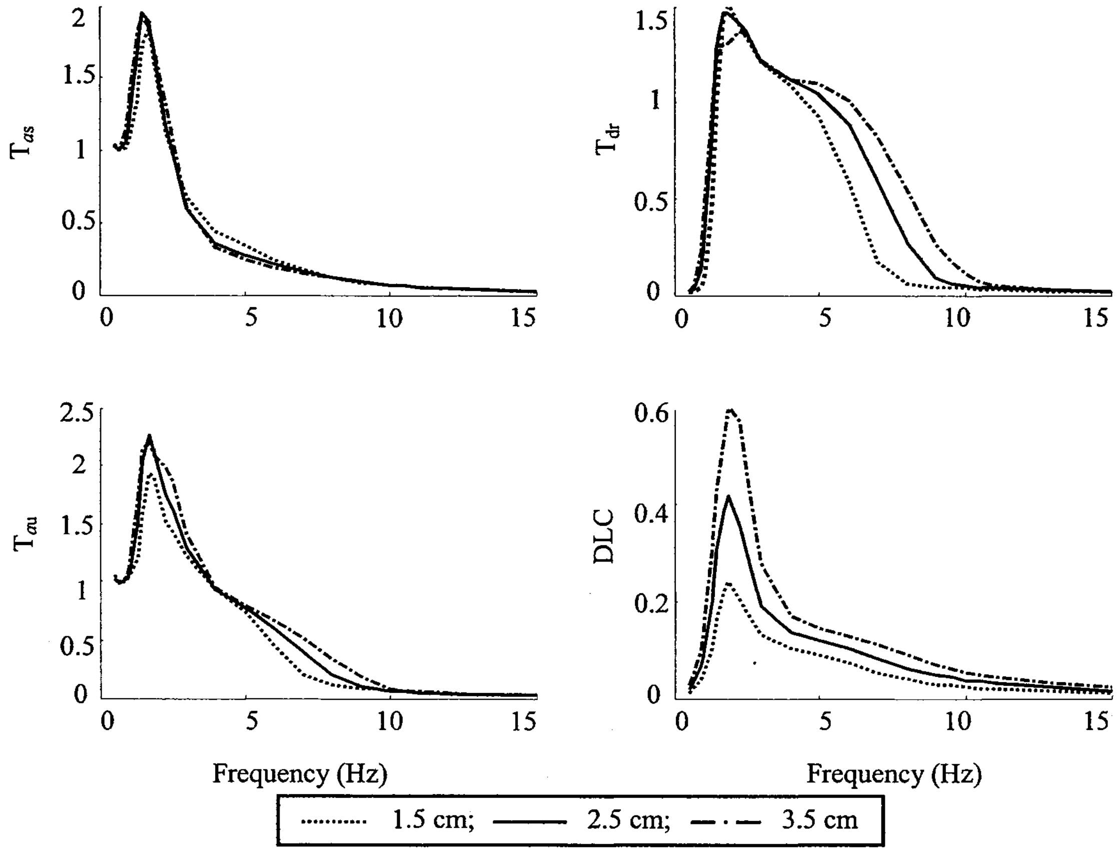

Figure 5.19: Influence of variations in harmonic excitation amplitude on the frequency response characteristics of the "inverse model"-based hi-lo semi-active ACM damping controller.

The results show that the influence on the sprung mass acceleration transmissibility is also very small in the entire frequency range. Lower excitation magnitude yields lower sprung mass acceleration near the sprung mass resonance due to relatively higher damping force. An increase in the excitation magnitude, however, does not alter the peak unsprung mass acceleration transmissibility (T_{au}). The DLC due to tire forces tends to increase significantly with increasing excitation magnitude due to higher dynamic deflection of the tire. This trend was also observed with the "skyhook"-based hi-lo semi-active damping.

Figure 5.20 illustrates the influences of variations in the peak displacement of the rounded pulse excitation on the transient responses of the "quarter-vehicle" model employing "inverse model"-based hi-lo semi-active ACM damping. The analyses are performed under these different peak displacement magnitudes, a_m=2, 3.5 and 5 cm, while all other parameters are held as t μ=3 and ω_0=10.4 rad/s.

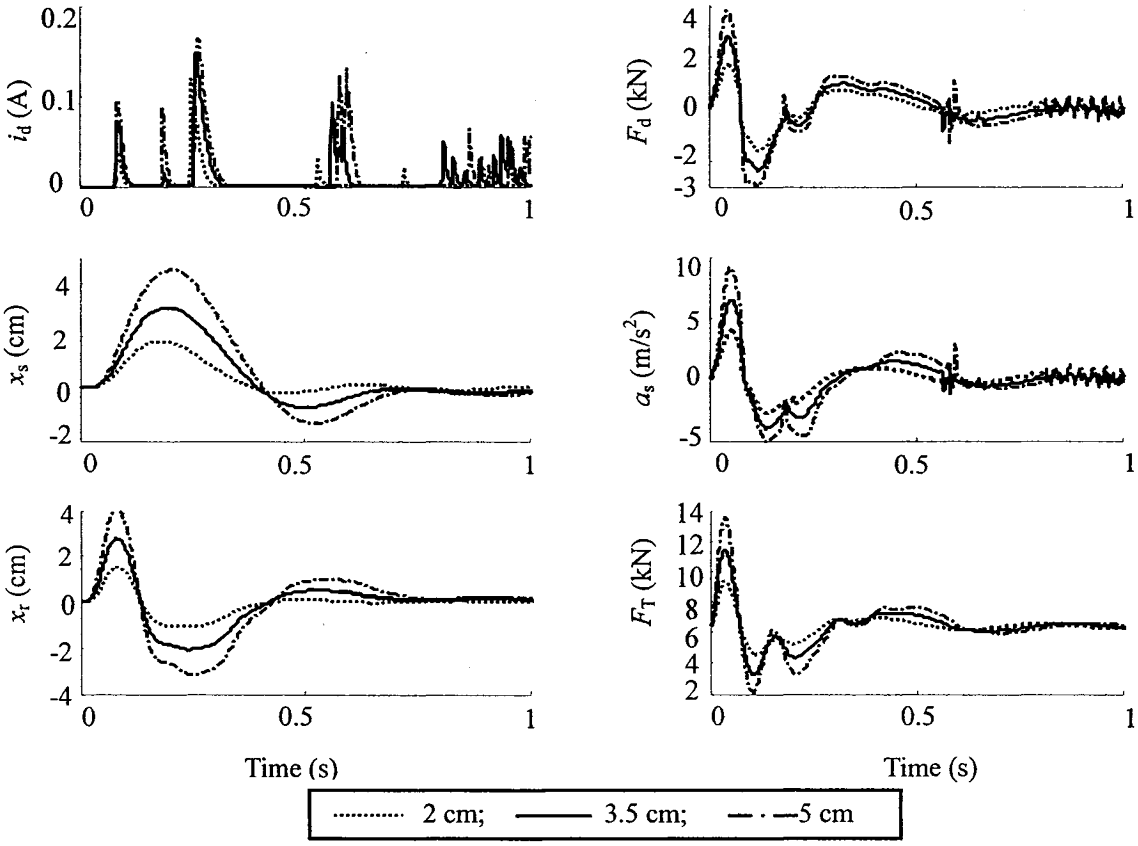

Figure 5.20: Influence of variations in peak rounded pulse displacement on the transient responses to a rounded pulse excitation.

The results illustrate that the variations in excitation magnitude yield notable variations in the drive current and thus the damping force. An increase in peak excitation displacement yields higher peak damping force in response to increased target force and thus higher sprung mass acceleration. The peak magnitudes of absolute and relative displacements of the sprung mass also increase with increasing excitation, as observed from results attained with "skyhook"-based hi-lo semi-active damping.

Transient response measures, summarized in Table 5.3, show relatively smaller deviations in the peak tire force. The peak force deviation (DTR) increases and decreases in the order of 29%, when peak displacement amplitude of the rounded pulse excitation is either increased or decreased by 43%. The results also show that the sprung mass displacement and acceleration ratios (SDR_s and SAR_s) increases and decreases by 5.5% and 3.3%, and 4% and 4%, respectively, when peak displacement is increases and decreased. The corresponding unsprung mass shock displacement and acceleration ratios (SDR_u and SAR_u) and relative displacement ratio (RDR) reveal increases and decreases by 0.9% and 0.9%, 0.8% and 0.8%, and 2.3% and 2.3%.

Table 5.3: Influence of road roughness variations on the transient response measures.

a_m (cm)	SDR_s	SAR_s	SDR_u	SAR_u	RDR	DTR
2.0	0.88	0.24	1.15	1.23	0.88	0.29
3.5	0.91	0.25	1.14	1.24	0.86	0
5.0	0.96	0.26	1.16	1.25	0.84	0.29

The influences of road roughness variations on the stochastic response characteristics are evaluated for the "quarter-vehicle" model employing the proposed "inverse model"-based hi-lo semi-active ACM synthesis. Figure 5.21 illustrates the PSD of F_d, a_s, a_u, x_r and F_T responses and time variations in i_d, when the model is subject to excitations due to medium-rough and rough road surfaces. The results show tendencies that are similar to those observed from the random responses of the "skyhook"-based hi-lo semi-active damping control, shown in Figure 4.21.

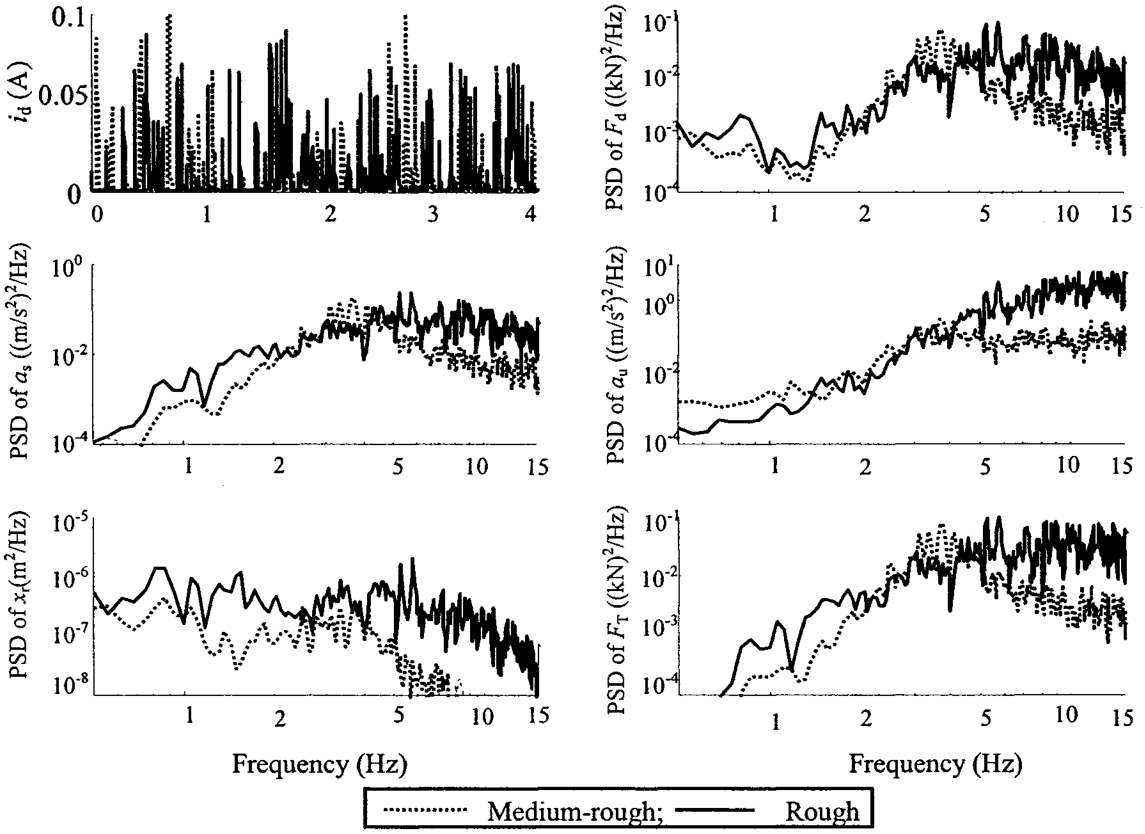

Figure 5.21: Influence of road roughness variations on the PSD characteristics of responses to the medium and rough random excitations.

The results suggest that operation on a road with higher surface roughness would yield higher damping force and sprung mass acceleration response in most of the frequency range. The relative displacement and tire force responses also increase with increasing roughness in most of the frequency range. The magnitudes of PSD of the responses, however, remain slightly insensitive to the road roughness variations in the important ride frequency range (2-5 Hz). The DLC due to tire force for the rough random road excitation is in the order of 0.113, which is considerably higher than 0.056 obtained for the medium-rough road excitation.

5.6 Summary

The hysteresis effect rejection and force-tracking properties of the “inverse model”-based hi-lo semi-active controller are investigated through analysis of the “quarter-vehicle” model with the hysteretic MR-damper model under deterministic as well as stochastic excitations. The sensitivity of the performance measures to variations in operating conditions, such as load, speed and excitation magnitude are further investigated. The results suggest that satisfactory force-tracking performance could be realized by increasing the low velocity damping force gain. The “inverse model”-based hi-lo semi-active ACM controller, however, can effectively reduce the hysteresis effects of the MR-damper. The results of the analyses are summarized below:

- The proposed “inverse model”-based hi-lo semi-active controller can effectively reduce the transient oscillations caused by the hysteresis nonlinearities of the MR-damper.
- The “inverse model”-based upon mean damping force characteristics coupled with the mean force MR-damper model would yield smooth responses, but these derivate significantly from the practically realizable responses.
- Proposed controller exhibits superior forcing-tracking ability at higher velocities, while the low pre-yield damping at low velocities is insufficient to track the target force related to the spring force. The tracking force performance of the MR-damper could thus be enhanced by introducing larger hysteron force.
- High pre-yield damping required for improved force-tracking performance causes degradation of the vibration transmission performance. The design of the “inverse

model"-based hi-lo semi-active control thus imposes difficult compromise between the force-tracking and suspension performance.

- The proposed "inverse model"-based hi-lo semi-active ACM controller exhibits desirable robust control performance with respect to variations in some of the operating parameters, namely, operating load and speed.
- The proposed "inverse model"-based hi-lo semi-active ACM controller offers merits of easy implementation since it involves directly measurable variables.

CHAPTER 6

PERFORMANCE ANALYSES OF INVERSE MODE BASED SLIDING MODE CONTROL

6.1 Introduction

A number of studies have analyzed the robustness of active and semi-active vehicle suspension controller in view of variations in the vehicle load [12, 82, 97, 100]. The robustness of the semi-active MR-suspension controller design is vital in view of not only the multi-objective performance requirements, but also the variations in operating load, speed and road roughness. The sliding mode (SM) control technique offers enhanced robustness and provides a systematic approach for maintaining the stability in the presence of modeling imprecision [12, 42, 70, 75-77]. Lam *et al.* [82] and Yokoyama *et al.* [12] proposed MR-suspension control syntheses using the sliding mode control law to generate the desired damping force by integrating a force feedback loop to regulate the control voltage. The proposed semi-active controller, however, resulted in poor force tracking due to the presence of damper hysteresis nonlinearities.

A sliding mode semi-active MR-damping synthesis involving the hysteretic inverse model has been formulated in section 3.4.4, in order to minimize the effects of hysteresis while maintaining high robustness of the semi-active controller under varying vehicle load, as schematically shown in Figure 3.11. A modified "skyhook"-based reference model is used to serve as the nominal control target, while the desirable damping force (F_c) is generated using the sliding mode control technique. The inverse model control is applied to reduce the hysteresis effects, which has been demonstrated in the previous chapter. The continuous modulation (CM) and ADFG functions are also integrated in the controller synthesis to effectively reduce the contribution due to current-switching discontinuities and to realize the asymmetric damping force from a symmetric MR-damper design. Similar to the analyses of "inverse model"-based hi-lo semi-active ACM controller, presented in section 5.2, the hysteresis and force-tracking properties of sliding mode controller are investigated through analysis of the "quarter-vehicle" model in conjunction with the hysteretic MR-damper models. The sensitivity of the performance measures to variations in operating conditions, such as speed, excitation magnitude and load, are further assessed under deterministic and random excitations.

6.2 Hysteresis Effects and Force-Tracking Properties

The proposed "inverse-model"-based sliding mode semi-active controller is initially analyzed to study the hysteresis effects and force-tracking performance. The analyses are performed using the "quarter-vehicle" model in conjunction with the MR-damper and inverse models. The controller structure of "inverse-model"-based sliding mode semi-active MR-suspension is schematically shown in Figure 3.8, and the controller in current form is formulated in EQ (3.35) with control condition z_c=-F_cF_h. The controller parameters are selected as: p_c=0 and ξ_c=150 for continuous modulation (CM) function; p=1 and ξ=30 for the ADFG function in symmetric control (SCM), while p=0 is chosen for the asymmetric control mode (ACM); c_{s0}=2.5 kNs/m and c_s=6.75 kNs/m for the modified "skyhook"-based reference model; and λ=0.5, ε=0.05, φ=1.6 for the sliding mode control synthesis.

The equations of motion for the "quarter-vehicle" model, EQ (3.1), are solved in conjunction with "inverse model"-based sliding mode semi-active controller equation, EQS (2.17) and (3.35), under harmonic excitations to obtain the drive current on the basis of the condition function z_c. As stated in section 5.2, the proposed hysteretic inverse model of MR-damper can be simplified to its mean value by letting $k_4=0$ in EQ (2.12). The target damping force in the controller synthesis is derived from the sliding mode control design, formulated in EQ (3.34). In a manner similar to that used for the "inverse-model"-based hi-lo controller, the hysteresis effects and the force-tracking abilities of the proposed "inverse-model"-based sliding mode SCM controller are initially investigated by letting $\xi=30$ and $p=1$, when subject to 2.5 cm harmonic excitation at 1.5 Hz.

Figures 6.1 to 6.2 show the time-histories of dynamic responses in terms of drive current (i_d), relative velocity (v_r), damping force (F_d), hysteron force (F_h) and the target force (F_c) of the "quarter-vehicle" model employing mean and hysteretic inverse models, respectively. The results are derived upon consideration of the damping hysteresis in both cases, while the modeling variations are limited to the inverse model alone. The results attained for the hysteretic MR-damper model coupled with mean value of the inverse model (Figure 6.1) exhibit relatively high magnitudes of transient responses near $v_r\approx0$, which can be attributed to larger hysteresis near zero velocity and switching. Such transients can be partly suppressed when the hysteretic inverse model is considered, as shown in Figure 6.2. The results thus suggest that the proposed "inverse-model"-based sliding mode semi-active controller could effectively compensate for the effects of hysteresis nonlinearity and thus improve the force-tracking performance, attributed to the controller synthesis involving the hysteretic inverse model.

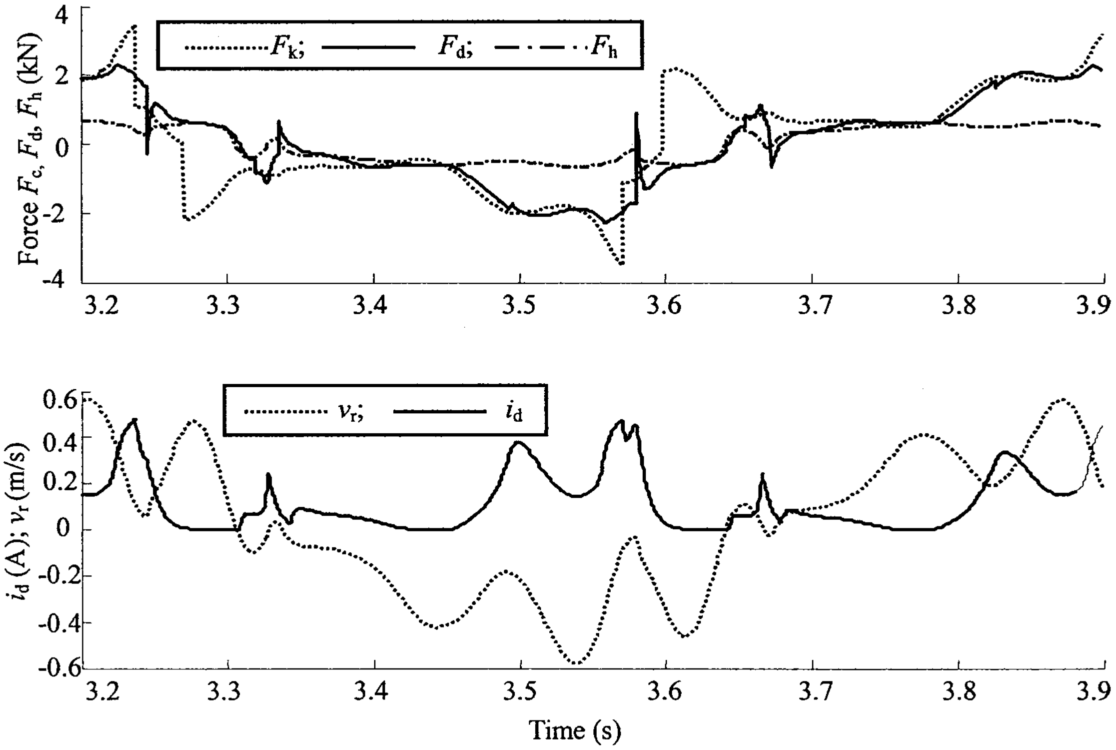

Figure 6.1: Response characteristics of the "quarter-vehicle" model employing hysteretic MR-damper and mean inverse models (f=1.5 Hz; a_m=2.5 cm).

The results from Figures 6.1 and 6.2 further show the variations in drive current and force-tracking performance of the proposed synthesis in response to the condition function. The drive current i_d is reduced to zero, when damping force ($F_hF_c>0$) tends to track the target force F_c, such that $F_d \approx F_c$. The results also show relatively poor force-tracking performance in the intervals $3.22 \leq t \leq 3.25$ and $3.56 \leq t \leq 3.59$, when relative velocity (v_r) is small, although i_d approaches higher values. The results illustrate that the proposed "inverse model"-based sliding mode controller can yield satisfactory forcing-tracking ability only at higher velocities, while the forcing-tracking ability at low velocities is severely limited due to low pre-yield damping forces, as concluded in section 5.2.

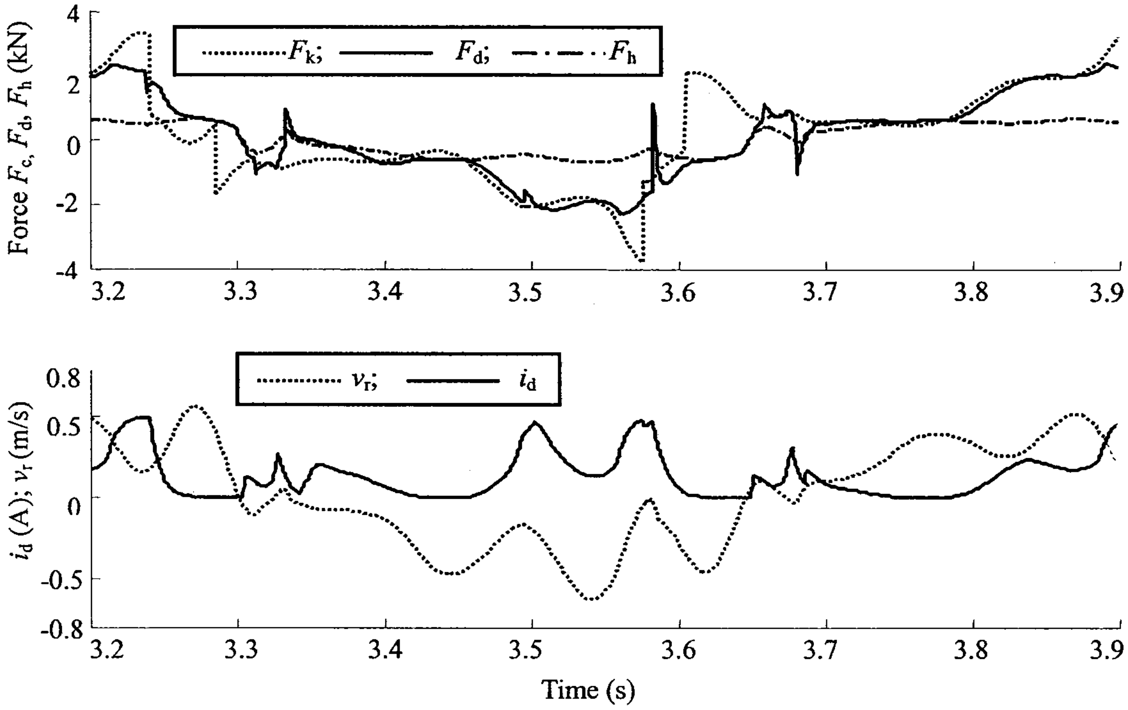

Figure 6.2: Response characteristics of the "quarter-vehicle" model employing hysteretic MR-damper and hysteretic inverse models (f=1.5 Hz; a_m=2.5 cm).

The force-tracking performance at low velocities could be enhanced through adequate design of the MR-damper that would yield lager pre-yield damping force, as described in section 5.3. A force gain k_d=2.5 on the passive hysteron force F_h is thus introduced to achieve higher pre-yield damping force. Subsequent response analyses are thus performed assuming the force gain of 2.5. The "quarter-vehicle" model employing both hysteretic MR-damper and "inverse model"–based sliding mode control in SCM and ACM are further analyzed with a force gain of 2.5, in order to demonstrate the potential benefits of higher passive hysteron force for enhancing the hysteresis rejection and force-tracking properties. The analyses are performed under 2.5 cm harmonic excitation at a frequency of 1.5 Hz, in the vicinity of the sprung mass resonant frequency.

Figures 6.3 and 6.4 present the time-histories of i_d, v_r, F_d, F_h and F_c of the "quarter-vehicle" model employing the "inverse model"-based sliding mode semi-active controller in SCM and ACM, respectively. The results show more smooth variations and lower magnitude transient oscillations in the drive current (i_d), passive hysteron force (F_h) and damping force (F_d), when compared with those shown in Figures 6.1 and 6.2 for the nominal damping force properties. The force-tracking ability of the controller is also considerably enhanced, as evident from the figures around t=3.5 s. The peak magnitudes of i_d, however, are considerably lower due to larger passive hysteron force F_h, which yields lower magnitude of the target force F_c.

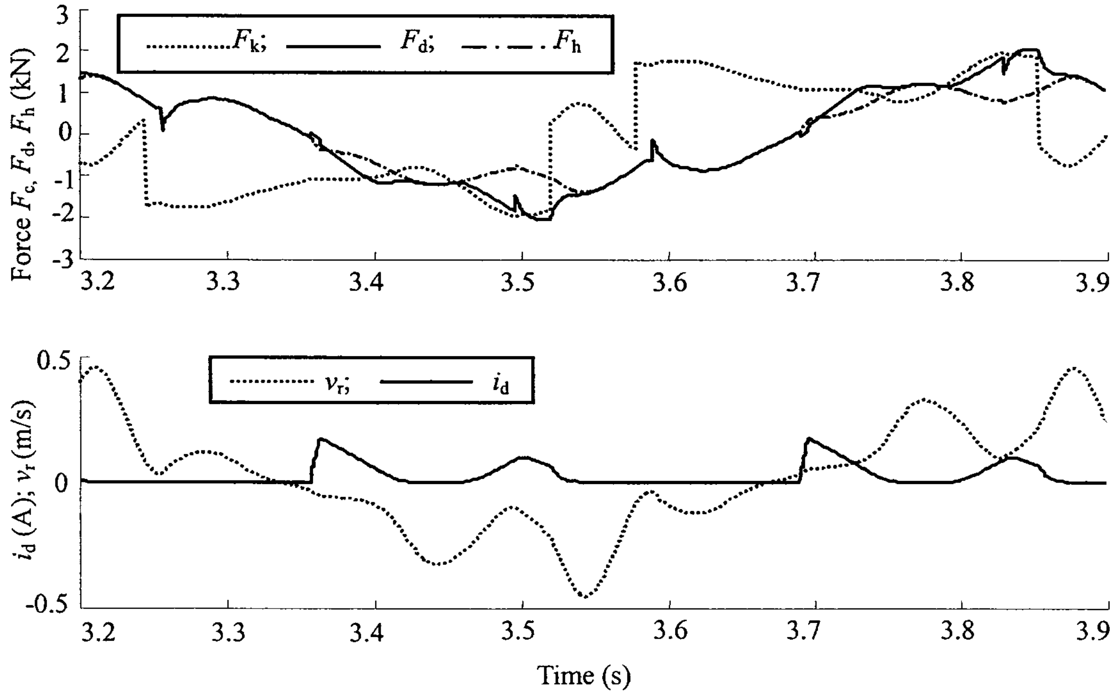

Figure 6.3: "Quarter-vehicle" model responses with hysteretic MR-damper and "inverse model"-based sliding mode SCM controller (f=1.5 Hz; a_m=2.5 cm).

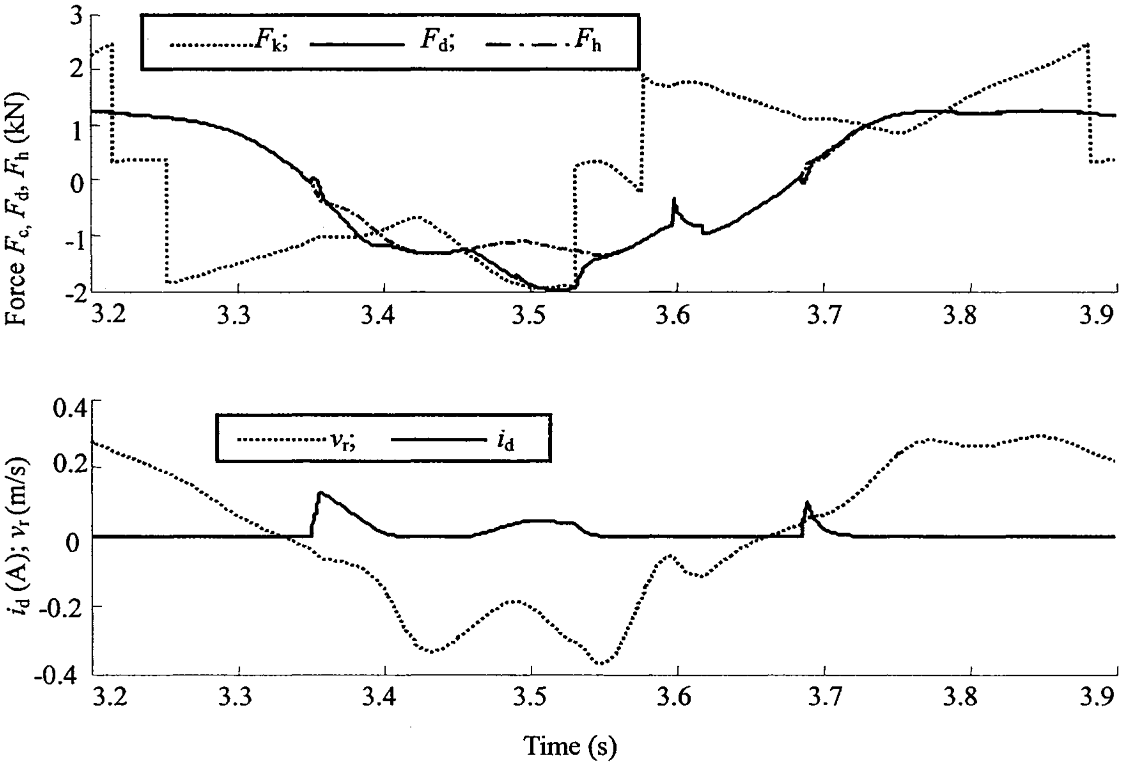

Figure 6.4: "Quarter-vehicle" model responses with hysteretic MR-damper and "inverse model"-based sliding mode ACM controller (f=1.5 Hz; a_m=2.5 cm).

The results further show that the ACM control can further reduce the power consumption by nearly 50% as observed from variations in i_d in Figure 6.4, when compared with that in the SCM (Figure 6.3). The ACM control yields improved force-tracking and transient response suppression than the SCM, which is particularly evident around t=3.5 s in Figures 6.3 and 6.4. The results suggest the "inverse model"-based sliding mode ACM controller could offer superior force-tracking and hysteresis rejection properties than the hi-lo semi-active controller, evaluated in Chapter 5, especially when a larger passive hysteron force is considered.

Figure 6.5 presents comparisons of time-histories of selected responses of the "quarter-vehicle" model employing the hysteretic "inverse model"-based sliding mode semi-active controller in ACM (k_d=2.5) and SCM (k_d=1 and 2.5), under 2.5cm harmonic excitation at 1.5Hz. The results show comparisons of the damping force (F_d), drive current (i_d), sprung and unsprung mass accelerations (a_s, a_u) and displacements (x_s, x_u), relative displacement (x_r) and tire force (F_T), attained using different values of the force gain. The results clearly show that the ACM control with a force gain of 2.5 yields more continuous variations and lower magnitude transient oscillations in i_d, F_d, a_s, a_u and F_T than those attained for the SCM control. Peak magnitudes of x_s, x_r and a_u for ACM control (k_d=2.5) are considerably lower than those obtained for the nominal force SCM control (k_d=1).

Figure 6.6 further shows the frequency response characteristics of the "quarter-vehicle" model employing the hysteretic "inverse model"-based sliding mode controller in ACM (k_d=2.5) and n SCM (k_d=1 and 2.5) under varying amplitude excitation in the 0.5 to 15 Hz frequency range. The peak sprung and unsprung mass acceleration and relative displacement transmissibility (T_{as}, T_{au}, T_{dr}) decrease significantly with higher force gain, while T_{as} and DLC response increase slightly in 1.5 to 8 frequency range. These trends are attributed to the larger force gain that also causes higher post-yield damping force. The results suggest that the ACM control could offer superior benefits in attenuating the peak magnitudes of T_{au} around the sprung mass natural frequency, although the T_{as}, T_{dr} and DLC responses are comparable in the entire frequency range.

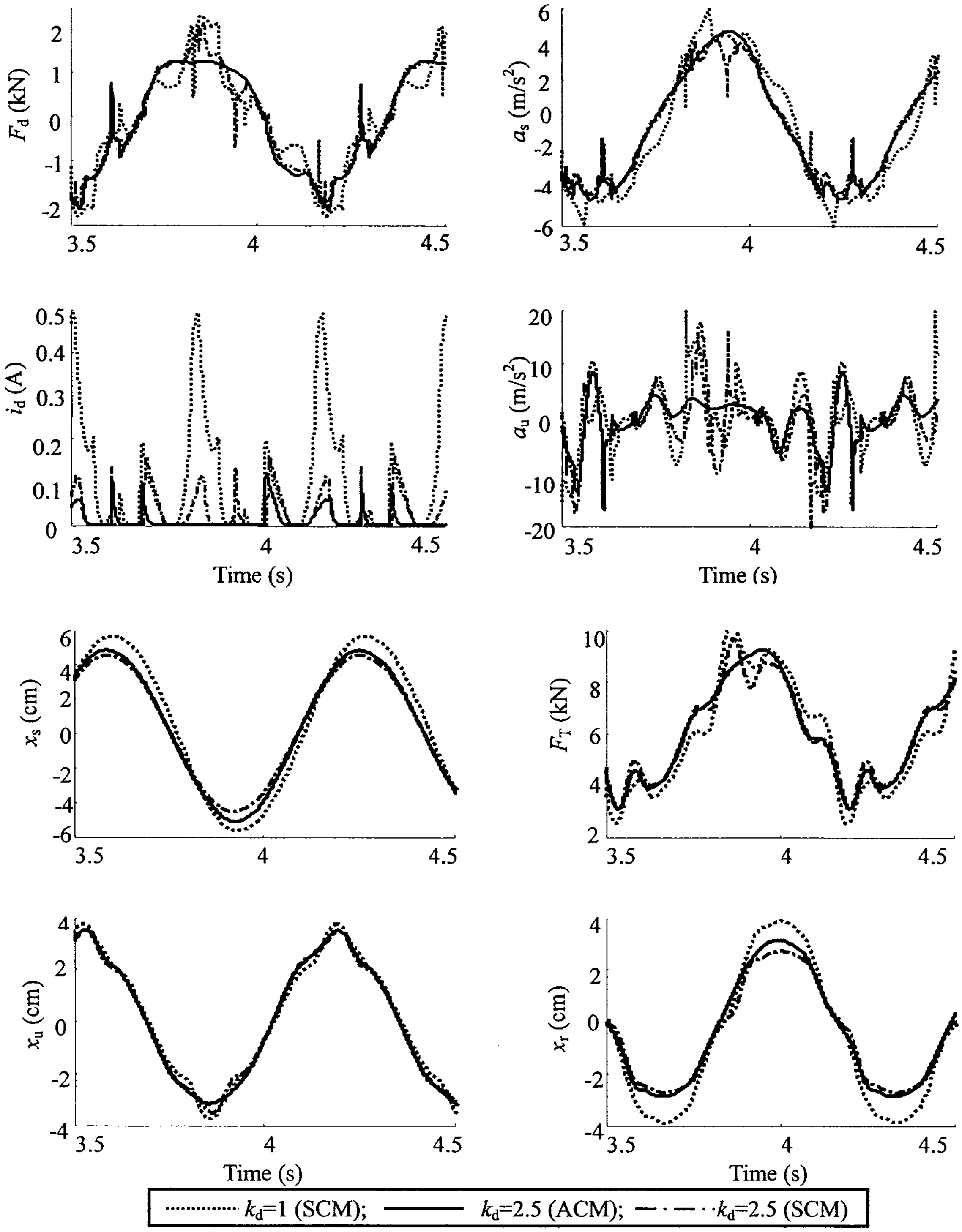

Figure 6.5: Comparisons of time-histories of responses of the "quarter-vehicle" model employing hysteretic "inverse model"-based sliding mode controller in ACM (k_d=2.5) and SCM (k_d=1 and 2.5).

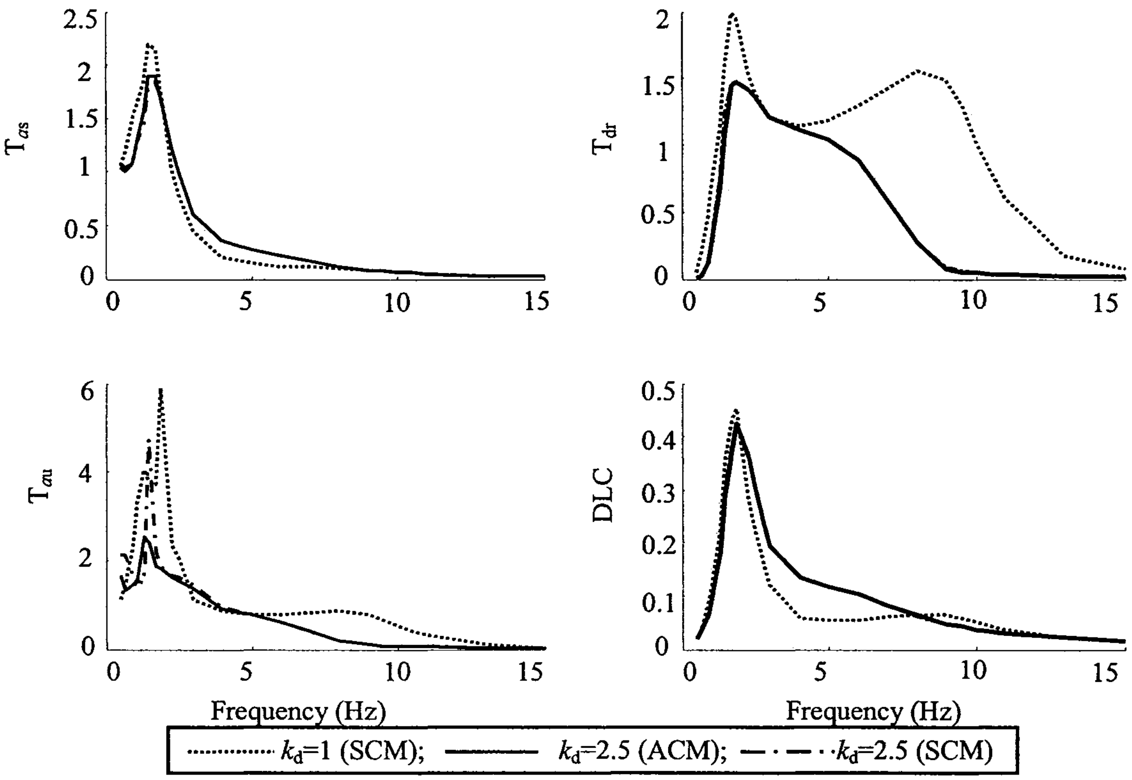

Figure 6.6: Comparisons of frequency responses of the "quarter-vehicle" model employing hysteretic "inverse model"-based sliding mode controller in ACM (k_d=2.5) and SCM (k_d=1 and 2.5) under harmonic excitations.

6.3 Response Analyses

The response characteristics of the "inverse model"-based sliding mode ACM damping control with k_d=2.5 are further evaluated under harmonic, transient and random excitations. The responses are also compared with those attained for different passive damping modes (i_d=0 and 0.1 A) to illustrate the relative performance gains.

Response to Harmonic Excitations

Figure 6.7 shows comparisons of time-histories of the dynamic responses of the asymmetric "inverse model"-based sliding mode semi-active and the passive damping modes, under a 2.5 cm harmonic excitation at a frequency of 1.5 Hz. The results show trends similar to those observed for the "inverse model"-based hi-lo semi-active ACM control, shown in Figure 5.7. The results show that the semi-active ACM damping mode effectively reduces the peak magnitudes of x_s, a_s, x_r, and F_T, when compared to those attained under light and higher passive damping modes (i_d=0 and 0.1 A). The results suggest that a higher damping force is desirable for limiting resonant responses. The responses of the "inverse model"-based sliding mode semi-active ACM damping show current modulation is well below 0.06 A in compression, while the current approaches 0.15 A in the rebound mode.

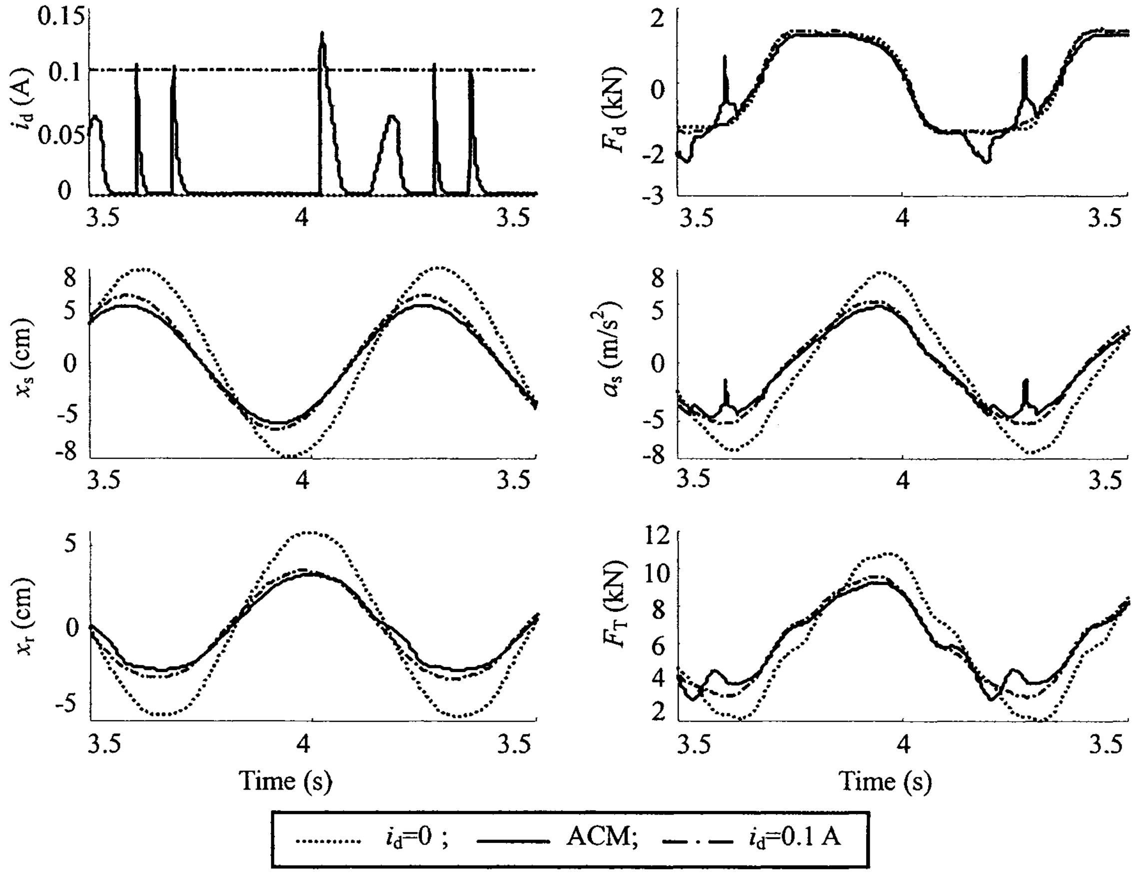

Figure 6.7: Comparison of time-histories of responses of "quarter-vehicle" model with passive (i_d=0; i_d=0.1 A) and "inverse model"-based sliding mode semi-active ACM damping (a_m=2.5 cm; f=1.5 Hz).

Figure 6.8 further illustrates comparisons of frequency response characteristics of the asymmetric "inverse model"-based sliding mode semi-active damping with those attained for the passive damping modes, under varying displacement amplitude harmonic excitations in the 0.5 to 15 Hz range. The results gain show trends comparable to those observed for the "inverse model"-based hi-lo damping control, shown in Figure 5.8. Both the passive damping modes yield higher resonant magnitudes of T_{as}, T_{dr} and DLC, while the light passive mode damping yields significantly higher unsprung mass acceleration near the unsprung mass resonance but slightly lower response near the sprung mass resonance.

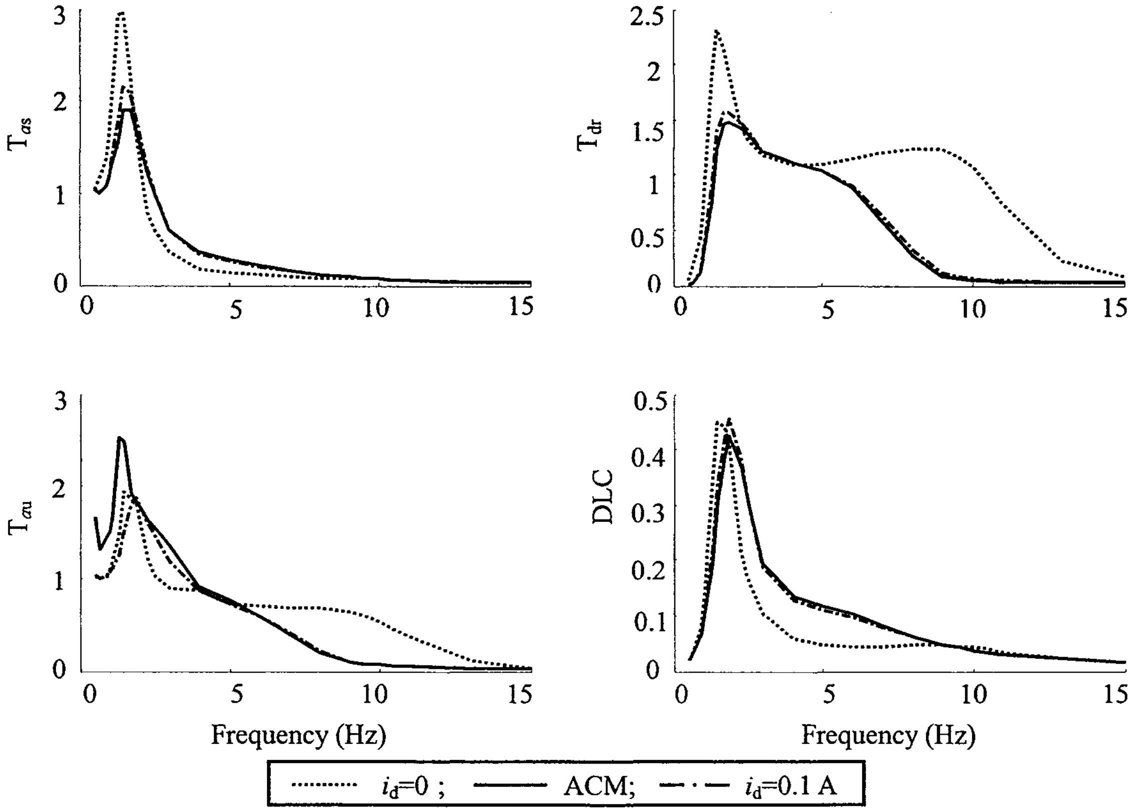

Figure 6.8: Comparisons of frequency responses of the "quarter-vehicle" model with passive (i_d=0; i_d=0.1 A) and "inverse model"-based sliding mode semi-active ACM damping.

The above results illustrate that the "inverse model"-based sliding mode semi-active damping yields improved resonance control but slightly higher vibration transmission in the important ride frequencies. The suspension rattle space requirements, however, could be considerably reduced with the proposed sliding mode-based force-tracking algorithm. The proposed controller can thus be considered to offer better compromise between the conflicting performance requirements.

Responses to Rounded Pulse Excitation

The relative transient response characteristics of the passive and inverse-model-based sliding mode semi-active ACM damping properties are further evaluated under a rounded pulse excitation (μ=3, ω_0=10.4 rad/s and a_m=5 cm). Figure 6.9 shows comparisons of the transient responses in terms of i_d, F_d, x_s, a_s, x_r and F_T. The "inverse model"-based sliding mode semi-active ACM and higher passive damping (i_d=0.1 A) yield rapid rate of decay and effectively reduce the peak amplitudes of x_s and x_r. Light passive damping (i_d=0), on the other hand, yields lower peak value of a_s, but higher peak values of x_s and considerably lower rate of decay. The drive current exceeds 0.1 A only for short durations in rebound, while the semi-active damping force is comparable with the passive force corresponding to 0.1 A for the excitation considered. The semi-active damping variations, however, cause slightly high rates of decay, as observed from the responses in terms of a_s, x_s, x_r and F_T.

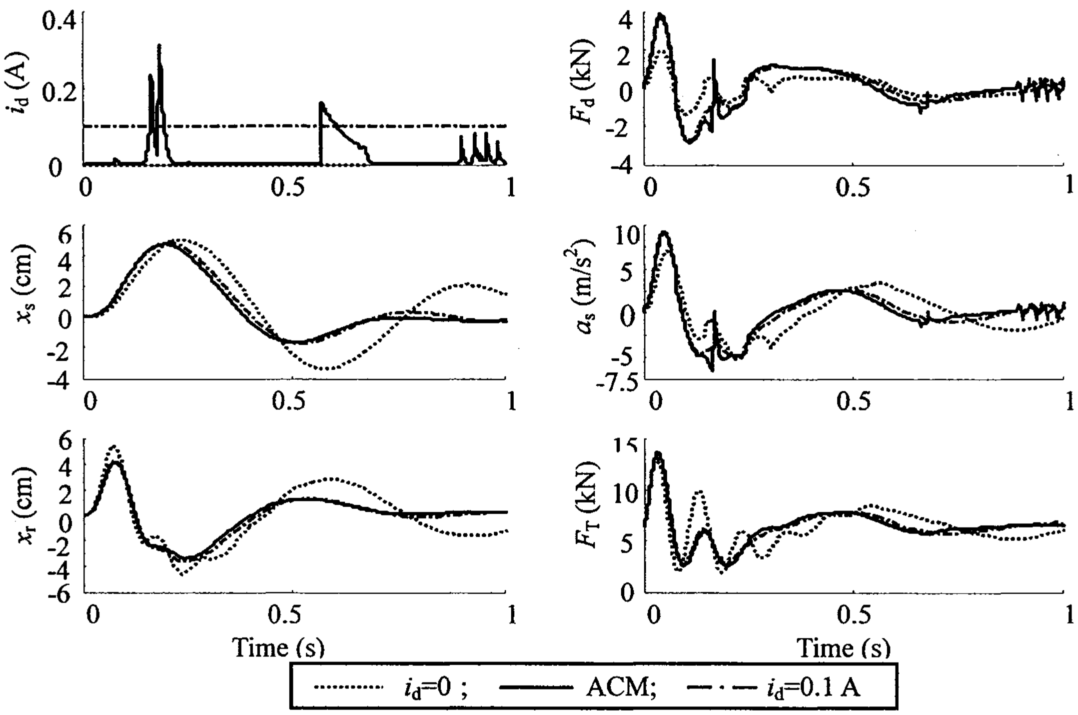

Figure 6.9: Comparisons of transient responses of passive (i_d=0 and 0.1 A) and "inverse model"-based sliding mode ACM semi-active damping.

Responses to Random Road Excitations

The performance characteristics of the "inverse model"-based sliding mode semi-active ACM damping variations are further evaluated under randomly distributed rough road excitation, assuming constant forward speed of 50 km/h, as described earlier in Figure 3.10(b). Figure 6.10 shows the comparisons of PSD of responses of F_d, a_s, a_u, x_r and F_T, and time variations in i_d of the "quarter-vehicle" model with light passive (i_d=0) and "inverse model"-based sliding mode semi-active ACM damping. The results show trends comparable to those attained for the "inverse model"-based hi-lo semi-active ACM control (Figure 5.1). The "inverse model"-based sliding mode semi-active controller yields significantly higher damping force than the passive mode damping (i_d=0) in the entire frequency range, due to higher hysteron force (k_d=2.5). The resulting high damping force tends to suppress the sprung mass acceleration near the resonant frequency but causes considerably higher acceleration responses in the ride frequency range.

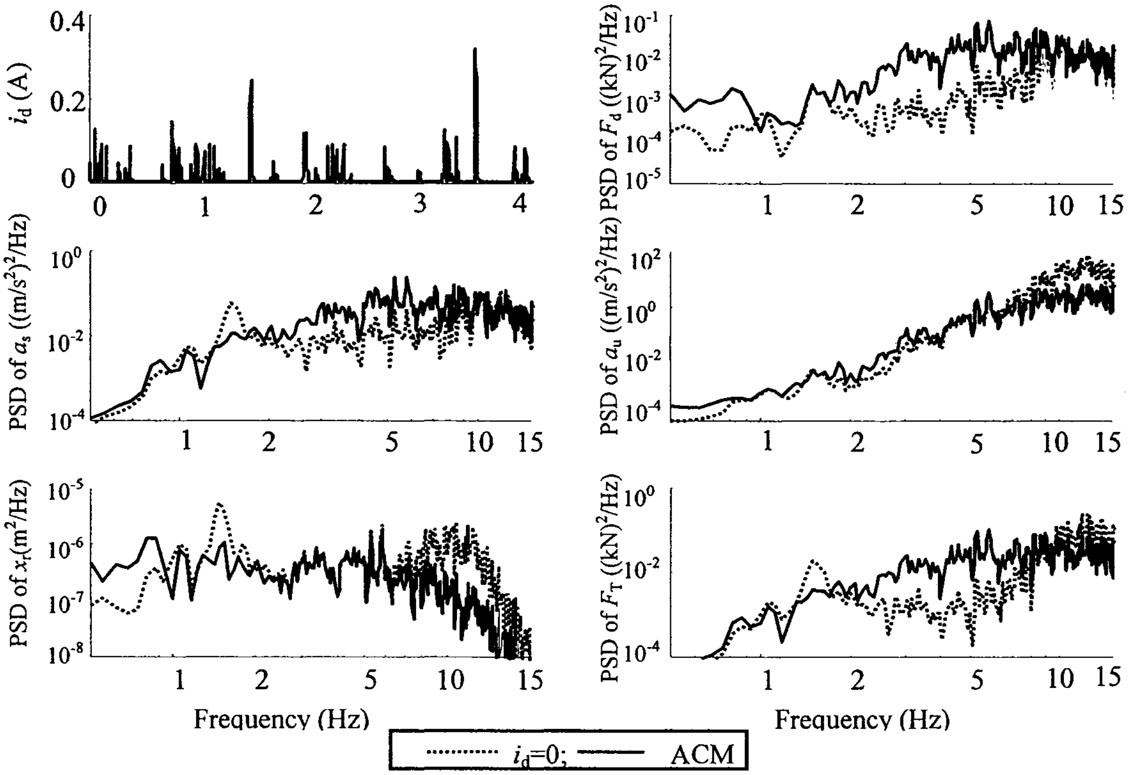

Figure 6.10: PSD comparisons of responses of the MR-suspension with the proposed "inverse model"-based sliding mode semi-active controller and passive damping modes under random excitation.

The results further illustrate that the vibration attenuation and road-holding performances in the ride frequency range (2-7 Hz), however, deteriorate, when compared to those of the fixed lightly damped passive MR-suspension, as evident form the PSD responses of a_s and F_T. The suspension travel and unsprung mass acceleration responses for the semi-active damping are comparable with those of the fixed passive damping in the ride frequency range. The DLC value due to dynamic tire force of the semi-active ACM damping mode is in the order of 0.112, which is slightly lower than 0.139 and 0.113 due to those with the fixed passive damping mode and "inverse model"-based hi-lo semi-active control, respectively.

6.4 Influences of Variations in Operating Parameters

The force tracking and performance characteristics of the "inverse model"-based sliding mode ACM damping are evaluated considering variations in operating load (m_s), forward speed (V) and road roughness. The analyses, considering variations in operating parameters, are performed under harmonic, transient and stochastic excitations, and a constant force gain of 2.5 is employed to realize satisfactory force-tracking performance. The results attained from the analyses are used to examine the robustness of the proposed "inverse model"-based sliding mode ACM damping formulation. For the analyses, the controller parameters are kept as: c_{s0}=2500Ns/m, c_s=6750Ns/m, λ=0.5, ε=0.05, φ=1.6, p_c=0, ξ_c=150, p=0 and ξ=30.

6.4.1 Variations in operating mass

Figure 6.11 illustrates the influence of sprung mass variations (±25% of the nominal value of 563 kg) on the responses of the "inverse model"-based sliding mode semi-active ACM controller, under 2.5 cm excitation at 1.5 Hz. The results show that the magnitude of the damping force (F_d) tends to increase with increasing sprung mass. The magnitudes of the drive current (i_d) and the resulting sprung and unsprung mass accelerations (a_s, a_u) and sprung mass displacement (x_s), decrease with increasing sprung mass. This is mostly attributed to the lower natural frequency with increasing mass. The suspension relative displacement (x_r) and the tire force (F_T), however, increase with increasing sprung mass due to higher tire deflections.

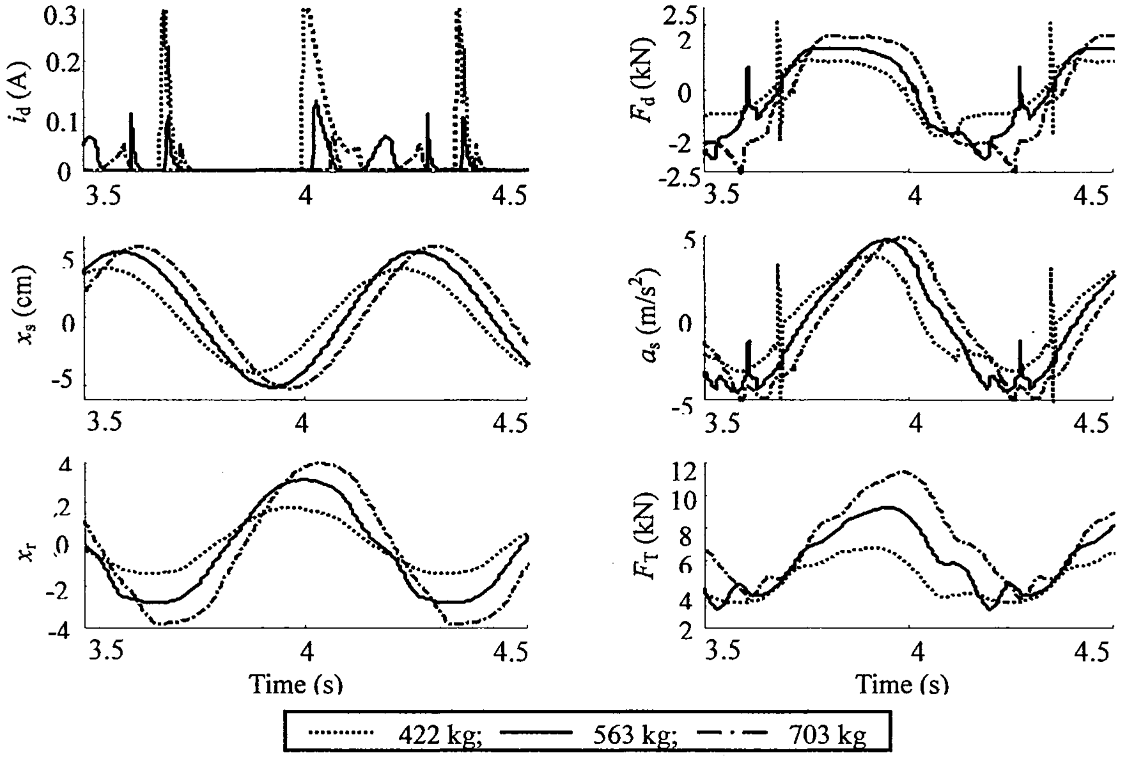

Figure 6.11: Influence of sprung mass variation on the time-histories of harmonic responses of the "inverse model"-based sliding mode semi-active ACM damping controller.

Figure 6.12 presents the influence of variations in sprung mass on the frequency response characteristics of the "quarter-vehicle" model employing "inverse model"-based sliding mode semi-active ACM synthesis. The peak magnitudes of T_{as} and T_{dr} increase only slightly with increasing sprung mass, while the peak magnitudes of T_{au} and DLC decrease. The responses in the vicinity of the unsprung mass resonance, however, remain relatively insensitive to variations in m_s, with the exception of DLC, which exhibits significant variations due to changes in m_s. Moreover, the responses in the ride frequency range decrease slightly with increasing sprung mass. The responses to harmonic excitations (Figures 6.11 and 6.12) generally suggest reasonably good robustness of the "inverse model"-based sliding mode ACM synthesis to variations in the sprung mass.

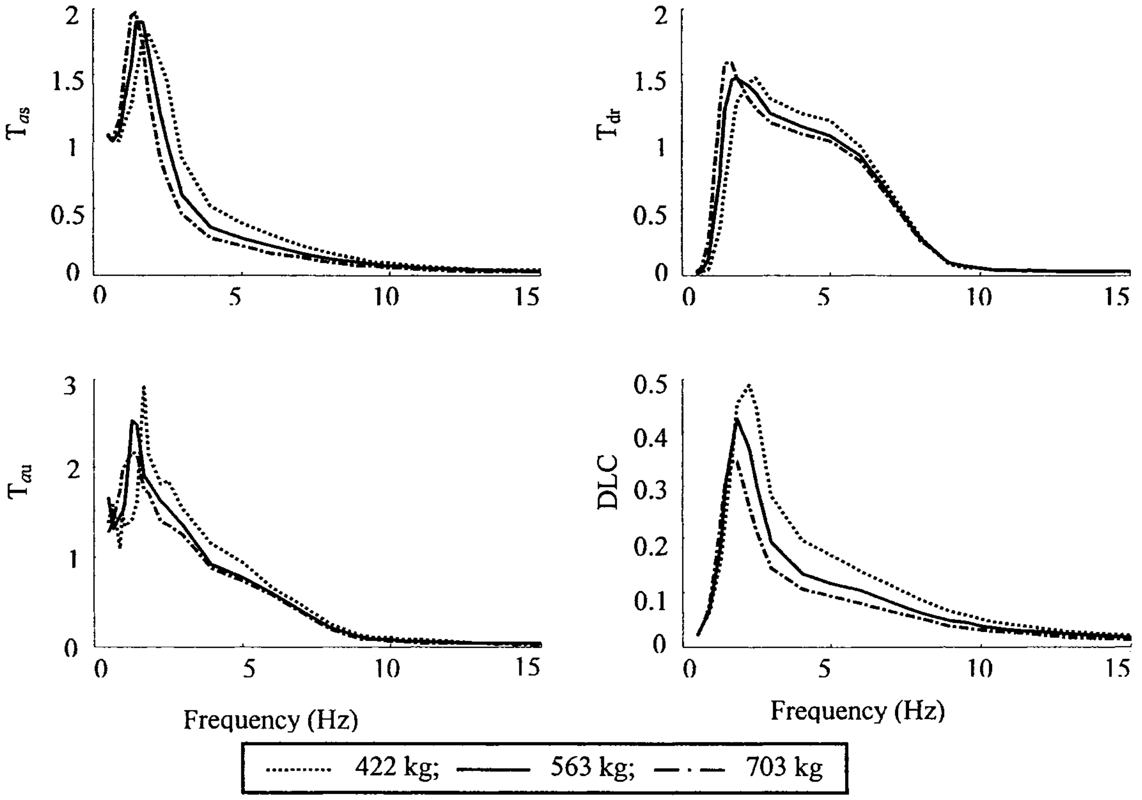

Figure 6.12: Influence of sprung mass variation on the frequency response characteristics of the "inverse model"-based sliding mode semi-active ACM damping controller.

The influences of sprung mass variations on the transient responses to a rounded pulse excitation (μ=3, ω_0=10.4 rad/s and a_m=3.5 cm) are illustrated in Figure 6.13. The results show trends that are comparable to those observed for the "inverse model"-based hi-lo semi-active controller, presented in Figure 5.14. The results suggest that the responses of the "inverse model"-based sliding mode damping control remain relatively insensitive to sprung mass variations considered in this study, particularly within the duration of the shock pulse. The magnitudes of sprung mass displacement and acceleration decrease with increasing sprung mass, and reveal high sensitivity to sprung mass variations, while the tire force exhibits a bias, as observed for the "skyhook"-based hi-lo and "inverse mode"-based hi-lo controls.

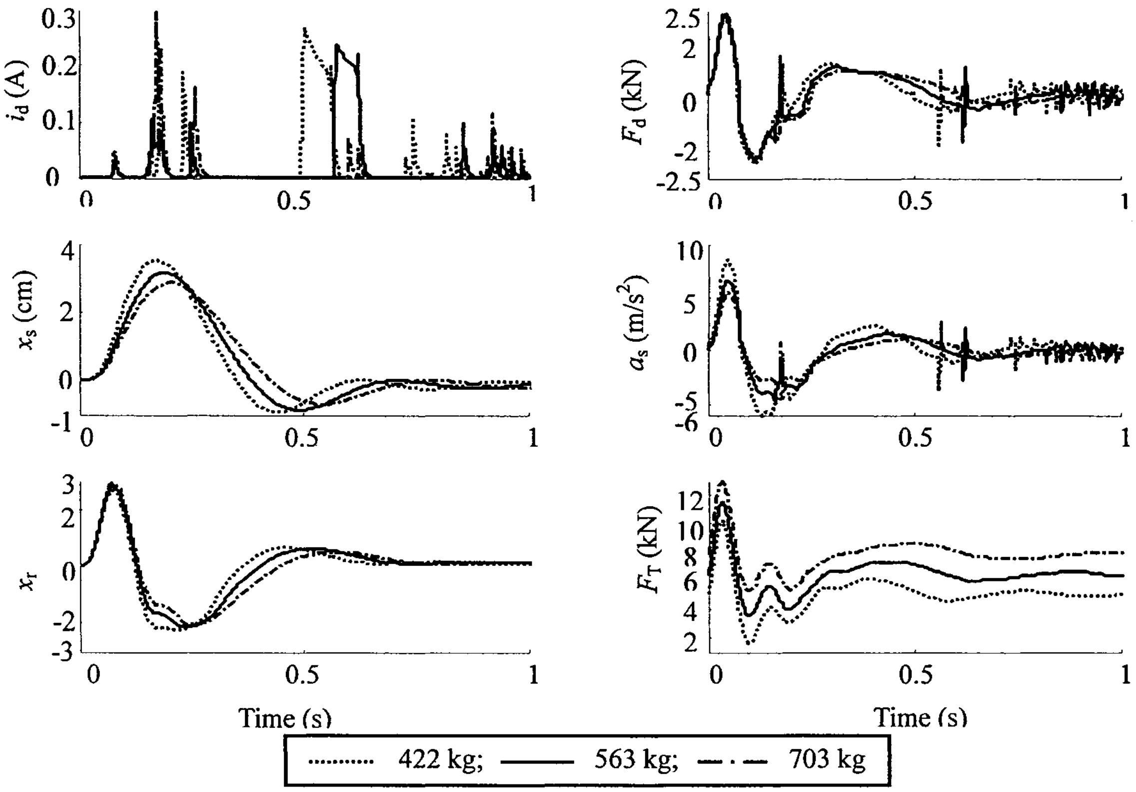

Figure 6.13: Influence of sprung mass variations on the transient responses to a rounded pulse excitation.

The transient response measures are also summarized in Table 6.1. The results show only slight influences of the sprung mass variations on the deviations in the peak tire force, unsprung mass responses (SDR_u and SAR_u), and relative displacement ratio (RDR). The peak force deviations (DTR) decreases and increases by 16% and 13%, when the sprung mass is decreased and increased by 25%, respectively. The sprung mass shock displacement (SDR_s) and acceleration ratios (SAR_s) increase with decreasing sprung mass. SDR_s increases and decreases by 13% and 7.9%, while the sprung mass acceleration ratio (SAR_s) increases and decreases by 19% and 22%, when m_s is decreased and increased by 25%, respectively. The results show relatively superior robustness of "inverse model"-based sliding mode semi-active control than the "inverse model"-based hi-lo semi-active control, in view of the sprung mass variations and transient responses.

Table 6.1: Influence of sprung masses variations on the transient response measures.

m_s (kg)	SDR_s	SAR_s	SDR_u	SAR_u	RDR	DTR
422	1.01	0.32	1.14	1.29	0.86	0.16
563	0.89	0.27	1.13	1.29	0.86	0
703	0.81	0.21	1.13	1.29	0.86	0.13

Figure 6.14 presents the influence of variations in m_s on the response characteristics of the "quarter-vehicle" model employing "inverse model"-based sliding mode semi-active ACM synthesis, under excitations arising from a rough road. Figure illustrates comparisons of PSD of F_d, a_s, a_u, x_r and F_T responses due to two extreme sprung masses (422 and 703 kg). The influence of sprung mass variations on the responses are similar to those obtained using the "inverse model"-based hi-lo semi-active controller, shown in Figure 5.15. Both the unsprung mass acceleration and relative displacement responses exhibit relatively small sensitivity to sprung mass variations, as observed under harmonic and transient excitations. The sprung mass acceleration response, however, increases with decreasing mass at higher frequencies. The DLC due to tire force also increases from 0.091 to 0.141, when m_s is increased from 422 to 703 kg. The corresponding increase for

the “inverse mode” -based hi-lo damping was observed from 0.091 to 0.147.

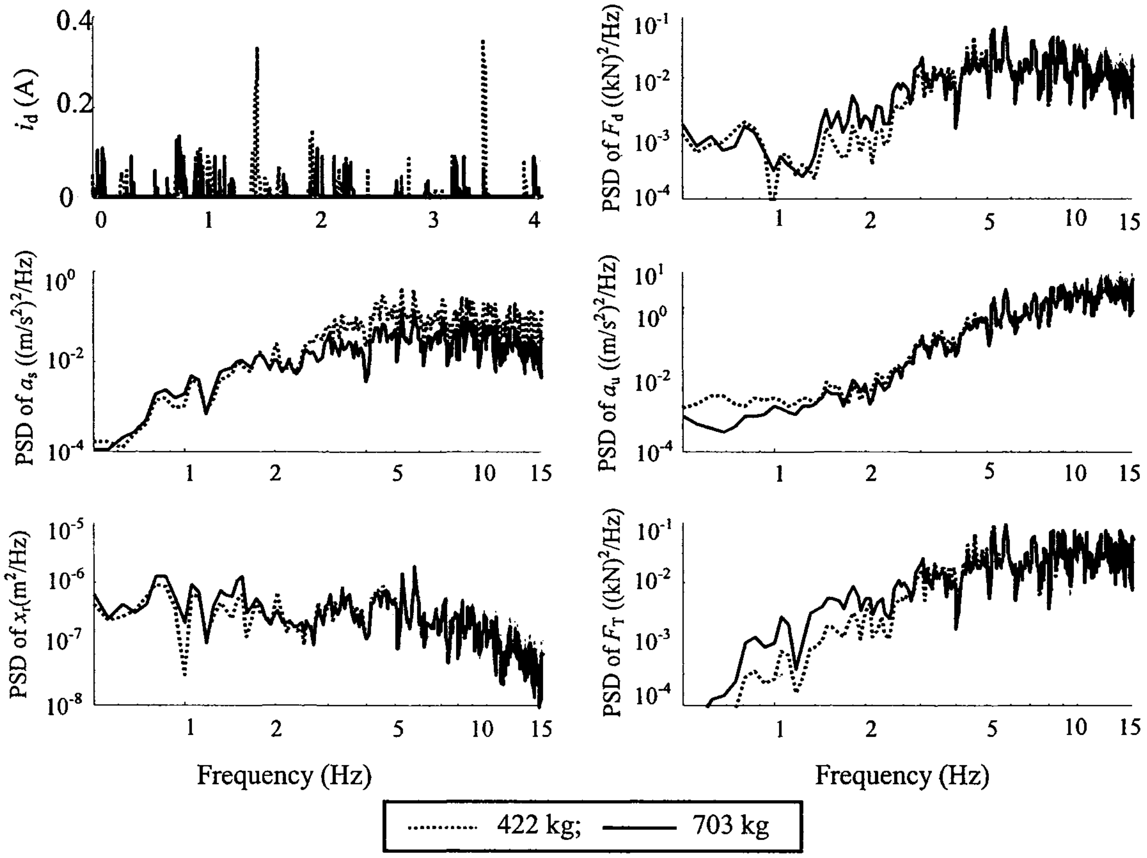

Figure 6.14: Influence of sprung mass variations on the PSD characteristics of responses to a rough random excitation.

6.4.2 Variations in operating speed

The influence of variations in the forward speed on the response measures is investigated by considering two different constant speeds, 50 and 100 km/h. Figure 6.15 illustrates the influence of speed on the responses to a rounded pulse excitation (μ=3, a_{m}=3.5 cm, and ω_0=10.4 and 20.8 rad/s). The results show influences comparable to those observed for the “inverse model”-based hi-lo damping control (Figure 5.16). Operation at a higher speed (V=100 km/h) results in higher demand on the damping force, and yields higher peak acceleration but lower sprung mass displacement. Higher damping force yields relatively faster decay in absolute and relative displacement responses, while it causes oscillations in the damping force and sprung mass acceleration. Similar trends were also observed with the "skyhook"-based hi-lo and "inverse model"-based hi-lo semi-active damping controls.

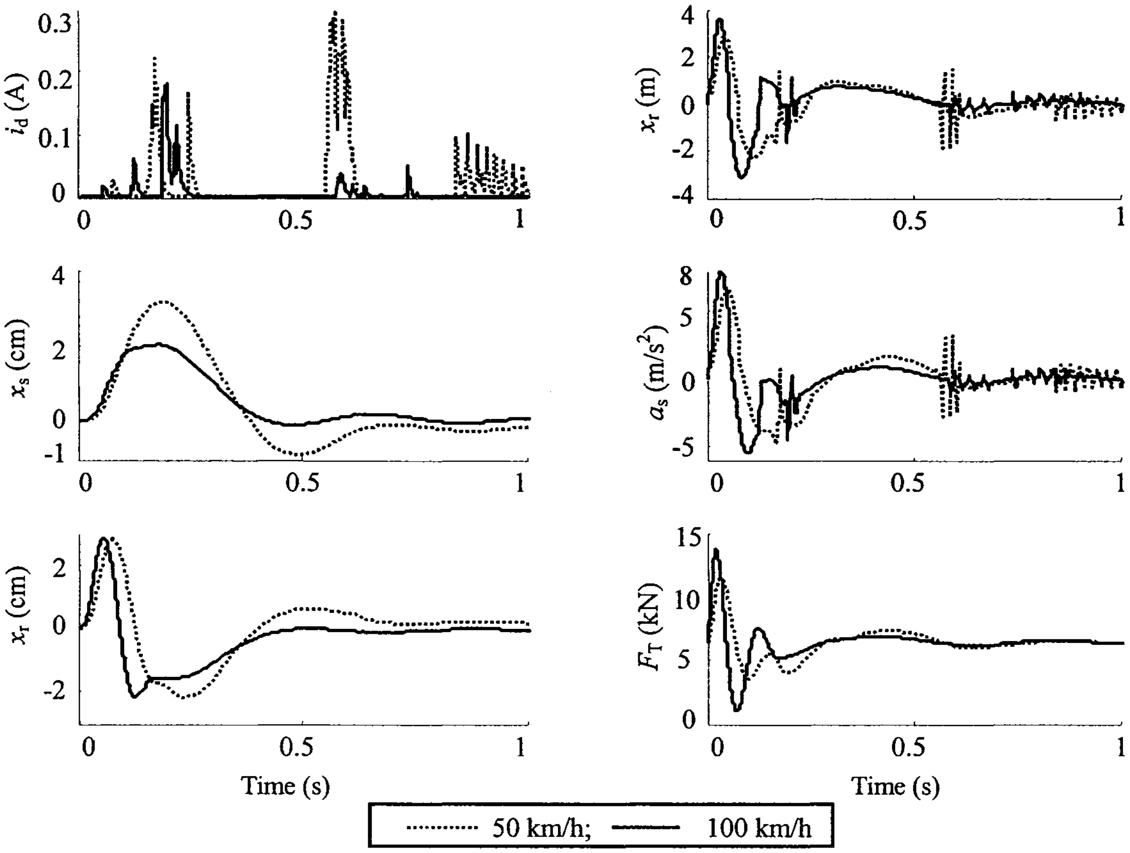

Figure 6.15: Influence of vehicle speed variations on the transient responses to a rounded pulse excitation.

Table 6.2 summarizes the influence of speed on the transient response measures. The results show relatively larger deviations in the peak tire force (DTR), which increases in the order of 35%, when vehicle speed is increased by 100%. The operation at such a speed would represent an extreme case when passing over a rounded pulse road profile. The results also show that the unsprung mass and relative displacement ratios (SDR_u and RDR) remain insensitive to variations in speed. The sprung mass displacement and acceleration ratios (SDR_s and SAR_s) and the unsprung mass acceleration ratio (SAR_u) decrease by 42%, 76% and 58%, respectively, when speed is increased from 50 to 100 km/h.

Table 6.2: Influence of vehicle speed variations on the transient response measures.

V (km/h)	SDR_s	SAR_s	SDR_u	SAR_u	RDR	STR
50	0.91	0.25	1.02	1.15	0.86	0
100	0.57	0.06	1.11	0.48	0.86	0.35

The influences of operating speed variations on the stochastic response characteristics are evaluated for the "quarter-vehicle" model employing the "inverse model"-based sliding mode semi-active ACM synthesis. Figure 6.16 illustrates the comparisons of PSD of F_d, a_s, a_u, x_r and F_T and time variations in i_d, attained for the two operating speeds considered.

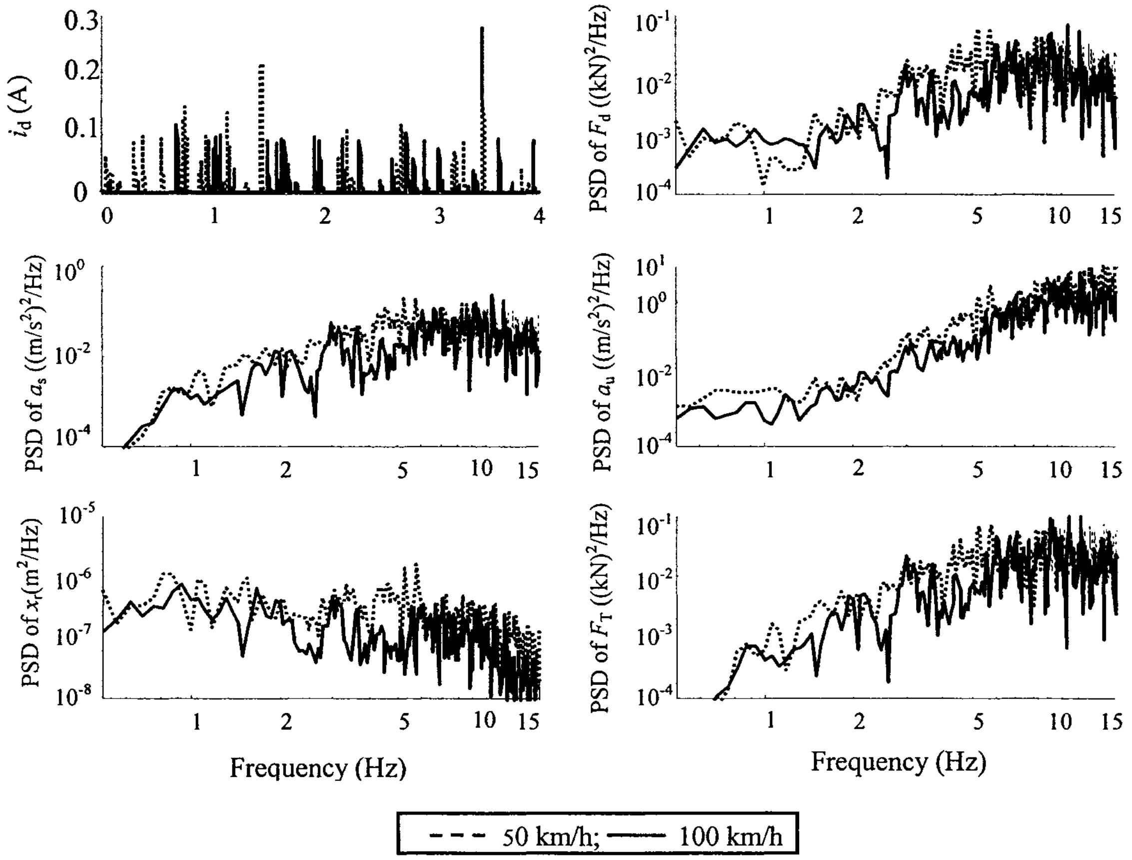

Figure 6.16: Influence of vehicle speed variations on the PSD characteristics of responses to a rough random excitation.

The results show that the influence of speed on the random responses are similar to those obtained with the "skyhook"- and "inverse model"-based hi-lo semi-active damping controls, shown in Figures 4.17 and 5.17, respectively. An increase in vehicle speed yields slightly lower PSD magnitudes of all responses in the vast majority of the frequency range. The DLC due to tire force at 100 km/h increases slightly to 0.114, compared to 0.112 at 50 km/h. The results thus show reasonably good robustness of the controller synthesis in view of vehicle speed variations.

6.4.3 Variations in excitation magnitude

The sensitivities of the responses to varying excitations are evaluated under different magnitudes of harmonic, transient and random road excitations. Figure 6.17 illustrates comparisons of time-histories of responses under harmonic excitations of different amplitudes (a_m=1.5, 2.5 and 3.5 cm) at 1.5 Hz. The results show tendencies similar to those observed for the "skyhook"- and "inverse model"-based hi-lo semi-active damping controls (Figures 4.18 and 5.18, respectively). The results show that an increase in excitation amplitude yields higher magnitudes of the target (spring) force (F_d), and sprung mass displacement and acceleration (x_s and a_s) and tire force (F_T) responses. The results thus suggest high sensitivity of the "inverse model"-based sliding mode semi-active ACM damping to variations in the excitation magnitude.

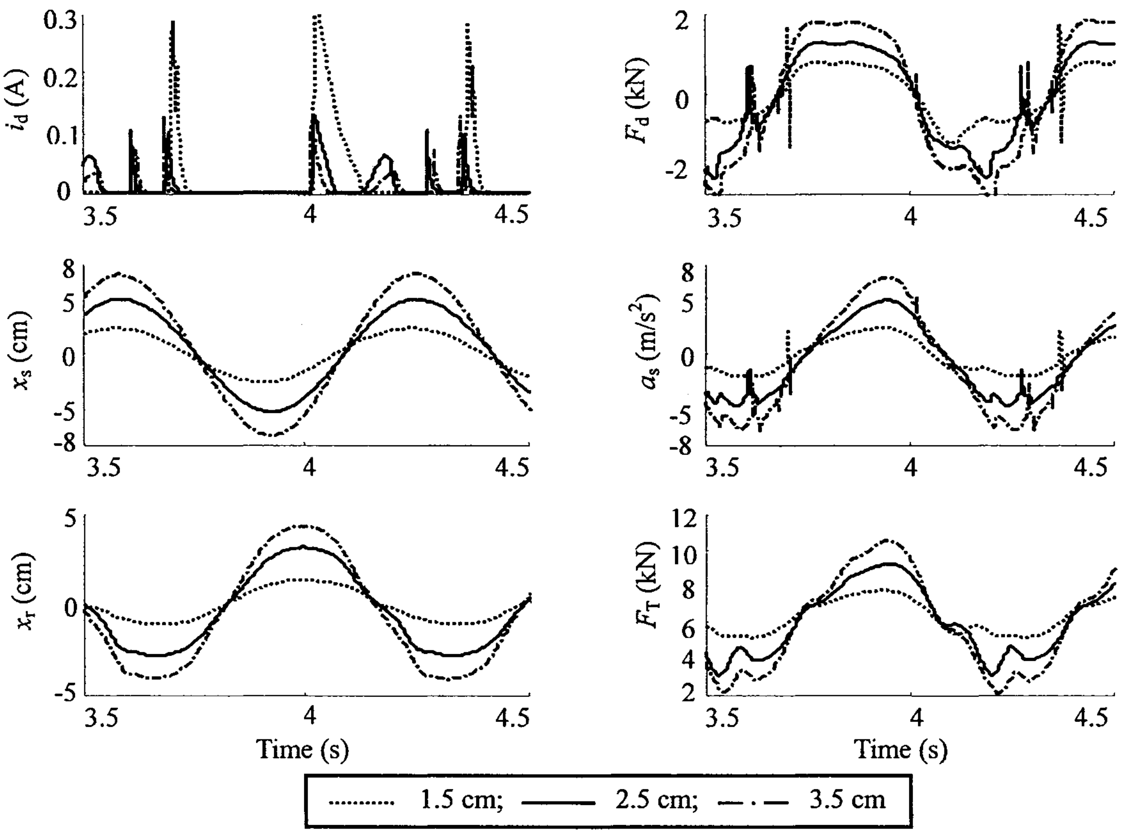

Figure 6.17: Influence of amplitude of harmonic excitation on the responses of the "inverse model"-based sliding mode semi-active ACM damping control.

Figure 6.18 illustrates the influence of variations in harmonic excitation amplitude (1.5, 2.5 and 3.5 cm) on the frequency response characteristics of the vehicle model with "inverse model"-based sliding mode semi-active ACM damping control. The results presented in terms of T_{as}, T_{au}, T_{dr}, and DLC show relatively small variations in T_{as} and T_{dr}, particularly when amplitude is varied from 2.5 to 3.5 cm. The influence of excitation amplitude on the sprung mass acceleration transmissibility is small in the entire frequency range. Lower excitation magnitude yields lower sprung mass acceleration near the sprung mass resonance due to relatively higher damping force. The lower excitation magnitude, however, causes undesirable variations in unsprung mass acceleration response (T_{au}) in the vicinity of sprung mass resonance. The DLC due to tire force increases significantly with increasing excitation magnitude due to higher dynamic deflection of the tire.

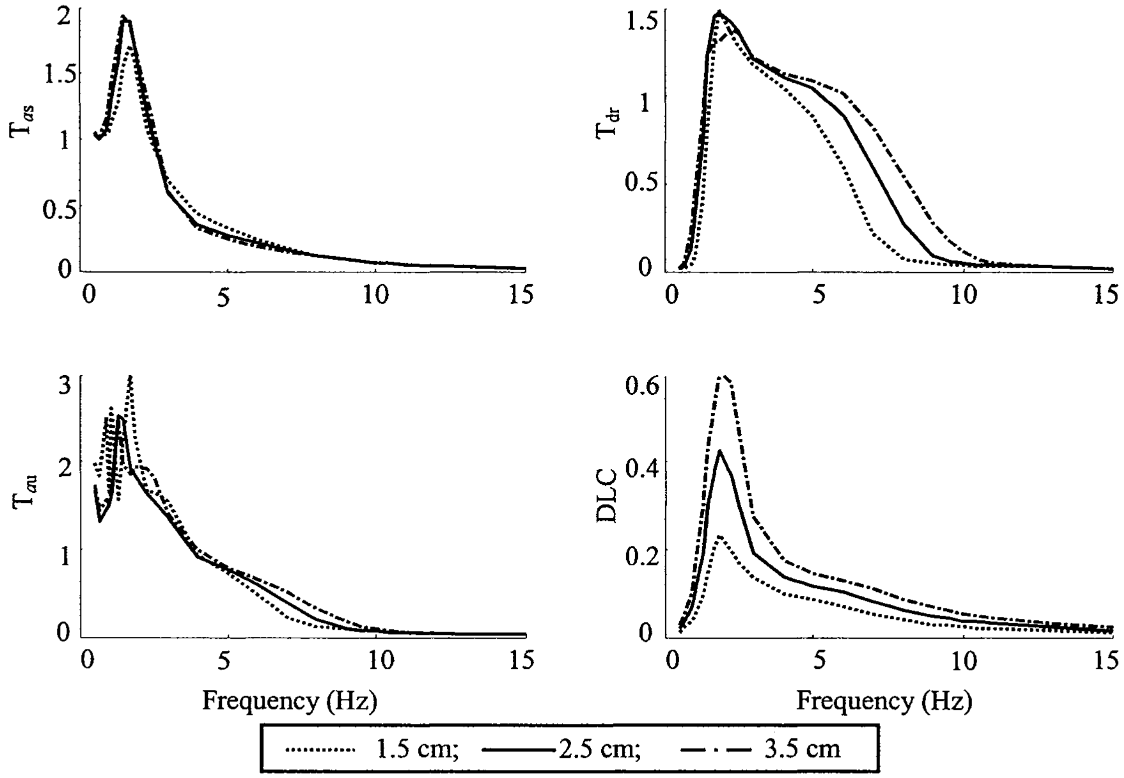

Figure 6.18: Influence of variations in excitation amplitude on the frequency response.

Figure 6.19 illustrates the influences of variations in the peak displacement (a_m=2, 3.5 and 5 cm) of the rounded pulse excitation on the transient responses of the quarter-vehicle model employing "inverse model"-based sliding mode ACM damping. The analyses are performed assuming identical values of all other parameters (μ=3 and ω_0=10.4 rad/s). The results show influences similar to those attained with the "inverse model"-based hi-lo semi-active damping (Figure 5.20). An increase in peak displacement yields higher peak damping force in response to the increased target force, and thus higher sprung mass acceleration. The peak magnitudes of absolute and relative displacements of the sprung mass also increase with increasing excitation.

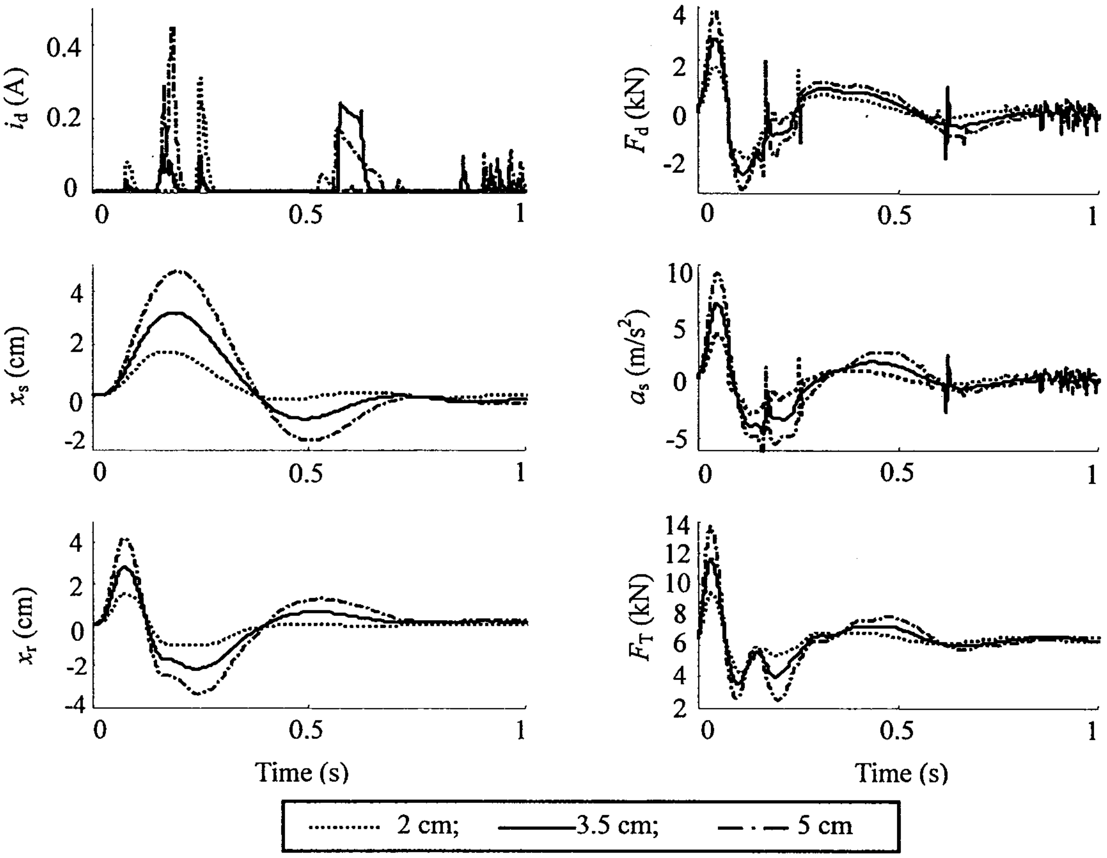

Figure 6.19: Influence of variations in peak rounded pulse displacement on the transient responses.

The transient response measures, summarized in Table 6.3, show relatively smaller deviations in the peak tire force due to variations in peak displacement of the rounded pulse. The peak force deviation (DTR) increases and decreases in the order of 30% and 29%, when the peak displacement is increased to 5 cm and decreased to 2 cm, respectively, from the nominal value of 3.5 cm. The corresponding changes in the sprung mass displacement and acceleration (SDR_s and SAR_s) ratios are +4.3% and -3.7%, while those in the unsprung mass shock displacement (SDR_u) ratio are +2.6% and -3.5%. Unsprung mass shock acceleration (SAR_u) and relative displacement (RDR) ratios, however, generally increase by 7.8% and 6.9%, and 6.2% and 7.5%, respectively, when peak displacement amplitudes are decreased and increased by 43%.

Table 6.3: Influence of road roughness variations on the transient response measures.

a_m (cm)	SDR_s	SAR_s	SDR_u	SAR_u	RDR	DTR
2.0	0.90	0.26	1.10	1.24	0.85	0.29
3.5	0.94	0.27	1.14	1.15	0.80	0
5.0	0.98	0.28	1.18	1.27	0.86	0.30

The influences of road roughness variations on the stochastic response characteristics are also evaluated by considering excitations due to medium-rough and rough roads, as described in Chapter 3. Figure 6.20 illustrates the influences of the road roughness on the PSD of the F_d, a_s, a_u, x_r and F_T responses and time variations in i_d. The results show tendencies that are similar to those observed from the random responses of the "skyhook"- and "inverse model"-based hi-lo semi-active damping controls, shown in Figures 4.21 and 5.21, respectively. The results suggest that operation on a road with higher surface roughness would yield higher damping force and sprung mass acceleration response in most of the frequency range. The relative displacement and tire force responses also increase with increasing roughness in most of the frequency range. The magnitudes of PSD of the responses, however, exhibit only slight sensitive to road roughness variations in the important ride frequency range (2-5 Hz). The DLC due to tire force for the rough random road excitation is in the order of 0.112, which is considerably higher than 0.054 obtained for the medium-rough road excitation.

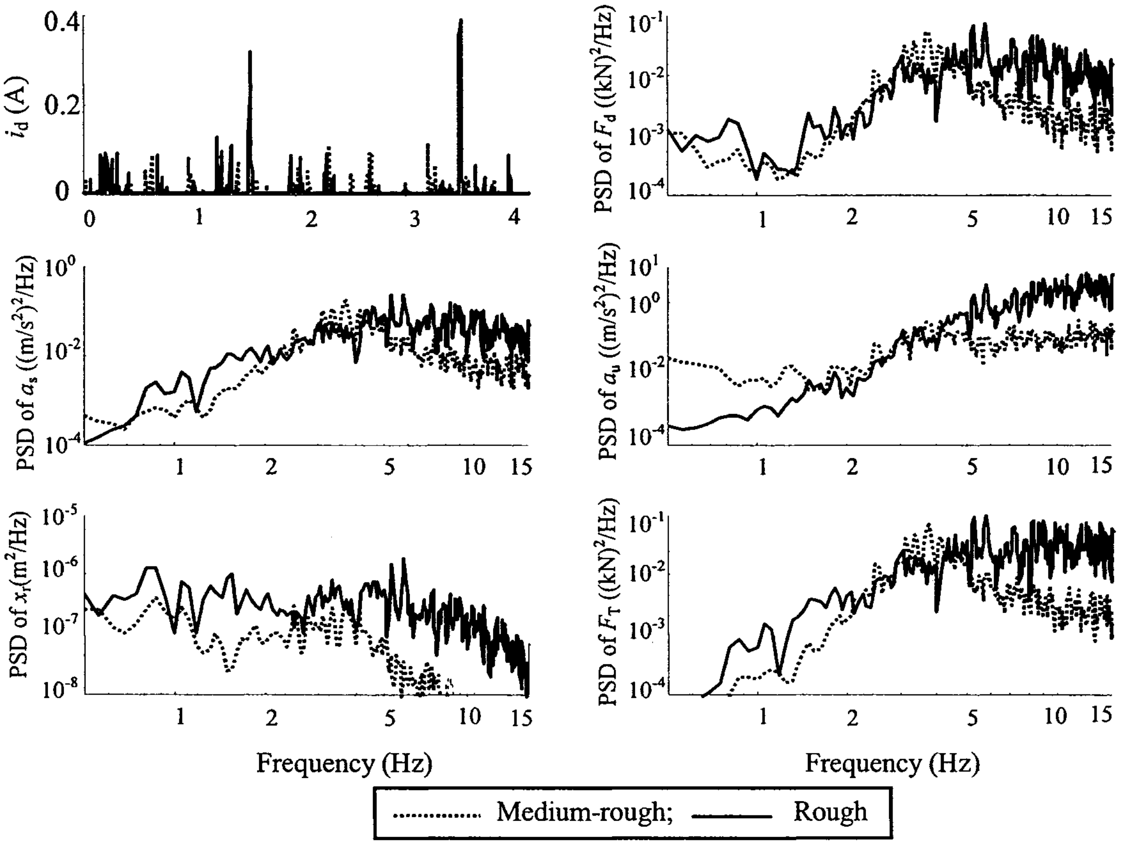

Figure 6.20: Influence of road roughness variations on the PSD characteristics of responses to the medium and rough random excitations.

6.5 Comparisons of Performance Characteristics of Different Controllers

The results presented in Chapters 4 to 6 suggest considerably different performance characteristics of the proposed "skyhook"-based hi-lo, "inverse model"-based hi-lo and "inverse model"-based sliding mode semi-active controllers, although some of the trends are comparable. The relative merits and disadvantages of the different controllers are discussed in view of measures related to the vehicle suspension performance.

Controller features

The proposed controllers are synthesized to realize hi-lo modulation in the drive current. The proposed continuous modulation (CM) function yields continuous variations in the command current for all the controller synthesis. The implementation of the ADFG function further suppresses the transient effects, while providing asymmetric damping control. The drive current in each synthesis is varied in the hi-lo manner to achieve light and hard damping on the basis of different semi-active conditions and controller algorithms, which reveal the following features:

- In the "skyhook"-based hi-lo controller, the drive current is limited to zero when $z_c = \dot{x}_s v_r \leq 0$, and varied in proportion to the sprung mass velocity using the controller order of 2, when $z_c<0$ This control algorithm offers far more significant potentials for realizing multi-objective suspension performances, when compared to the "inverse model"-based algorithms. The controller can also effectively suppress the transient oscillations in responses attributed to current switching and hysteresis nonlinearities of the MR-damper. The controller, however, poses a challenging task for measuring the sprung mass velocity for its real implementation.

- The "inverse model"-based hi-lo controller is based on the on-off semi-active control law, which generates light damping when the condition function $z_c = \dot{x}_r x_r \geq 0$. The controller is required to track the spring force F_k, when $z_c<0$. The drive current is derived using the proposed inverse model of the MR-damper. The proposed controller is based upon directly measurable response quantities, and offers superior merits in effectively compensating for the hysteresis effects. The controller, however, exhibits poor force-tracking ability in the low velocity range due to very light pre-yield damping of the MR-damper at low. While the force-tracking performance could be enhanced by increasing the pre-yield damping force, the corresponding increase in the post-yield damping tends to deteriorate the suspension performance in the important ride frequency range. The controller thus poses difficult compromise between the force-tracking and suspension performance.

- The "inverse model"-based sliding mode semi-active controller is based on the motion of sprung mass to track that of a nominal reference model. The sliding mode control law is used to design the target force (F_c), while the inverse model control law is integrated to realize the damping force F_d that tracks the target force F_c, when $z_c = F_c F_h > 0$. The controller can effectively compensate for the hysteresis effects and offers superior robustness on uncertainties due to sprung mass variations. The force-tracking ability of the controller, however, is very poor particularly in the pre-yield at low velocities, as described above for the hi-lo synthesis.

Suspension performances

The relative performance characteristics of the three control syntheses are evaluated under harmonic, rounded pulse and random excitations. The relative merits and limitations of the controllers are discussed on the basis of the responses attained under these excitations.

- The relative ride performance potentials of the semi-active damping syntheses could be evaluated from the frequency response characteristics. Comparisons of vibration transmissibility responses of the sprung mass acceleration (T_{as}) suggest that the "skyhook"-based hi-lo semi-active ACM controller of order 2 could offer both superior resonance control and vibration attenuation in nearly entire frequency range. The "inverse model"-based hi-lo sliding mode ACM controllers, on the other hand, yield slightly poor vibration attenuation in the important ride frequency range (2-7 Hz) but superior resonance control. Moreover, the "skyhook"-based hi-lo semi-active controller offers superior control of the peak shock ratio of the sprung mass acceleration, than the other two controllers. The PSD of the sprung mass acceleration responses attained for all three controllers further validate the above conclusion.

- For the road-holding performance, the results show that the "skyhook"-based hi-lo semi-active ACM controller offers superior unsprung mass acceleration (T_{au}) response in the vicinity of sprung mass natural frequency and lower values of DLC in the important ride frequency range (2-7 Hz) than the other two controllers. This synthesis, however, yields slightly higher unsprung mass response in the vicinity of the unsprung mass natural frequency.

- For the suspension rattle space performance, the results suggest that all three controllers yield superior relative displacement transmissibility (T_{dr}). The "skyhook"-based hi-lo semi-active ACM controller, however, yields slight higher rattle space response in the vicinity of unsprung mass natural frequency than the two inverse-model-based controllers.

Robustness on variations of operating parameters

The influences of variations of operating load, speed and road roughness are evaluated under harmonic, rounded pulse and random excitations for the different semi-active ACM controllers. The relative robustness of the control algorithms are discussed in view of the sensitivity of the responses to variations in the operating conditions.

- The proposed controllers generally suggest reasonably good robustness on the sprung mass variations, when frequency responses are considered under ±25% variation in the sprung mass (Figures 4.13, 5.13 and 6.12). The "inverse model"-based sliding mode semi-active ACM controller, particularly, yields superior robustness in view of the sprung mass resonance control than the other two controllers. This controller in ACM damping mode reveals relatively small deviations in peak tire forces, as evident form DTR in Tables 4.1, 5.1 and 6.1. The "inverse model"-based sliding mode semi-active ACM controller also yields relatively small changes in the sprung mass acceleration PSD response under the sprung mass variations considered, when compared to those observed for the other two controllers (Figures 4.15, 5.15 and 6.14). The DLC due to tire force increases by 54%, 61% and 55% for the "skyhook"-based hi-lo, "inverse model"-based hi-lo and "inverse model"-based sliding mode ACM controllers, respectively, when m_s is increased from 422 to 703 kg.

- For vehicle speed variations, the "inverse model"-based sliding mode semi-active ACM controller yields relatively smaller variations in the responses, when compared to those obtained for the other two controllers. This is particularly observed in the sprung mass displacement ratio (SDR_s) and the peak tire force (DTR) responses to a rounded pulse excitation, as evident from Tables 4.2, 5.2 and 6.2. The sprung mass accelerations PSD responses also exhibit relatively lower sensitivity to speed variations for the "inverse model"-based sliding mode ACM controller, as shown in Figures 4.17, 5.17 and 6.16.

- The "skyhook"-based hi-lo ACM controller yields relatively larger deviations in the response measures when excitation magnitudes are varied. This is particularly evident from the peak sprung and unsprung mass acceleration and relative displacement transmissibilities (T_{as}, T_{au} and T_{dr}). The same controller synthesis also yields relatively higher sensitivity of T_{au} and T_{dr} to variations in excitation magnitude, as evident from Figures 4.19, 5.19 and 6.18. The above observation is also supported by the stochastic responses of the three controllers under two different roughness excitations, as shown in Figures 4.21, 5.21 and 6.20.

6.6 Summary

In this chapter, the hysteresis effect reduction and force-tracking property of the proposed "inverse model"-based sliding mode semi-active controller are investigated through analysis of the "quarter-vehicle" model. The performance characteristics of the proposed "inverse model"-based sliding mode semi-active ACM controller are evaluated under deterministic as well as stochastic excitations. The sensitivity of the performance measures to variations in operating conditions, such load, speed and excitation magnitude are further investigated. The results are compared with those derived for the "inverse model"-based hi-lo semi-active ACM controller and the passive damping realized by setting fixed drive current. The results suggest that the proposed "inverse model"-based sliding mode semi-active ACM controller can effectively reduce the hysteresis effects of the MR-damper, and improve the force-tracking ability with larger passive hysteron force.

The results of the analyses are summarized below:

- The "inverse model"-based sliding mode controller can effectively reduce the transient oscillations caused by hysteresis nonlinearities of the MR-damper.
- The proposed controller exhibits superior force-tracking ability at higher velocities, but poor tracking at low velocities, as observed for the "inverse model"-based hi-lo controller. The force tracking performance could be enhanced by introducing higher passive hysteron force.
- The "inverse model"-based sliding mode ACM controller exhibits relatively lower sensitivity to variations in operating load.

CHAPTER 7

EXPERIMENTAL VALIDATIONS USING HARDWARE IN THE LOOP SIMULATIONS

7.1 Introduction

Assessments based on analytical formulations necessitate experimental validations, which may be performed either at the component or at the system level. The component level assessments are considered to be more efficient and permit thorough insight into dynamic behaviors of the component when uncoupled from the system. The validations at the system level, on the other hand, are quite complex and more demanding on the resources. Hardware-in-the-loop (HiL) test and simulation techniques offer assessments at the component level together with the coupling effects within the total system. The HiL technique is a real time simulation tool for efficient evaluations of electronic and mechanical components, and control systems, and has been implemented for wide ranges of applications in the automotive sector [19, 89-93]. The technique is ideally suited for experimental analyses of the MR-damper and the controller in conjunction with the "quarter-vehicle" model. The technique integrates the forces developed by the actual MR-damper within the "quarter-vehicle" model software in real-time.

The HiL simulation technique can be thus effectively applied to formulate and assess controller synthesis and the vehicle suspension performances using the idealized "quarter-vehicle" model. However, only a few studies have utilized the HiL technique for experimental assessments and tuning of the semi-active controller synthesis. Hwang *et al.*

[19] presented a method for assessing a continuously controlled semi-active suspension using HiL technique. Besinger *et al.* [91] described the laboratory tests for hydraulic dampers using HiL technique. Krohm *et al.* [92] applied HiL simulations and tests for developing an electronic clutch management system, used for automatic engagement of the clutch during start and for gear change. The hardware requirements and various capabilities of the HiL real-time simulation and test techniques have been summarized by Hansselmann [89, 90].

A HiL test platform was developed in the laboratory to validate the proposed analytical model of the MR-damper, and "quarter-vehicle" model performance with passive as well as semi-actively controlled MR-damper. Owing to the superior performance of the "skyhook"-based semi-active damping in relation to those of the "inverse model"-based controllers, the study is limited to the "skyhook"-based hi-lo semi-active MR-damping control. The "quarter-vehicle" model with both the passive and "skyhook"-based hi-lo semi-active damping is evaluated in symmetric (SCM) as well as asymmetric (ACM) modes. The passive damping mode with zero or nonzero constant currents is used to validate the MR-damper model formulation, in conjunction with the open-loop "quarter-vehicle" MR-suspension model.

7.2 Development of Hardware in the Loop Test Platform

The hardware in-the-loop (HiL) simulation technique can provide a realistic and repeatable testing environment with a relative low power hydraulic actuator. The schematic diagram of a HiL test platform developed in this study is shown in Figure 7.1. The platform comprises three major components: (i) damper hardware; (ii) "quarter-vehicle" simulation model; and (iii) interface between the hardware and the simulation model. The candidate MR-damper is installed on a servo-hydraulic motion generator, while its rod-end is attached to an inertial frame through a strain gage-based force sensor (capacity=8.8 kN) to measure the damping force. A linear variable differential transformer (LVDT) is integrated within the actuator to measure the actuator displacement and thus the compression/extension of the damper.

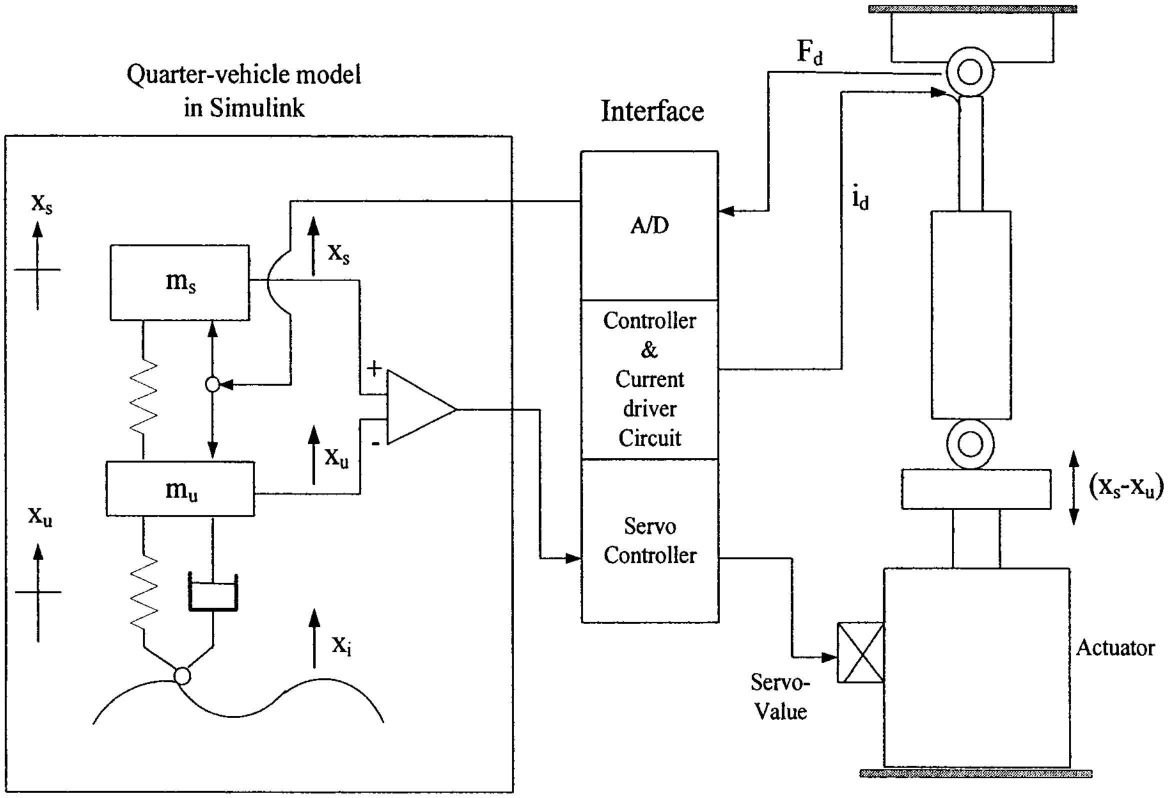

Figure 7.1: Schematic diagram of the HiL test platform for MR-suspension study.

The "quarter-vehicle" simulation model in the absence of MR-damper is developed in the Matlab-Simulink environment, as illustrated in Figure 7.1. The simulation component involves Matlab Simulink equation solver for the "quarter-vehicle" model in the absence of the MR-damper. The relative deflection response across the suspension is used to derive the command signal for the servo-actuator, which is fed to the servo controller (MTS 407) through the digital-to-analogue (D/A) converter. The resulting motion of the hydraulic actuator is identical to the instantaneous relative motion across the damper. The resulting force developed by the damper hardware in response to instantaneous velocity and drive current is measured using the force sensor. This force is supplied to the sprung and unsprung masses of the model through the analogue-to-digital (A/D) converter to close the loop and permit the analysis of the total quarter-vehicle model with the MR-damper. The Simulink program further permits the controller synthesis and the feedback variables required for the controller synthesis. The interface component includes the servo-controller to generate the desired actuator motion, A/D and D/A converters, and the voltage to current circuit to supply the desired drive current for the MR-damper. The dynamic data exchange is further integrated to download the measured data in an Excel Worksheet. Macros are developed for on-line displays of the response and excitation variables, and performance measures of interest. The method enables the study of variations in vehicle model parameters to facilitate analyses of controller syntheses under wide ranges of operating conditions.

7.2.1 Test methodologies

The HiL test and simulation technique is used to examine the validity of the MR-damper model, and the "quarter-vehicle" model with passive as well as "skyhook"-based hi-lo semi-active MR-damper. The experiments are performed under harmonic, transient and random excitations, formulated within the Simulink platform. Experiments with passive damping were initially conducted under 1.5 cm amplitude harmonic excitation at 1.5 Hz. The amplitude of excitation was increased to 2 cm for the semi-active damping. Frequency response characteristics of the passive as well as semi-active damper were derived from responses attained under excitations at different discrete frequencies (0.75, 1, 1.25, 1.75, 2, 2.5, 3, 4, 5.0, 6, 8, 10, 12 and 15 Hz). The amplitude was held at 1.5 cm and 2 cm for passive and semi-active dampers, respectively, at frequencies below 2 Hz. The amplitudes, however, were gradually decreased to maintain constant acceleration peak equal to that attained at 2 Hz, as described in Chapter 3.

The responses were also measured under a rounded pulse excitation of peak displacement of 2 cm, ω_0=10.4rad/s and μ=3, as described in section 3.5.1. The road roughness data described for the rough road in Chapter 3 was scaled to 50% and supplied as the input file for the Simulink program, while the experiments and simulations were performed at a speed of 50 km/h. The assessments under harmonic excitations were performed for two levels of fixed current, i_d=0 and i_d=0.1 A. Owing to occasional high velocities under transient and random excitations, the higher current value was limited to 0.05 A to ensure safety of the damper and the test system. The measurements were performed in the symmetric (SCM) and asymmetric (ACM) modes, where the command signals were derived from EQ (3.16), using p=0 (for ACM) and p=1 (for SCM).

7.2.2 Description of HiL platform and drive circuit

The HiL test system, pictorially shown in Figure 7.2, consists of: (i) a servo-hydraulic exciter and MTS-407 controller; (ii) a load cell to measure the damper force; (iii) a LVDT displacement transducer built within the actuator; (iv) A/D to D/A boards to interface the instantaneous force and displacement data; (v) a thermocouple to monitor the damper temperature; (vi) Visual Designer software and Excel Workbook for on-line analyses and display of the data; and (vii) a command current drive circuit. A personal computer, equipped with a digital signal processing (DSP) board containing eight channels of 12-bit A/D and D/A converters, was interfaced with the hardware. The simulation program was developed to generate the damper command current following specific control laws to study the effectiveness of a particular synthesis.

The MR-damper was driven by the hydraulic actuator, which tracks the desired suspension displacement. A current driver was designed to provide command current to the MR-damper in accordance with the controller design through the D/A interface. The vehicle model in the HiL apparatus was excited by synthesized harmonic, transient and random road profiles, described above. The damper body temperature was constantly monitored using a thermocouple mounted on the damper body, while the measurements were taken in the 30~40°C range. The MR-damper is controlled by an input current, while the maximum current output of the DSP-Board was only 25 mA at its maximum voltage of 10 V. A specific direct current (DC) drive circuit, shown in Fig. 7.2, was thus designed to amplify the command signal to meet the power requirement of the MR-damper.

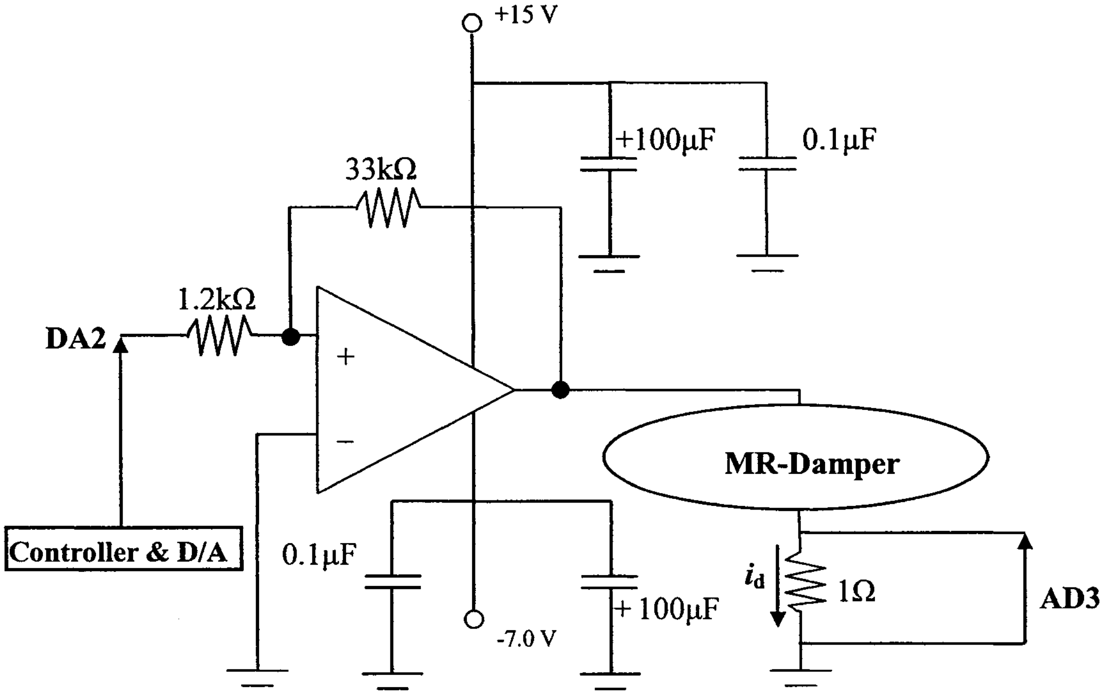

Figure 7.2: Command current amplification circuit.

Owing to the time delays associated with the servo-controller and drive current circuit, a PID feedback technique was employed to compensate for the delays in the drive current. For this purpose, a resistance (1Ω) was integrated in the current amplifier circuit to provide the feedback signal, as shown in the Figure. The proportional, integral and derivative (K_P, K_I and K_D) gains were adjusted in order to minimize the delay. Repetitive measurements revealed that gain values of K_P=1, K_D=0 and K_I=3000 could effectively reduce the rise time and the steady-state error. A nonzero derivative gain is not recommended, as it causes excessive noise in the velocity and acceleration signals. The drive current was limited to 0.3 A to ensure safe operation of the employed MR-damper and the force transducer. The PID regulator was formulated within the Simulink platform, where the controller signal and the PID regulator served as the input to drive current generator (DA2). The output current i_d, through the sampling voltage across the 1Ω resistor (AD3), formed the feedback signal for the PID regulator through the A/D converter.

7.2.3 Design of HiL simulation monitor

A real-time monitor was designed to assess and monitor the responses of the quarter-vehicle model in the HiL platform, and to select the excitation, controller synthesis, and the output displays. Figure 7.3 illustrates a sample display of the designed monitor. The control options in the layout consisted of three main modules: (i) controller option, (ii) excitation option; and (iii) associated switches. The controller option allowed for selection of control laws. A total of five control laws were formulated in the monitor: passive damping (i_d=0), fixed current damping ($i_d \neq 0$), "skyhook"-based hi-lo, "inverse model"-based hi-lo and "inverse model"-based sliding mode semi-active damping. The excitation option also permitted for selection of the excitation signal, $x_i(t)$, together with the parameters: a zero input at the beginning and end of an experiment (x_i=0), harmonic excitation (frequency and amplitude), transient excitation, and random road excitation. The associated switches allowed for selection of asymmetry factor (p) for changing the damping mode (SCM or ACM), sprung mass (m_s) to vary the vehicle load parameter, controller gain (k_c) for "skyhook"-based hi-lo semi-active controller. Moreover, this option allowed for entering the parameters of the "quarter-vehicle" model.

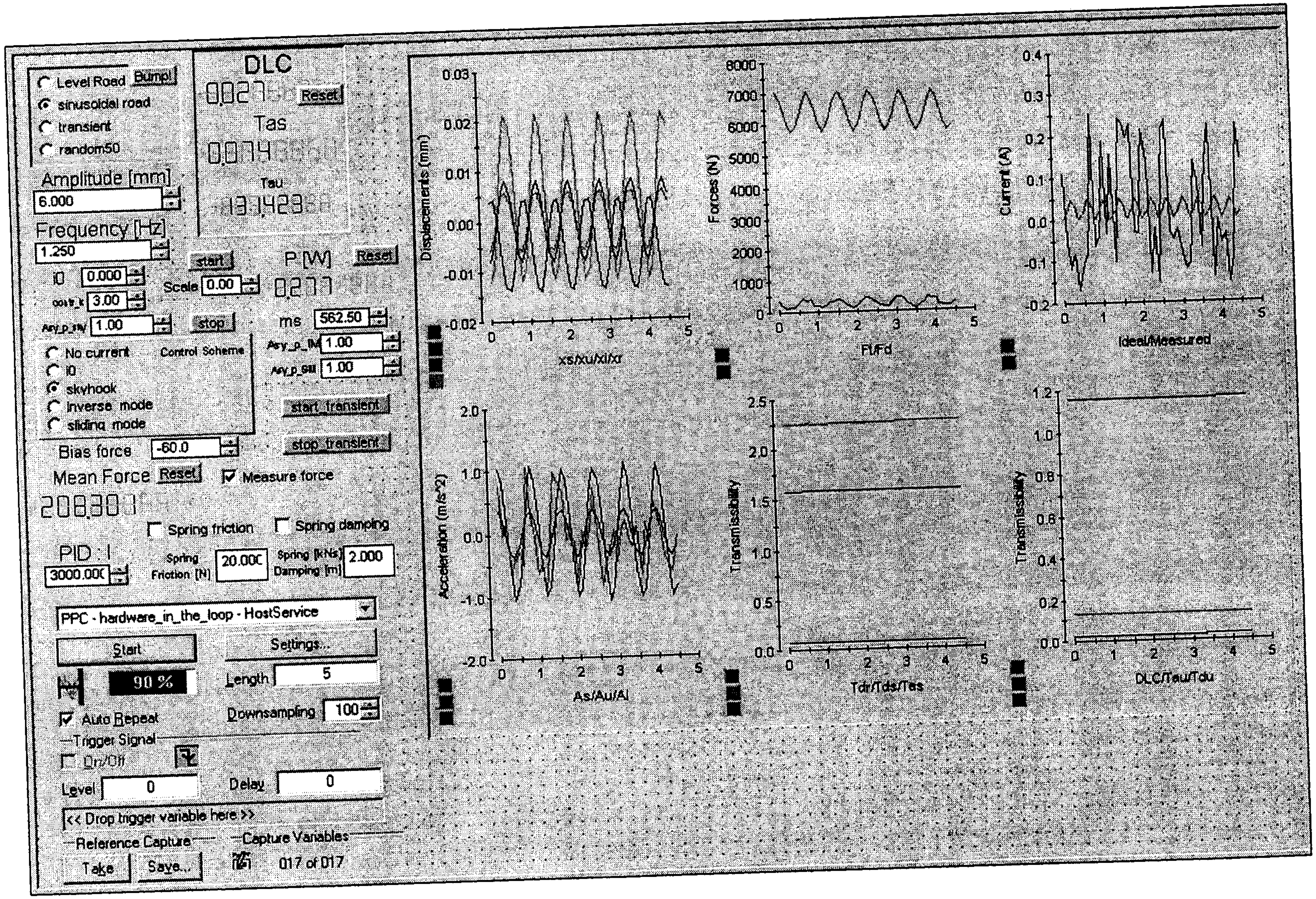

○ Level Road
● sinusoidal road
○ transient
○ random50

Amplitude [mm] 6.000

Frequency [Hz] 1.250

i0 0.000

coulr_k 3.00

Ary_p_my 1.00

Scale 0.00

ms 562.50

Ary_p_IM 1.00

Ary_p_sM 1.00

DLC 0.027

Tas 0.074

Tau 13.1423

P [W] 0.277

Control Scheme
○ No current
○ i0
● skyhook
○ inverse mode
○ sliding mode

Bias force -60.0

Mean Force 20830.1

☑ Measure force

☐ Spring friction

☐ Spring damping

PID : I 3000.000

Spring Friction [N] 20.000

Spring [kNs] Damping [m] 2.000

PPC - hardware_in_the_loop - HostService

90 %

Length 5

☑ Auto Repeat

Downsampling 100

Trigger Signal

☐ On/Off

Level 0

Delay 0

<< Drop trigger variable here >>

Reference Capture

Capture Variables

017 of 017

Figure 7.3: A dSpace layout for monitoring responses and controlling test parameters.

Selected dynamic responses and measures of suspension performance were also displayed in the monitor. These included measured and computed drive current (i_{dm}, i_d) and MR-damper force (F_{dm}, F_d), computed dynamic tire force (F_t), displacement and acceleration responses of the sprung and unsprung masses (x_s, a_s, x_u, a_u), suspension relative displacement (x_r), and displacement and acceleration due to excitation (x_i, a_i). The displayed suspension performances included the displacement and acceleration transmissibilities of the sprung and unsprung masses (T_{ds}, T_{as}, T_{du}, T_{au}), rattle space transmissibility (T_{dr}) and dynamic load coefficient due to tire force (DLC). The displayed dynamic responses and suspension performance measures were simultaneously recorded through creating a Dynamic Data Exchange (DDE) stream linked to the Excel Workbook. The panel on the lower left-hand side further allowed for acquisition parameters and sorting the curves, such as acquisition period, triggering, and sampling rate.

Prior to an experiment, the hydraulic actuator was reset at its desired equilibrium position and the force signal was zeroed, while the current was set to 0 A to prevent accidental damages. The equilibrium position was chosen as the mid-compression of the damper. The Simulink model was then loaded and servo-controller was activated by setting the desired span. Additional light viscous damping was introduced in parallel to the MR-damping force to eliminate the transient noise during the start-up. This damping was suppressed after the start-up. The quarter-vehicle MR-suspension model was programmed in Matlab Simulink, where the MR-damper model was replaced by the measured damping force (F_{dm}). The Simulink program was developed including different controller schemes, as shown in Figure 7.4. Figures 7.5 and 7.6 illustrate the detailed controller and excitation blocks

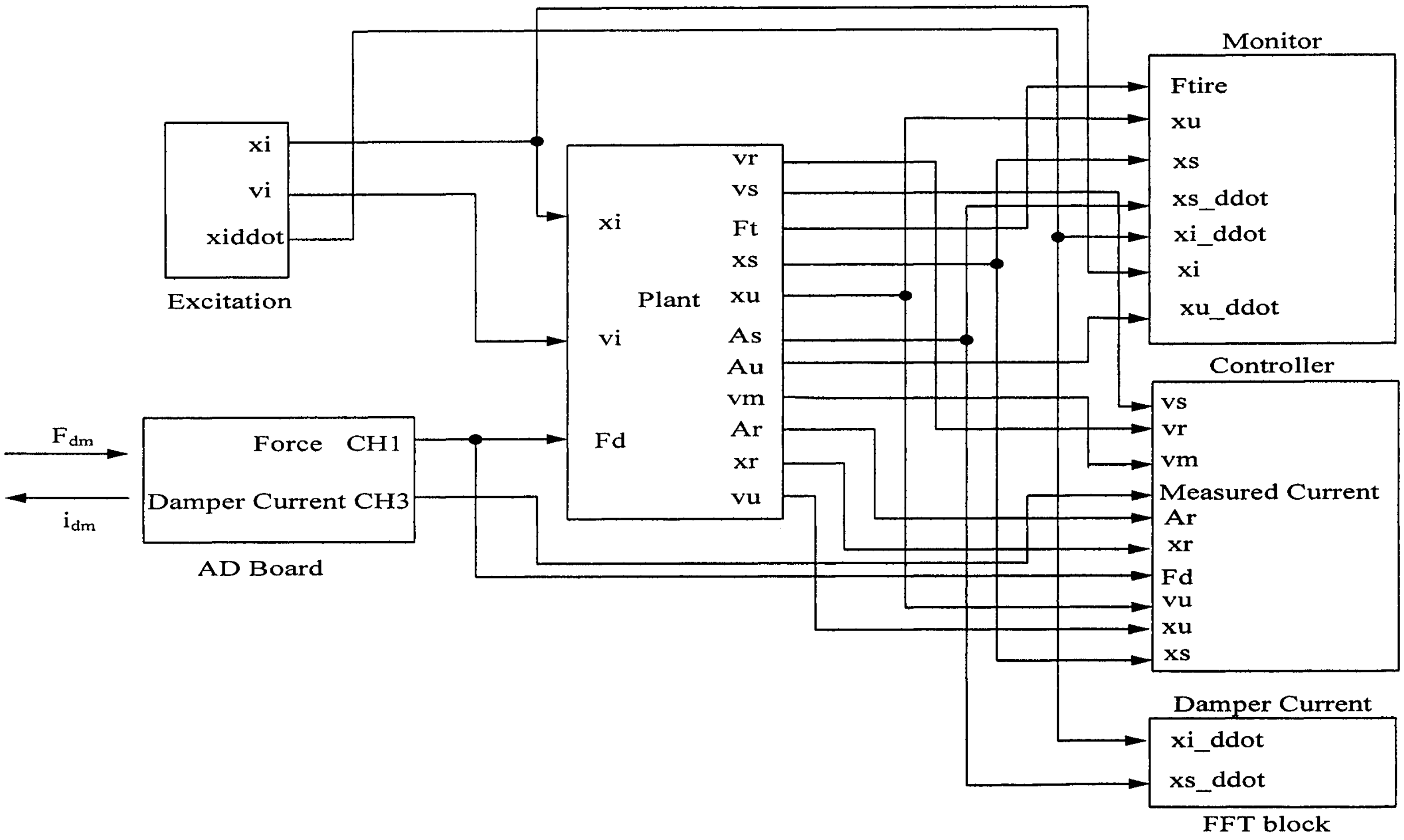

Figure 7.4: Structure of the Simulink model of the MR-suspension system.

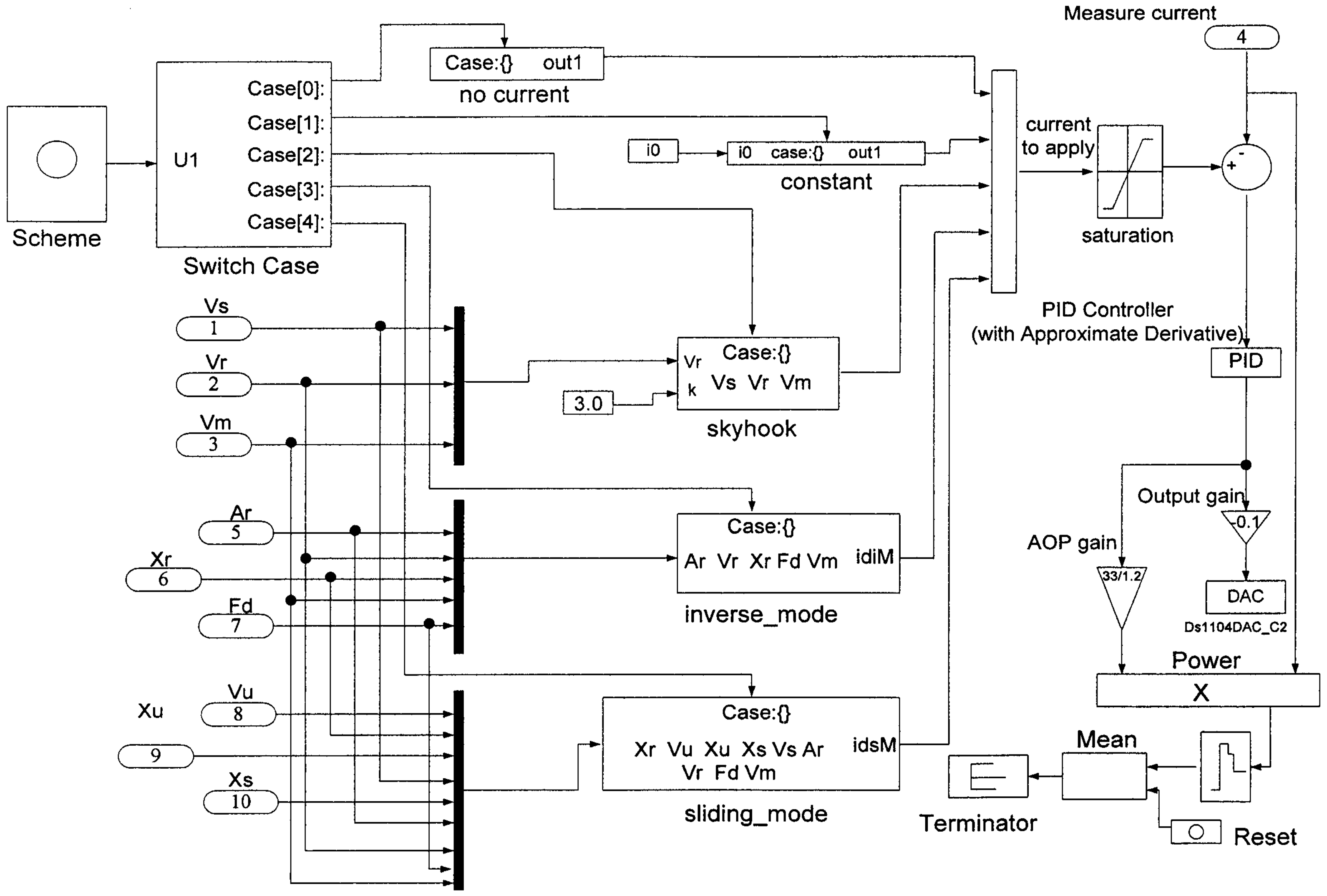

Figure 7.5: Controller block.

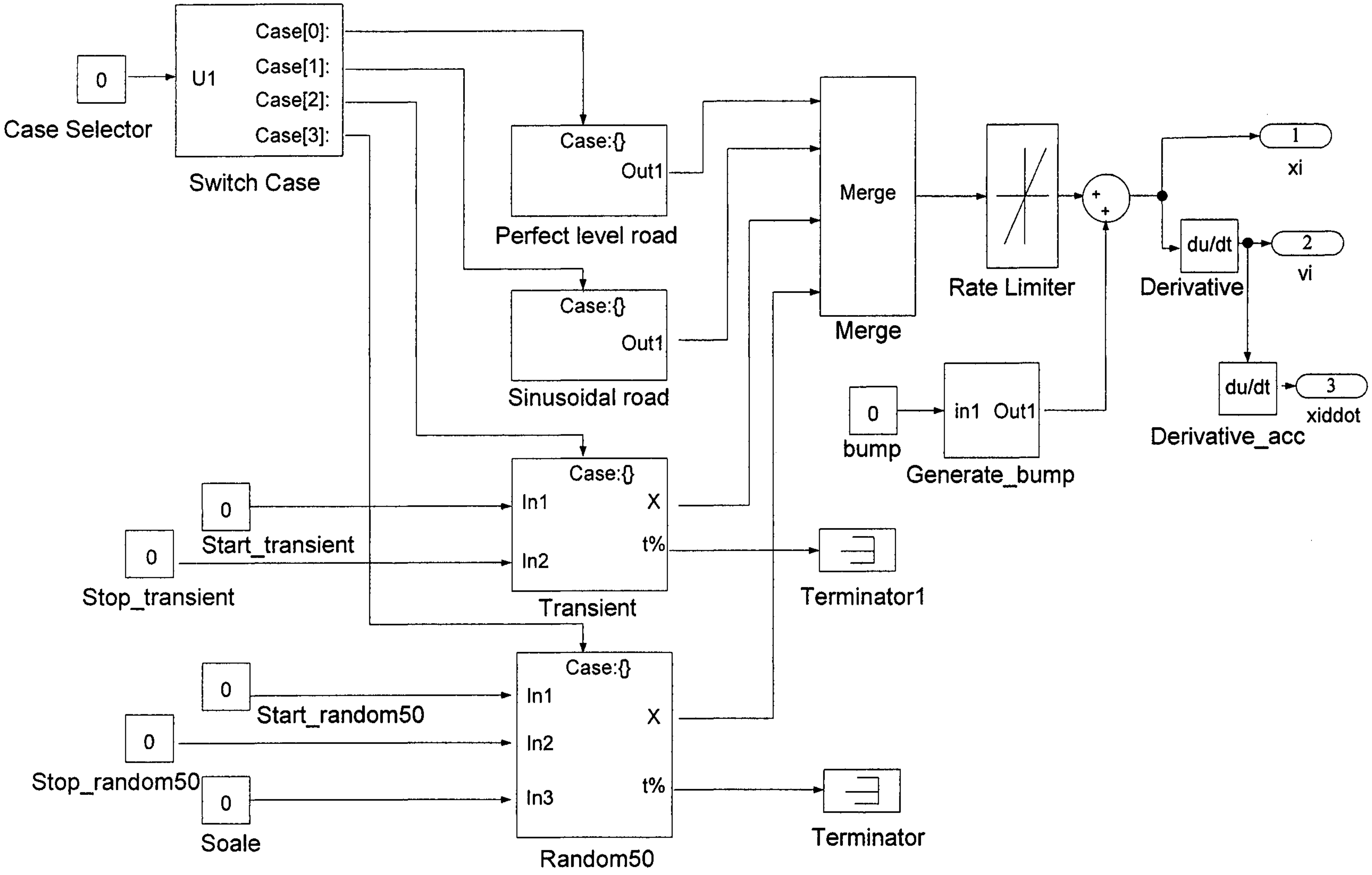

Figure 7.6: Excitation block.

7.3 HiL Simulation and Test Results

HiL simulations and tests were performed under different excitations, and damper and controller settings. The results were compared with those derived from analyses of the corresponding models to examine the model validity. The results derived for the "quarter-vehicle" models with passive and "skyhook"-based hi-lo semi-active damping are presented and discussed in the following sections.

7.3.1 Validation of the passive MR-damping suspension

The experiments were initially performed under constant levels of damper current to realize passive damping mode. Two levels of fixed drive currents were used, and the measured data are compared with the results derived from the "quarter-vehicle" model (section 4.3.2) to demonstrate validity of the model and the HiL test technique. The force-velocity data acquired for the damper are further used to demonstrate the validate of the nonlinear MR-damper model, described in EQ (2.15).

Response to Harmonic Excitations

Figure 7.7 shows the comparisons of time-histories of the measured and computed responses of the "quarter-vehicle" model with passive MR-suspension damping (i_d=0.1), while subject to 1.5 cm harmonic displacement excitation at a frequency of 1.5 Hz. The results are presented in terms of damping force (F_d), drive current (i_d), sprung and unsprung mass accelerations (a_s, a_u), tire force (F_T), suspension travel (x_r) and sprung and unsprung mass displacements (x_s and x_u). The simulation results show reasonably good agreements with the measured data, except for relatively small deviations in peak response amplitudes. The measured drive current exhibits high frequency noise in the order of 2%, which is attributed to the noise induced by the drive circuit shown in Figure 7.2.

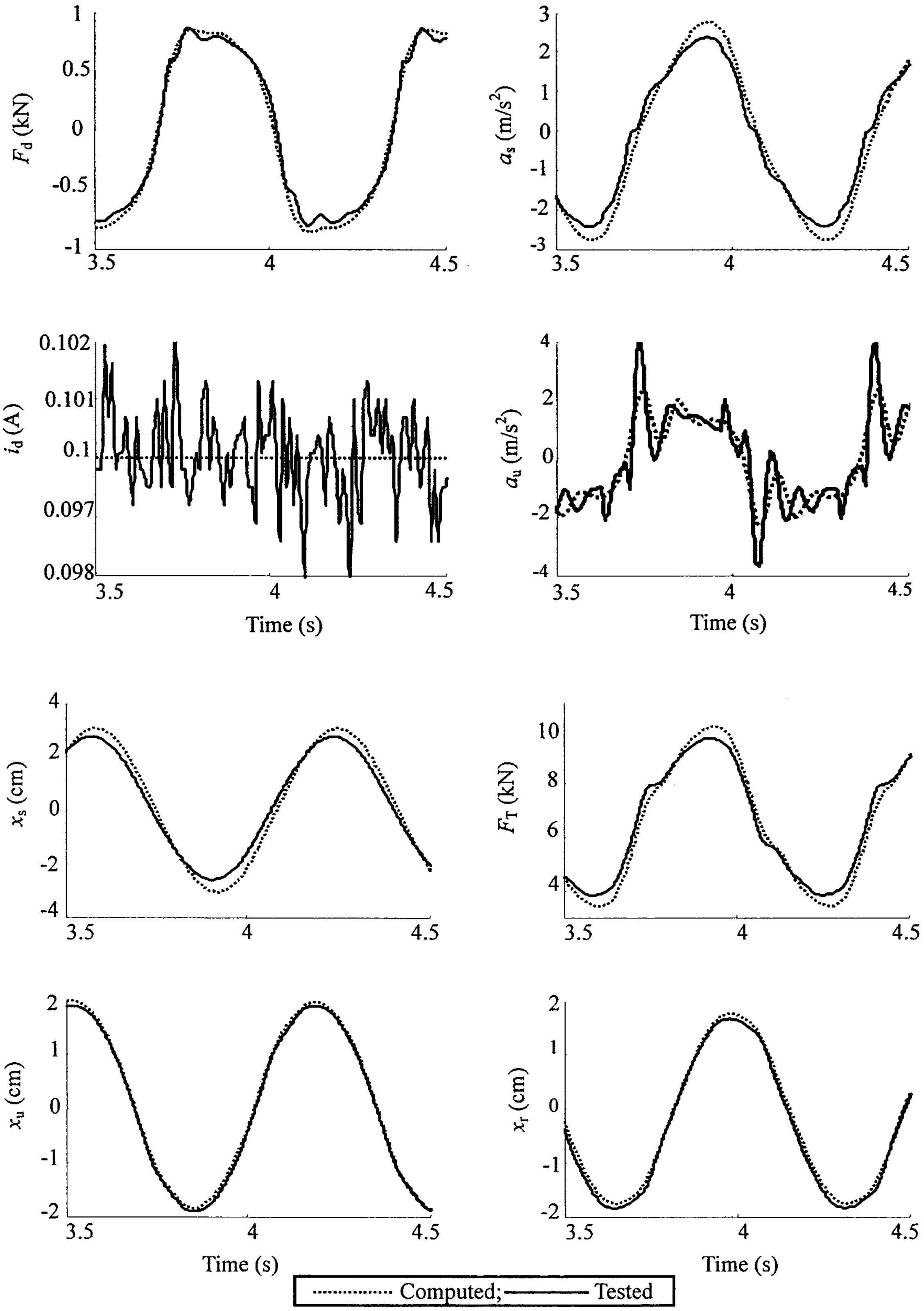

Figure 7.7: Comparisons of model and measured responses of "quarter-vehicle" model with passive MR-suspension damping under harmonic excitation (f=1.5 Hz and a_m=1.5 cm).

The measured damping force and velocity are further analyzed to derive the force-velocity characteristics of the damper under the selected excitation. The measured characteristics are compared with those derived from the generalized model of the MR-damper, presented in Chapter 2. Figure 7.8 shows a comparison of the measured and computed *F-v* characteristics of the passive MR-suspension with i_d=0.1A. The measured data exhibits trends similar to those observed from the model results with some deviations. The distortions observed in the measured *F-v* curve are believed to be caused by the slight time delays of the HiL test system.

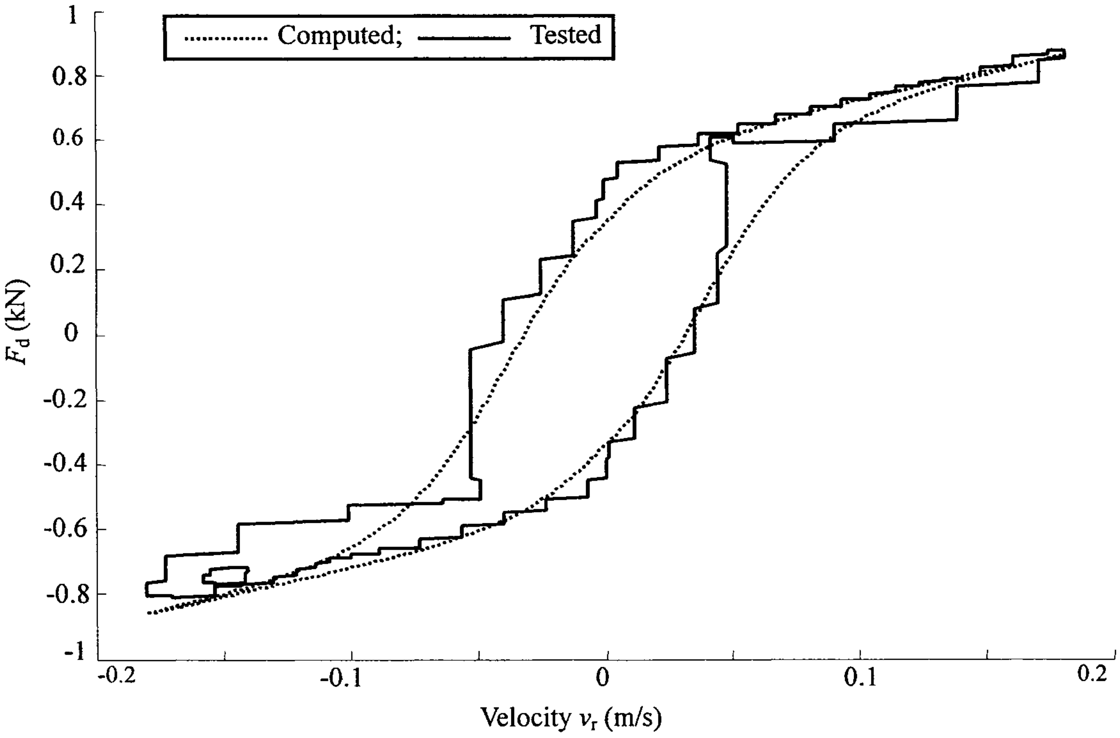

Figure 7.8: Comparison of the computed and measured *F-v* characteristics of the MR-damper (i_d=0.1 A, *f*=1.5 Hz, a_m=1.5 cm).

Figure 7.9 further presents comparisons of the measured and computed frequency responses of the "quarter-vehicle" model with passive MR-damper (i_d=0 and 0.1 A) in terms of sprung and unsprung mass acceleration transmissibilities ($T_{\alpha s}$, $T_{\alpha u}$) and relative displacement transmissibility (T_{dr}), and DLC due to tire force. The experiments were performed under harmonic excitations at different discrete frequencies (0.75, 1, 1.25, 1.75, 2, 2.5, 3, 4, 5.0, 6, 8, 10, 12 and 15 Hz). The displacement amplitude was maintained as 1.5 cm at frequencies equal to or less than 2 Hz, which was gradually decreased as $1.5\times(2.0/f)^2$ cm at frequencies above 2 Hz to ensure constant acceleration excitation, as described in section 3.5.1. The results generally show reasonably good agreements between the measured and model responses in majority of the frequency range. The results also show some deviations in the unsprung mass acceleration and tire force responses. These differences, particularly at higher frequencies, are attributed to poor damper performance under high frequency excitation, as described in section 2.2.2. Owing to somewhat discontinues and oscillatory damping force, the model parameters were identified on the basis of the measured data at lower frequencies (0.5-5 Hz).

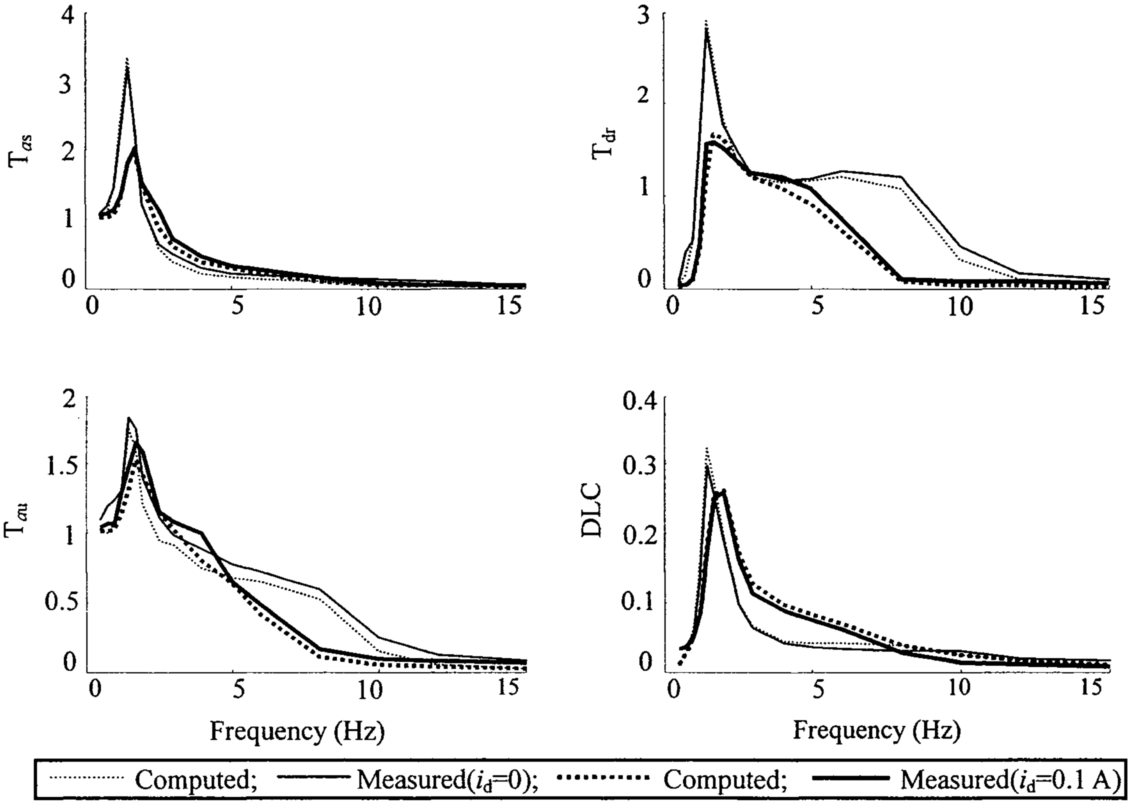

Figure 7.9: Comparisons of computed and measured frequency responses of the "quarter-vehicle" model with passive MR-damping (i_d=0 and 0.1 A).

The results show that the higher passive damping (i_d=0.1 A) yields lower peak magnitudes of T_{as}, T_{au}, T_{dr} and DLC when compared to those obtained with lower damping (i_d=0) in the vicinity of the sprung mass resonance. The magnitudes of T_{au} and T_{dr} for i_d=0.1 A are also lower than those attained with lower damping in the important ride frequency range. The magnitudes of T_{as} and DLC in the middle frequency range, however, tend to be slightly higher with higher damping. From the results, it can be concluded that the proposed MR-damper model can accurately characterize the "quarter-vehicle" responses in the frequency range of interest. Moreover, the results confirm the earlier observations that passive damping with non-zero control current yields superior control of sprung mass resonance response and road-holding performances than that of the MR-suspension with the light damping. Higher current and thus damping force tends to deteriorate the vibration isolation performance slightly in the ride frequency range.

Response to Rounded Pulse Excitation

A rounded pulse excitation (μ=3, ω_0=10.4rad/s and a_m=2 cm) is applied in the Simulink model and the transient damping force and responses of the passively-damped "quarter-vehicle" model. Owing to the high magnitude peak responses, the drive current in this case was chosen as 0.05 A. Figure 7.10 illustrates comparisons of the measured data with the corresponding model responses in i_d, F_d, x_s, a_s, a_u, x_r and F_T. The results show very good agreements between the measured and computed sprung mass responses, and reasonably good trends in the acceleration, and damping and tire force responses. The measured responses, however, do not show the primary shock response peak, which is attributed to high frequency nature of the shock response. It should be noted that the

MR-damper model parameters were identified on the basis of the measured data attained in the lower frequency range (0.5-5 Hz). The model may thus yield errors at higher frequencies. Moreover, the limited band-width of the servo-hydraulic system would also cause distortion of the transient response.

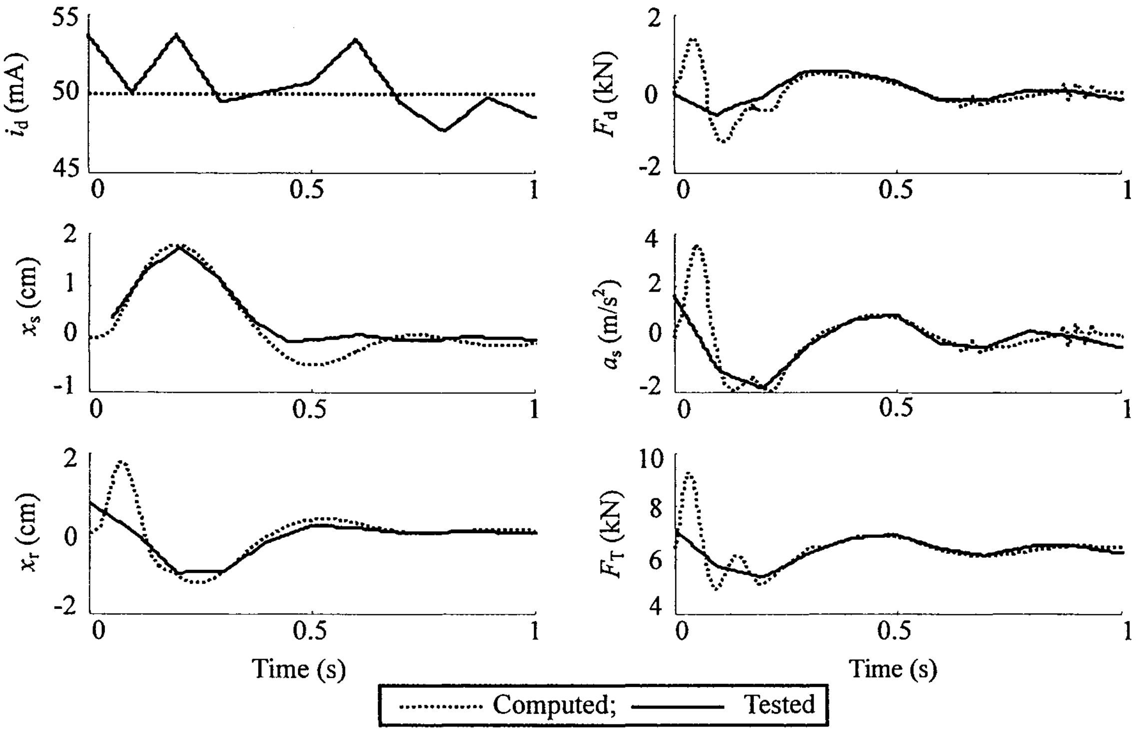

\

Figure 7.10: Comparisons of computed and measured transient responses of the "quarter-vehicle" model with passive MR-damper (i_d=0.05 A) under a rounded pulse excitation (μ=3, ω_0=10.4rad/s and a_m=2 cm).

Responses to Random Excitation

The experiments are also performed under excitation due to random rough road, described in Figure 3.10(b). The road elevations, however, are attenuated by 50% to ensure safety oif the damper hardware and the force transducer, while the forward speed is chosen as 50 km/h. The quarter-vehicle model with passive MR-damper is also analyzed under the same excitation. Model results are compared with the measured data in Figure 7.11. The results are presented for two levels of passive damping realized upon setting drive current of 0 and 0.05 A. Figures 7.11 (a) and (b) show comparisons of PSD of the measured and model responses (a_s, x_s, a_u, x_u) of the passive MR-suspension with i_d=0 and 0.05 A, respectively.

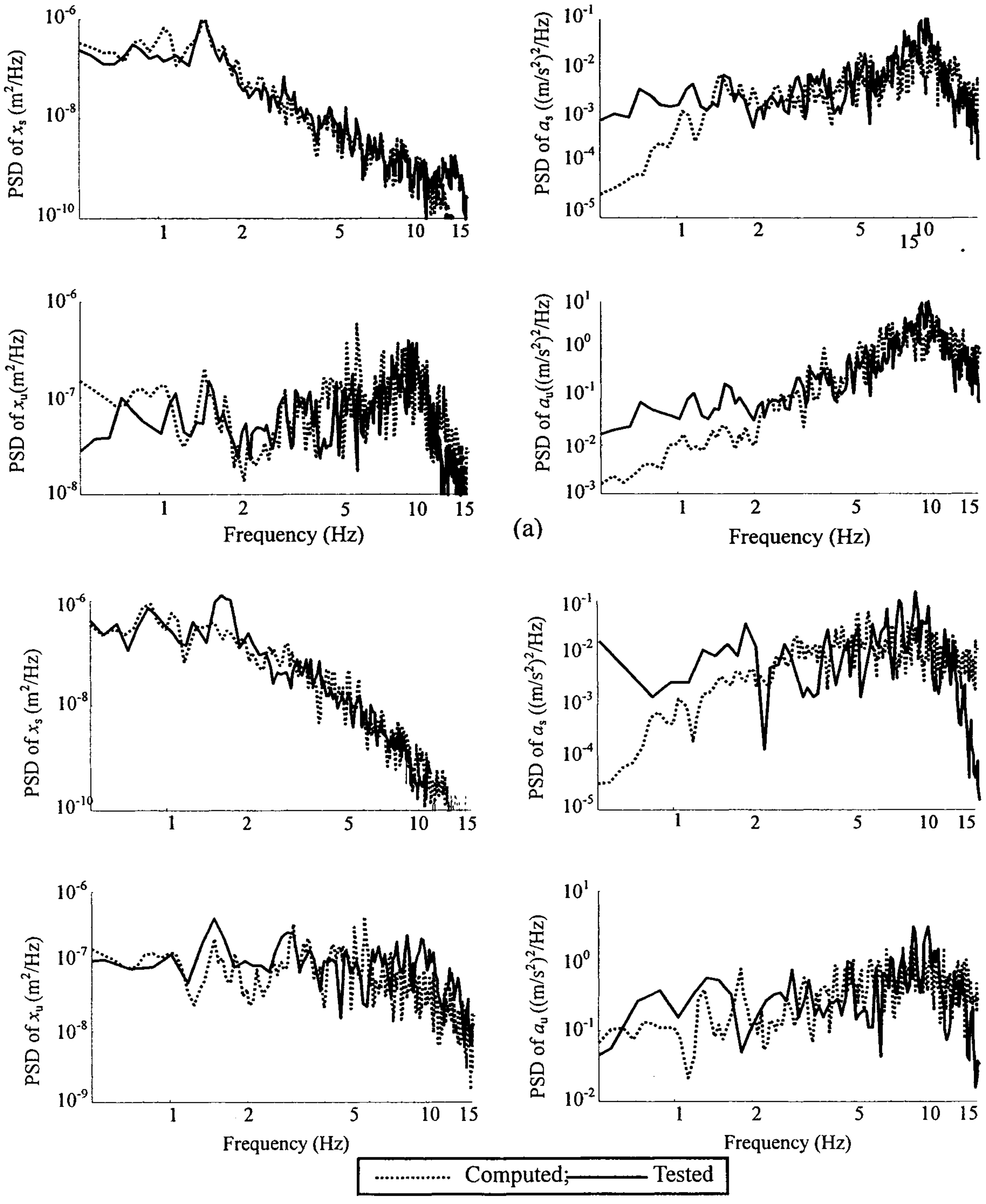

(b)

Figure 7.11: Comparisons of PSD of the measured and computed responses of the "quarter-vehicle" model with passive MR-damping under random road excitation: (a) i_d=0; and (b) i_d=0.05 A.

The results show reasonably good agreements between the measured and calculated responses. Some deviations, however, are evident in the acceleration responses at very low frequencies, which are attributed to noise in the low frequency acceleration signals that are of relatively lower magnitudes. The results thus suggest that the proposed MR-damper model can accurately characterize the property of the MR-damper hardware and the "quarter-vehicle" model under random road excitations. A higher passive damping is desirable for improved resonance control.

The above comparisons between the measured and simulation results for the quarter-vehicle model with passive MR-damper demonstrate reasonably good validity of the proposed MR-damper model under zero and non-zero control currents, and different deterministic and random excitations.

7.3.2 Validations of the skyhook based hi-lo semi-active suspension

The validity of the proposed "skyhook"-based hi-lo semi-active damping formulation in SCM and ACM, described in EQ (3.23), is examined through HiL measurements under deterministic and stochastic excitations. The HiL simulation is configured to realize the "skyhook"-based semi-active damping in both the symmetric and asymmetric modes using the control algorithm and condition function described in section 2.3.1. The nominal sprung mass is chosen as 563 kg and the drive current and selected responses are monitored using the monitor. The influence of variations in the sprung mass on the damping force and quarter-vehicle model responses are also measured and compared with the corresponding model responses. For this purpose, the sprung mass is increased to 703 kg. The controller parameters for all cases are chosen as: n=2, k_c=3, p_c=0, ξ_c=10, ξ=4.5 and p=1 for the symmetric damping control mode (SCM) and p=0 for asymmetric control mode (ACM).

Harmonic excitations

The experiments are initially performed under 2 cm harmonic displacement excitation at 1.5 Hz to study the sprung mass resonance response and control performance of the "skyhook"-based hi-lo semi-active MR-suspension. Subsequently, the measurements are performed under harmonic excitations at different discrete frequencies (0.75, 1, 1.25, 1.75, 2, 2.5, 3, 4, 5, 6, 8, 10, 12 and 15 Hz), as described in the previous section for the passive MR-damper. Figures 7.12 and 7.13 show comparisons of the measured and computed dynamic responses of the quarter-vehicle model with "skyhook"-based hi-lo semi-active MR-damper in SCM and ACM controls, respectively, under 2 cm harmonic displacement excitation at 1.5 Hz. The figures show time variations in F_d, i_d, a_s and a_u, F_T, x_r, x_s and x_u. The results show reasonably good agreements between the measured and model responses for both damping control modes. The results further show that the hysteresis and force-limiting nonlinearities effects of the MR-damper are effectively compensated, while the implementations of the continuous modulation (CM) and ADFG functions help suppress the switching transients.

The ACM control mode generates larger damping force (F_d) in rebound than in compression, and thus yields shifts in the sprung mass and relative displacement (x_s, x_r) responses. The asymmetric control mode yields asymmetric variations in current and slightly higher magnitudes of a_s, x_s and x_r, as evident from Figure 7.13. As stated in the previous chapters, the ACM control offers superior benefits for improved road-holding performance than the SCM control. The results presented in Figures 7.12 and 7.13 demonstrate validity of the proposed semi-active suspension model under harmonic excitation in the vicinity of the sprung mass resonance frequency.

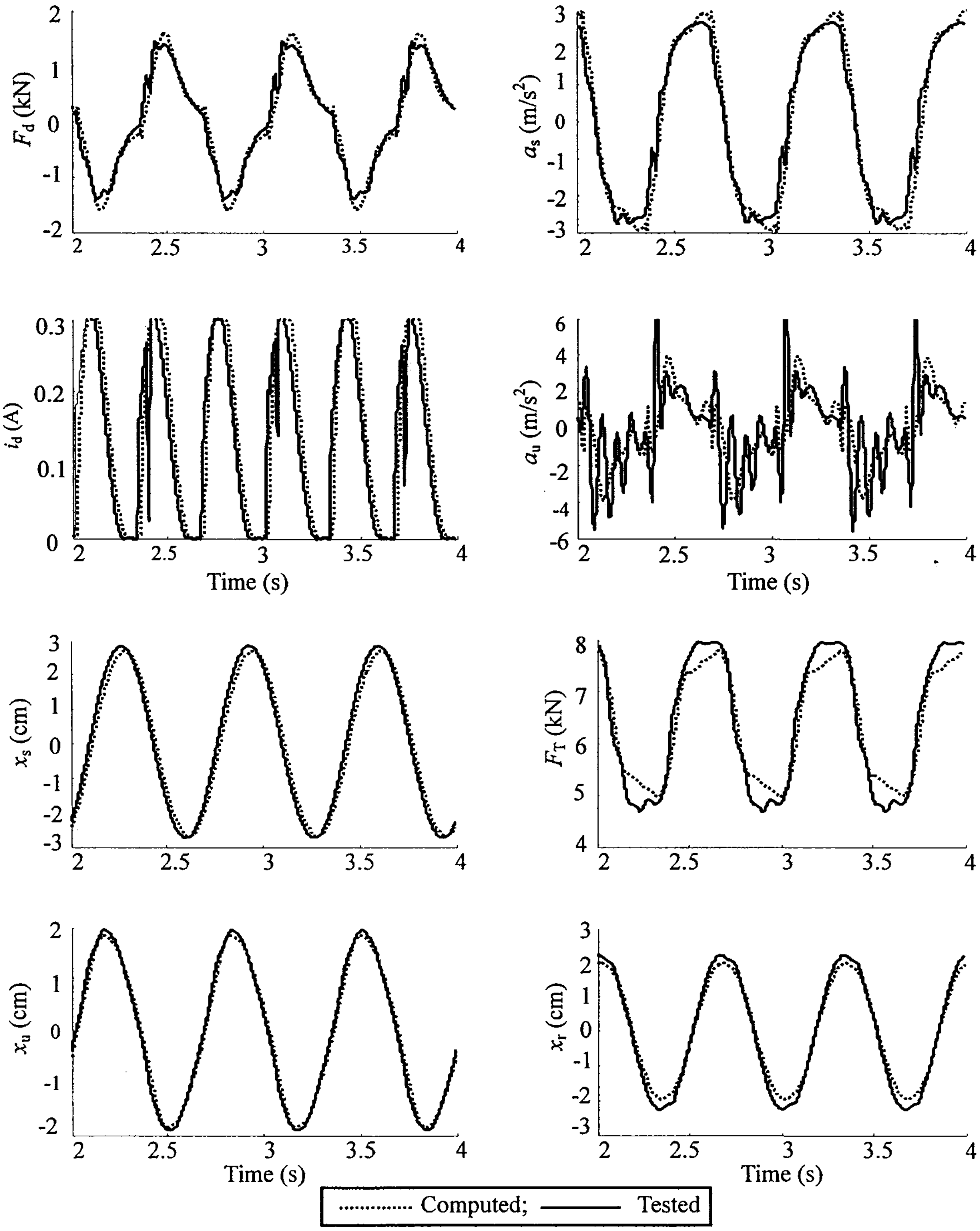

Figure 7.12: Comparisons of computed and measured responses of the "quarter-vehicle" model employing "skyhook"-based hi-lo semi-active SCM damping (m_s=563 kg, f=1.5 Hz and a_m=2 cm).

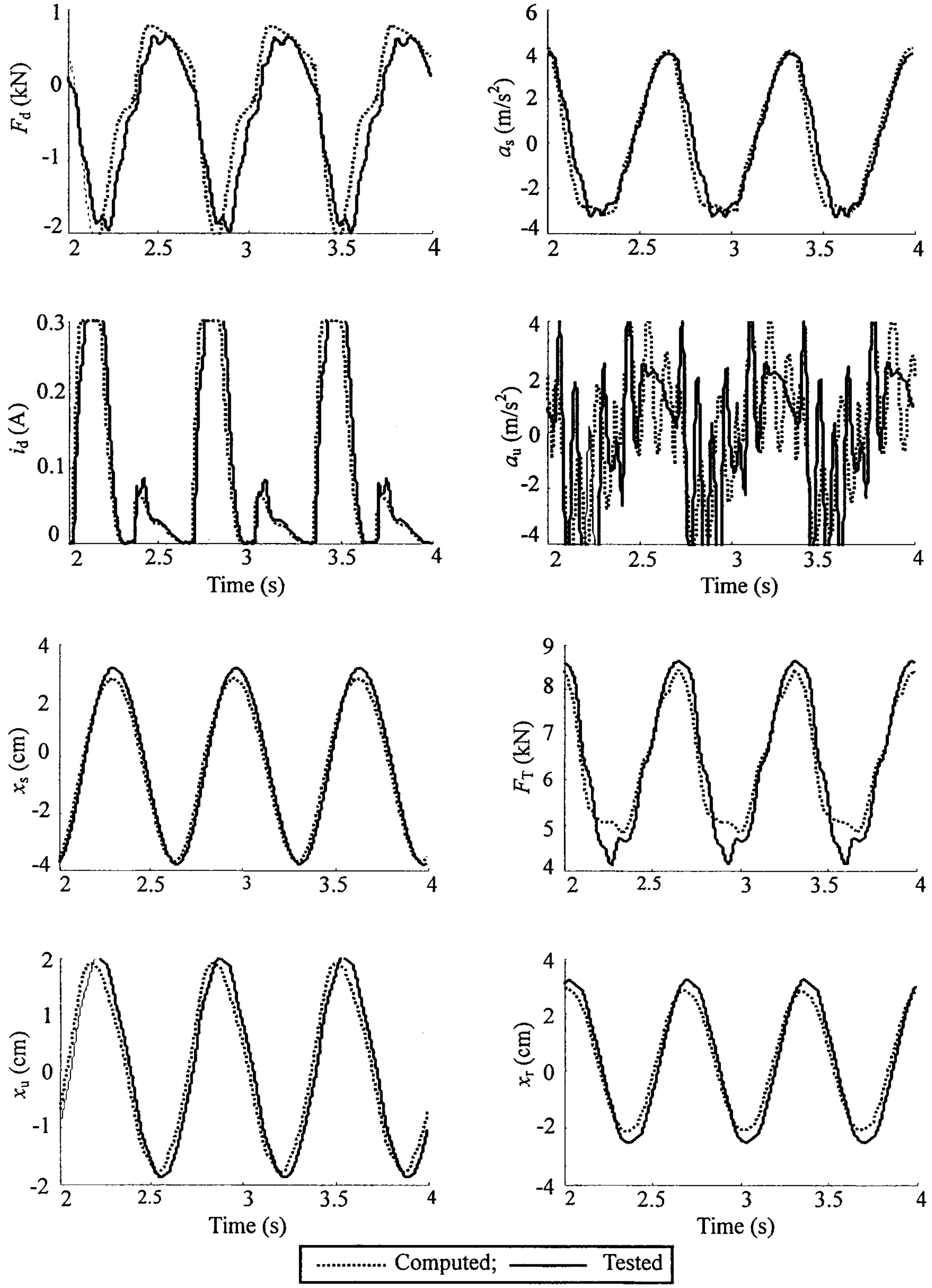

Figure 7.13: Comparisons of computed and measured responses of the "quarter-vehicle" model employing "skyhook"-based hi-lo semi-active ACM damping (m_s=563 kg, f=1.5 Hz and a_m=2 cm).

Figure 7.14 presents comparisons of the measured and computed dynamic responses of the "skyhook"-based hi-lo semi-active MR-suspension in ACM control, when the sprung mass is increased to 703 kg. The results also show reasonably good agreements between the measured and model responses under 2 cm harmonic excitation at 1.5 Hz. The damping force tends to increase and approaches its limiting value in the compression mode, while the rebound mode damping force is considerably higher, suggesting asymmetry factor in the order of 3. A comparison with the results attained for the nominal sprung mass (Figure 7.13) reveals only slight differences in the peak magnitudes of responses, except for the shift in tire force (F_T) due to higher tire load under higher sprung mass. The measured results further support the findings from the analytical model that the proposed "skyhook"-based ACM semi-active controller offers high robustness against variations in the vehicle load.

Figures 7.15 further illustrate comparisons of the measured and computed frequency response characteristics of the controlled MR-suspension in SCM and ACM. The performance measures are evaluated in terms of sprung and unsprung mass acceleration transmissibilities (T_{as}, T_{au}), relative displacement transmissibility (T_{dr}), and DLC due to tire force. Figures 7.15 (a) and (b) show the frequency responses of the "quarter-vehicle" model with nominal sprung mass (m_s=563 kg) and the controller operating in SCM and ACM modes, respectively. Figure 7.16 shows the measured and computed frequency responses of the vehicle model with sprung mass of 703 kg and the controller operating in ACM. The results show good agreements between the measured and model responses, and further validate the properties of the proposed "skyhook"-based hi-lo semi-active controller in SCM and ACM, and their superior robustness in view of the sprung mass variations.

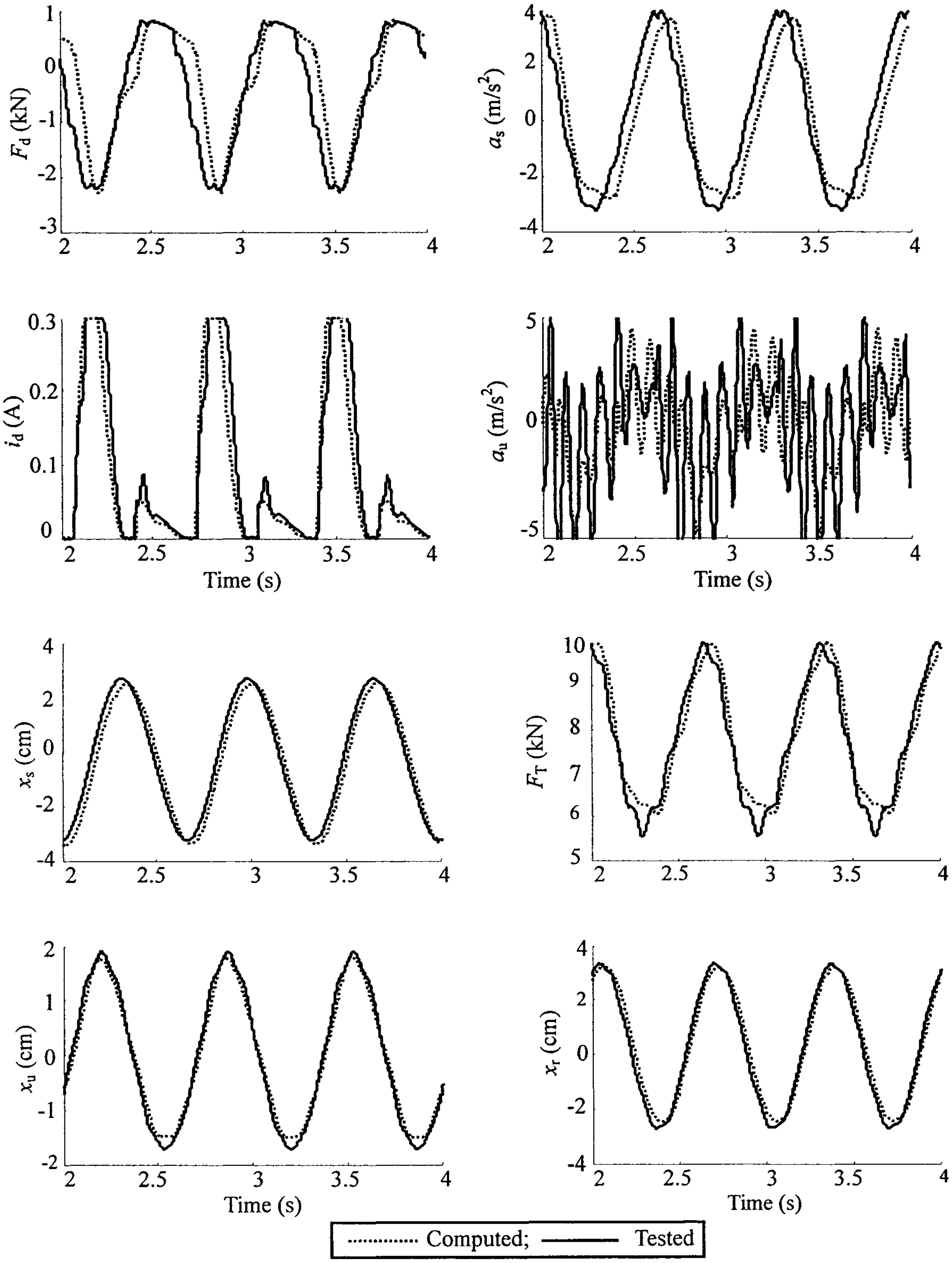

Figure 7.14: Comparisons of computed and measured responses of the "quarter-vehicle" model employing "skyhook"-based hi-lo semi-active ACM damping (m_s=703 kg, f=1.5 Hz and a_m=2 cm).

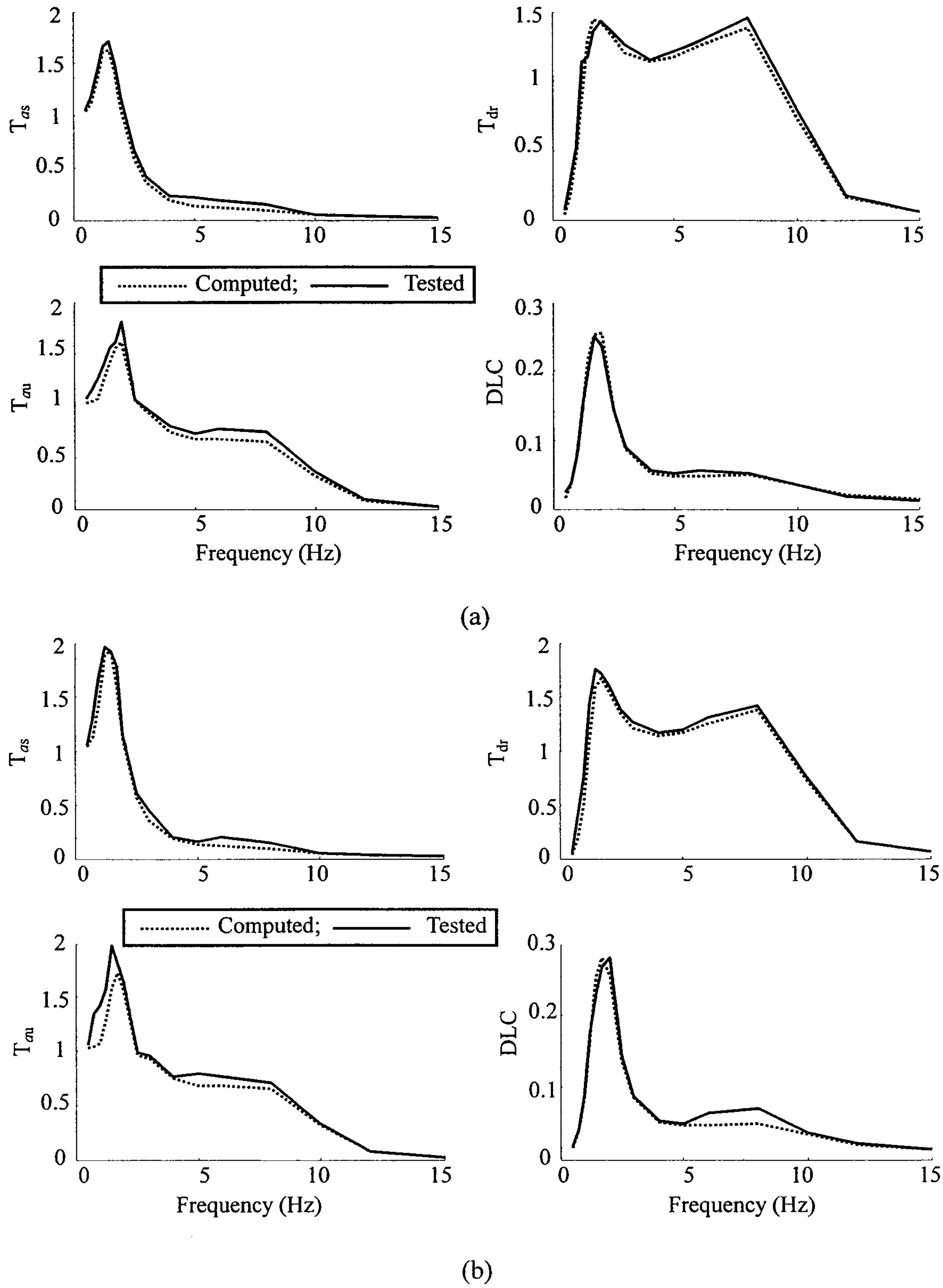

Figure 7.15: Comparisons of computed and measured frequency responses of the "quarter-vehicle" model with "skyhook"-based hi-lo semi-active SCM and ACM damping; m_s=563 kg (a) SCM; (b) ACM.

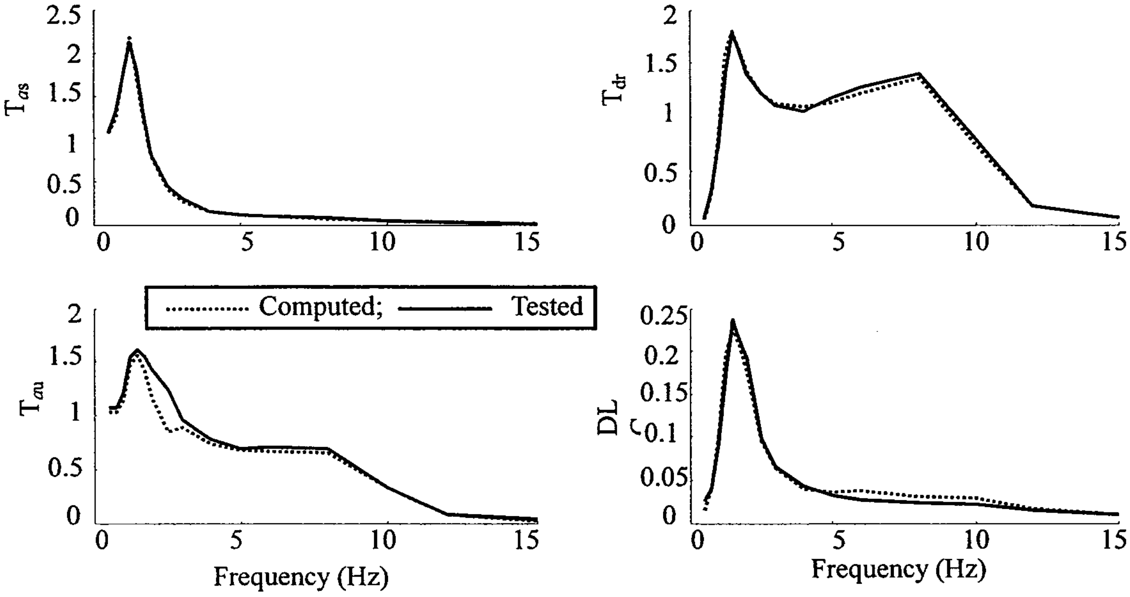

Figure 7.16: Comparisons of computed and measured frequency responses of quarter-vehicle model with "skyhook"-based hi-lo semi-active ACM damping; m_s=703 kg.

Transient excitation

The transient response characteristics of the proposed skyhook-based hi-lo semi-active controller are also measured under a rounded pulse excitation (μ=3, ω_0=10.4rad/s and a_m=2 cm). The measured responses are compared with the model results in Figure 7.17 on the basis of the semi-active hi-lo SCM controller and nominal sprung mass. While the measured results show trends similar to those observed in the model results, considerable deviations exist in the peak shock responses. The attenuations of the peak responses in the measured data, particularly the acceleration and force responses, are attributed to limited bandwidth of the servo-hydraulic system. Figure 7.18 further shows comparisons of the measured transient responses of the "quarter-vehicle" model with MR-suspension with skyhook-based hi-lo semi-active ACM controller and two different sprung masses (m_s=563 and 703 kg) The results show comparable responses for both model masses and thus validate the earlier findings that the proposed ACM synthesis offers superior robustness in view of vehicle load variations.

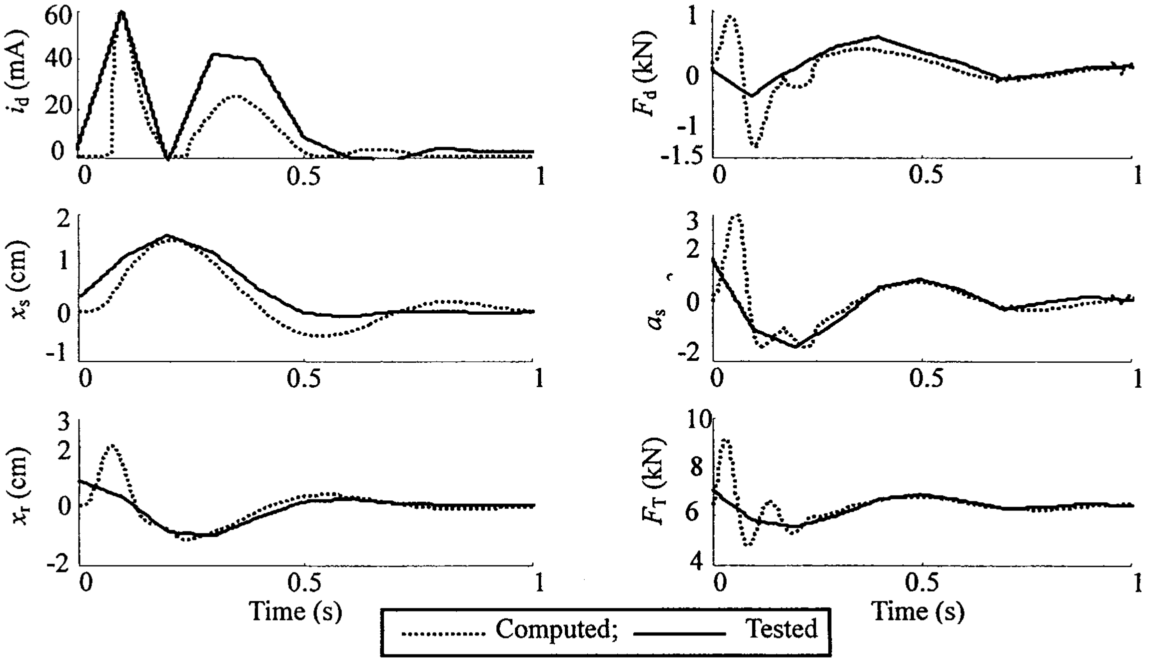

Figure 7.17: Comparisons of measured and computed transient responses of the "quarter-vehicle" with "skyhook"-based hi-lo semi-active SCM MR-damping under a rounded pulse excitation (μ=3, ω_0=10.4rad/s and a_m=2 cm).

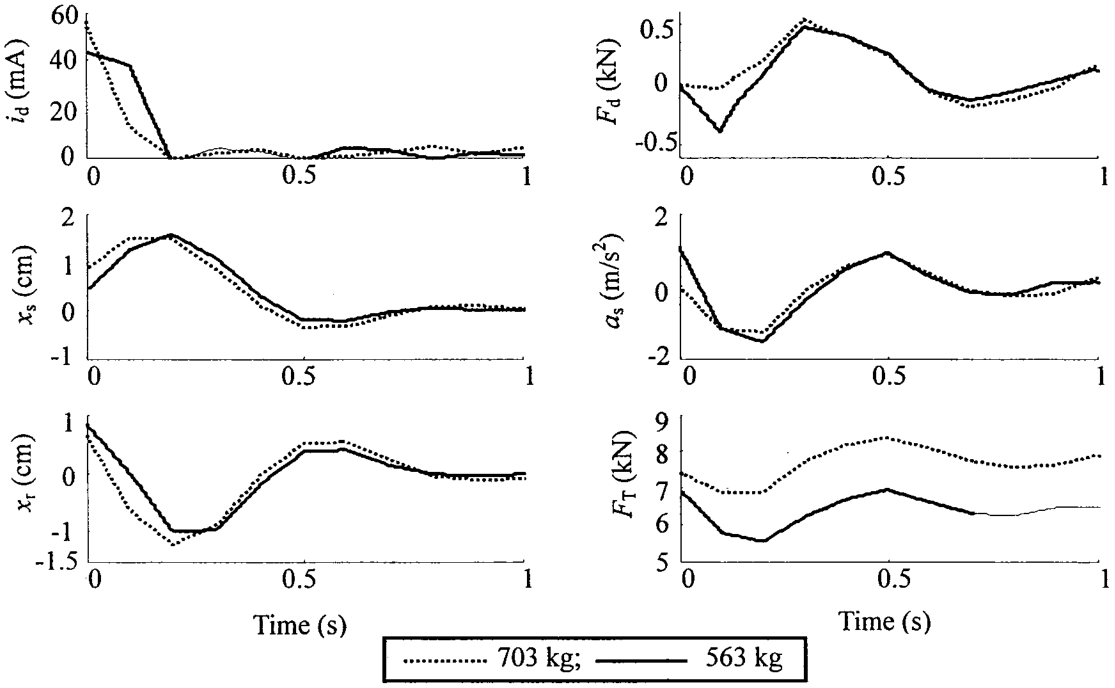

Figure 7.18: Comparisons of measured transient responses of the "quarter-vehicle" model with "skyhook"-based hi-lo semi-active ACM MR damping under two different sprung masses and a rounded pulse excitation (μ=3, ω_0=10.4rad/s and a_m=2 cm).

Random excitation

The experiments are also performed under excitation due to the random rough road, with elevations scaled to 50% of the actual road profile, while the forward speed is chosen as 50 km/h. The "quarter-vehicle" models with "skyhook"-based MR-damping control in SCM and ACM are also analyzed under the same excitation. Model results are compared with the measured data in Figures 7.19 and 7.20, respectively for the symmetric and asymmetric control modes. The results show reasonably good agreements between the measured and model responses for both damping control modes. Relatively larger deviations, however, are evident in the acceleration responses alone in the very low frequency range. Such deviations were also observed in the passive system responses, and were attributed to noise associated with low frequency acceleration signals.

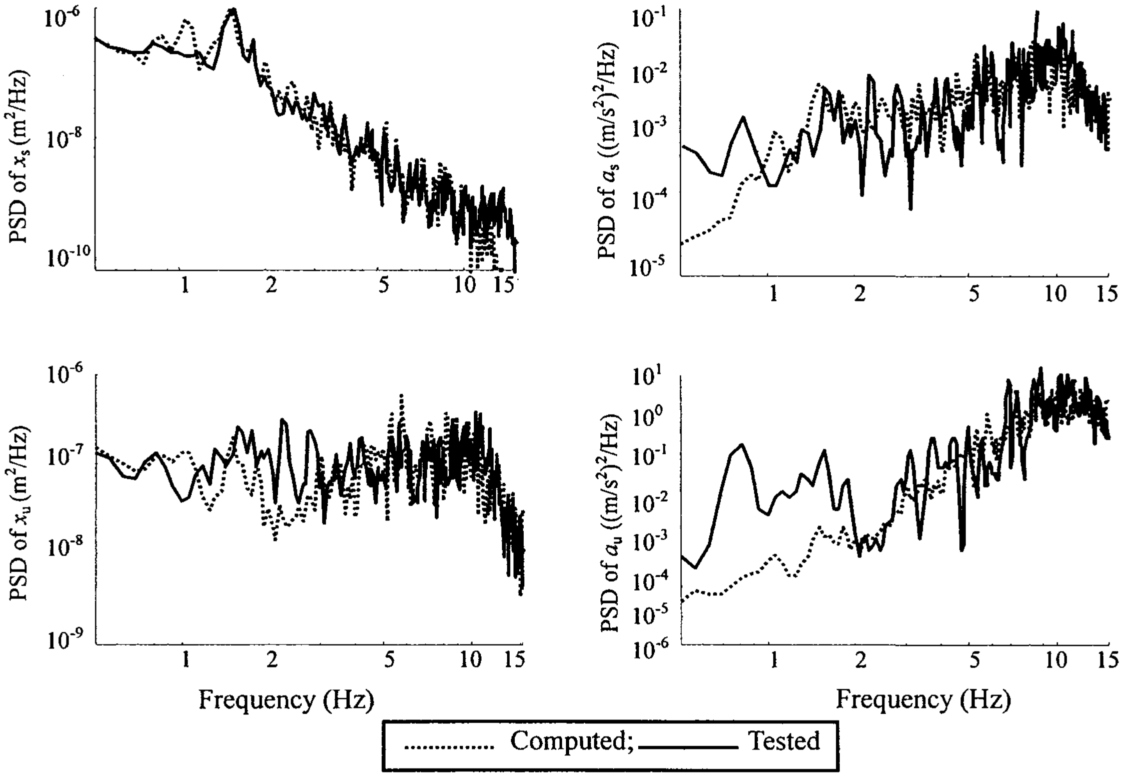

Figure 7.19: Comparisons of measured and computed responses of the model with "skyhook"-based hi-lo MR damping in SCM under random excitation (m_s=563 kg).

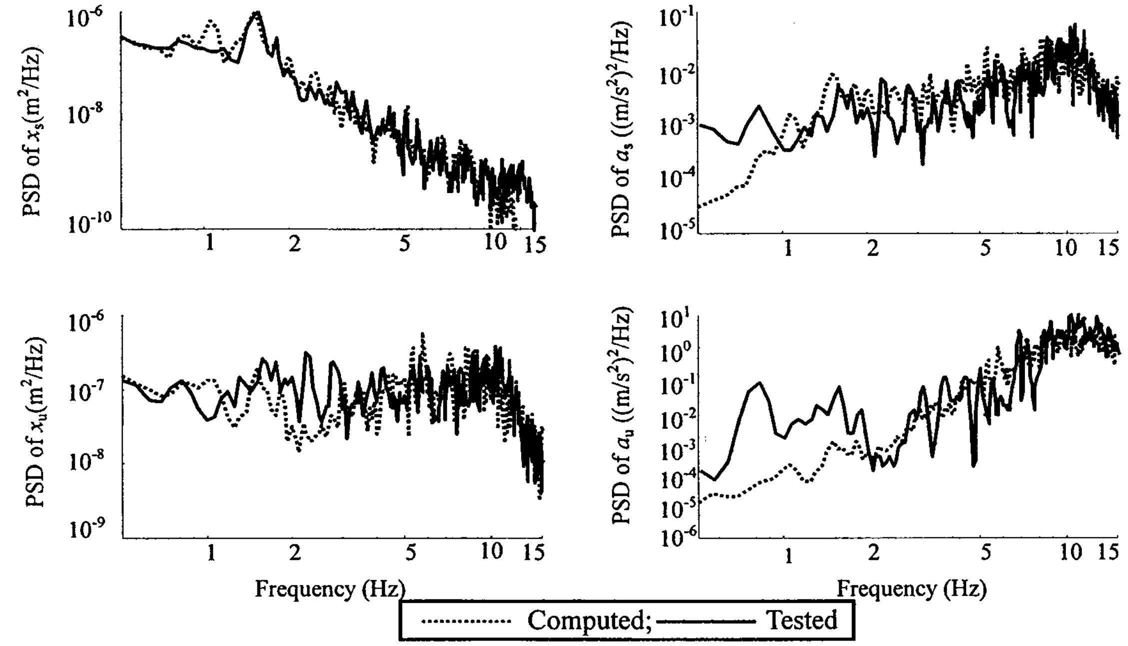

Figure 7.20: Comparisons of measured and computed responses of the model with "skyhook"-based hi-lo MR damping in ACM under random excitation (m_s=563 kg).

Figure 7.21 presents the influence of variation in the sprung mass on the random responses of the "quarter-vehicle" model with "skyhook"-based asymmetric semi-active MR damping variations (ACM).

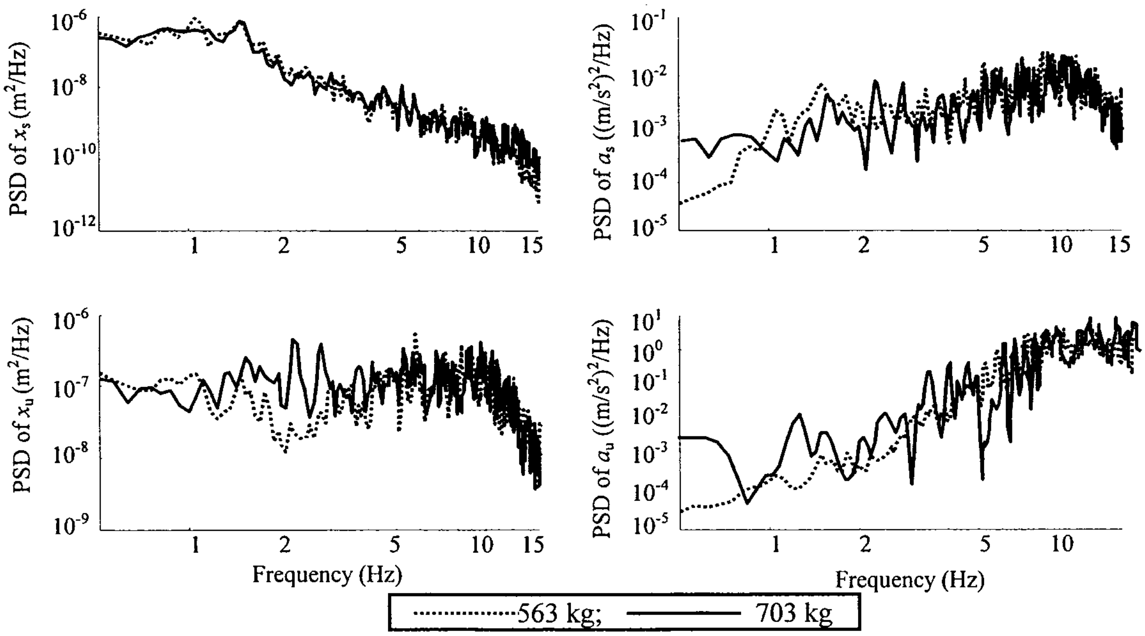

Figure 7.21: Comparisons of measured responses of the "quarter-vehicle" model with "skyhook"-based hi-lo ACM damping and two different sprung masses (563 and 703 kg).

The results show measured responses for two different sprung masses, 563 kg and 703 kg. The results again support the finding that the proposed ACM control offers high robustness against variations in the sprung mass.

7.4 Summary

A hardware-in-the-loop (HiL) experimental platform is developed in the laboratory to evaluate the performance characteristics of the proposed controllers and examine the validity of the MR-damper and controller models. Experiments are performed to measure the responses of the "quarter-vehicle" models with fixed current MR-damper, and the proposed "skyhook"-based hi-lo semi-active controller in the symmetric and asymmetric control modes (SCM and ACM). The measured data are acquired under harmonic, rounded pulse and random road excitations. The measured data are compared with the corresponding model results to examine the model and controller validity. The results revealed generally good agreements in the model and measured results, except for transient peak responses, which were attenuated due to limited bandwidth of the servo-hydraulic system. The measurements were further performed for a higher sprung mass (703 kg) of the "quarter-vehicle" model. The results revealed very little sensitivity of the measured responses to variations in the sprung mass, which further validated the observations that the proposed semi-active damping control offers high robustness against vehicle load variations.

CHAPTER 8

CONCLUSIONS AND RECOMMENDATIONS FOR FUTURE WORK

8.1 Major Contributions and Highlights

This dissertation research focuses on the use of controllable MR-fluid dampers to achieve intelligent vehicle suspension designs that can provide better compromise among different conflicting requirements, namely, the ride, road-holding and suspension rattle space. The MR-fluid dampers offer excellent potential to achieve variable damping with a wide bandwidth. The hysteresis and force-limiting nonlinearities of the damper, however, could affect the force-tracking performance in an adverse manner. Such nonlinearities were adequately modeled to greatly simplify the controller design. The controller designs were realized upon consideration of the hysteresis and switching discontinuities.

Three types of controllers were synthesized to realize semi-active damping variations in an adaptive manner. These included four different hi-lo schemes, an "inverse model"-based hi-lo scheme and an "inverse model"-based sliding mode control scheme. The control schemes were further synthesized in the symmetric (SCM) as well as asymmetric damping modes (ACM) in conjunction with continuous modulation (CM) and asymmetric damping force generation (ADFG) functions to minimize the switching effects. The relative performance characteristics of different controller syntheses are investigated using a simple "quarter-vehicle" model and a set of performance measures. The results suggest that the "skyhook"-based hi-lo semi-active controller in ACM could provide better compromise among different conflicting measures and high robustness against varying vehicle loads. The validity of the analytical controller synthesis and the nonlinear damper model are demonstrated on the basis of the data acquired using hardware-in-the-loop (HiL) test and simulations in the laboratory. The major contributions of the thesis research are summarized below:

- A generalized model of a MR-damper is developed on the basis of its physical features to characterize the hysteretic force-velocity (*F-v*) properties with force saturation in the post-yield as functions of the applied current and nature excitation and response. The model is further generalized to characterize asymmetric *F-v* properties in compression and rebound. Laboratory experiments are performed to characterize the *F-v* properties of a candidate MR-damper over a wide range of motion and current excitations. The validity of the model is demonstrated by comparing the model results with the measured data over a wide range of excitation conditions. The proposed model offers significant merits in relation to the reported models, since it accurately characterizes the nonlinear current dependence, and the hysteretic and force-limiting behaviors of the MR-damper.
- An independent current control gain function is proposed and integrated within the generalized damper model to characterize the current dependency of the damping force. This current function could be applied to the reported models to enhance their applicability for characterizing the current dependent property.
- On the basis of the proposed nonlinear model, a velocity-based hysteretic inverse damping force model of the MR-damper is derived to facilitate the formulations of "inverse-model"-based controllers. The inverse model allows for deriving the command current on the basis of the desired target force and thus helps to effectively suppress the hysteresis effects and simplify the semi-active controller syntheses.
- A current modulation (CM) algorithm is originally developed to realize continuous variations in the drive current for exciting the MR-damper, so as to minimize the switching transient effects in the on-off and hi-lo damping force modulations.
- An asymmetric damping force generation (ADFG) algorithm is originally developed to realize asymmetric damping force in compression and rebound from the symmetric MR-damper design. The ADFG algorithm further helps in suppressing the switching discontinuity effects and could yield improved road-holding performance of the vehicle suspension due to higher damping force

in rebound than in compression.

- A hybrid "skyhook"-based hi-lo semi-active controller in the symmetric and asymmetric control modes (SCM and ACM) is formulated by integrating the well-known "skyhook" semi-active control law with the damper model. The proposed controller is formulated in the command current form in conjunction with the proposed current modulation and ADFG algorithms to effectively suppress the hysteresis effects and switching transient oscillations in responses. An exponent is further introduced in the control law to enhance the damping force bandwidth and smoothen the switching transient effects. The proposed controller could yield improved multi-objective suspension performances in terms of ride, road-holding and suspension rattle space, as well as better robustness on the operating parameter variations, such as vehicle load, speed and road roughness. The validity of the controller synthesis is also demonstrated through the HiL experiments performed in the laboratory.

- An "inverse model"-based hi-lo semi-active ACM controller is developed by applying the on-off control law using directly measurable relative velocity. The effectiveness of the controller in effectively suppressing the hysteresis effects of the MR-damper is demonstrated through simulation results. Moreover, the application of the inverse model and the use of directly measurable feedback signals would facilitate the controller realization and implementation. The CM and ADFG functions are also integrated in the controller synthesis to effectively reduce the contribution due to current-switching discontinuities and to realize the asymmetric damping force from a symmetric MR-damper design. It is proposed that the adequate force-tracking performance could be realized only with high pre-yield damping force.

- An "inverse model"-based sliding mode controller is synthesized to further suppress the hysteresis effects and enhance the robustness of an intelligent vehicle suspension design. A modified "skyhook"-based reference model is used to serve as the nominal control target, while the desirable damping force is generated using the sliding mode control technique. The inverse model control is applied to eliminate the effects of the hysteresis, while the CM and ADFG functions are integrated in the controller synthesis to effectively reduce the current-switching discontinuities and to realize asymmetric damping force.

- A set of performance measures comprising measures related to ride, road holding, rattle space and dynamic tire forces is formulated to conduct relative assessment of different controller syntheses. The analyses are performed under deterministic and random continuous vibration, and shock inputs to assess the relative merits and limitations of different controller formulations.

- A hardware-in-the-loop test platform is configured to synthesize a controller and to experimentally assess its responses to deterministic as well as random excitations. The measured data are used to demonstrate the validity of the nonlinear damper model and that of the "skyhook"-based hi-lo semi-active formulations in the symmetric as well as asymmetric control modes.

8.2 Major Conclusions

Major conclusions derived from this dissertation research are summarized below:

- Despite extensive developments in active and semi-active suspensions, their implementations have been severely limited primarily due to either high power requirements or limited bandwidth. The MR fluids exhibit significant and rapid variations in their rheological properties, and thus offer high potential to realize variable damping with high bandwidth and minimal power requirements.
- The laboratory-measured properties of a MR-damper revealed highly nonlinear *F-v* characteristics. These revealed low damping coefficients in the pre-yield at low velocities, force saturation in post-yield at high velocities, considerable hysteresis, which showed strong dependence on the intensity of the applied magnetic field, and magnitudes of excitation and response.
- The generalized model of the MR-damper, derived on the basis of symmetric and asymmetric sigmoid functions, could accurately characterize the *F-v* properties over a wide range of current and excitation conditions. The proposed independent current control gain function effectively accounts for the current dependence of the hysteretic damping force and force saturation. This current function could be conveniently applied to various reported models to enhance their general applicability.
- The proposed asymmetric damping force generation (ADFG) algorithm could be effectively applied to generate asymmetric damping forces in compression and rebound from the symmetric design of the MR-damper. Moreover, the proposed function helps to suppress the transient oscillations caused by switching discontinuities of semi-active control syntheses.
- The hysteretic inverse model of the MR-damper can conveniently provide the desired control current in response to a defined target force, and thus facilitate the implementation within "inverse model"-based controllers for improved suppression of the hysteresis effects.
- The "skyhook"-based hi-lo control policy can provide semi-active modulation in the damping force to achieve improved compromise among different

performance requirements. The proposed continuous modulation (CM) function helps to suppress the transient effects of switching discontinuities in the hi-lo mode of modulation.

- The integration of the proposed asymmetric damping force generation (ADFG) algorithm within the control policies not only permits for realization of asymmetric force in compression and rebound but also minimizes the effects of switching transients. The ADFG function can be easily tuned to attain desired asymmetry factor for the MR-damper force.
- It is further concluded that a higher order "skyhook" control can provide higher damping force bandwidth and more continuous modulation of the damping force from 'lo' to 'hi' state and vice-verse.
- The force hysteresis and saturation nonlinearities of the MR-damper have significant influences on the performance of vehicle suspension with MR-damper. The force saturation in the post-yield at higher velocities could cause strong oscillations in the unsprung mass acceleration response, irrespective of the open- or closed-loop operation of the MR-suspension. The hysteresis property of the MR-damper would invariably yield transient oscillations in the damping force, and sprung and unsprung mass acceleration responses, when the semi-active control scheme is utilized.
- On the basis of the relative response characteristics of the proposed four different hi-lo algorithms, it is concluded that the "skyhook"-based hi-lo semi-active MR-suspension of the second-order and in the asymmetric mode (ACM) could yield relatively superior dynamic responses to meet the multi-objective suspension performance requirements.
- The "skyhook"-based hi-lo semi-active control syntheses involving drive current modulation in response to sprung mass velocity offers superior vibration attenuation, tire force and rattle space performance, when compared to those of other control syntheses formulated in the study.
- The transients oscillations in the responses of a controlled MR-suspension, caused by the force hysteresis and saturation nonlinearities can be effectively reduced by employing the continuous modulation (CM) and asymmetric damping force generation (ADFG) functions and by integrating an exponent in the controllers (high controller order).
- The "skyhook"-based hi-lo semi-active MR-suspension in ACM exhibits desirable robust performance with respect to variations in the operating parameters, such as load, speed and road roughness. Relatively high robustness is

also demonstrated for variation in the controller parameters, namely the controller gain and order, under deterministic and random road excitations.

- The "inverse model"-based upon mean damping force characteristics coupled with the mean force MR-damper model yields smooth responses, but these deviate significantly from the practically realizable responses. The "inverse model"-based hi-lo semi-active ACM controller can effectively reduce the hysteresis effects of the MR-damper.

- The "inverse model"-based hi-lo and sliding-mode semi-active ACM controllers exhibit superior force-tracking ability at higher velocities, while the low pre-yield damping at low velocities is insufficient to track the target force related to the spring force. The tracking force performance of the controllers could be enhanced by introducing larger hysteron force through appropriate design of the MR-damper.

- High pre-yield damping required for improving the force-tracking performance, however, causes degradation of the vibration transmission performance of both "inverse model"-based controllers. The design of the "inverse model"-based control thus imposes difficult compromise between the force-tracking and suspension performance.

- The "inverse model"-based hi-lo and sliding-mode ACM controllers exhibit desirable robust control performance with respect to variations in some of the operating parameters, namely, operating load and speed. Moreover, the hi-lo controller offers considerable merits for implementation since it involves directly measurable variables.

- The "inverse-model"-based sliding mode ACM controller exhibits relatively lower sensitivity to variations in operating load.

- The controller synthesis can be conveniently realized and assessed in a HiL test and simulation environment, which offers added flexibility for tuning of the controller.

- The measured data acquired from the HiL experiments in the passive damping mode show reasonably good validity of the nonlinear MR-damper model over a wide range of operating conditions. The model, however, yields errors under high frequency excitations.

- The measured data attained for the "quarter-vehicle" model with passively controlled MR-damper hardware revealed generally good agreements with the model results under harmonic and random excitations, while considerable deviations in the peak responses under shock excitations were observed. Such deviations were attributed to limited bandwidth of the servo-hydraulic system within the HiL platform.

- The measured data acquired for the "skyhook"-based hi-lo semi-active control under deterministic and random excitations also revealed reasonably good agreements with the model results, except for peak responses under transient excitations.
- The measured data further confirms the high robustness of the controller against variations in the vehicle load.

8.3 Recommendations for Future Work

This dissertation research involved a number of fundamental studies, such as characterization and modeling of the nonlinear behavior of the MR-damper, and hybrid semi-active controller syntheses for realizing multi-objective suspension performances, hysteresis and transient oscillation rejection, and high robustness against varying operating conditions. Moreover, the analyses are based upon an idealized "quarter-vehicle" model. Considerable further efforts would thus be needed to achieve reliable and easily implementable controller design that would provide not only satisfactory compromise among different measures but also high robustness against variations in different operating conditions. Some of the suggested further efforts are summarized below:

- It is recommended that the formulations should incorporate a "full-vehicle" model with multiple-wheel MR-suspension to realize controller designs upon considerations of the roll and pitch dynamics.
- The performance measures need to be enhanced by incorporating measures of handling, braking and roll dynamics. The use of a "full-vehicle" model would permit for more comprehensive controller design and synthesis.
- Owing to the superior performance of the "skyhook"-based hi-lo semi-active

algorithm, it is vital to explore methods for measurement of the sprung mass velocity. Signal filter functions may be explored to derive the sprung mass velocity signal from directly measurable acceleration, although the phase response would need to be examined.

- Alternate designs of MR-damper need to be explored to realize high pre-yield damping force, such that the force tracking performance of the inverse model based controllers could be enhanced. Moreover, high pre-yield damping would also provide higher damping force bandwidth for the controller. The post-yield damping force however must be limited to ensure adequate vibration isolation in the mid- or ride-frequency range.
- The MR dampers should be designed to provide asymmetric forces in compression and rebound through appropriate designs of the electro-magnetic coils on the basis of the direction of the pressure differential. This would simplify the controller syntheses and hardware requirements.

REFERENCES

[1] Rakheja, S. and Woodrooffe, J. Role of suspension damping in enhancement of road friendliness of heavy vehicles. *Heavy Vehicle System, Int. J. of Vehicle Design*, 1996, 3(1-4): 363-381.

[2] Cebon D. Handbook of vehicle-Road Interaction. 1999, ISBN 90 265 1554 5.

[3] Margolis D L. Procedure for comparing passive, active, and semi-active approaches to vibration isolation. *J. of the Franklin Institute*, 1983, 315(4): 225-238.

[4] Redfield R C. Performance of low-bandwidth, semi-active damping concepts for suspension control. *Vehicle Dynamic System*, 1991, 20: 245-267.

[5] Carlson J D. Magneto-rheological fluid actuators. *Chapter in Adaptronics and Smart Materials,* edited by *H. Janocha, Verlag, Berlin*, 1999: 180-195.

[6] Choi S B, Lee S K, and Park Y P. A hysteresis model for the field-dependent damping force of a magneto-rheological damper. *J. of Sound and Vibration*, 1997, 245(2): 375-383.

[7] Spencer B F, Dyke D J, Sain K M, and Carlson J D. Phenomenological model of a magneto-rheological damper. *J. of Eng. Mech.,* 1997, 123(3): 230-238.

[8] Wereley N M, Pang L, and Kamath G M. Idealized hysteresis modeling of electro-rheological dampers. *J. of Intelligent Material Systems and Structures,* 1999, 9(8): 642-649.

[9] Atray V S and Roschke P N. Design, fabrication, testing, and fuzzy modeling of a large magneto-rheological damper for vibration control in a railcar. *Proc. of the IEEE/ASME Joint Railroad Conference*, 2003: 223-229.

[10] Muriuki M G and Clark W W. Modeling and testing of the force-generating characteristics of magneto-rheological dampers. *Int. J. of Vehicle Design*, 2003, 33(1-3): 171-188.

[11] Maranville C W and Ginder J M. Magneto-rheological fluid damper dynamics: Models and measurements. *Proc. of SPIE - The Int. Society for Optical Engineering*, 2003, 5056: 524-533.

[12] Yokoyama M, Hedrick J K, and Toyama S. A model following sliding mode controller for semi-active suspension systems with MR dampers. *Proc. of the American Control Conference*, 2001, 4: 2652-2657.

[13] Lee H S and Choi S B. Control and response characteristics of a magneto-rheological fluid damper for passenger vehicles. *J. of Intelligent Material Systems and Structures*, 2000, 11(1): 80-87.

[14] Wang D H and Liao W H. Neural network modeling and controllers for magneto-rheological fluid dampers. *IEEE Int. Conf. on Fuzzy Systems*, 2002, 3: 1323-1326.

[15] Sun Q, Zhang K, Zhou J, and Zhang L. New type magneto-rheological damper and its application on semi-active control of structural seismic response. *Process in Safety Science and Technology Part A*, 2002, 3: 376-382.

[16] Wen Y K. Method for random vibration of hysteretic systems. *J. of Engineering Mechanics Division*, 1976: 249-263.

[17] Wong J Y. *Theory of ground vehicle. John Wiley & Sons, Inc.*, 1993.

[18] Yi K and Hedrick J K. Active and semi-active heavy truck suspension to reduce pavement damage. *SAE Trans*, 892486 (SP 802), 1989: 29-36.

[19] Hwang, S, Heo S, Kim H and Lee, K. Vehicle dynamic analysis and evaluation of continuously controlled semi-active suspension using hardware-in-the-loop simulation. *Vehicle System Dynamics*, 1997, 27(5-6): 423-434.

[20] Lu S. Optimum design of "road-friendly" vehicle suspension systems subjected to rough pavement surfaces. *J. of Applied Mathematical Modeling*, 2002, 26(5): 635-652.

[21] Goncalves P C, Joae, Ambrosio A C, and Jorqe. Optimization of vehicle suspension systems for improved comfort of road vehicles using flexible multibody dynamics. *J. of Nonlinear Dynamics*, 2003, 34(1-2):113-131.

[22] Sammier D, Sename O, and Dugard L. Skyhook and H_∞ Control of semi-active Suspensions: Some practical aspects. *Vehicle System Dynamics*, 2003, 39(4): 279-308.

[23] Chalasani R M. Ride performance potential of active suspension systems. Part I: simplified analysis based on quarter-car models. *ASME Symposium on Simulation of Ground Vehicles and Transport Systems, Anaheim CA*, ASME, 1986.

[24] Cole D J. Fundamental issue in suspension for heavy road vehicle. *Vehicle System Dynamics*, 2001, 35(4-5): 319-360.

[25] Sharp R S and Hassen S A. The fundamentals of passive automotive suspension system design. *Society of Environmental Engineers, Conf. on Dynamics in Automative Engineering*, 1984: 104-115.

[26] Sharp R S and Pilneam C. Achievability and value of passive suspension for minimum pitch response. *Proc. of IMechE Conf. on Vehicle Ride and Handling, MEP, Ltd., London*, 1993: 243-259.

[27] Gole D J and Cebon D. Truck suspension design to minimize road damage. *Proc. of Institution of Mechanical Engineers*, 210: 2, 1996, Part D: 95-107.

[28] Tong R T, Amirouche F, and Palkovics L. Ride control-a two state suspension design. 1997, paper No. 973260.

[29] Naude A F and Snyman J A. Optimization of road vehicle passive suspension systems. Part 2: Qualification and case study. *J. of Applied Mathematical Modeling*, 2003, 27(4): 263-274.

[30] Nishiyama S, Uesugi N, Takeshima K Y, and Togii H. Research on vibration characteristics between human body and seat, steering wheel, and roads. *J. of Sound and Vibration*, 2000, 236(1): 1-21.

[31] Graf P L and Shoureshi R. Modeling and implementation of semi-active hydraulic engine mounts. *J. of Dynamic Systems, Measurement and Control, Transactions ASME*, 1988, 110(4): 422-429.

[32] Karadayi R and Masada G Y. A nonlinear shock absorber model. *ASME, AMP*(80), DSC(2), 1989: 149-165.

[33] Milliken W F and Douglas L M. *Race car vehicle dynamics, Society of Automotive Engineers, PA, USA*, 1995.

[34] Mansfield N J and Griffin M J. Effect of magnitude of vertical whole-body vibration on absorbed power for seated human body. *J. of Sound and Vibration*, 1998, 215(4): 813-825.

[35] Jang H K and Griffin M J. Effect of phase, frequency, magnitude and posture on discomfort associated with differential vertical vibration at the seat and feet. *J. of Sound and Vibration*, 2000, 229(2): 273-286.

[36] Youn and Hac A. Semi-active with adaptive capability. *J. of Sound and Vibration*, 1995, 180(93): 475-492.

[37] Ibrahim I M, Crolla D A, and Barton D C. Active suspension for trucks incorporating frame flexibility effects. *Heavy Vehicle System, Int. J. of Vehicle Design*, 1995, 2(1): 1-7.

[38] Anon. Mechanical vibration and shock-evaluation of human exposure to whole-body

vibration. *Int. Organization for Standardization ISO* 2631-1, 1997.

[39] Griffin M J. A comparison of standardized methods for predicting the hazards for whole-body vibration and repeated shocks. *J. of Sound and Vibration*, 1998, 215(4): 883-914.

[40] Rakheja S and Sanker S. Vibration and shock isolation performance of a semi-active "on-off" damper. Transactions of the ASME, *J. of Vibration, Acoustics, Reliability in Design*, 1985, 107: 398-403.

[41] Vallurupalli S S. Real time computer controlled adaptive active suspension: An analytical and experimental investigation. *Ph. D Thesis, Concordia University, Canada, Subject code*: 0548, 1996.

[42] Gaspar P, Szaszi I, and Bokor J. Design of robust controllers for active vehicle suspension using the mixed synthesis. *Vehicle System Dynamics*, 2003, 40(4): 193-228.

[43] Crosby M and Karnopp D C. The active damper-a new concept for shock and vibration control. *Shock Vib. Bull., Part H, Washington D C*, 1973.

[44] Alanoly J and Sankar S. Semi-active force generators for shock isolation. *J. of Sound and Vibration*, 1988, 126(1): 145-156.

[45] Carlson J D and Sproston J L. Controllable fluids in 2000 - Status of ER and MR fluid technology. *7th Int. Conf. on New Actuator, Bermen, Germany*, 2000: 126-130.

[46] Stanway R, Sproston J L, and El-Wahed A K. Application of electro-rheological fluids in vibration control: a survey. *J. of Smart Materials and Structures,* 1996, 5(4): 464-482.

[47] Xu Y L, Qu W L, and Ko J M. Seismic response control of frame structures using magneto-rheological/electro-rheological dampers. *Earthquake Engineering and Structural Dynamics*, 2000, 29(5): 557-575.

[48] Wereley N M, Pang L. Nondimensional analysis of semi-active electro-rheological and magneto-rheological dampers using approximate parallel plate models. *J. of Smart Materials and Structures*, 2000, 7: 732-743.

[49] Ruangrassamee A and Kawashima K. Semi-active control of bridges with use of magneto-rheological dampers. *Proc. of SPIE-The Int. Society for Optical Engineering*, 2001, 4330: 323-332.

[50] Zhou G Y and Zhang P Q. Investigation of the dynamic mechanical behavior of the double-barreled configuration in a magneto-rheological fluid damper. *J. of Smart*

Materials and Structures, 2002, 11(2): 230-238.

[51] Hiwatashi T, Shiozaki Y, et al. Shaking table tests on semi-active base-isolation system by magneto-rheological fluid damper. *Proc. of SPIE-The Int. Society for Optical Engineering*, 2003, 5056: 400-411.

[52] Rabinow J. The magnetic fluid clutch. *AIEE Trans.*, 1948, 67: 1308-1315.

[53] Winslow W M. Induced vibration of suspension. *J. of Applied Physics*, 1949, 20: 1137-1140.

[54] Carlson J D, Catanzarite D M, and Clair K A St. Commercial magneto-rheological fluid devices. *5th Int. Conf. ER, MR Suspensions Associated Technology, Sheffield, England*, 1995.

[55] Carlson J D. New cost effective braking damping and vibration control devices made with magneto-rheological fluids. *J. of Materials Technology*, 1998, 13: 96-99.

[56] Thomas Lord Research Center. Lord Corporation. Designing with MR fluids. *Engineering Note,* 1999.

[57] McManus S J and St. Clair K A. E. Evaluation of vibration and shock attenuation performance of a suspension seat with a semi-active magneto-rheological fluid damper. *J. of Sound and Vibration*, 2002, 253(1): 313-327.

[58] Choi S B, Lee B K, Nam M H, and Cheong C C. Vibration control of a MR seat damper for commercial vehicles. *Smart Structure and Materials 2000: Smart Structures and Integrated System, Proc. of SPIE*, 2000, 3958: 491-496.

[59] Choi S B, Lee B K, Hong S R, and Cheong C C. Control and response characteristics of a magneto-rheological fluid damper for passenger vehicle. *Smart Structure and Materials 2000: Smart Structures and Integrated System, Proc. of SPIE*, 2000, 3958: 438-443.

[60] Kim K and Jeon D. Vibration suppression in an MR-fluid damper suspension system. *J. of Intelligent Material Systems and Structures*, 2000, 10(10): 779-786.

[61] Lai C Y and Liao W H. Vibration control of a suspension system via a magneto-rheological fluid damper. *J. of Vibration and Control*, 2002, 8(4): 527-547.

[62] Simon T M, Reitich F, Jolly M R, Ito K, and Banks H T. The effective magnetic properties of magneto-rheological fluids. *J. of Mathematical and Computer Modeling*, 2001, 33: 273-284.

[63] Snyder R A, Kamath C M, and Wereley N M. Characterization and analysis of magneto-rheological damper behavior due to sinusoidal loading. *Proc. of SPIE-The Int. Society for Optical Engineering*, 2000, 3989: 213-229.

[64] Wang D H and Liao W H. Neural network modeling and controllers for magneto-rheological fluid dampers. *IEEE Int. Conf. on Fuzzy Systems*, 2002, 3: 1323-1326.

[65] Xia P Q. An inverse model of MR damper using optimal neural network and system identification. *J. of Sound and Vibration*, 2003, 266(5): 1009-1023.

[66] Caughey T K. Sinusoidal excitation of a system with bilinear hysteresis. *ASME J. of Applied Mechanics*, 1960, 27: 640-643.

[67] Coleman B D and Hodgdon M L. A constitutive relation for rate-independent hysteresis in ferromagnetically soft materials. *J. of Engineering Science*, 1986, 24: 897-919.

[68] Croft D and Devasia S. Hysteresis and vibration compensation for piezoactuators. *AIAA*, 1998, 21: 710-717.

[69] Majima S, Kodama K, and Hasegawa T. Modeling of shape memory actuator and tracking control system with the model. *IEEE Transactions on Control Systems Technology*, 2001, 9(1): 54-59.

[70] Khalil H. Nonlinear system. *Prentice Hall, Inc., Upper Saddle River*, NJ 07458, 2002.

[71] Symens W, Al-Bender F, Swevers J, and Van Brussel H. Dynamic characterization of hysteresis elements in mechanical systems. *Proc. of the American Control Conference, Anchorage, AK,* May 8-10, 2002.

[72] Gong J Q, Guo L, Lee H S, and Yao B. Modeling and cancellation of pivot nonlinearity in hard disk driver. *Proc. of the American Control Conference, Anchorage, AK*, May 8-10, 2002.

[73] Tao G and Kokotovic P V. Adaptive control of plants with unknown hysteresis. *IEEE Transaction on Automatic Control*, 1995, 40(2): 200-212.

[74] Ge P, Jouaneh M. Tracking control of a piezoceramic actuator. *IEEE Transactions on Control Systems Technology*, 1996, 4(3): 209-215.

[75] Su C Y, Stepanenko Y, Svoboda J, and Leung T P. Robust adaptive control of a class of nonlinear systems with unknown backlash-like hysteresis. *IEEE Transactions on Automatic Control,* 2000, 45(12): 2427-2431.

[76] Cruz-Hernandez J M and Hayward V. Phase control approach to hysteresis reduction. *IEEE Transactions on Control Systems Technology*, 2001, 9(1): 17-26.

[77] Gorbet R B, Morris K A, and Wang D W L. Passivity- based stability and control of hysteresis in smart actuators. *IEEE Trans on Control Systems Technology*, 2001, 9(1): 5-16.

[78] Ralph C S, et al. Model development and inverse compensator design for high speed nanopositioning. *Proc. of the 41st IEEE Conf. on Decision and Control, Las Vegas, Nevada USA*, 2002.

[79] Corradini M L and Orlando G. Robust stabilization of nonlinear uncertain plants with backlash or dead zone in the actuator. *IEEE Transactions on Control Systems Technology*, 2002, 10(1): 158-166.

[80] Choi S B, Lee H S, Hong S R, and Cheong C C. Control and response characteristics of a magneto-rheological fluid damper for passenger vehicles. *J. of Smart Structures & Materials, Proc. of SPIE,* 2000: 438-443.

[81] Choi S B, Lee H S, and Park Y P. H_∞ control performance of a full-vehicle suspension featuring magneto-rheological dampers. *Vehicle System Dynamics*, 2002, 38(5): 341-360.

[82] Lam H F and Liao W H. Semi-active control of automotive suspension systems with magneto-rheological dampers. *Proc. of SPIE, the Int. Society for Optical Engineering*, 2001, 4327: 125-136.

[83] Hiu F L and Wei H L. Semi-active control of automotive suspension systems with magneto-rheological dampers. *Proc. of SPIE-The Int. Society for Optical Engineering,* 2001, 4327: 125-136.

[84] Yao G Z, Yap F F, Chen G, Li W H, and Yeo S H. MR damper and its application for semi-active control of vehicle suspension system. *Mechatronics*, 2002, 12(7): 963-973.

[85] Liao W H and Wang D H. Semi-active vibration control of train suspension systems via magneto-rheological dampers. *J. of Intelligent Material Systems and Structures*, 2003, 14(3): 161-172.

[86] Guo D L, Hu H Y, and Yi J Q. Neural Network Control for a Semi-Active Vehicle Suspension with a Magneto-rheological Damper. *J. of Vibration and Control*, 2004, 10(3): 461-471.

[87] Karnopp D C, Crosby M J, and Harwood R A. Vibration controlling semi-active generators. *J. of Engineering for Industries*, 1974, 96, Sar. B(2): 619-626.

[88] Kempf D, Bonderson L S, and Slafer L I. Real time simulation for applications to ABS development. *SAE Paper No.* 870336, 1987.

[89] Hanselmann H. Hardware-in-the-loop simulation as a standard approach for development, cost optimization, and production test. *SAE Paper No.* 930207, 1993.

[90] Hanselmann H. DSP-based automotive sensor signal generation for hardware-in-the-loop simulation. *SAE Paper No.* 940185, 1994.

[91] Besinger F H, Cebon D, and Cole D J. Damper models for heavy vehicle ride dynamics. *Vehicle System Dynamics*, 1995, 24(1): 35.

[92] Krohm H. Hardware-in-the-loop simulation for an electronic clutch management system. *SAE Paper No.* 95xxxx, 1995.

[93] Balike M, Rakheja S, and Hoa S V. Study of an energy dissipating under-ride guard using hardware-in-the-loop. *Proc. of the Symposium on Recent Advances in Vehicle Systems and Technologies, CSME Forum 98, Toronto, Canada*, 1998.

[94] Jolly M R and Miller L R. The control of semi-active dampers using relative feedback signals. *Society of Automotive Engineers*, paper No. 892483, 1989.

[95] Carrera web site, http://www.carrerashocks.com, 2002.

[96] Lord Corporation web site, http://www.lord.com, 2002.

[97] Kim C and Ro P I. A sliding mode controller for vehicle active suspension systems with nonlinearities. *Procs. of the Inst. of Mech. Engrs., Part D, J. of Automobile Engineering*, 212: 79-92, 1999.

[98] Damien T M et al. Pavement profiling various pavements: Ottawa/ Smith Falls. *John Emery Geotechnical Engineering*, 1992.

[99] Raj R I S. Influence of road roughness and directional maneuvers on the dynamic performance of heavy vehicle. *MASC Thesis*, *Concordia University*, 1998.

[100] Huang Y H, Gao W, and Huang J C. Variable structure control: a survey. *IEEE Transactions on Industrial Electronics*, 40(1), 1993.